Characterization of radiation damage induced by swift heavy ions in graphite

Zur Erlangung des akademischen Grades Doktor-Ingenieur (Dr.-Ing.)
genehmigte Dissertation von M.Eng. Christian Hubert aus Aschaffenburg
Tag der Einreichung: 01.02.16, Tag der Prüfung: 15.04.16
Darmstadt, Mai 2016 — D 17

1. Gutachten: Prof. Dr. Christina Trautmann
2. Gutachten: Prof. Dr. Ralph Krupke

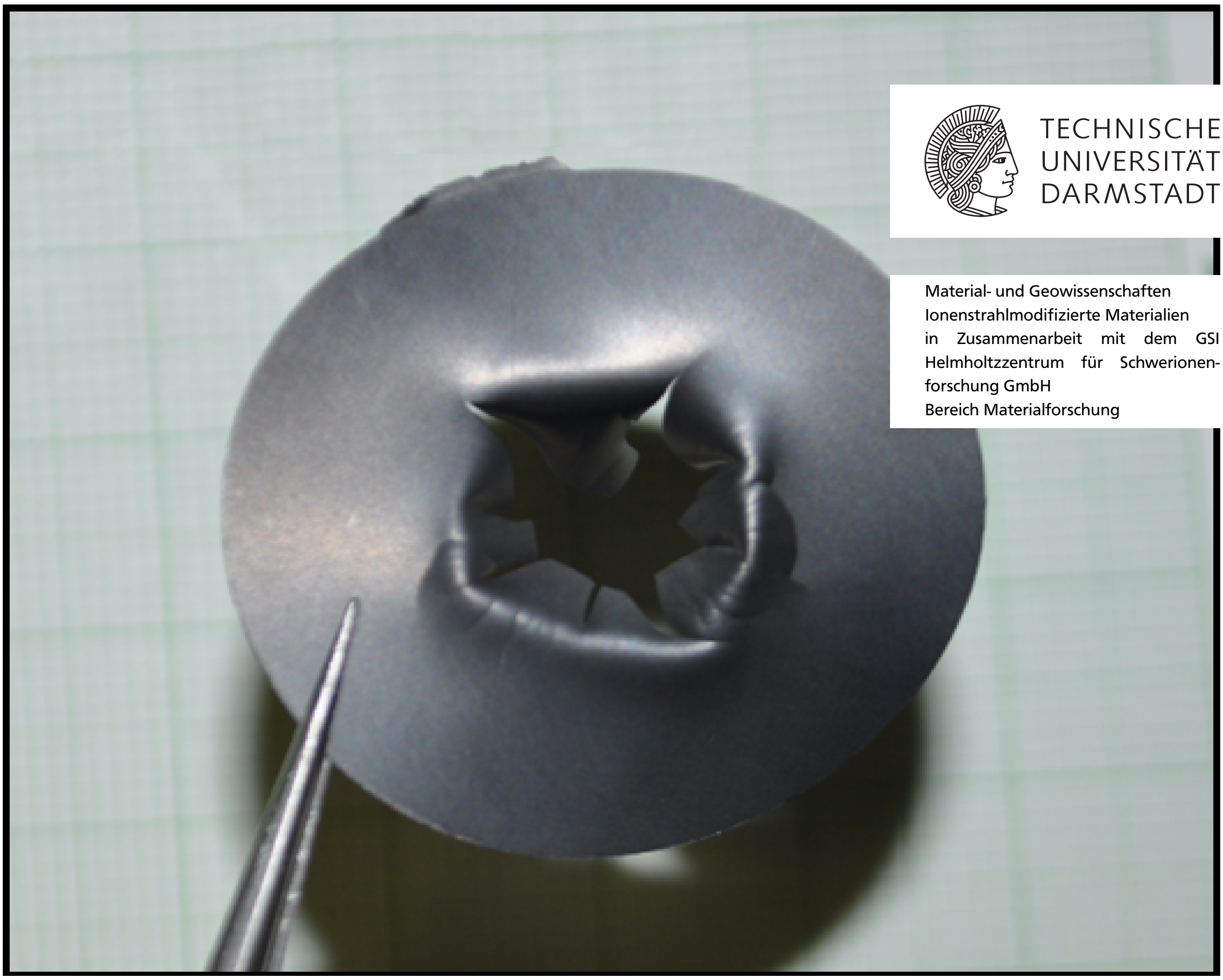

TECHNISCHE
UNIVERSITÄT
DARMSTADT

Material- und Geowissenschaften
Ionenstrahlmodifizierte Materialien
in Zusammenarbeit mit dem GSI Helmholtzzentrum für Schwerionenforschung GmbH
Bereich Materialforschung

Characterization of radiation damage induced by swift heavy ions in graphite

Genehmigte Dissertation von M.Eng. Christian Hubert aus Aschaffenburg

1. Gutachten: Prof. Dr. Christina Trautmann
2. Gutachten: Prof. Dr. Ralph Krupke

Tag der Einreichung: 01.02.16
Tag der Prüfung: 15.04.16

Darmstadt — D 17

Erklärung zur Dissertation

Hiermit versichere ich, die vorliegende Dissertation ohne Hilfe Dritter nur mit den angegebenen Quellen und Hilfsmitteln angefertigt zu haben. Alle Stellen, die aus Quellen entnommen wurden, sind als solche kenntlich gemacht. Diese Arbeit hat in gleicher oder ähnlicher Form noch keiner Prüfungsbehörde vorgelegen.

Darmstadt, den 29.01.16

(Christian Hubert)

Abstract

Graphite is a classical material in neutron radiation environments, being widely used in nuclear reactors and power plants as a moderator. For high energy particle accelerators, graphite provides ideal material properties because of the low Z of carbon and its corresponding low stopping power, thus when ion projectiles interact with graphite is the energy deposition rather low. This work aims to improve the understanding of how the irradiation with swift heavy ions (SHI) of kinetic energies in the range of MeV to GeV affects the structure of graphite and other carbon-based materials. Special focus of this project is given to beam induced changes of thermo-mechanical properties. For this purpose the Highly oriented pyrolytic graphite (HOPG) and glassy carbon (GC) (both serving as model materials), isotropic high density polycrystalline graphite (PG) and other carbon based materials like carbon fiber carbon composites (CFC), chemically expanded graphite (FG) and molybdenum carbide enhanced graphite composites (MoC) were exposed to different ions ranging from ^{131}Xe to ^{238}U provided by the UNILAC accelerator at GSI in Darmstadt, Germany. To investigate structural changes, various in-situ and off-line measurements were performed including Raman spectroscopy, x-ray diffraction and x-ray photo-electron spectroscopy. Thermo-mechanical properties were investigated using the laser-flash-analysis method, differential scanning calorimetry, micro/nano-indentation and 4-point electrical resistivity measurements. Beam induced stresses were investigated using profilometry. Obtained results provided clear evidence that ion beam-induced radiation damage leads to structural changes and degradation of thermal, mechanical and electrical properties of graphite. PG transforms towards a disordered sp^2 structure, comparable to GC at high fluences. Irradiation-induced embrittlement is strongly reducing the lifetime of most high-dose exposed accelerator components. For irradiation temperatures above 200 °C damage formation is mitigated due to defect annealing. Thus a controlled temperature of accelerator components is desirable in order to increase the lifetime. This thesis contributes to a better understanding of radiation damage in swift heavy ion-exposed graphite with the aim to optimize the design of beam catchers and production targets for secondary ion beams for the Super Fragment Separator (Super-FRS) at FAIR. Moreover, the results of this work provide important input data for simulations to describe the beam response and lifetime of high-dose exposed critical accelerator components.

Abstract

Graphit ist ein klassisches Material für den Einsatz in der Umgebung von Neutronenstrahlen und wird weit verbreitet in Kernreaktoren und Atomkraftwerken als Moderator eingesetzt. Für Teilchenbeschleuniger bietet Graphit ebenfalls ideale Materialeigenschaften wegen der geringen Ordnungszahl Z und des daraus folgenden geringen Bremsvermögens welches wiederum zu einer relativ geringeren Energiefreigabe führt. Diese Arbeit hat das Ziel das Verständnis der Interaktionen von Hoch energetischen Schwerionen (SHI) in Energiebereichen von MeV zu GeV mit der Struktur von Graphit und anderen Kohlenstoffbasierten Materialien zu verbessern. Ein spezieller Fokus liegt hierbei auf den Ionenstrahlinduzierten Veränderungen der thermo-mechanischen Materialeigenschaften. Zu diesem Zweck wurden Hoch orientierter pyrolytischer Graphit (HOPG) und glasartiger Kohlenstoff (GC) (beide fungieren als Modellmaterialien), isotropischer polykristalliner Graphit hoher Dichter (PG) und andere kohlenstoffbasierte Materialien wie Kohlenstofffaser Kohlenstoffkomposite (CFC), chemisch expandierter Graphit (FG) und Molybdencarbid verstärktes Graphitkomposit (MoC) mit verschiedenen Ionenspezies von ^{131}Xe bis zu ^{238}U bestrahlt, die vom UNILAC Beschleuniger am GSI Helmholtzzentrum in Darmstadt, Deutschland, bereit gestellt wurden. Um Änderungen der Struktur zu untersuchen wurden zahlreichen in-situ und ex-situ Experimente durchgeführt, darunter Ramanspektroskopie, Röntgenbeugung und Röntgenphotoelektronenspektroskopie. Veränderungen der thermo-mechanischen Eigenschaften wurden mit der Laser-Flash Methode, dynamischer Differenzkalorimetrie, Mikro/Nanoindentierung und 4-Punkt Widerstandsmessungen untersucht. Die gewonnen Ergebnisse sind deutliche Beweise für eine Änderungen der Struktur von Graphit und in Folge dessen einer Verminderung der thermischen, mechanischen und elektrischen Materialeigenschaften auf Grund von Ionenstrahlinduzierten Strahlenschäden. PG ändert seine Struktur hin zu einer ungeordneten sp^2 Struktur welche bei sehr hohen Fluenzen der von GC ähnelt. Ionenstrahlinduzierte Versprödung reduziert die Lebenszeit der meisten Beschleunigerkomponenten die hohen Strahlendosen ausgesetzt sind. Bei Bestrahlungstemperaturen von mehr als 200 °C wird die Entstehung von Strahlenschäden auf Grund Defektausheilung deutlich abgeschwächt. Deshalb ist eine Kontrolle der Temperatur für Beschleunigerbauteile wünschenswert, um die Laufzeiten zu erhöhen. Diese Thesis trägt zu einem besseren Verständnis von Strahlenschäden durch hoch energetische Schwerionen in Graphit bei, mit dem Ziel das Design von Strahlfängern und Produktionstargets für sekundäre Strahlen des Super Fragment Separator (Super-FRS) Experiments an FAIR zu optimieren. Des Weiteren liefern die Ergebnisse dieser Arbeit wichtige Daten für Simulationen zur Bestimmung der Lebenszeit und

des Verhaltens während der Bestrahlung und von kritischen Beschleunigerbauteilen die hohen Strahlendosen ausgesetzt sind.

Contents

1 Introduction and Motivation **8**

2 Radiation effects of energetic ions in solids **10**

2.1 Energy loss 10

2.1.1 Nuclear energy loss 12

2.1.2 Electronic energy loss 13

2.2 Track formation and defect creation mechanism 14

2.2.1 Coulomb explosion 15

2.2.2 Inelastic thermal-spike model 16

3 Graphite and carbon-based materials **18**

3.1 Description of the used materials 18

3.1.1 Highly Oriented Pyrolytic Graphite (HOPG) 20

3.1.2 Polycrystalline Graphite (PG) 21

3.1.3 Other carbon materials (CFC, FG, GC) 21

3.2 Irradiation induced defects in graphite 22

3.3 Recombination and transformation of defects 23

4 Experimental **29**

4.1 Used specimen 29

4.2 Irradiation 29

4.3 Post irradiation analysis 33

4.3.1 Raman spectroscopy 34

4.3.2 X-ray diffraction (XRD) 42

4.3.3 Laser flash analysis (LFA) 46

4.3.4 Nano/Micro-indentation 51

4.3.5 Electrical resistivity 58

4.3.6 Profilometry study of beam induced stress/swelling 60

4.3.7 X-Ray Photoelectron Spectroscopy (XPS) 62

4.3.8 Differential Scanning Calorimetry (DSC) 64

4.3.9 Scanning electron microscopy (SEM) 66

4.4 In situ Measurements 67
4.4.1 X-ray diffraction 67
4.4.2 Raman spectroscopy 68
4.4.3 IR thermography 70
4.4.4 Electrical resistivity 71

5 Results and Discussion **76**
5.1 Beam-induced surface effects in carbon materials studied by SEM 76
5.2 Beam-induced structural changes studied by Raman spectroscopy 79
5.2.1 Post-irradiation investigations 80
5.2.2 In situ experiments at UNILAC 93
5.3 Beam-induced structural changes studied by XRD 98
5.3.1 In situ XRD at M2-beamline at UNILAC 98
5.3.2 Synchrotron radiation XRD 99
5.4 Beam-induced phase transitions and disordering studied by XPS 103
5.5 Beam-induced swelling/stress studied by profilometry 106
5.6 Online monitoring of electrical resistivity degradation during heavy ion irradiation 110
5.7 Beam-induced changes to the thermal diffusivity studied by LFA 113
5.8 Investigation of defect annealing in ion irradiated graphite using DSC 117
5.9 Beam-induced changes of hardness and elastic modulus studied by Micro/Nano-indentation 118
5.10 Influence of the beam flux on the defect creation in carbon materials 131

6 Conclusions and Outlook **136**

7 Acknowledgments **140**

8 Appendix **165**

9 Curriculum Vitae **172**

List of abbreviations

- FAIR - **F**acility for **A**ntiproton and heavy **I**on **R**esearch
- GSI - **G**esellschaft fuer **S**chwer**I**onenforschung
- CERN - **C**onseil **E**uropéen pour la **R**echerche **N**ucléaire
- HOPG - **H**ighly **O**riented **P**yrolytic **G**raphite
- PG - **P**olycrystalline **G**raphite
- FG - **F**lexible **G**raphite
- GC - **G**lassy **C**arbon
- CFC - **C**arbon **F**iber **C**omposite
- MoC - **M**olybdenum **G**raphite
- XRD - **X-R**ay **D**iffraction
- XPS - **X**-ray **P**hotoelectron **S**pectroscopy
- DSC - **D**ifferential **S**canning **C**alorimetry
- SHI - **S**wift **H**eavy **I**on
- LSS - **L**indhard **S**charff **S**chott
- HR-TEM - **H**igh **R**esolution-**T**ransmission **E**lectron **M**icroscopy
- SEM - **S**canning **E**lectron **M**icroscopy
- UNILAC - **Uni**versal **L**inear **Ac**celerator
- SIS 18 - **S**chwer**i**onen**s**ynchrotron-18(18 Tm bending power)
- LHC - **L**arge **H**adron **C**ollider
- FRS - **Fr**agment **S**eparator
- SRIM - **S**topping and **R**anges of **I**ons in **M**atter
- SNG - a graphite grade

1 Introduction and Motivation

The continuous effort to increase the beam energy and intensity of high-power accelerator facilities like the Large Hadron Collider (LHC) at CERN in Geneva or the planned Facility for Antiproton and Ion Research (FAIR) in Darmstadt increases the demand on radiation-hard materials capable to withstand extreme pressure, temperature and ionizing radiation conditions. When high-intensity heavy ion beams interact with target materials, they can induce severe radiation damage, thermal stress and shock waves which eventually results in failure or even complete destruction of a given component. To increase the lifetime of critical beam-facing components, intelligent design and material solutions are needed to fulfill the demanded requirements. Due to its various excellent properties in neutron radiation environments, graphite is a classical material being widely used for fission, fusion and accelerator applications. This work is part of an effort to characterize radiation damage by swift heavy ions (SHI) in graphite, which will be used in beam facing components. For such components, materials of a low atomic number (low-Z materials) are of interest because the energy deposition scales with Z and thus is much lower in carbon-based materials than, e.g., in metals. Another important property for beam facing materials is a high thermal conductivity in order to easily dissipate the thermal load generated by the heavy ion beam and allow for efficient cooling. For many components a low electrical resistivity and high mechanical strength is of fundamental importance. Considering these properties and their evolution with increasing radiation damage and temperature, the figure of merit of graphite is very high compared to other materials. Swift heavy ions interact differently with matter than neutrons which are typically responsible for radiation damage in nuclear reactors. In the MeV-GeV energy range, SHI transfer their kinetic energy to the target electrons and not directly to the atoms as the neutrons do. In most insulators SHI create tracks, narrow damage trails formed along the trajectory of each projectile. Tracks form in most insulators and only in a few selected metals. In graphite tracks form as well, but the process requires ions of rather high energy loss (dE/dx). The radiation hardness of graphite is based on graphene - the building block of a graphite crystal - with strong 2-dimensional bonds and the ability to quickly anneal and recombine defects from ion impacts - even at temperatures around 25 °C [1]. This work is based on the current knowledge about SHI-induced radiation damage in graphite that has been established by many research groups. Liu et al. [2, 3, 4, 5] and Tripathi et al. [6] studied the effect of swift heavy ions with energies in the range of GeV on highly oriented pyrolytic graphite (HOPG). By scanning tunneling microscopy, they characterized track formation and damage creation at the sample surface. Raman spectroscopy is a very powerful tool to characterize disordering in graphite and in other carbon-based materials. Due to its simple nature combined with fast and reliable data acquisition, Raman spectroscopy is a very suitable method as demonstrated by the extensive work of Ferrari et al. [7, 8] and Cançado et al. [9, 10]. They showed that Raman spectroscopy is able to characterize disordering in graphene and graphite and that the three main features of a graphite Raman spectrum (D, G and 2D bands) contain information about the inherent structure of the specimen. Nano-indentation is a powerful tool to determine the mechanical properties of graphite. Oliver and Pharr [11, 12] modernized this technique and made it viable for many applications. Within this work the following carbon-based materials were irradiated and tested: (1) highly oriented pyrolytic graphite as a model for a single-crystalline graphite, (2) glassy carbon (GC) as a model material for completely disordered graphite, (3) quasi-isotropic polycrystalline graphite (PG) of different grades and densities as promising candidate for accelerator components, (4) carbon fiber composites (CFC) as material for collimators, (5) chemically expanded graphite (flexible graphite) as a possible material for beam catchers and collimators and (6) molybdenum-carbide graphite composite (MoC) as a new material type being presently developed for beam collimation systems.

2 Radiation effects of energetic ions in solids

This chapter focuses on the basic interaction processes of high-energy charged particles with solid matter. High-energy ions that interact mainly with the electronic subsystem of the target are commonly called swift heavy ions (SHI). Common models, defect mechanisms and resulting defects will be introduced and briefly discussed. Currently the formation of tracks by swift heavy ions is best described by the so called inelastic thermal spike model. Another model describing track formation in solids is represented within the coulomb explosion model.

2.1 Energy loss

When a fast charged particle collides with a solid, it decelerates and deposits its kinetic energy in the solid. The energy is first deposited to the electrons of the solid and subsequently via electron-phonon coupling to the atoms. Most of that energy leads to luminescence and lattice vibrations (heat), but a significant part is used to create defects, such as vacancies, interstitials, lattice distortions or even phase changes and amorphization [13]. In most insulators, in many semiconductors and in some metals the ion produces a trail of damage along its trajectory, the so called ion track [14]. While decelerating, the energy loss of the ions to the surrounding lattice depends on the ion velocity. The amount of energy transferred over distance unit is generally referred to as the energy loss $S = -(dE/dx)$ or the so called stopping power with the most commonly used unit of keV/nm. This deceleration process (energy loss) of the ion can be divided in 2 different regimes (nuclear and electronic) that are corresponding to different processes as depicted in figure 2.1 [15]. Which of these mechanisms is the dominant one depends on the velocity (specific energy) of the ion. For specific energies above 1 MeV/u, electronic excitation and ionization processes are the dominant mechanics. They are in general referred to as electronic stopping or electronic energy loss. For energies below 100 keV/u mostly elastic collisions and recoil losses account for the stopping and they are generally called nuclear stopping or nuclear energy loss. Electronic stopping events mainly transfer energy to the electrons, while nuclear stopping events transfer energy directly to the target atoms. The total energy loss is the sum of nuclear and electronic stopping.

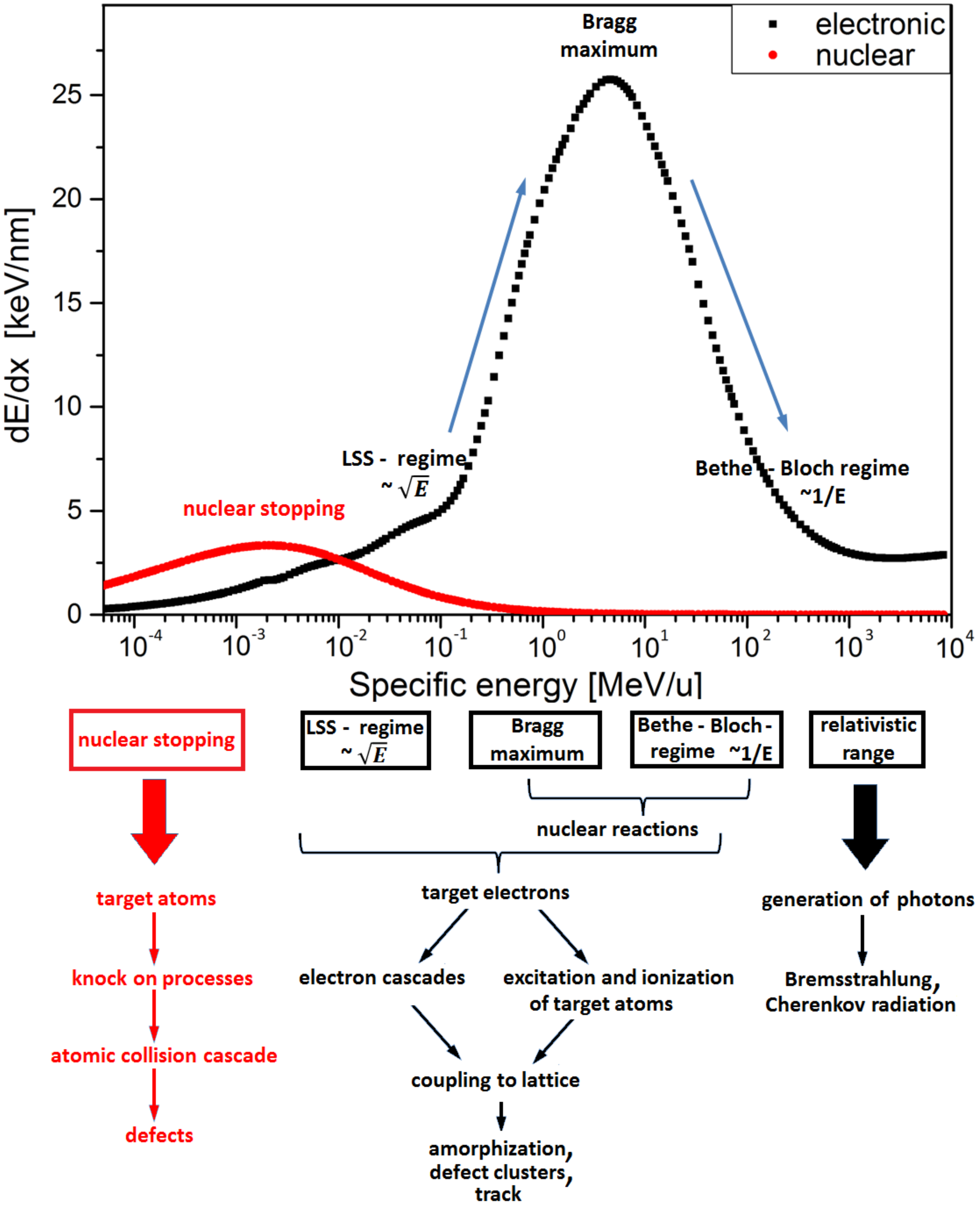

Figure 2.1: Energy loss dE/dx of ^{238}U in carbon with a density of 1.84 g/cm^2 [16]; Representation (top) of the nuclear energy loss(red) and the electronic energy loss (black) as a function of projectile specific energy, with its 3 sub-regimes:1) Lindhard, Scharff, Schott(LSS); 2) Bethe-Bloch; 3) Relativistic;

A single ion activates all the different mechanisms while decelerating in a solid. Which mechanism is the dominant at each corresponding specific energy is represented in figure 2.1 which shows the nuclear and electronic stopping powers as a function of specific energy (projectile velocity) [16, 17]. With increasing specific energy nuclear stopping events like collisions and recoils have a smaller cross section [17]. If enough energy is available to penetrate the Coulomb barrier, nuclear reactions and events like spallation, fragmentation and fission may occur in the target material or in the ion. This depends mainly on the Z of the target atom and projectile and leads to the unique feature that incoming ions exhibit an energy loss decrease with energies above the so called Bragg maximum depicted in figure 2.2 [16, 17]. Ions with relativistic energies (above a specific energy of 10^4 MeV/u) generate photons, via Bremsstrahlung (X-rays and γ-rays) and Cherenkov radiation. At relativistic speeds the energy loss increases again the closer the ions get to the speed of light [17].

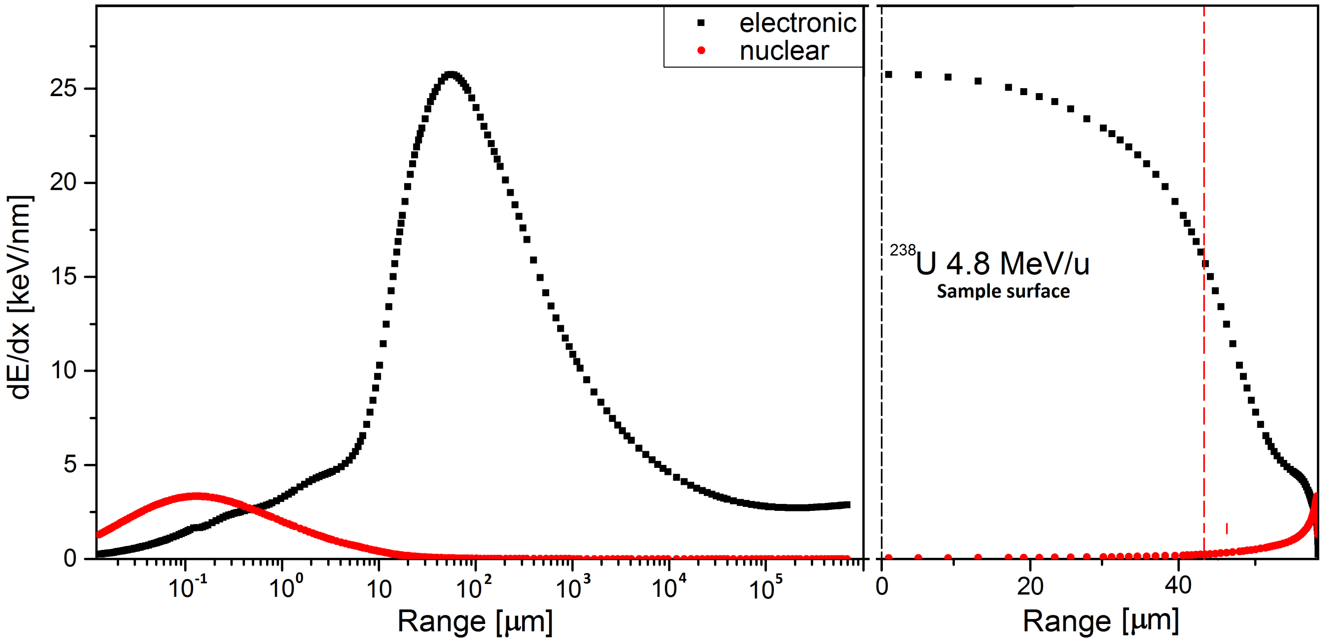

Figure 2.2: Presented is the energy loss dE/dx of an ^{238}U ion in graphite with a density of 1.84 g/cm^2; Left: dE/dx as a function of the particle range [16]; Right: dE/dx of 4.8 MeV/u ^{238}U as a function of ion-penetration depth. The black dashed line represents electronic stopping power, the red dashed line indicates the range dominated by nuclear stopping

2.1.1 Nuclear energy loss

Heavy ions with specific energies below 100 keV/u experience mainly (but not exclusively) nuclear energy loss via atomic collisions when interacting with matter. Nuclear energy loss for graphite is starting to play a role around the last 10 to 5 μm of the ion trajectory as shown in figure 2.2 [16]. Close to the stopping of the ion, nuclear energy loss dominates, where ions hit and recoil target atoms in elastic collisions, so called knock on processes, and cause further collision cascades [17]. These kind of elastic collisions lead to defect formation in the lattice. Usually vacancies and interstitials are the most important defects caused by nuclear energy loss. When a target atom is kicked out of its initial position in the lattice, a vacancy is created where the atom was positioned within the lattice. The atom kicked into a new position is called an interstitial. These displacements of target atoms will initiate large scale lattice distortions and/or lead to stacking order defects. It is also possible for vacancies to form larger clusters, dislocation loops and voids. The nuclear energy loss is significant in the last few μm of the ion range. For the samples discussed in this thesis these effects are negligible when surface characterization methods like Raman spectroscopy or nano-indentation are used. When the samples are measured along the ion trajectory with sufficient vertical resolution, defects induced by predominant elastic collisions can be observed in the last 10 μm region at the end of the ion tracks.

2.1.2 Electronic energy loss

Heavy ions with specific energies above 1 MeV/u experience mainly electronic energy loss. Electronic energy loss produces ionization and excitation of the target atoms. The momentum transfer of a binary collision process between a projectile and an electron is limited due to the small electron mass. Due to this limited energy transfer, the ion is not deflected from its trajectory. These changes in the ions trajectory (lateral- and transversal-scattering) usually only occur when nuclear energy loss starts to become important. The electronic energy loss of an ion in a medium depends mainly on Z and on the energy v_p of the ion. It is generally described by the Bethe-Bloch equation which considers a momentum transfer to the target electrons within a Coulomb potential and also adds several corrections [17, 18, 19].

$$\left(-\frac{dE}{dx}\right)_e = \frac{4 \cdot \pi \cdot (Z_p^{eff})^2 \cdot Z_t \cdot N_t}{m_e \cdot v_p^2} \times \left(ln \cdot \frac{2 \cdot m_e \cdot v_p^2}{I} - ln \cdot (1-\beta) - \beta^2 \right) \tag{2.1}$$

with:

- Z_p^{eff} = effective charge of the projectile
- Z_t = atomic charge of the target material
- N_t = amount of target atoms per volume unit
- m_e= electron mass
- e = electron charge
- I = effective ionization potential of the target material

- β = ratio between ion velocity and speed of light

The equation shows that dE/dx is mainly a function of $(Z_p^{eff})^2$ and Z_t. This explains why materials with a low Z are favorable. In order to maximize the radiation-induced damage, high Z projectiles are used to create large dE/dx within the samples.

2.2 Track formation and defect creation mechanism

As mentioned above, the highly charged swift heavy ions have a large ionization potential as the electronic stopping is the main way to transfer the kinetic energy to the lattice. The ionization of the target atoms produces free electrons that further ionize more atoms, causing ionization cascades [17]. it is also possible that Auger electrons are created if electrons are ejected from a lower shell. These secondary electrons are called δ-electrons [17]. It is important to note that these ionization processes happen on a very small time scale within the order of 10^{-17} to 10^{-16} s. Around 10^{-14} s the ionization cascades of all δ-electrons have ended [14]. The ionizing projectile transfers its energy according to a radial distribution of around $\frac{1}{r^2}$ where r represents the distance to the ions trajectory. This leads to the formation of cylindrical damage regions. The size and if these ion tracks are created depends on the target material and the dE/dx of the projectile [17, 20]. Ion tracks typically have a diameter of up to 10 nm. For carbon and graphite the diameter of these tracks is 2 to 5 nm [21]. Within the damaged region, the defect distribution is not homogeneous. The defect density is highest close to the ion trajectory and is surrounded by a halo of lower defect densities.

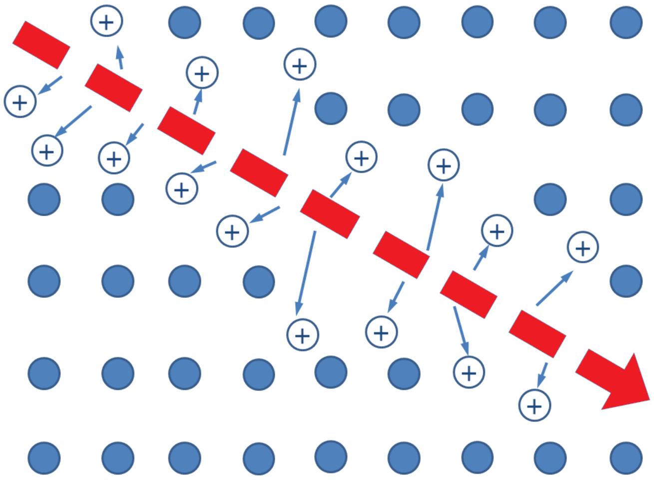

Figure 2.3: Ion displacements along the ion track of a fast moving ion inside of a solid target adapted from [17]

The ionization through ionic displacements of an ion passing through a solid target is presented in figure 2.3. The figure presents a swift, highly charged particle that enters a target lattice. The projectile is stripped of its electrons and δ-electrons are radially emitted along the trajectory following the ionization of the lattice electrons. Ionization cascades are triggered by the δ-electrons. These ionization stages occur without the interaction of the lattice atoms. A coupling to the target lattice is only possible after a relaxation time of around 10^{-13} s, corresponding to one lattice vibration [17]. What mechanism is responsible for the transfer of the kinetic energy of the electrons to the lattice is still not fully understood. The models that are accepted today are the Coulomb explosion (or ionic spike) model and the inelastic thermal-spike model [22, 23].

2.2.1 Coulomb explosion

The Coulomb explosion describes what happens in the initial stage directly after the impact of the ion in the solid target. At this time an energy transfer by heat (lattice vibrations) is not possible yet. The model was first introduced by Fleischer et al. [24] in the 1960s for describing the track formation process in an insulating material. This model splits the track formation process into several sub steps. First the ion passes through the target and is forming an ion cloud along its trajectory with the δ-electrons beeing ejected outwards, orthogonal to the path of the ion. This leaves behind a cylindrical volume in the target atomic system with positively charged ions around the ion trajectory. Now these positively charged target atoms start to repel each other and distort the lattice [14, 24]. This formation of many interstitial positions creates large strains on the lattice. As the strain will eventually relax by lattice movements and readjustments, a large core with many vacancies surrounded by many interstitials along the ion trajectory is formed. Due to the many vacancies along the ion path, there is an increase in overall volume, or a decrease in density along the trajectory of the ion, radially distributed from lowest density in the center towards initial density at the border. This phenomenon induces swelling and can be observed experimentally, but is not unique to the Coulomb explosion model. This core with vacancies surrounded by interstitials which creates interstitial planes and other lattice defects and deformations is corresponding to the ion track. Track sizes are in the order of several nm according to the Coulomb explosion model and are highly dependent on the following factors [14, 24, 25]:

- energy of the ion
- charge state of the ion
- mass of the ion
- number of free electrons in the target material
- thermal stability of the target material

2.2.2 Inelastic thermal-spike model

The inelastic thermal-spike model takes another approach how energy is transferred to the lattice. The model was first described by F. Dessauer in 1923 [26]. Since then it has been revised and improved by many other groups over the years [27]. The most recent development has been done by M. Toulemonde [28, 29, 30]. The inelastic thermal spike model concentrates on heat deposited in the electronic subsystem shortly after the ion impact. Energy is initially transferred to the electrons with the consequence that the electronic subsystem is rapidly heated towards temperatures close the Fermi level [31]. This leads to a strong contrast between the hot electrons and cold lattice [29]. This energy is then passed from the electrons to the lattice by electron-phonon coupling, heating up the target lattice. The model describes the evolution of this heating process and heat transfer using the following two differential equations [31].

$$C_e(T_e) \cdot \frac{\partial T_e}{\partial t} = \frac{1}{r} \cdot \frac{\partial}{\partial r}\left(r \cdot K_e(T_e) \cdot \frac{\partial T_e}{\partial t}\right) - g \cdot (T_e - T_a) + A(r,t) \tag{2.2}$$

and

$$C_a(T_a) \cdot \frac{\partial T_a}{\partial t} = \frac{1}{r} \cdot \frac{\partial}{\partial r}\left(r \cdot K_a(T_a) \cdot \frac{\partial T_a}{\partial t}\right) + g \cdot (T_e - T_a) \tag{2.3}$$

with:

- C_a = specific heat of the atoms
- C_e = specific heat of the electrons
- K_a = thermal conductivity of the lattice subsystem
- K_e = thermal conductivity of the electronic subsystem
- T_a = temperature of the lattice atoms
- T_e = temperature of the electronic subsystem
- r = radius
- t = time after initial ion impact
- $A(r,t)$ deposited energy to the electronic subsystem depending on r and t
- g = electron phonon coupling constant

In this equation, only the electron phonon coupling constant g is a free parameter. g is linked directly to the electron mean free path $\lambda = \frac{K_e}{g}$ [30, 31]. The inelastic thermal-spike model is based on the two-temperature model [32] which describes the temperature of the lattice and the electrons in non-equilibrium states. Over time thermal energy from the lattice and electrons diffuses and the two separate systems exchange energy. This heat exchange process is defined by the difference in thermal energy and by g [32]. If the conditions are right, meaning a strong electron-phonon coupling and a melting point lower than the induced temperature increase, the material along the ion path is melting locally. Rapid quenching of this melt results in a ’frozen’ disordered volume. This frozen volume along the ion trajectory is referred to as the ion track and may be defect-rich, amorphous or even have a different phase than the original material [30, 32]. The lack of ion tracks in most metals is explained, as for the Coulomb explosion model, due to an overabundance of free electrons in the lattice of metals. Consequently the energy which is transferred to the electrons can diffuse quickly and thus no melting takes place within the metal lattice, inhibiting the formation of ion tracks [31]. In contrast to the Coulomb explosion model, the inelastic thermal spike model has successfully produced quantitative results such as the evolution of the ion track diameter with the energy loss [30, 32].

3 Graphite and carbon-based materials

3.1 Description of the used materials

The following sections gives a short introduction to graphite and other carbon-based materials. Graphite and carbon-based materials are often the choice for radiation exposed accelerator and reactor components. Carbon is the 6th element in the Mendeleev table (periodic table of elements). The name is derived from the ancient Latin „carbo“ which translates into „coal“. It is located in the 4th main group, being a tetravalent element and a non-metal. For carbon there exist more allotropes than for any other element. The reason is the ability of carbon to form various structures with sp, sp^2 and sp^3 bonds. In nature carbon appears in varying phases composed by the different sp^{1-3} bonds. The most widely known allotropes of carbon are diamond and graphite. The diamond phase consists of tightly bound sp^3 carbon bonds which align to a very dense ($3.5\ to\ 3.53\ g/cm^3$) three-dimensional carbon structure [33]. The less dense graphite phase is a layered structure. Its basic building block is graphene, a hexagonal structure of sp^2 carbon atoms.

In graphene the carbon atoms form a hexagonal structure as shown in Figure 3.1. In the sp^2 hybridized structure, each carbon atom is bound to three other carbon atoms by a strong σ-bond and to one more atom by a significantly weaker π-bond [35, 36]. The distance between two atoms i.e. the bond length of the strong σ-bonds is 1.415 Å. In graphite individual basal planes are layered in an ABAB-stacking order as shown in Figure 3.2 [37]. The distance between two consecutive layers is 3.354 Å respectively. It is also possible to form an ABC-stacking phase as presented in Figure 3.2 which is called rombohedral graphite [35, 36, 37]. While in the two dimensional graphene the π-bond is to one of the neighbor atoms, in a graphite assembly of graphene sheets, this weak π-bond is the connection of adjacent layers and thus forms a semi-metallic system. It was long thought that there are Van der Waal's forces in between graphene layers, but this was disproven when Charlier et al. [38] assigned the forces between the layers to the covalent band-structure of graphite and a subsequent overlap in the delocalized π-electron system of each carbon layer [37]. This lack of a covalent interlayer bond leads to a strong macroscopical anisotropy and is the reason that graphite is very easy to cleave along the layers interface. Single crystalline graphite without any defects and impurities has a theoretical density of $2.27\ g/cm^3$ [35, 36, 39]. The unit cell and 1st Brillouine-zone are depicted in figure 3.3. The unit cell contains two atoms generally referred to as A and B atom and with the corresponding lattice vectors (a_1,a_2,b_1 and b_2) it spans the hexagonal honeycomb structure of graphene.

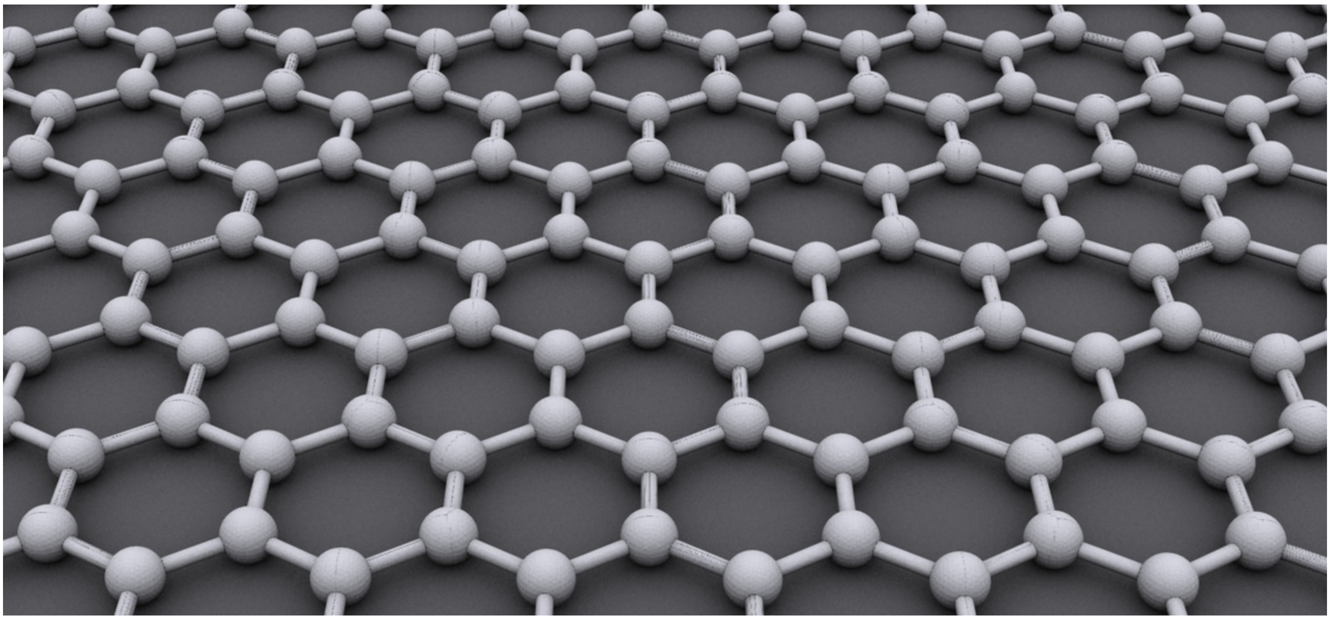

Figure 3.1: Schematic drawing of a graphene sheet adapted from [34]

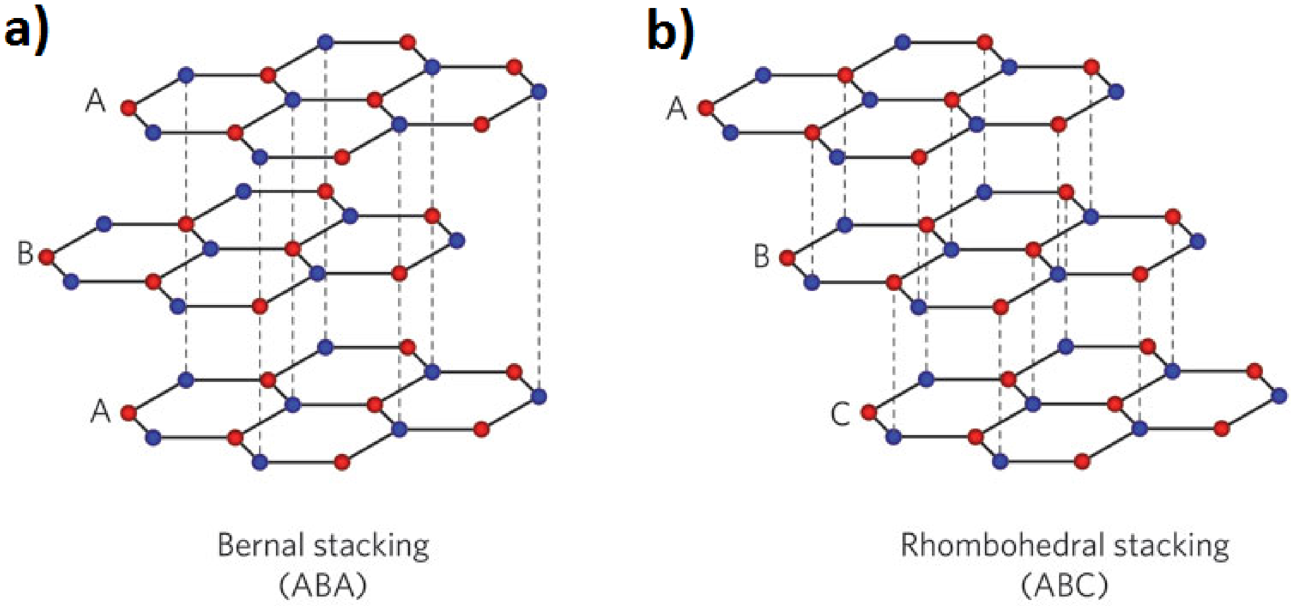

Figure 3.2: a) Basal planes stacked as in graphite (ABAB); b) Basal planes stacked as in rombohedral graphite(ABC); adapted from [40]

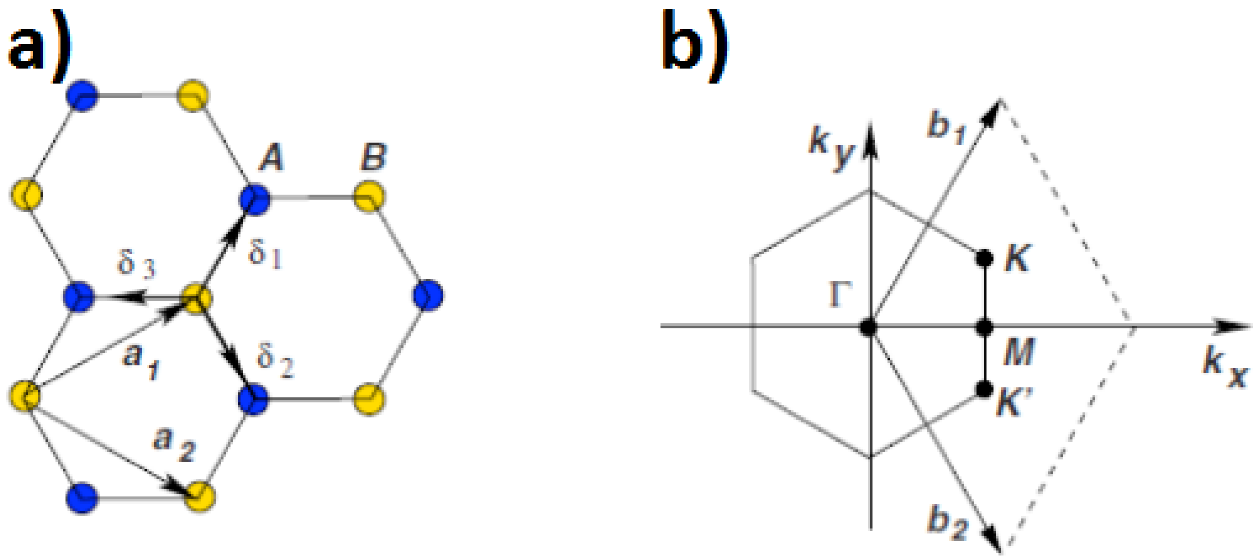

Figure 3.3: a) Lattice structure of graphene with unit cell containing two atoms (A and B), the lattice vectors of the unit cell (a_1 and a_2) and the nearest neighbor vectors (δ_1, δ_2 and δ_3); b) $1st$ Brillouin zone of the graphene unit cell. The $K$and the K' point are the locations of the Dirac cones; adapted from [41]

3.1.1 Highly Oriented Pyrolytic Graphite (HOPG)

Highly Oriented Pyrolytic Graphite (**HOPG**) can be regarded as a model system for a perfect graphite crystal. It consists of many layers of graphene stacked together in an ABAB arrangement. These columnar perfect graphite crystals are stacked together to form the bulk HOPG. Depending on the mosaic spread - the distribution in regard to angular orientations of the columnar graphite crystals to each other - there are three different grades available. The term mosaic spread originates from the x-ray crystallography. It describes the full width at half maximum (FWHM) of the (002) diffraction reflex. Imperfect alignment of the graphite crystals within HOPG will lead to a broader (002) diffraction reflex. Thus the mosaic spread describes directly the grade of the HOPG using the FWHM of a Cu-K_α rocking curve measured in degree [42]. The ZYA-grade is the best grade of graphite available with a corresponding mosaic spread of $0.4° \pm 0.1°$. Grade ZYB is the second purest grade with a mosaic spread of $0.8° \pm 0.2°$ and finally ZYH-grade contains all forms with larger spread angles than 0.8° up to 3.5° ±1.5° [43]. Available thicknesses on the market range between 1 and 2 mm depending on grade and manufacturer. Typical domain size of HOPG is between 1 and 10 μm in plane and ≥0.1 μm perpendicular to the basal planes [44, 45]. The density of HOPG is between 2.25 g/cm^3 and 2.27 g/cm^3. This material is ideal for an in-depth analysis of the general defect creation in graphene and graphite grains because it is very easy to cleave. Furthermore Raman-spectroscopy can be used to quickly and accurately characterize structural changes due to irradiation. Apart from being a model for the graphite crystal, HOPG is also similar to the fibers in Carbon Fiber carbon Composites (CFCs) which are composed of rolled basal planes. The HOPG samples used in this work were supplied by the manufacturers **Momentive** and **NT-MDT** in grade ZYB with the dimensions of 12 mm × 12 mm × 2 mm. For irradiation, the samples where cleaved to thicknesses from 300 μm to 500 μm.

3.1.2 Polycrystalline Graphite (PG)

Polycrystalline Graphite (**PG**) represents the attempt to create a quasi-isotropic material out of small graphite grains. Nuclear grade graphite as the used SIGRAFINE®6650 (previously known as R6650, RINGSDORFF®, SIGRAFORM®, SIGRAMENT®and CRYSTAL-SIL®) from SGL-carbon has a density of 1.84 g/cm^3. The orientation of the graphite grains is random and can be considered isotropic over the bulk volume. The average grain size for the SIGRAFINE®6650 is 7 to 8 μm. Due to its mechanical isotropy, high radiation hardness and large availability, graphite has become a classical candidate for radiation exposed accelerator components. It is also widely used in nuclear reactors as a moderator. For beam intercepting devices at FAIR and at other high power high energy accelerators, graphite and carbon based materials are generally considered to have a very favorable figure of merit in comparison to other materials.

3.1.3 Other carbon materials (CFC, FG, GC)

There are many other carbon based materials which find use in accelerator applications. Flexible Graphite (**FG**) for example SIGRAFLEX® from the SGL-Carbon group is an expanded graphite. It has a very high flexibility at a low density (0.7 - 1.3 g/cm^3) and it represents a possible material for beam-catchers. Its shock absorbing property makes it less prone to succumb to impacts and shock waves and the very high thermal conductivity (180 - 200 W/K·m) is ideal to diffuse the heat generated by the ion beam. The structural flexibility and high impact resistance comes at the cost of a very low elasticity and hardness, which makes larger freestanding structures without additional mechanical support a challenge. Over all, the Flexible Graphite proved to be a very radiation hard material that resists even high intensity beam duty cycles without major damage. Materials used in this work are summarized in table 4.1.

Glassy carbon (**GC**) from the manufacturer **HTW** (HochTemperaturWerkstoffe GmbH) was used in an approach to understand how amorphous carbon material behave under irradiation and how their physical properties can be changed by the heavy ion beam. Glassy carbon acted as a model material for graphite that has been severely disordered by the ion beam. In glassy carbon, the carbon atoms are mostly sp^2 hybridized and are aligned similar to graphite in hexagonal systems. But additional pentagons and heptagons bend graphite planes and distort them.

The manufacturer **HTW** describes the structure of GC related to fullerenes where pentagons and heptagons are distributed among hexagons to form curved graphite planes [46]. The result is a highly disoriented interwoven structure that has densities between 1.42 and 1.54 g/cm^3 (depending on the grade) and is quite strong in terms of mechanical stability (35 GPa Youngs's modulus). This model would also explain the key features of the GC, namely low reactivity, low density and high hardness and elasticity [47]. TEM pictures of the GC structure can be viewed in the appendix (8.5).

Carbon fiber-carbon composites (**CFCs**) represent an attempt to reinforce a graphite matrix with carbon fibers for mechanical strengthening and increased thermal conductivity. The results are an overall increased elasticity and hardness in fiber direction, while maintaining the structural integrity perpendicular to the fibers by the graphite matrix. CFCs are planned to be used in beam line applications like beam collimation systems or beam dumps.

Molybdenum Graphite (**MoC**) is the result of latest research to create new material solutions for high energy density deposition. Even though the material will not be discussed extensively in the thesis, it is mentioned here to broaden the view on possible materials. To create this compound, molybdenum grains are sintered together with graphite flakes and carbon fibers. The molybdenum forms carbide particles strengthening the matrix. This drastically lowers the directional anisotropy of the material since "pull-out" or "slip and slide processes" between matrix and fibers are largely reduced.

The appendix (chapter 8) provides, if available, the complete data sheets for the relevant materials mentioned in this chapter.

3.2 Irradiation induced defects in graphite

The following sections will focus primarily on the defect creation in graphite. A consequence of ion irradiation and track formation, as discussed in the previous section, many different types of defects are quenched in the hexagonal layered material. The basic type of defects are Frenkel pairs consisting of vacancy and interstitial [48]. Vacancies and interstitials (figure 3.4) are the first step towards larger defects. In carbon, single vacancy and interstitial defects are very mobile (vacancies are more mobile than interstitials but limited in their range) and can either quickly anneal and recombine with the lattice or form larger clusters. Di-vacancies tend to form octagons and pentagons, larger vacancy clusters form similar structurs containing pentagons and deformed hexagons as shown in figure 3.4. Even larger vacancy clusters can transition into voids (large vacancies) or dislocation loops as depicted in figure 3.5. Dislocation loops and voids often enable the formation of new planes and stacking faults.

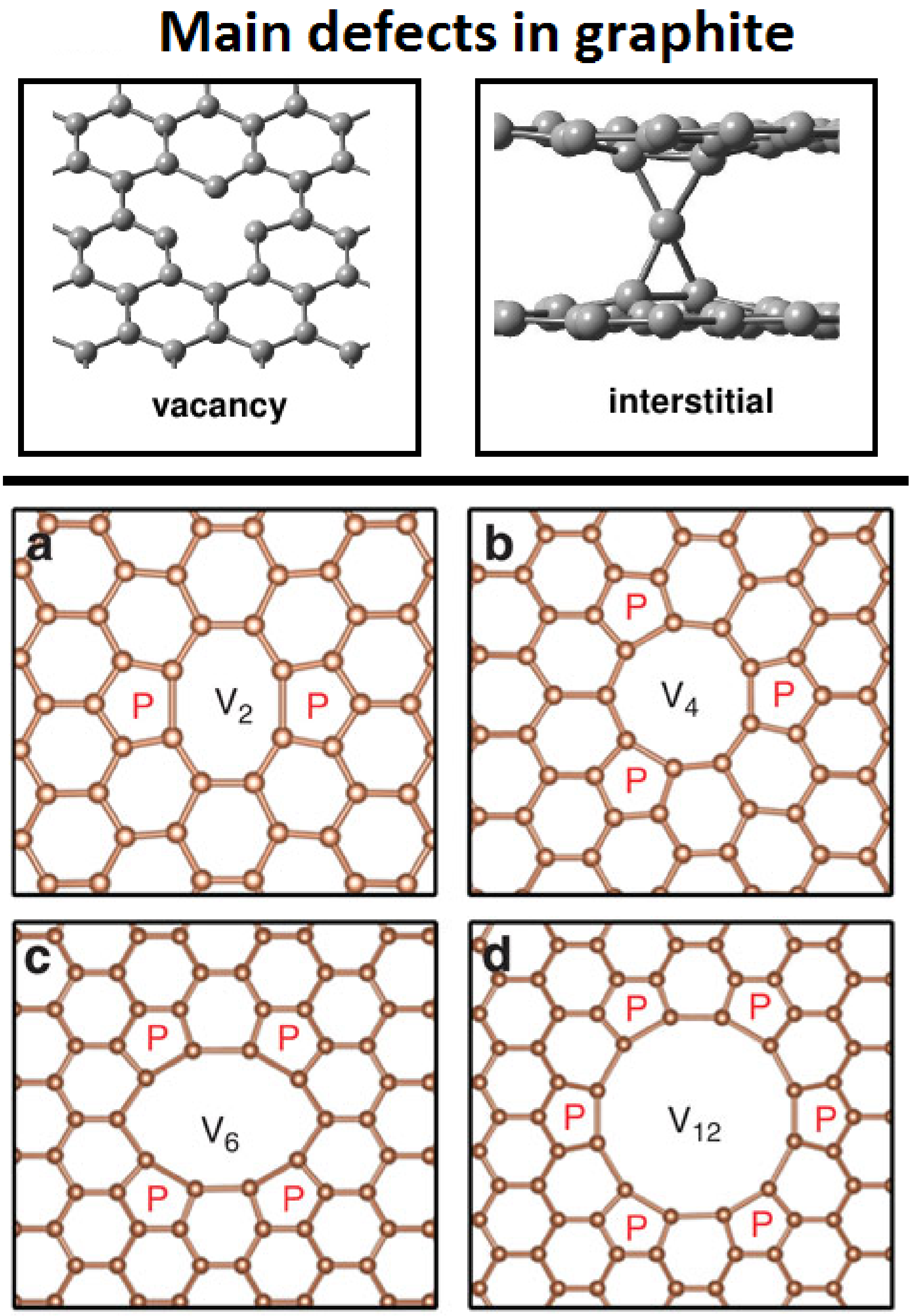

Figure 3.4: Basic defects in graphite induced by swift heavy ions; Top: mono vacancy and interstitial in graphite [49]. Bottom: Relaxed vacancy clusters (a-d) within a graphene layer (n = 2, 4, 6 and 12 respectively); P indicates 5 atom carbon rings and n indicates the number of missing C-atoms [50].

3.3 Recombination and transformation of defects

Recombination of interstitials and vacancies can happen due to energetic ion beam excitation or a thermally-induced mobility increase. When defects recombine, energy is released. A well-known example for this energy release is the Wigner effect [51], often appearing in graphite

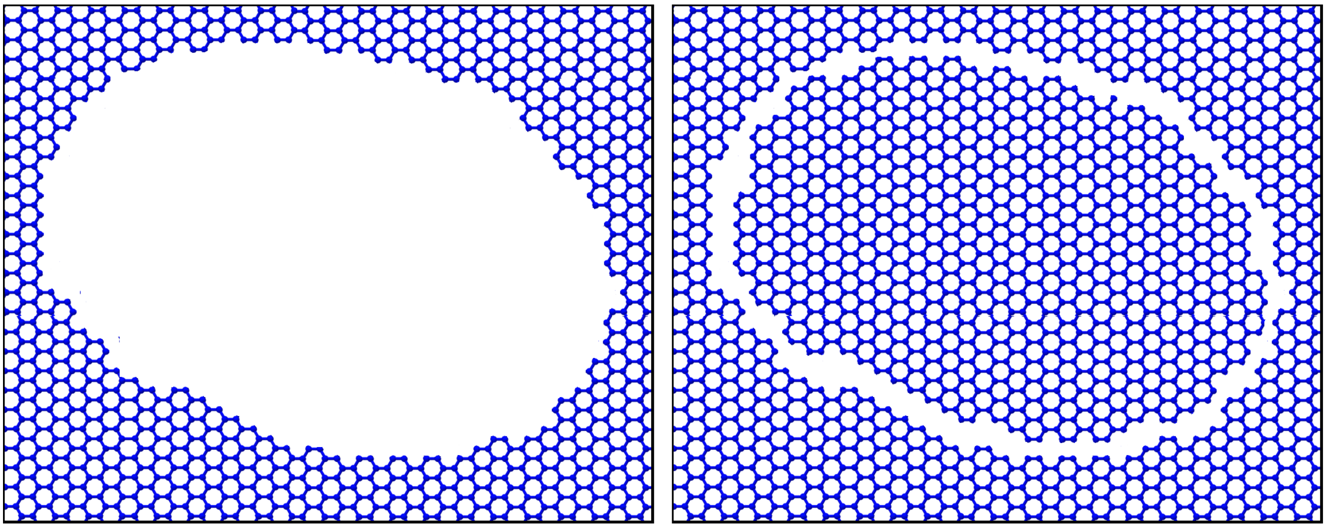

Figure 3.5: Vacancy cluster defects within carbon; Left picture shows a void, the cluster of many vacancies; Right picture shows a dislocation loop.

components of nuclear applications, which describes the excess heat generation by recombination of an intimate Frenkel pair [1, 51]. Many initial defects within the basal planes of graphite are instable and can energetically be optimized or even completely annealed by recombination. By diffusion and recombination, new structures can be created within the hexagonal lattice of graphene. The formation of heptagons, octagons, nonagons or even larger void structures is possible when one or more vacancies fuse together in basal planes, which leads to an energetically more favorable state of the lattice [1]. The formation of these defects is presented in figure 3.6. These larger clusters can be offset points for larger lattice defects such as dislocation and interstitial planes. New disk-like layers such as dislocation loops can lead to a change in the stacking order and of the lattice constant. Stacking order defects are represented in figure 3.7. The most common stacking orders of graphite are the AB (hexagonal) stacking, the AA (orthorhombic) stacking or the ABC (rhombohedral) stacking. After severe disordering of the graphite, a turbostratic graphite phase is formed. The turbostratic graphite structure is a step towards the structure of glassy carbon.

In order for these recombinations to happen an energy barrier has to be overcome [1, 51]. Some structures are energetically more stable than others and thus more likely to form. Since graphite is a layered material, it is interesting to note that even though the in-plane defect diffusion and mobility is large, diffusion between adjacent layers is also possible. If e.g. two mono-vacancies are present in two adjacent layers, both mono-vacancies hold together more energy than a di-vacancy configuration. Thus a formation of one di-vacancy would be energetically more favorable. As a consequence the defect in one layer is annealed and the perfect hexagonal configuration is reinstated, while the other layer forms a di-vacancy via inter layer vacancy diffusion [1]. Since the newly formed state now has a lower energy, the excess energy is

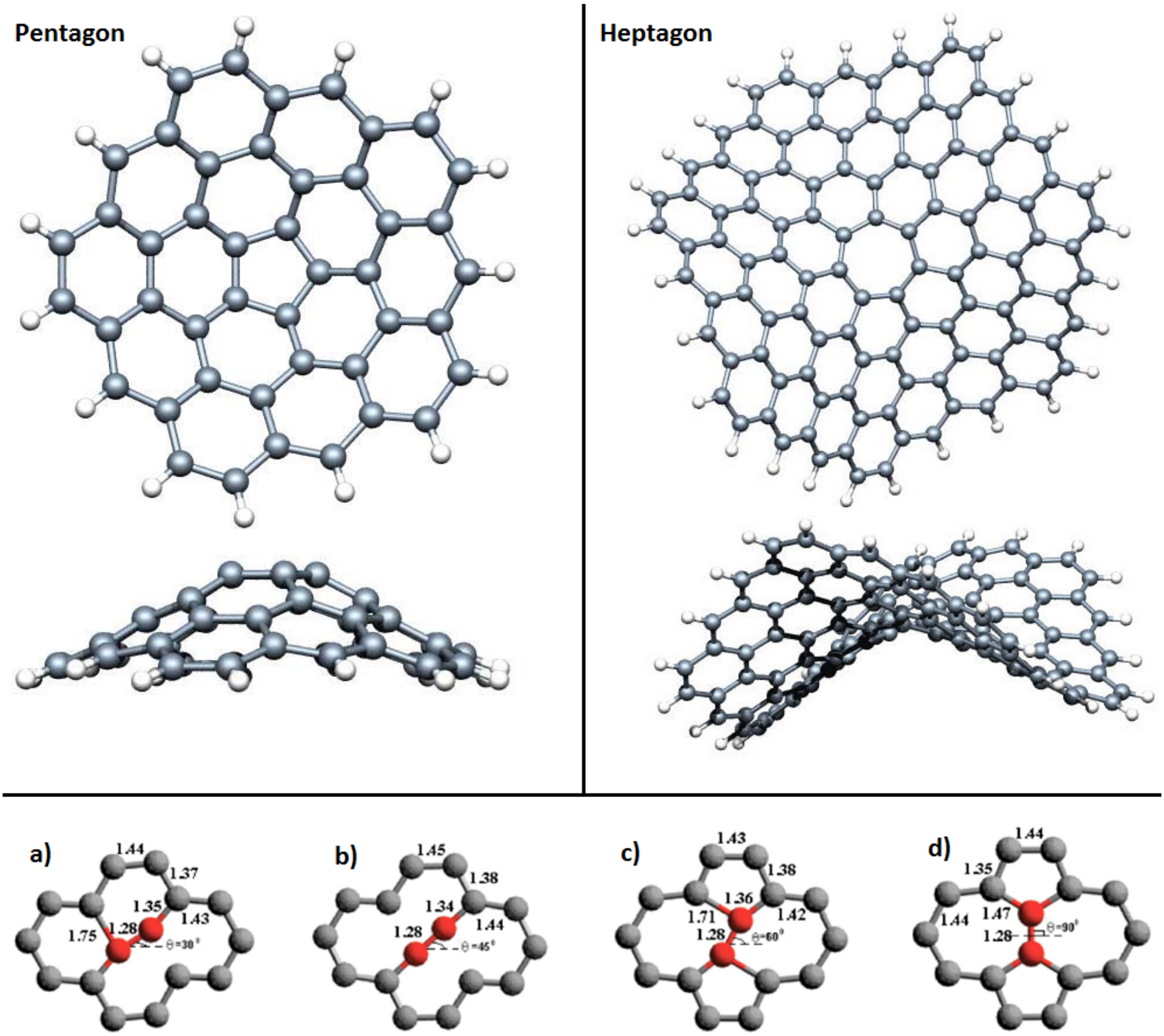

Figure 3.6: Top: Pentagon and heptagon within a graphene layer as top and side view [52]; Bottom: (a-d) Formation of a 5-7-7-5 configuration by a Stonewalls transformation; numbers indicate corresponding atom spacing [1, 51, 53].

transferred to the lattice in the form of vibrations. Some examples of this process are described in figure 3.8.

Another important aspect of the presence of interstitials and vacancy defects is the change of inter atomic spacing and of the lattice constants. These defects lead to carbon-carbon bonds where the atoms are not in the ideal position within the lattice. These resulting shortened or enlarged bonds then bend the layer as presented in figure 3.9 [56]. As a consequence the graphene layers start to bend and warp. This bending leads to stresses within the graphite system which enable defect recombinations or ultimately break the graphite crystal in order to relax the stresses. These bent graphene sheets also help to nuclide the formation of new

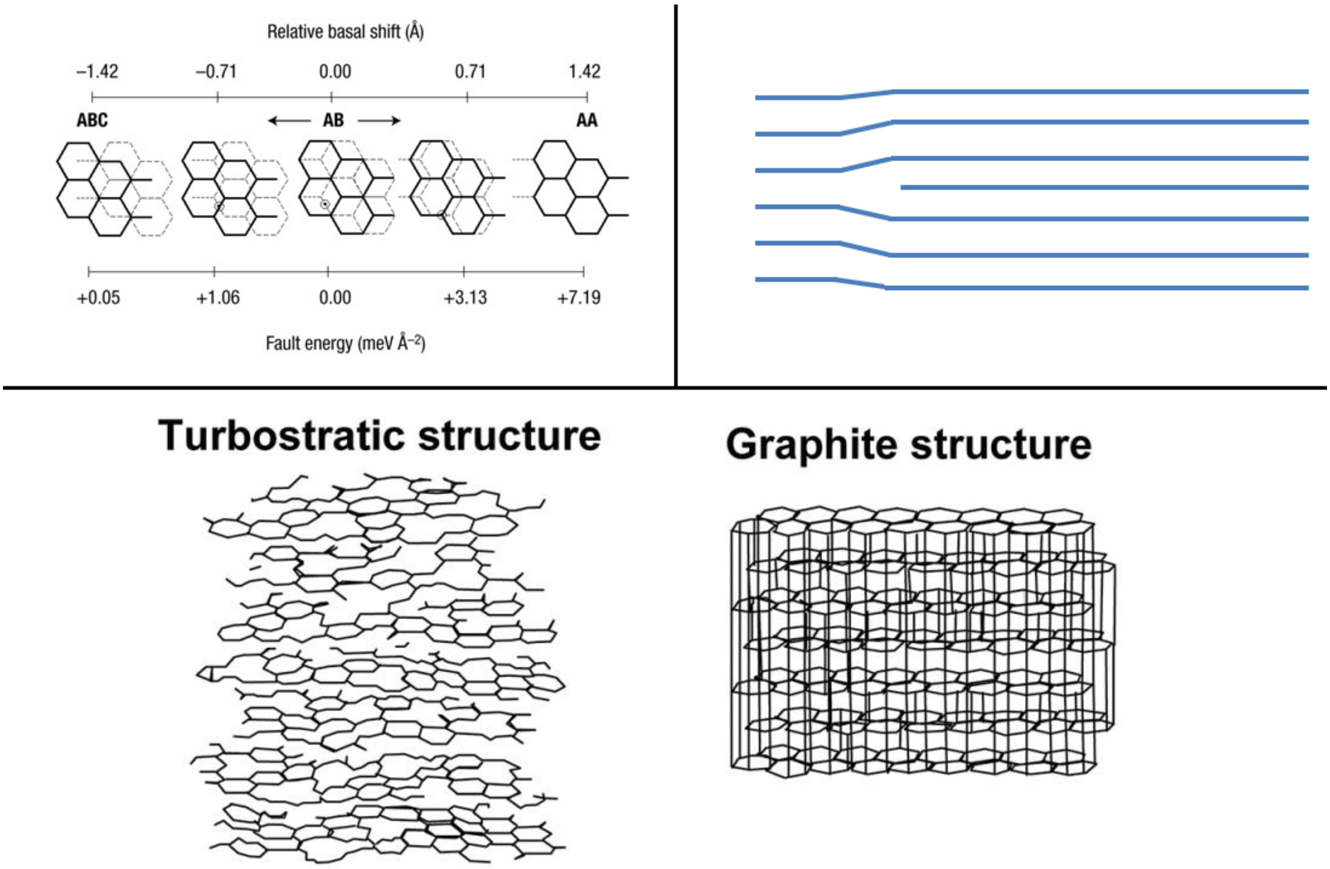

Figure 3.7: Stacking order defects in graphitic structures; Top left: The shift in stacking between two/three graphene layers with in graphite; Top axis represents the basal shift, Bottom axis indicates the energy state [49]. Top right: Formation of new layers and a resulting bending of the existing layers [54]; Bottom picture: Turbostratic stacking and graphite stacking [55].

interstitial planes. With increasing defect densities and stresses within the graphite structure, the formation of differently oriented graphite crystallites is possible when the graphene sheets break. This enables the formation of a 3D-structure away from the 2D-layered structure of the perfect crystal.

Within the ion track, phase transitions and amorphization can take place. For graphite this means a reconfiguration of the bond structure from a sp^2 hybridized system towards sp^3 systems. A phase transition may be related to formation of nano-crystalline diamond structures or amorphous carbon [57]. Amorphous structures are comprised of small disordered carbon aggregations with free dangling bonds. Diamond structures on the other hand are carbon atoms purely bound in the sp^3 configuration. These phase transitions are another consequence of the ion impact and need enough energy to be triggered. The dE/dx threshold required to form diamond in graphite has been discussed by A. Dunlop et al. and is believed to be around 17 keV/nm [57]. Carbon exhibits another feature during ion irradiation. When the energy loss is below 18 keV/nm, then no continuous tracks are formed within the graphite [21]. This phenomenon has been studied by J. Liu et al. using STM (Scanning Tunneling Microscopy)

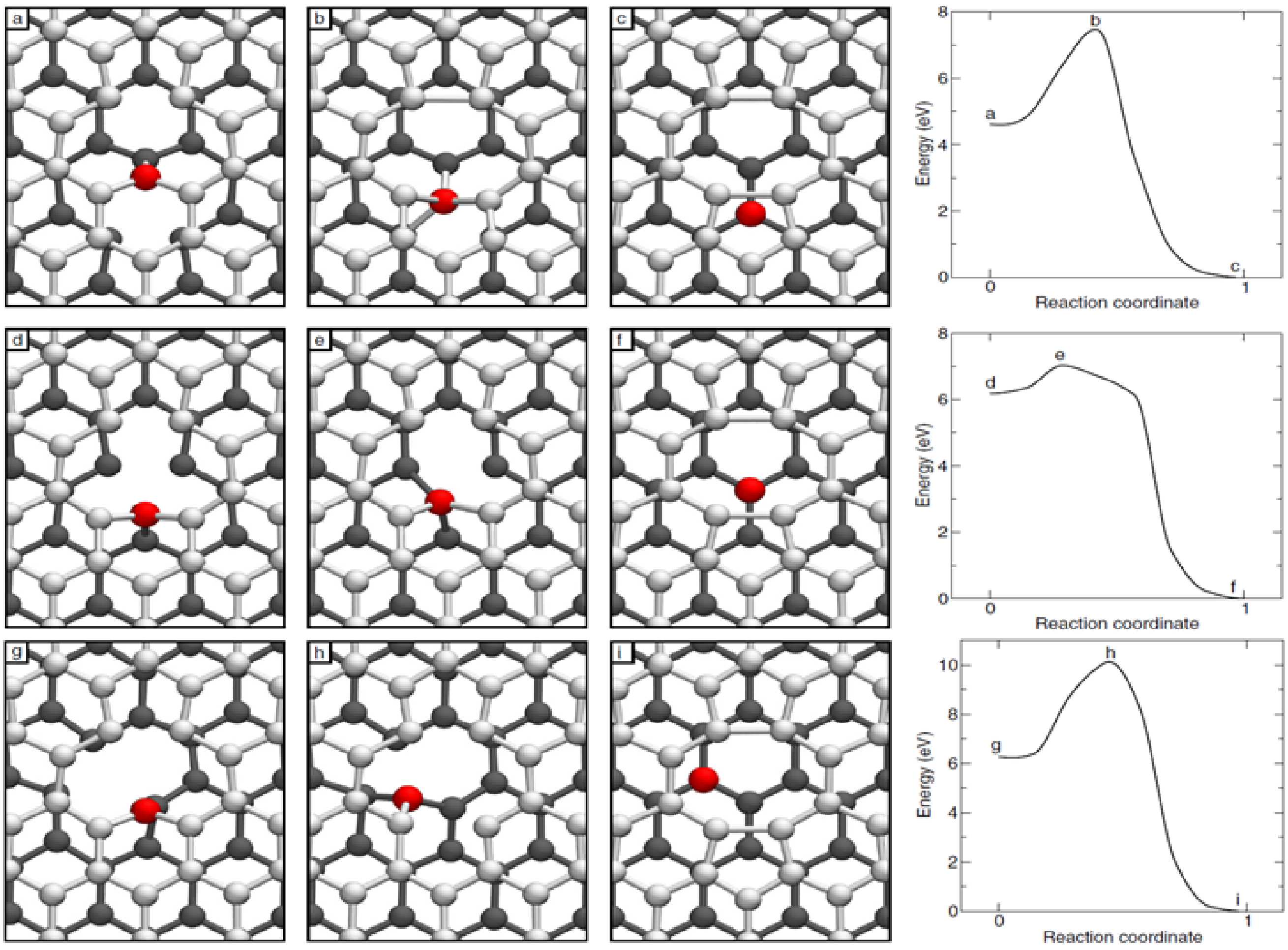

Figure 3.8: Interlayer diffusion of two mono vacancies. Three different vacancy configurations are presented(a-c,d-f,g-i) and the subsequent formation of a 5-8-5 on one layer and recombination to the perfect hexagonal structure on the other layer; The minimum energy paths to make the corresponding transition is shown on the right side [1].

on HOPG (Highly Oriented Pyrolytic Graphite), which usually serves as a model material due its quasi-mono crystalline characteristics. Consequently smaller effective damage cross-sections and inhomogeneous defect densities along the ion track are formed compared to PG. In the results and discussion section of this thesis, the impact of these defects on the thermo-physical properties in a bulk volume of the specimen will be studied and discussed.

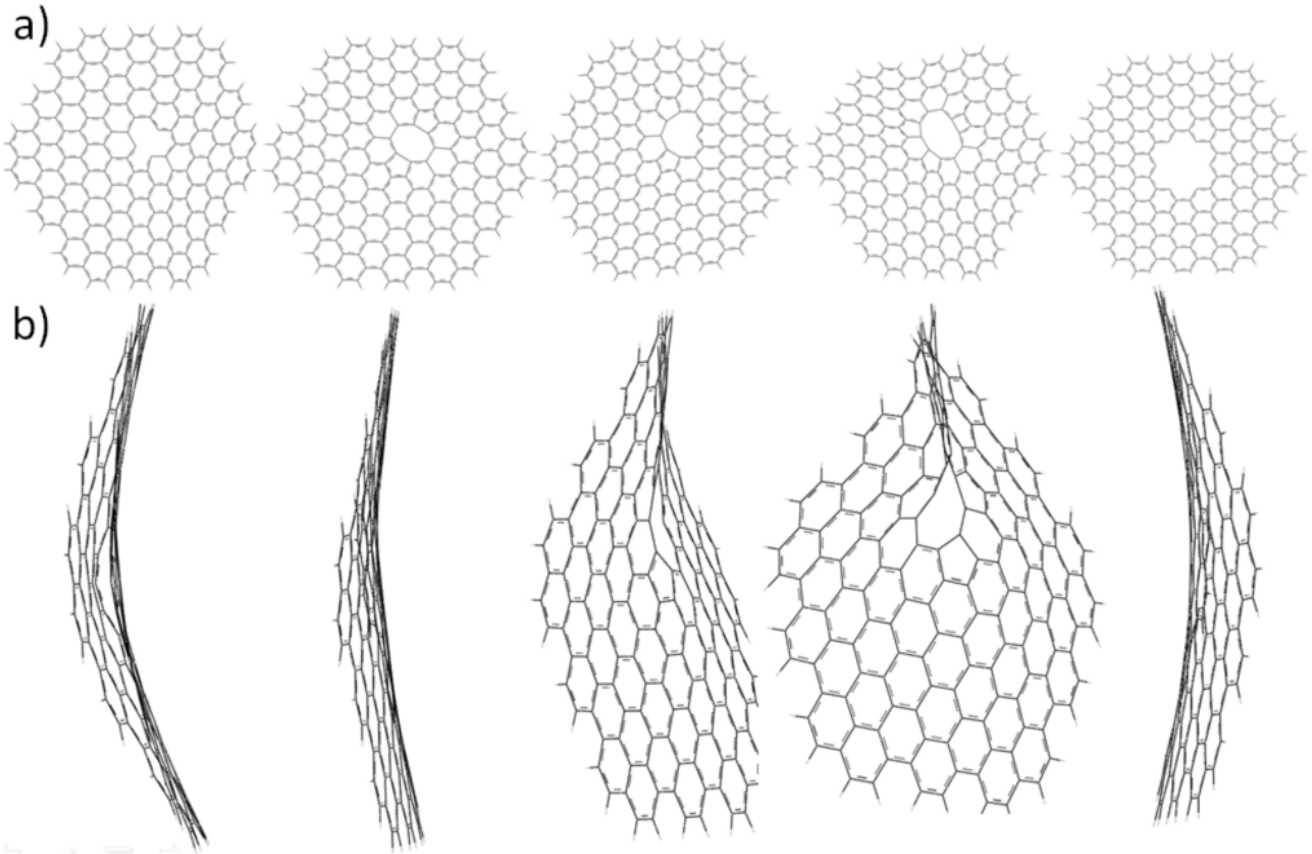

Figure 3.9: Illustration of different vacancy configurations and the subsequent deformation of a graphene layer; a) top view and b) side view; From left to right:mono-vacancy, di-vacancy, tri-vacancy, tetra-vacancy, hexa-vacancy [56]

4 Experimental

The following chapter gives a description of the samples, irradiation conditions and various experimental methods and setups which have been employed in this thesis. The first two sections (3.1 and 4.2) are dedicated to the atomic structure of the investigated materials and the irradiation procedure for each investigated technique. Section 4.3 and 4.4 focus on the theoretical principles of the different methods. For each method we explain the basics, features in regard to the investigated materials and information that one can extract for carbon materials.

4.1 Used specimen

The within the framework of this thesis used carbon-based materials are listed in table 4.1. Typical sample geometries are shown in figure 4.1. HOPG acts as the model material of the perfect graphite crystal. Glassy carbon (GC) acts as the model of a highly disordered graphite material. PG, SNG 398 and SNG 953 are different grades of a quasi-isotropic high density polycrystalline graphite. The grades mainly differ in density, grain and pore size. FG is a chemically expanded (exfoliated) graphite that is laminated into sheets. CFC represents the attempt to introduce HOPG like fibers into a graphite matrix in order to increase the thermal conductivity along the fiber direction. MoC is graphite enhanced by molybdenum in order to limit radiation induced embrittlement and increase the thermal conductivity.

4.2 Irradiation

The following section gives a short insight into the accelerator facility at GSI. The basic principles of accelerator physics are not discussed in this thesis due to the vast extent of the topic and the limited space provided by the frame of this work. The focus of this section will be set on the used beam parameters and beam structures during the corresponding irradiation experiments. The GSI accelerator facility houses two main accelerators that are interconnected. The linear accelerator UNILAC (Universal Linear Accelerator) is able to accelerate any ion ranging from protons ($^{1}H^{+}$) to $^{238}U^{29+}$ to energies of up to 11.4 MeV/u. The SIS 18 (Schwerionensynchrotron - heavy ion synchrotron) receives pre-accelerated ions by the UNILAC and can accelerate any ion up to 1000 MeV/u using magnets with a maximum field strength of 1.8 T and a maximum magnetic rigidity of 18 Tm. Figure 4.2 gives an overview of the accelerator facility at GSI.

The UNILAC is composed of several ion sources, a bunching section, two stripper sections and an Alvarez accelerator. Ions are first extracted out of the ion source, then bunched and pre-accelerated in a radio frequency quadrupole (RFQ). Following the bunching, a gas stripper increases the charge state of the ions by removing (stripping) electrons from the ion. The increased charge state enables acceleration of the ion to higher energies using the Alvarez accelerator. Figure 4.3 shows the important sections of the UNILAC and the experimental hall. All samples used within this thesis were either irradiated in the M-branch (beamline-M2 and M3) or at the X0-beamline, both beamlines are dedicated to material science. Additional information about the specific configuration of the accelerator sections can be found in reference [59].

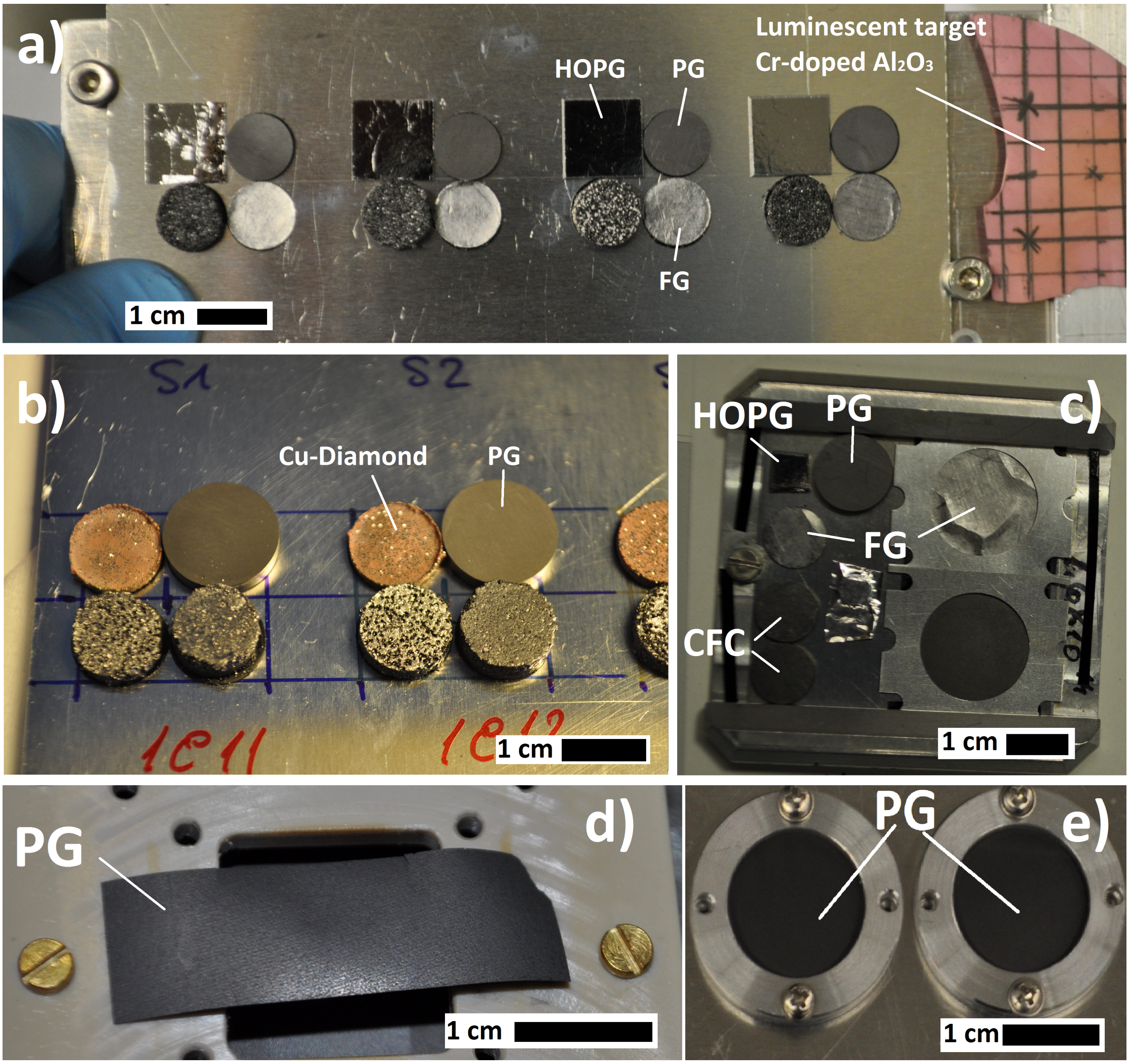

Figure 4.1: Examples of typical sample geometries; a) and b) different carbon samples glued on a sample holder for irradiation at the M3-heater chamber; c) different carbon samples glued on a sample holder for irradiation at the X0 beamline; d) a slightly cracked PG sample to be mounted for 4-point resistivity measurements; e) LFA samples (PG) mounted for irradiation.

Material	Density in g/cm^3	Default sample dimensions in mm^3
HOPG	2.25 to 2.27	$12 \times 12 \times 2$
PG	1.84	$10-12 \times 10-12 \times 1-2$ $Ø10-12 \times 1-2$
SNG 398	1.79	$Ø8-20 \times 1-2$
SNG 953	1.71	$Ø8-20 \times 1-2$
FG	0.7 to 1.3	$Ø8-20 \times 0.15-2$
CFC	1.76	$10-12 \times 10-12 \times 1-2$ $Ø10-12 \times 1-2$
GC	1.42 to 1.54	$10\times 10\times 0.5-1$ $Ø10\times 0.5-1$
MoC	≈ 2.5	$Ø10-12 \times 1-2$

Table 4.1: Overview of the investigated carbon materials with densities and sample dimensions. Note that for some methods (TMA, DSC, LFA, online-resistivity etc.) the dimensions need to be adjusted accordingly; Densities for the MoC compound vary between 2.4 and 2.6 g/cm^3according to the Mo content

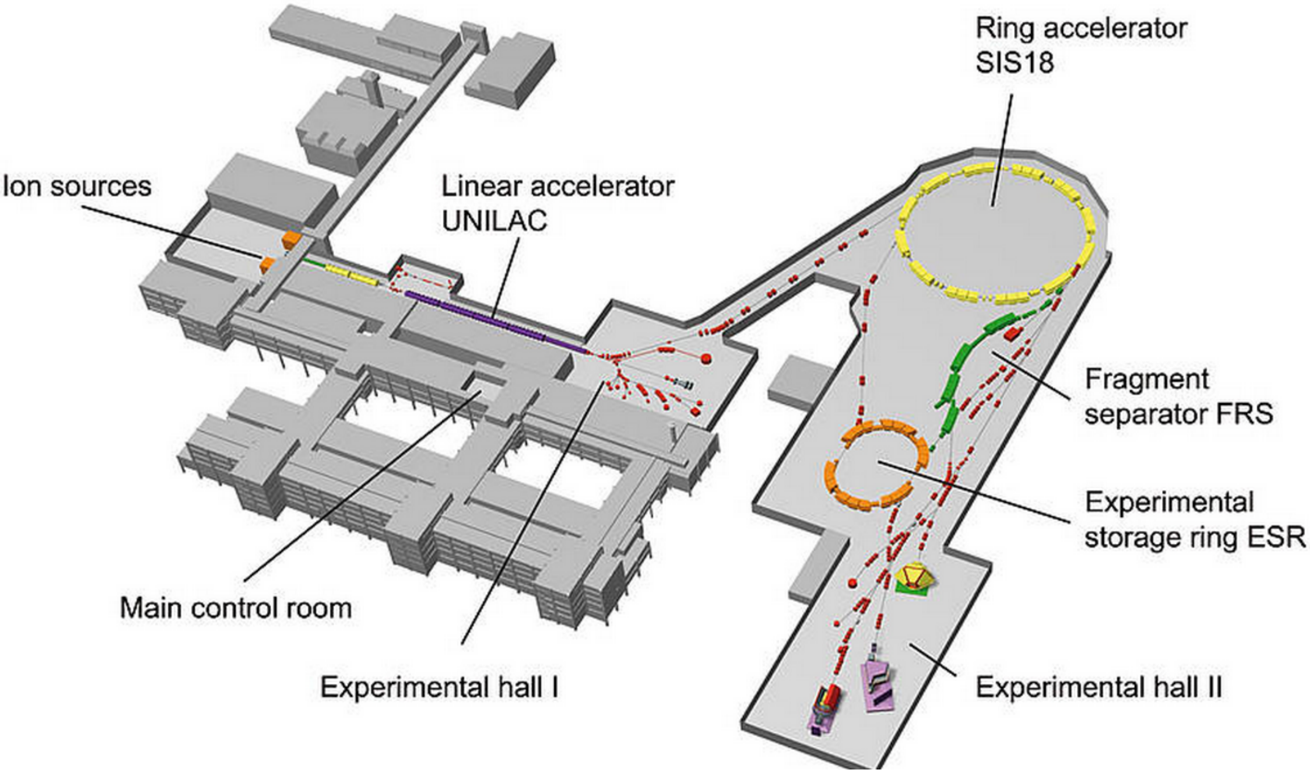

Figure 4.2: Schematic of the GSI facility including the linear accelerator UNILAC that serves as an injector for the heavy ion synchrotron SIS18 [58]

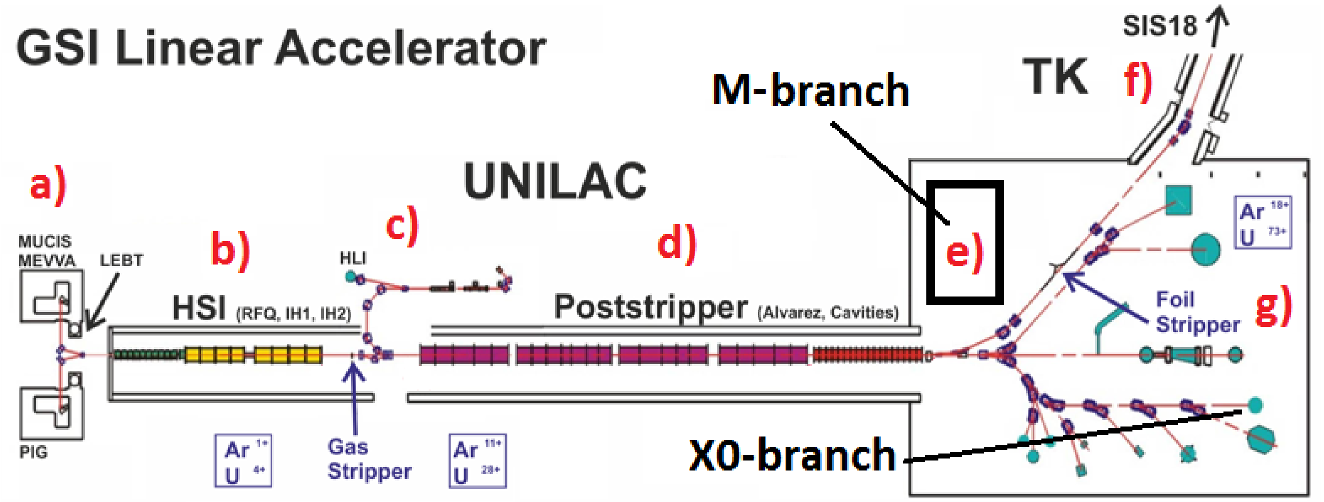

Figure 4.3: Schematic of UNILAC (Universal Linear Accelerator) adapted from [60] a) position of the ion sources (Penning and MEVVA; b) RFQ (radio frequency quadrupol) and pre-stripping acceleration, c) gas stripper; d) Alvarez accelerator; e) M-branch experimental hall; f) TK section (transfer channel towards the synchrotron) and additional foil stripper; g) X0-beamline

Ion	Pulse length in ms	Frequency in Hz	Flux in $ions/cm^2s$	Fluence in $ions/cm^2$
^{131}Xe	1.2	4-45	$1 \times 10^8 to 2 \times 10^{10}$	$1 \times 10^{10} to 5 \times 10^{14}$
^{150}Sm	1.2	3-5	$1 \times 10^8 to 2 \times 10^{10}$	$1 \times 10^{10} to 5 \times 10^{14}$
^{197}Au	2-3	4-50	$1 \times 10^8 to 2 \times 10^{10}$	$1 \times 10^{10} to 5 \times 10^{14}$
^{238}U	0.2-0.5	0.5-2	$1 \times 10^8 to 2 \times 10^{10}$	$1 \times 10^{10} to 5 \times 10^{14}$

Table 4.2: Beam parameters of the used ion beams. Energies ranged from 3.6 to 11.4 MeV/u, for more details view the appendix

The UNILAC operates at frequencies up to 50 Hz. Depending on the ion source and the duty cycle required by a given experiment different modes and duty cycles are used. At a low duty cycle mode typically at frequencies around 0.5 - 1 Hz and short (≈0.1 ms - 0.5 ms) high intensity pulses (up to 1×10^{10} $ions/cm^2$ per pulse) were obtained. The high duty cycle mode operated at up to 50 Hz with longer pulses (up to 5 ms) but lower pulse intensities (up to 1×10^8 $ions/cm^2$ per pulse). Beam sharing on a pulse to pulse base allows GSI to run different experiments in parallel. The intensity per pulse and the corresponding beam current (flux) depend on the ion source, ion species, charge state and energy of the ion. The gas stripper is operated with argon and enables acceleration in the Alvarez section up to energies of 11.4 MeV/u. The four energy steps available depend on the selected Alvarez sections providing energies of 11.4, 8.6, 4.8 or 3.6 MeV/u.

Table 4.2 summarizes the important beam parameters for the irradiated samples in this thesis. Further details about specific beam parameters are given in the results section corresponding to each experimental method.

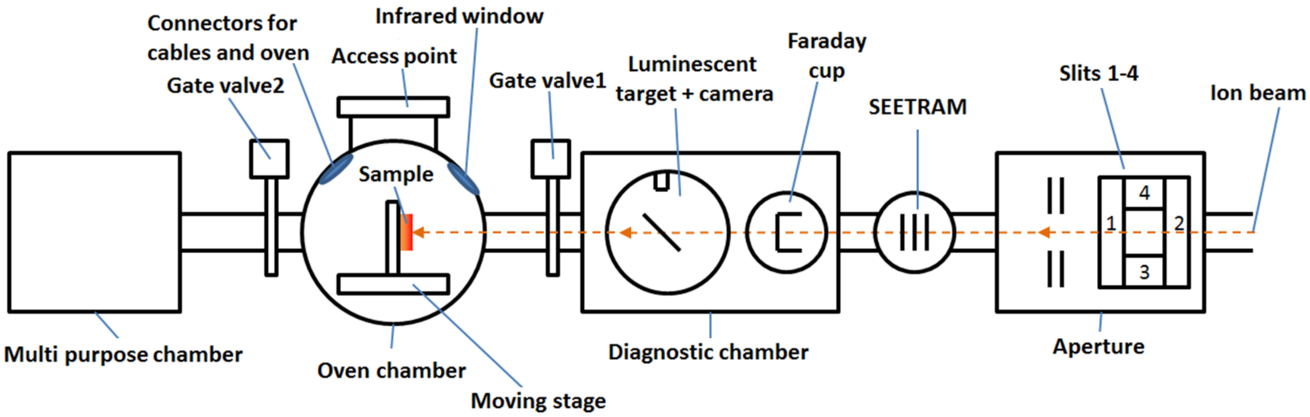

Figure 4.4: Schematic drawing of the M3 beamline at UNILAC adapted from Baake et al. [61]

All irradiations were performed at the M2- and M3-beamline. Figure 4.4 depicts the basic outline of the M3-beam line. Most irradiations were performed in the so called the heater chamber(figure 4.4).

At the M3-branch, the beam is monitored using luminescent targets made from Cr doped Al_20_3 that glow orange/red when hit by the ion beam. While magnetic lenses are used to adjust the homogeneity and size of the beam spot, an aperture is used to cut the beam to the desired geometry. This aperture is later also used to monitor the beam flux on-line during the irradiation. For that purpose, the beam is cut and observed on a luminescent target to determine the exact size of the beam-spot. Due to a negative voltage of 1000 V set on the aperture, each positively charged ion generates a current, according to the charge state of the ion. This measured current is compared and normalized using a Faraday-cup. After this calibration process the Faraday-cup is removed. During the irradiation process both, ion-flux and accumulated fluence is monitored via the current generated on the slits of the aperture. This method works very well for stable beams, but yields errors ranging from 5 % to 10 % if there are intensity fluctuations during the calibration process doe to unstable ion sources. During irradiation with many parallel experiments, the kicker magnets (magnets that divert the beam into the desired beam-line) can heat up and become inaccurate (not ramping fast enough) which also contributes to an error in the monitoring of the beam. In this thesis we consider an error of 10% for fluence and flux. If high fluxes are required, the beam has to be focused resulting in reduced homogenity of the beam spot. For most experiments an intermediate flux was chosen in order to maintain an acceptable beam-spot homogenity.

4.3 Post irradiation analysis

The following section is dedicated to off-line experiments performed to characterize ion beam induced modifications. It describes both the experimental setup and the essential principles for each method. The focus is on the thesis relevant aspects for each method in connection to carbon based materials, in particular for graphite and graphene.

4.3.1 Raman spectroscopy

The Raman effect has been predicted by Adolph Gustav Stephan Smekal, an Austrian physicist in 1923 and has been experimentally verified by the Indian physicist Sir Chandrasekhara Venkata Raman in 1928. For modern science, Raman spectroscopy has become one of the most used tools to characterize structural changes of samples. The Raman effect describes the inelastic scattering process of photons on matter. During the elastic scattering of light, the so called Rayleigh scattering, the energy is conserved, but light emerging after inelastic scattering (Raman-scattering) has a different energy compared to the incoming photons. The change of the photons energy after the interaction with the solid is connected to different excitation processes. Including vibrations of molecules (vibrons), spin excitations in materials with magnet order transitions (magnons) and most common lattice vibrations (phonons). As C. Kittel states, all vibrations inside crystals can be regarded as a superposition of plane waves that virtually propagate to infinity [62]. These plane waves are most commonly referred to as the normal modes of vibration and they are modeled by quasi-particles called phonons [63]. The ability to probe a sample for structural characteristics linked to different vibration modes within the lattice makes Raman spectroscopy a powerful tool for many applications. To investigate a sample using Raman spectroscopy, one needs a light source to provide the necessary excitation. Typically a laser with monochromatic light within the UV-visible spectrum is used for that purpose [64]. The laser is focused on the surface of the sample and the scattered light is observed with a detector. The signal observed by the detector consist primarily of the incident wave length of the light source (Rayleigh scattering) but also some parts of different wavelength (Raman scattering). The intensities of the Raman scattering are between 5 and 8 orders of magnitude lower than the intensities of the incident beam [64]. Due to this relatively small amount of inelastic scattering, the Raman spectroscopy became popular only after the invention of the laser which lead to a signal boost due to a much larger phonon flux on the sample. Rayleigh and Raman scattering processes can be described in terms of energy levels as represented in figure 4.5.

At room temperature, nearly all molecules of a given sample are at their respective ground state according to the distribution law of Maxwell and Boltzmann ($N \approx e^{-\frac{E}{kT}}$). When exposed to a light source, the photons interact with the electrons of the target molecules and cause polarization. In general this polarization is described as an excitation from the ground energy level to a virtual state. The energy level of the virtual state is determined by the wavelength of the photons that caused the excitation. As shown in figure 4.5, molecules return to their original state of energy during Rayleigh scattering. Consequently photons with the same energy as the incident photons are emitted. But the excitation could also cause the electron to return to a higher energy level and thus emitting photons with lower energy compared to the incident photons, which subsequently puts the molecule into a higher vibrational state (Stokes Raman scattering). The third possibility for the molecule is to be already at an excited state. After the excitation the molecule makes a transition to a lower vibrational state and thus emitts photons with higher energy than those that triggered the excitation (anti-Stokes Raman scattering). The relative intensities of these three type of scatterings are represented in figuer 4.6. If one discusses Raman spectroscopy, the Stokes Raman scattering process is usually meant due to the higher intensities (if not stated otherwise).

When a molecule is excited by the electric field of electromagnetic radiation $E = E_0 \cdot cos(\omega \cdot t)$, the dipole moment of the molecule is defined as:

$$P = \mu_0 + \alpha \cdot E \tag{4.1}$$

with μ_0 being the permanent dipolar moment and $\alpha \cdot E$ being the induced dipolar moment [64]. To what extent a molecule can be polarized is determined by its polarizability α which is generally represented by a second order tensor α_{ij} which depends on the symmetry of the molecule. If we consider small harmonic vibrations, the normal coordinate $q_n(t)$ can be described by equation 4.2:

$$q_n(t) = cos(\omega_n t) \tag{4.2}$$

with q_n being the amplitude of the vibration and ω_n being the frequency of the normal mode n. If we combine equation 4.2 and equation 4.1 while considering the power series expansion of α, μ and q_n and accounting only for the first order terms, we will get the following equation to describe the total dipolar momentum of the excitation [64]:

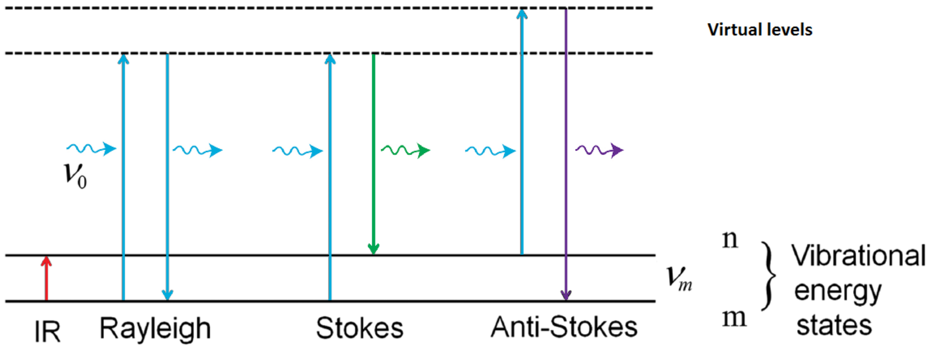

Figure 4.5: Energy levels of Rayleigh scattering and the two forms of Raman scattering (Stokes and Anti-Stokes) [64].

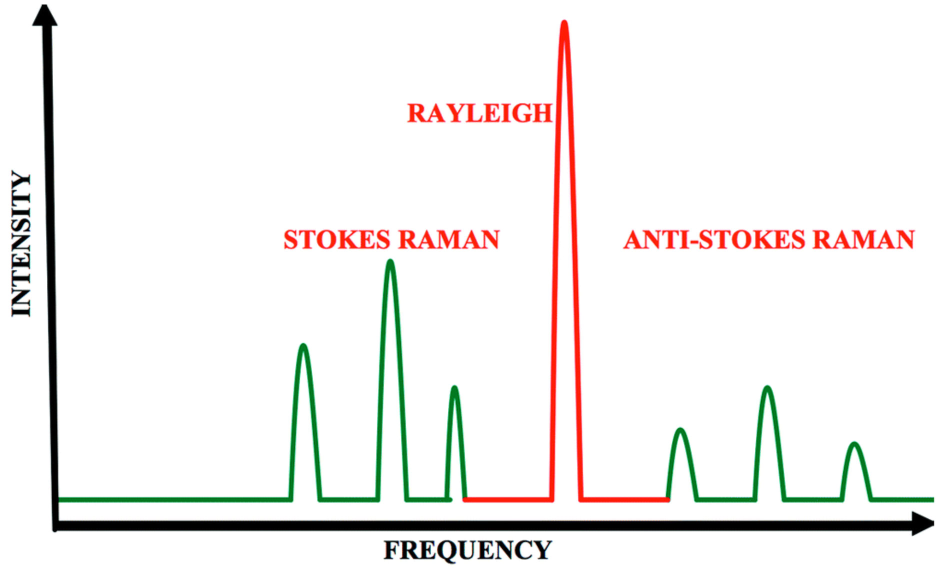

Figure 4.6: Intensities of Rayleigh scattering and the two forms of Raman scattering (Stokes and Anti-Stokes) [64, 65]

$$\begin{aligned} p = \mu_0 + \underbrace{\alpha(0)E_0 \cdot cos(\omega \cdot t)}_{Rayleigh-scattering} + \underbrace{\sum_{i=1}^{Q} \left(\frac{\partial \mu}{\partial q_n}\right) q_{n0} \cdot cos(\omega_n \cdot t)}_{Infrared} \\ \underbrace{+ \frac{1}{2} \cdot E_0 \cdot \sum_{i=1}^{Q} \left(\frac{\partial \alpha}{\partial q_n}\right) \cdot q_{n0} \cdot [\underbrace{cos(\omega + \omega_n) \cdot t}_{Anti-Stokes} + \underbrace{cos(\omega - \omega_n) \cdot t}_{Stokes}]}_{Raman-scattering} \end{aligned} \tag{4.3}$$

The most important aspect of the equation is the change in polarizability. If the electric field of the exciting photons cannot change the polarizability then $(\frac{\partial \alpha}{\partial q_n}) \cdot q_0 = 0$. Subsequently the terms for Raman-scattering will become 0 and thus the corresponding molecular vibration is not Raman-active and will not appear within the Raman spectrum. Equation 4.3 also shows that the measured energy shift of the scattered light is directly related to the wavelength of the incident light. This is called the Raman shift which gives directly the corresponding energy of the measured vibration and is thus independent from the excitation wavelength. Only in some cases, where resonance events occur, the Raman-shift is dependent on the excitation wavelength [66]. The general unit of the Raman-shift $\Delta\omega$ is wave numbers (cm^{-1}). The conversion from wavelength in nm to wave numbers in cm^{-1} can be done by the following equation:

$$\Delta\omega(cm^{-1}) = \left(\frac{1}{\lambda_0(nm)} - \frac{1}{\lambda_1(nm)}\right) \cdot \frac{10^7 nm}{cm} \tag{4.4}$$

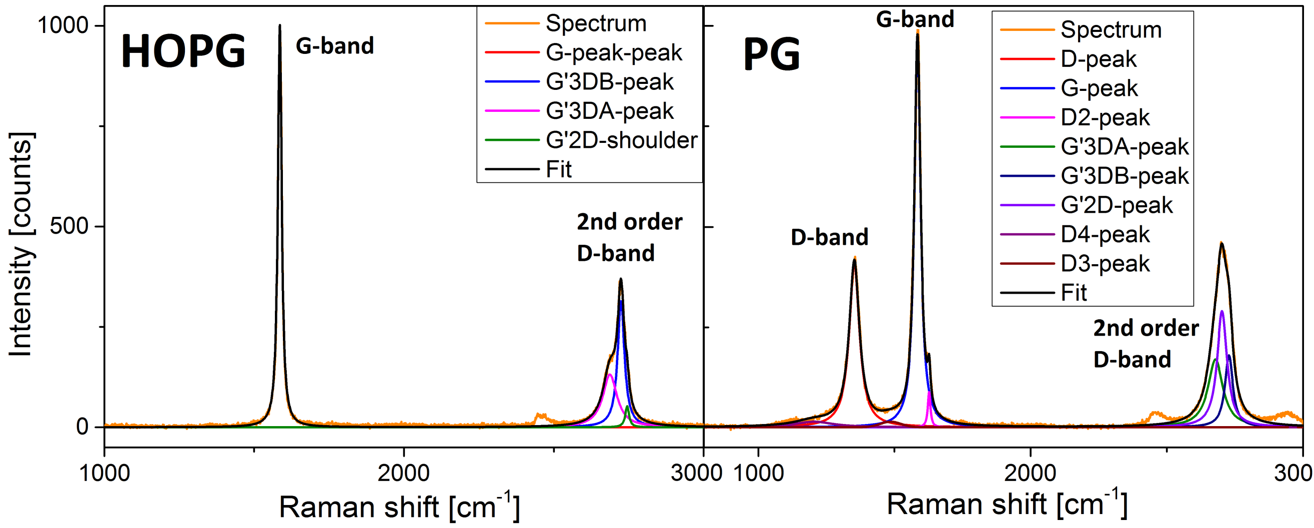

Figure 4.7: Raman spectra of non-irradiated HOPG and isotropic graphite (PG) and their corresponding deconvolution

where $\Delta\omega$ being the Raman-shift, λ_0 being the excitation wavelength and λ_1 being the Raman wavelength. The only reason for this conversion is that the units are more practical to work with (3 orders of magnitude instead of 2) [64]. In short, Raman spectroscopy uses light to probe a sample for its possible vibrational modes and is thus able to characterize the structure of the molecules. In the deconvolution and interpretation of the resulting spectra, many overlapping peaks or inhomogeneous backgrounds as well as fluorescence effects might falsify the information obtained and sometimes make a quantitative interpretation of the data difficult.

The following section explains the deconvolution of the Raman spectra of graphite and shows possibilities to further characterize the sample using data obtained by Raman spectroscopy. For graphite and other carbon based materials, Raman spectroscopy provides an effective tool to characterize defects in the graphene layers. In the spectra there occur only 3 dominant peaks and the background is linear due to a general lack of fluorescence of the graphite excited with visible light. The main peaks for graphite are the so called D-peak, the G-peak and the 2nd order D-peak, which are located at approximately 1380 cm^{-1}, 1580 cm^{-1} and 2700 cm^{-1} respectively. The G-peak can be connected to the stretching mode of sp^2 bonds and occurs in both rings and chains of carbon atoms [7, 8, 67]. The D-peak appears due to a breathing mode vibration of the carbon sp^2 bonds within rings [7, 9, 8, 67]. While the D-band is excitation energy dependent, the G-band has a fixed position [7]. In HOPG and graphene, the primary D-band at 1380 cm^{-1} is not present since it is initially not Raman active, only with the presence of vacancy defects, the band becomes active. The reason is that only then can the double resonance appear to make the D-peak visible [66]. The D-band becomes more prominent with larger vacancy clusters and the higher the defect density within the graphene layers.

With large beam induced disordering in HOPG also 3 additional features of the D-peaks can be seen. The D2-peak, also referred to as D'-peak located at around 1620 cm^{-1} only appears in highly disordered graphite. Additionally the D3- and D4-peaks may appear at 1500 and 1200 cm^{-1} [68]. The D4-peak can be linked to stretching vibrations in between single and double carbon-carbon bonds in sp^2 and sp^3 hybridized carbon, as well as to ionic impurities [68]. Another important indicator is the full width half maximum (FWHM) of the G-peak that can be used to characterize the crystallinity. Broadening indicates a disordering. The ratio of the peak intensities of the first and second order D-peak and the primary G-peak give information about the average grain size, defect density and also about the bending of graphene layers as described in figure 3.9. To deconvolute this information, the following empirical equations 4.5, 4.6 and 4.7 were proposed by Cançado et al. and have been verified by using different excitation energies and other experimental methods such as x-ray diffraction [9, 69, 70]. The equations describe how the in-plane grain size L_a, the average defect density n_d and the average defect spacing L_d are connected to the excitation energy of the used laser and how they are proportional to the ratio of the intensities of the D-band and G-band (I_D over I_G).

$$L_a = (2.4 \cdot 10^{-10}) \cdot {\lambda_{laser}}^4 \cdot \left(\frac{I_D}{I_G}\right)^{-1} \tag{4.5}$$

$$L_d = \sqrt{((1.8 \pm 0.5) \cdot 10^{-9}) \cdot {\lambda_{laser}}^4 \cdot \left(\frac{I_D}{I_G}\right)^{-1}} \tag{4.6}$$

$$n_d = \frac{((1.8 \pm 0.5) \cdot 10^{22})}{{\lambda_{laser}}^4} \cdot \left(\frac{I_D}{I_G}\right) \tag{4.7}$$

Where L_a is the in-plane grain size in nm, n_d is the average defect density in-plane in nm^2, L_d is the average defect spacing in nm in-plane in nm, λ_{laser} is the wavelength of the used laser in nm, and I_D and I_G are the primary D-peak and G-peak intensities of the corresponding Raman spectrum. Formation of pentagons and heptagons leads to a curving of the graphene sheets due to new bond formation around missing carbon atoms in the hexagonal layer and thus the formation of shorter bonds that bend the graphene sheets. This bending is described as tortuosity and can be estimated using the equation 4.8 proposed by Larouche et al. [67].

$$R_{Tor} = \left(\frac{2 \cdot A_{2D}}{A_G}\right) \underbrace{\cdot (1 \pm 0.35)}_{correction factor} \tag{4.8}$$

where R_{Tor} is the average tortuosity of the graphene sheets, A_{2D} and A_G are the integrated areas of the second order D-peak and the primary G-peak of the corresponding Raman spectrum. The factor 2 connected to A_{2D} in equation 4.8 originates from the fact that each incoming photon generates 2 phonons in the second order [67]. The authors also added a correction factor of 1 ± 0.35 due to the dispersion of the D-band with the excitation energy [67]. In our calculations we implemented this correction factor into the assessment of the uncertainties. That leads to seemingly large uncertainties that are purely introduced by the equation and not by the used experimental methods. Raman spectroscopy also makes it possible to observe stacking order defects within the graphite by analyzing the 2nd order D-peak. Cançado et al. used an approach that describes the shapes of ordered and disordered (turbostratic) graphite. These equations propose that the 2nd overtone of the D-peak in the Raman spectra enables the determination of out-of-plane lattice parameters and corresponding changes in the stacking order [9, 10]. Figure 4.8 shows a fit of the 2nd order D-peak of irradiated HOPG and pristine HOPG. It is important to note that the shape of the graphs changes with the disordering so that the spectrum can not be fit using only the G'3DA-peak and the G'3DB-peak. With R being the ratio of two peaks ($I_{G'3DB}$ and $I_{G'2D}$) which are connected to 2-dimensional and 3-dimensional crystal structures in graphite and c being the out-of-plane lattice constant. G'3DB and G'3DA represent an ordered graphitic stacking of graphene sheets while G'2D represents a turbostratic (disordered) stacking.

$$R = \frac{I_{G3DB}}{I_{G3DB} + I_{G2D}} \tag{4.9}$$

$$c(nm) = 0.682 - 0.011 \cdot R \tag{4.10}$$

Furthermore it is possible to extract the tortuosity R_{tor} and the average in-plane crystal size L_a from the ratio of D-peak and G-peak intensities (see equations 4.5 and 4.8).

Using the tortuosity R_{Tor} and the lattice parameter c, it is possible to calculate the average graphene sheet length L_{eq} (equation (4.12)) and the average out of plane crystal size L_c (equation (4.11)) [67, 71].

$$L_c(nm) = 10 + \frac{10}{1.05 - 0.05 \cdot R} \tag{4.11}$$

$$L_{eq}(nm) = R_{Tor} \cdot L_a \tag{4.12}$$

The real graphene sheet length L_{eq} is larger than the in-plane projection of the crystal size L_a by the ratio of bending which is described by the tortuosity R_{Tor}. The average out of plane crystal size L_c is connected to the out of plane lattice parameter. Last but not least, it is possible to use the Raman spectra to derive stresses in the lattice. Tensions within the sample is in general

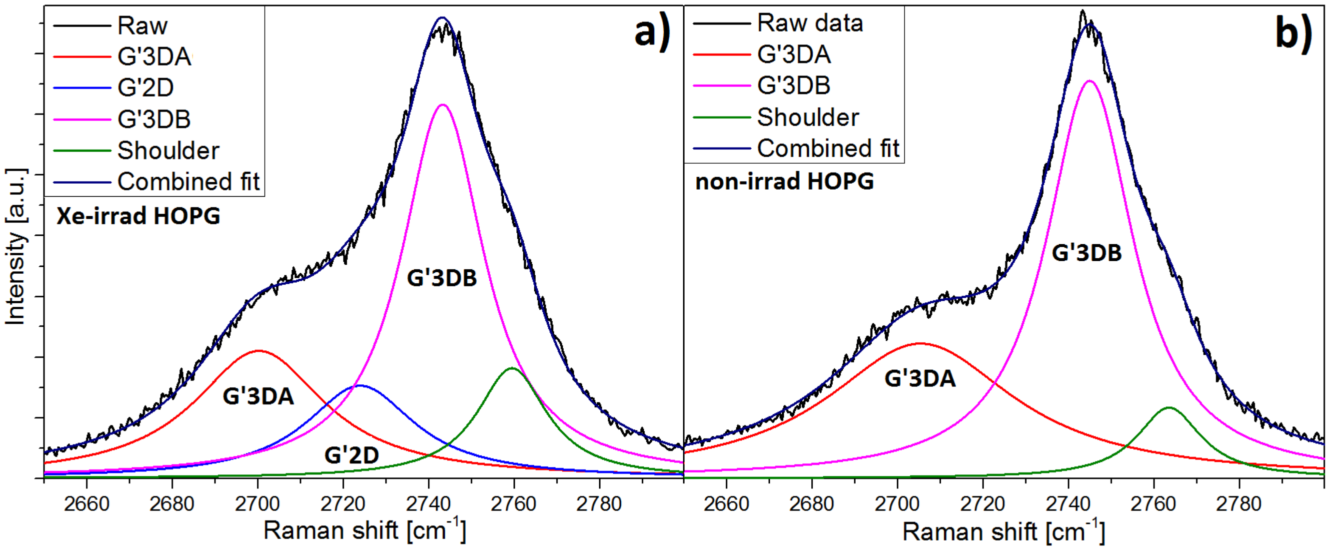

Figure 4.8: Deconvoluted Raman spectra of HOPG. a) 2nd order D-peak of HOPG irradiated with 6.5e13 ions/cm^2; b) 2nd order D-peak of non-irradiated HOPG; In the irradiated sample the G'2D-peak in between the G'3DA-peak and the G'3DB-peak can be observed while the non irradiated HOPG only shows the typical G'3DA-peak and the G'3DB-peak; In all of our HOPG samples an additional shoulder at around 2765 cm^{-1} was present.

associated to a shift of the peaks while a broadening of the peak represents a disordering of the structure.

Experimental setup: The samples were investigated using a LabRAM HR Evolution confocal Raman spectrometer from Horiba using a reflection setup. For probing the samples, 10 to 100 points were randomly chosen (distances in between points around 50 μm) in the center of the irradiated part and the resulting average spectrum was analyzed. Since HOPG, GC and FG present very good reproducibility of the scans, 10 points provided sufficient statistics. PG was scanned using mappings with up to 100 points.

Parameters of the measurements:

- Laser wavelength = 473 nm; Laser power = 20 mW
- 100x Objective
- acquisition time = 30 sec
- rescanning of each point 3 times
- measurement range from 100 to 3000 cm^{-1}
- calibration by a Si standard

The data were fit according to the above mentioned methods. The ratio I_D over I_G uses the peak maximum intensity in counts, not the integrated area. Errors include the uncertainties of the data fits and the systematic error of the detector. For conclusions of empirical methods

($L_d n_d L_c R_{Tor}$ etc.) additional errors of up to 10% are assumed. Some empirical methods yield errors of up to 35 % and are thus mainly used to show trends and qualitative changes within the sample. For the ion fluence an error of 10% is assumed (see chapter 4.2). Data was fit using the Fityk 0.9.8 software [72]. The background was removed using the LabSpec software and linear fits. **Analysis:**

4.3.2 X-ray diffraction (XRD)

X-ray diffraction (XRD) is one of the most used non destructive tools to analyze the structure of a material. x-rays are produced by stopping electrons within matter (Bremsstrahlung), by recombination processes of electrons or by changing the trajectory of a very fast electron (synchrotron-radiation) [73, 74, 75]. The wave length of the x-rays is similar to the inter atomic distances within solid matter around 0.1 to 10 nm. This makes x-rays ideal to study the structure of materials by diffraction. The photons are diffracted at the electrons of the specimen atoms, in contrast to neutron diffraction, where the nucleus itself is diffracting the probe (in this case the neutrons). The reflected photons may interfere constructively or destructively with each other depending on the angle and on the inter-atomic distances. Due to the periodicity of the unit cells within a crystal lattice, this constructive interference can only appear at fixed angles. To each angle, one can associate the corresponding inter-atomic distances according to the Bragg law described in equation 4.13.

$$n \cdot \lambda = 2 \cdot d_{hkl} \cdot sin\Theta_{hkl} \tag{4.13}$$

Where n is the order of constructive interference, λ is the wavelength of the x-rays, d_{hkl} is the inter-atomic spacing between the planes within the lattice and Θ_{hkl} is the angle between the scattered and the incident x-rays. When the photon is diffracted by an atom, the result is a spherical wave with the electron cloud of the atom as diffraction center. The direction (2 Θ) of the constructive interference is determined by the Bragg law. With the known x-ray wavelength λ, one can calculate the corresponding inter atomic spacing between planes in the lattice d_{hkl}, the so called d-spacing. When the crystal structure is known, the lattice constants a, b and c of the unit cell can be derived using the following equation 4.14:

$$d_{hkl} = \frac{1}{\sqrt{\left(\frac{h}{a}\right)^2 + \left(\frac{k}{b}\right)^2 + \left(\frac{l}{c}\right)^2}} \tag{4.14}$$

For crystals and structures with a higher symmetry, this equation becomes less complex e.g. within a cubic system $a = b = c$. A Fourier transformation enables a translation of the data from the real space into the reciprocal space [73]. All measured intensities I_{hkl} are proportional to the structure factor F_{hkl} [76]. The structure factor is given by the types of atoms and their respective positions within the unit cell. It is described by a Fourier transformation of the electron density distribution $\rho(x, y, z)$ [76]. It is also described by the sum of the scattering factors f_i of all the atoms (N) within the unit cell as in equation 4.15 [77].

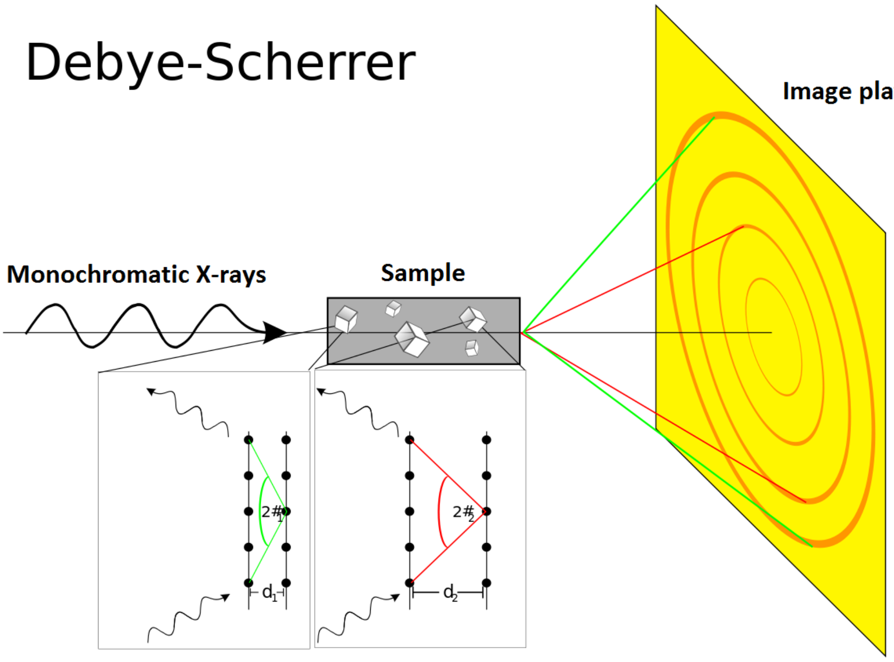

Figure 4.9: Schematic of the Debey-Scherrer method and the corresponding signal recorded on an image plate[78]

$$F_{hkl} = \sum_{i=1}^{N} f_i \cdot e^{2\pi i \cdot (hx_i + ky_i + lz_i)} \tag{4.15}$$

There are two methods typically used in x-ray diffraction experiments. The first one is the Laue method, which uses white radiation as probing species. It is generally used to sample monocrystalline structures. The second is the Debey-Scherrer methode as depicted in figure 4.9. The sample is exposed to monochromatic light and the scattered light is collected by an image plate. The resulting rings can be integrated and transformed into the classical 2Θ data. After the deconvolution of the spectrum, one can calculate the lattice constants. The spectra allow to detect new phases, structures or damage with the specimen.

The off-line XRD measurements were all done at the P02.2-beam line of DESY-PETRA III (Deutsches Elektronen Synchrotron) in Hamburg, Germany. The advantage of a synchrotron over a standard laboratory x-ray source is the brilliance i.e. the quality of the light source that can be described by the following equation 4.16:

$$Brilliance = \frac{Photons}{time \cdot area \cdot mrad^2 \cdot 0.1\% BW} \tag{4.16}$$

with the time typically given in seconds, $mrad^2$ being the angular divergence of the photons (beam spread), area being the cross section of the beam, and 0.1% BW being the number of photons falling into a 0.1% band width of the central wavelength of the beam. The biggest

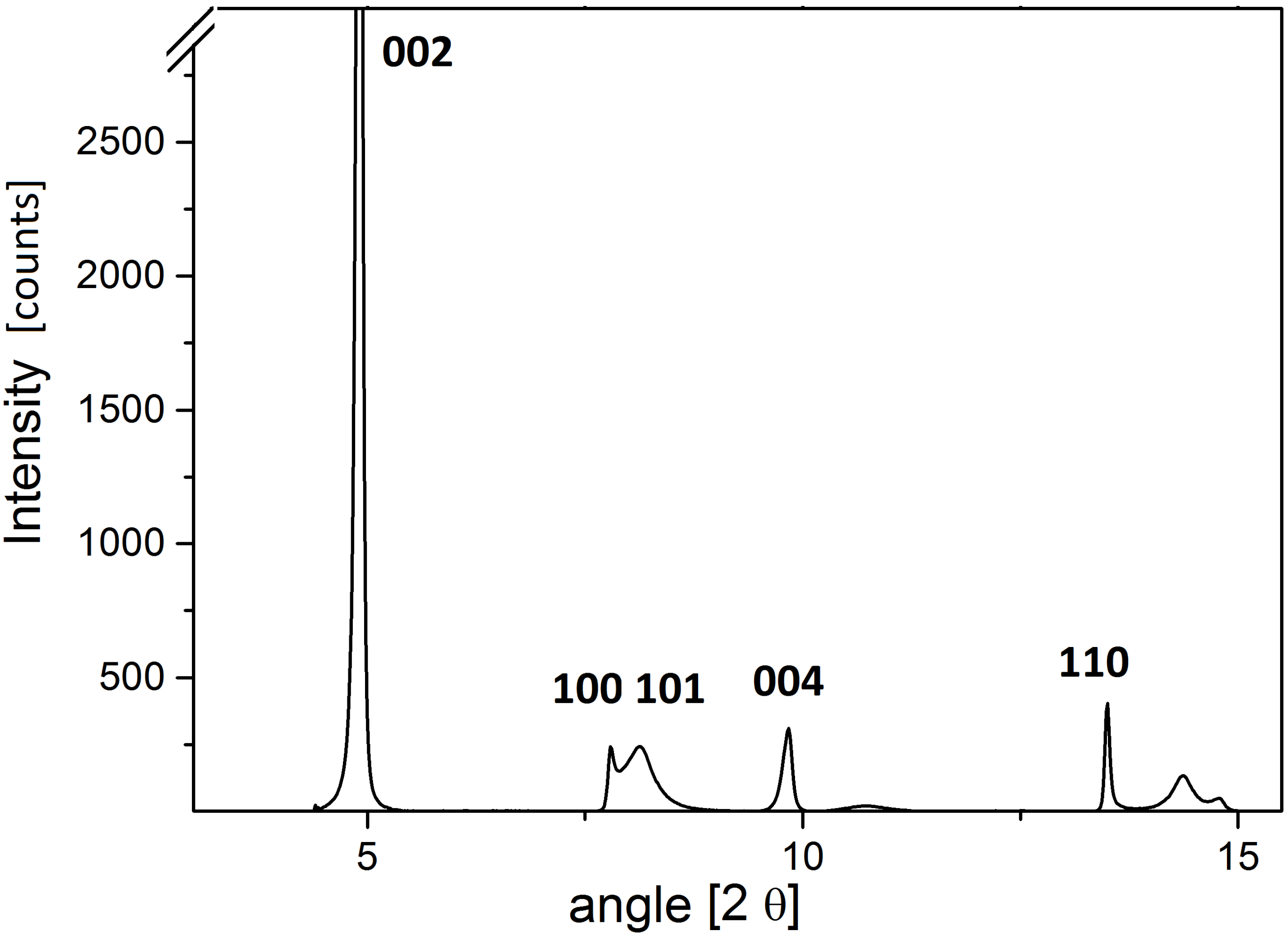

Figure 4.10: Typical spectrum for isotropic graphite, recorded at the DESY-PETRA III P02.2 - beam line

advantage for using photons from a synchrotron is not only the higher resolution, but also the much shorter measurement times due to higher intensity. Compared to a laboratory x-ray source, a synchrotron can provide a photon flux that produces the same quality spectra within seconds instead of hours or days. The wavelength of the used x-rays was set to 0.029 nm and the beam was focused to 2 μm × 2 μm.

A typical spectrum for graphite is shown in figure 4.10. The important peaks for graphite are the most prominent reflex (002), the (100) - (101), the (110) and (004). The (002)-reflex describes the layers of the graphite in the ABAB stacking and is the most pronounced signal in the spectrum.

Experimental setup: The samples were scanned using synchrotron x-rays at the P02.2 beam line of the DESY in Hamburg, Germany. The setup is described in figure 4.11. A Perkin-Elmer (XRD1621) detector with a 16 bit digital resolution of 200 μm and a total image size of 2048×2048 pixels was used. The beam is focused using Kirkpatrick Baez mirrors and Be-lenses [79]. The sample is positioned on a movable stage and can be translated along all three axes (x, y, z) and rotated around the z-axis with a resolution of $\approx$0.2 μm. Calibration is done with a CeO_2 standard.

Parameters:

- beam energy $= 42.560$ keV ($\lambda = 0.2913$ Å)
- photon flux $= \approx 10^{12}\ photons/s$
- distance between detector and sample $= 650$ mm
- measurement angles up to 25° (2θ)
- beam-spot $2\times2\ \mu$m

Additional parameters can be viewed in the following ref [79].

Analysis: The 2D diffraction image was converted (radially integrated) to a spectrum using Fit2d [80]. The spectra were fit using Gauss functions in Fityk 0.9.8 [72]. The background was removed in Fityk 0.9.8. Uncertainties include the errors of the data-fits and the errors of the detector. For the ion-fluence an error of 10% is assumed (see chapter 4.2).

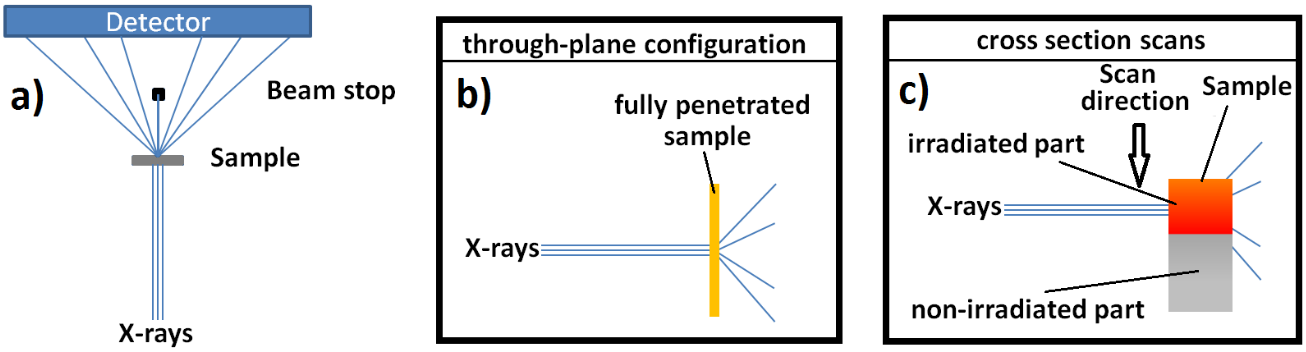

Figure 4.11: Schematic of the experimental setup at DESY - Petra III P02 in Hamburg; a) general setup; b) through-plane setup; c) cross section setup.

4.3.3 Laser flash analysis (LFA)

Thermal properties of carbon-based materials and their radiation induced degradation are of high importance for nuclear and accelerator applications. A dedicated method to measure the thermal diffusivity and conductivity of a material is the Laser Flash Analysis method (LFA). The thermal conductivity K , given in $Wm^{-1}K^{-1}$ is described by Fourier's law of heat conduction presented in equation 4.17 [81].

$$q = -K\nabla T \tag{4.17}$$

With q being the heat flux and ∇T being the temperature gradient. Phonons and electrons are the main mechanisms of heat transfer by conduction within a solid material. That is why the thermal conductivity K is described as a sum of the conductivity by phonons K_p and electrons K_e with both parameters depending on the temperature. K_e is further described by the Wiedemann-Franz-Law presented in equation 4.18 [62, 81].

$$\frac{K_e}{\sigma \cdot T} = \frac{\pi^2 \cdot k_B^2}{3 \cdot e^2} \tag{4.18}$$

where σ is the electrical conductivity, e is the elementary charge and k_b is the Boltzmann constant. Equation 4.19 finally connects the thermal conductivity to the thermal diffusivity [81, 62]

$$K(T) = \alpha(T) \cdot \rho(T) \cdot c_p(T) \tag{4.19}$$

with $\alpha(T)$ being the thermal diffusivity, $\rho(T)$ being the density, $c_p(T)$ being the specific heat capacity.

Further considering the geometric dimensions of the specimen, a calculation of the total thermal resistance is possible. Carbon materials usually exhibit anisotropic thermal conductivity behavior since the conductivity is smaller transversal to the graphene planes compared to the conductivity within the planes. Most carbon based materials have a very large conductance by phonons due to the very low number of free charge carriers [81, 82]. The thermal diffusivity is then directly proportional to the mean free path of the phonons v_p which is further inversely proportional to the temperature. Figure 4.12 visualizes this inverse dependency of the diffusivity on the temperature for isotropic graphite. This temperature dependence can be observed for most materials where the main mechanism of conductivity are phonons.

The LFA method was used to determine the thermal diffusivity, α, of investigated materials. A sample heated (or cooled) to temperatures ranging from $-120\ ^{\circ}C\ up\ to\ 2800\ ^{\circ}C$ is exposed to a short (0.3 ms to 1.5 ms) high intensity laser pulse. The pulse is exposed to the rear surface and a nitrogen cooled IR-detector records the temperature evolution of the front surface yielding the information on the thermal diffusivity [83, 84, 85].

Figure 4.13 presents the typical setup of an LFA measurement. A furnace oven enables the heating of the sample, the laser is generated by an external laser system and transported to the sample site by fiber optics. The specimen is protected by argon gas during the measurements. The thermal diffusivity can be described by a function of the so called halftime $t_{0.5}$ and the thickness of the specimen l as seen in equation 4.20 [85].

$$\alpha(T) = 0.1388 \cdot \frac{l^2}{t_{0.5}} \tag{4.20}$$

The half-time is defined as the time between the initial energy deposition by the laser beam and reaching 50 % of the maximum temperature at the front surface facing the detector. To deconvolute the thermal diffusivity out of the raw signal, several models exist. The basic adiabatic

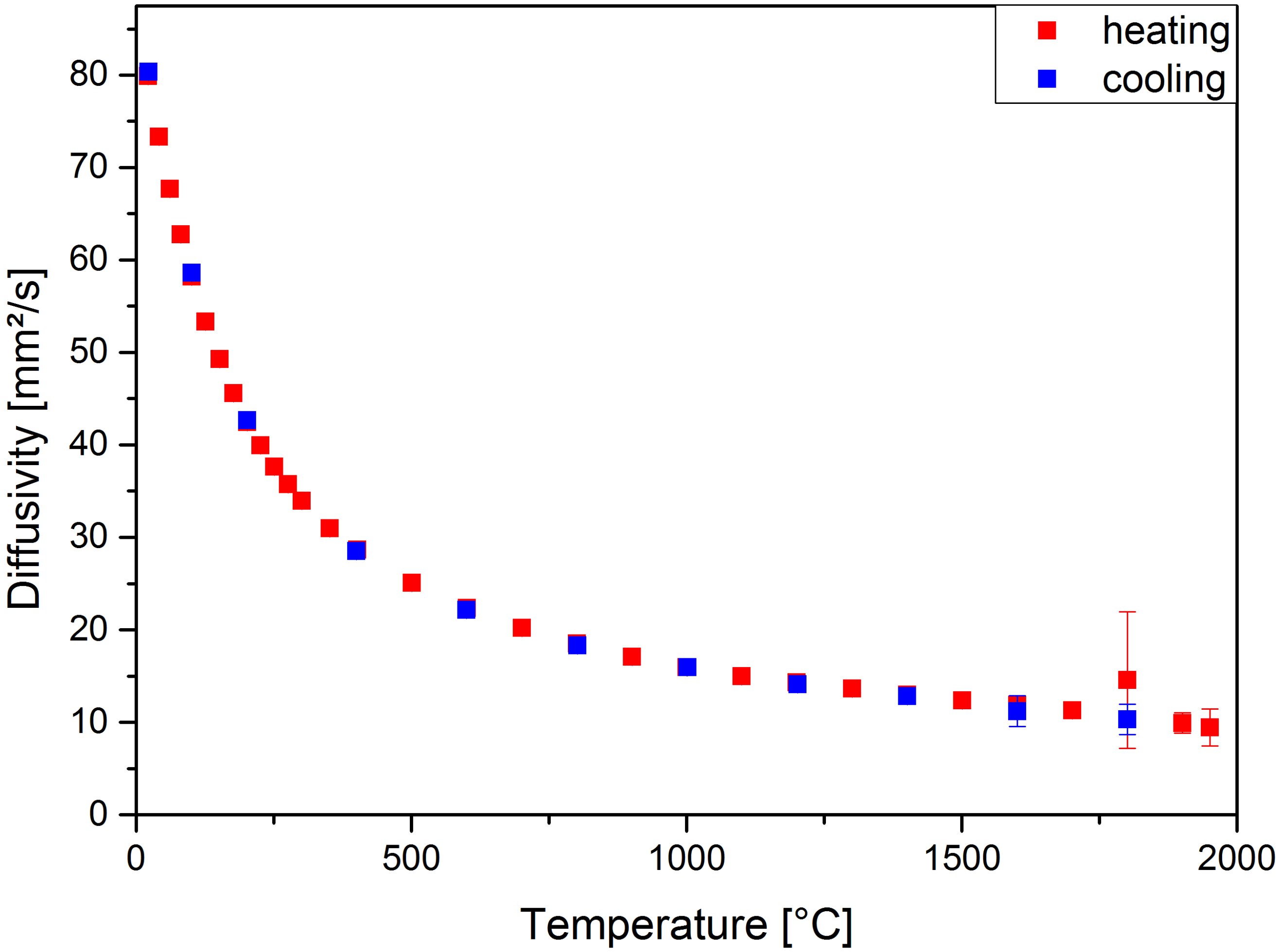

Figure 4.12: Thermal diffusivity of non-irradiated polycrystalline graphite with a density of 1.84 g/cm^3 as a function of temperature.

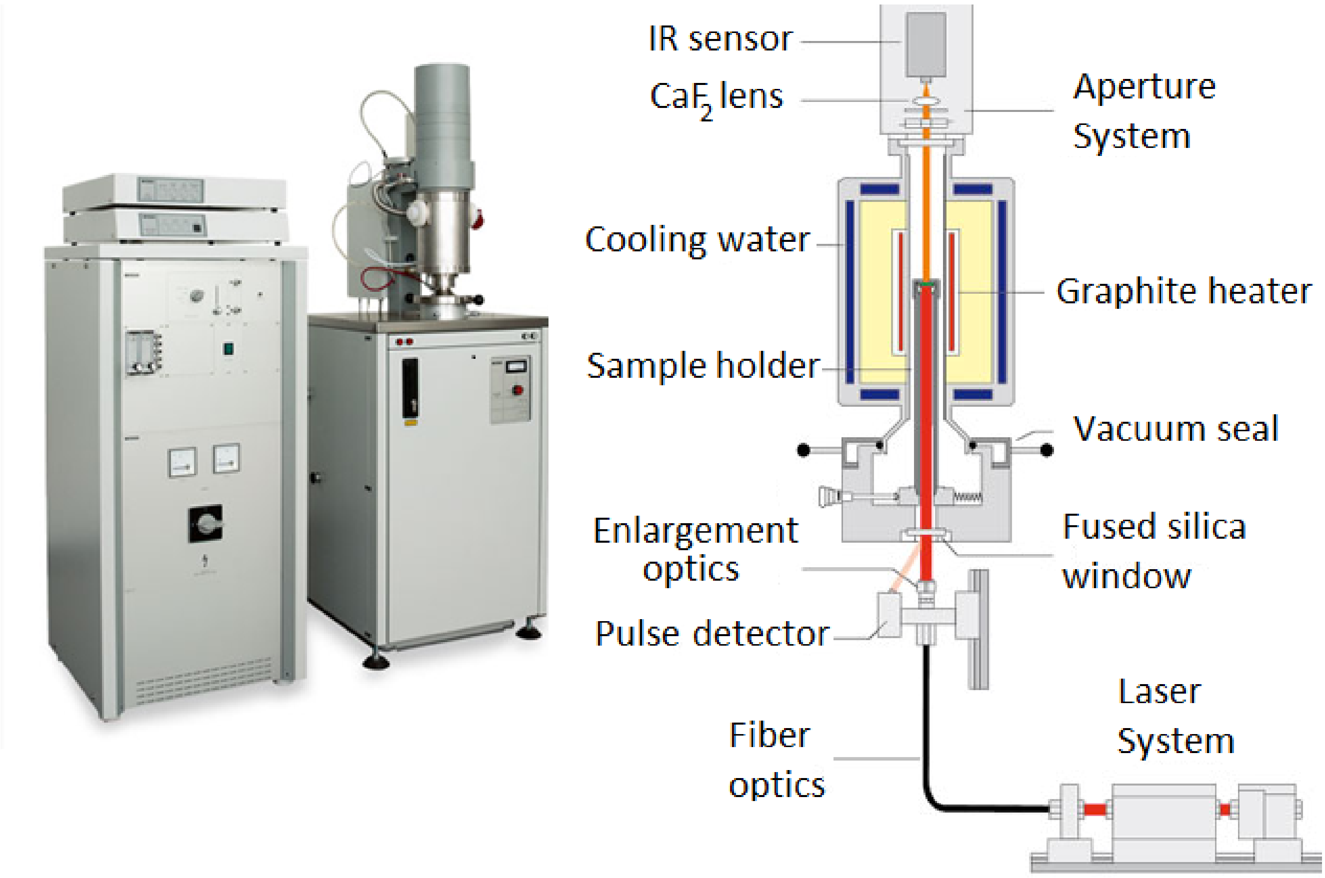

Figure 4.13: Photo (left) and scheme (right) of The Laser Flash Analysis 427 equipment from Netzsch [83].

model only considers heat conduction according to Fourier's law and ignores convection at the sample surface or heat loss through thermal radiation. A mathematical description of the adiabatic model given by Parker et al. is presented in equation 4.21 and further reduced to 4.22 [85]. These models are state of the art descriptions and are generally used when measuring thermal diffusivity and conductivity by the laser flash technique.

$$T(l,t) = \frac{Q}{\rho \cdot c_p \cdot l} \cdot \left(1 + 2 \cdot \sum_{n=1}^{\infty} (-1)^n exp\left(-n^2 \cdot \pi^2 \cdot \frac{\alpha \cdot t}{l^2}\right)\right) \tag{4.21}$$

$$\Theta = 1 + 2 \cdot \sum_{n=1}^{\infty} (-1)^n exp\left(-n^2 \cdot \pi^2 \cdot \frac{\alpha \cdot t}{l^2}\right) \tag{4.22}$$

With $T(l,t)$ being the temperature of the front surface, Q being the amount of energy absorbed by the rear surface. In equation 4.22 a new dimension less factor Θ that is defined as the temperature evolution of the front surface in relation to the maximum reached temperature at the front surface ($T(l,t)/T_{Max}$) is introduced [85]. With the introduction of Θ only the qualitative temperature difference (percentage) is required to calculate the diffusivity [85]. This standard adiabatic model works fine for large bulk samples and gives a rough approximation. But since the adiabatic model does not consider heat losses, it is not very accurate for materials that exhibit heat loss, like in the case of very thin samples or for measurements at high temperatures.

To correct the deconvolution for radiation and convection heat loss of the samples during the measurement, Cowan et al. introduced a correction into the model. Equation 4.23 represents the combination of the correction term and equation 4.22 [86].

$$\Theta_{Cowan} = exp\left(-b\frac{\alpha \cdot t}{l^2}\right) + 2 \cdot \sum_{n=1}^{\infty}(-1)^n exp\left(-n^2 \cdot \pi^2 \cdot \frac{\alpha \cdot t}{l^2}\right) \tag{4.23}$$

Where Θ_{Cowan} is the corrected temperature ratio, b is the correction factor that includes the heat loss from both surfaces. This model does not consider radial losses, which have to be limited by the sample size. Equation 4.24 describes the estimation of the factor a, where $5 \cdot t_{0.5}$ and $(10 \cdot t_{0.5})$ represents the remaining temperature after 5/10 times the half time [86]. Another way to roughly estimate b is to consider the emissivity of the sample.

$$b \approx \frac{\Theta(5 \cdot t_{0.5})}{\Theta_{(}t_{0.5})} \quad or \quad b \approx \frac{\Theta(10 \cdot t_{0.5})}{\Theta_{(}t_{0.5})} \tag{4.24}$$

In addition to heat loss corrections, it is advised to correct for the duration of the laser pulse, if the sample is highly conductive and has a large diffusivity. If a deconvolution over time of a laser pulse and the temperature increase by the absorption of this laser pulse is not possible in the IR-detector, the laser pulse has to be shortened or a thicker sample has to be used. In the ideal case one adjusts the laser pulse to the diffusivity of the sample and to the dimensions. In order to produce accurate data, the half time $t_{0.5}$ should be ten times larger than the pulse length of the laser.

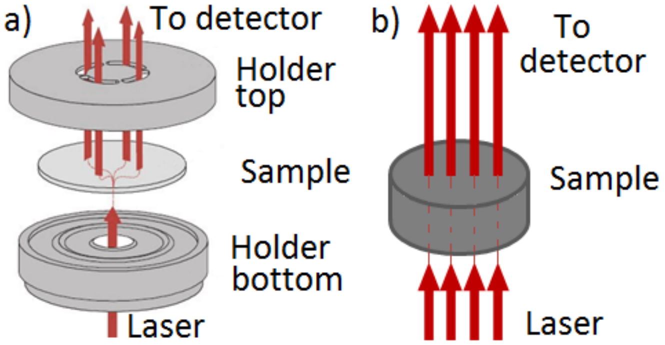

Figure 4.14: a)In-plane sample holder geometry for thin samples; b) through-plane method for bulk samples [83]

Experimental setup: The used LFA 427 from Netzsch features a graphite oven for measurements up to temperatures of 2000°C and an InSb IR-detector that is cooled by liquid N_2 [83]. Polycrystalline graphite samples are measured in the in-plane geometry as presented in figure 4.14. This method is suitable for very thin samples since it helps to increase the diffusion length for the induced heat. While normally the diffusion length is the thickness of the sample, within the in-plane configuration the diffusion length is the radial distance from the laser exposed part of the sample (center) towards the point on the sample measured by the IR detector. Both surfaces are partially masked by stainless steel holders to create the necessary conditions for in-plane heat transport measurements. The laser is a Nd: YAG (neodymium: yttrium aluminum garnet) with a maximum power of 25 J/pulse. For through plane measurements, graphite sample holders are used (max. temperature up to ≈2000°C, for in-plane measurements stainless steel is used (max. temperature to ≈1000°C). All measurements were performed under argon atmosphere provided by purging the chamber with vacuum and Ar 5.0 to ensure an oxygen free environment. The Ar 5.0 gas flow was set to 100 ml/min for measurements below 1000 $^{\circ}C$ and to 150 ml/min for temperatures above 1000 $^{\circ}C$. During each temperature step, 5 to 30 measurements were taken in order to get some statistics and check the reproducibility of the measurements.

Parameters:

- laser wavelength = 1064 nm
- laser power 14 J/pulse
- laser pulse length = 0.5 ms
- temperatures: 20 to 22°C for RT and up to 2000°C for high temperature measurements
- heating rate = 5 K/min
- cooling rate = 10 K/min
- 20 shots at each temperature step

Analysis: The data were fit using NETZSCH Proteus® software. All in-plane data points were fit with Cowan's model and all bulk samples with the adiabatic model by Parker. Errors include the errors of the data-fits (models), the errors of the detector and statistical errors.

4.3.4 Nano/Micro-indentation

Micro- and nano-indentation measurements are powerful to characterize the hardness and Young‘s modulus of a material. Hardness is defined as the resistance of a material against indentation. The values are generally given in the unit of MPa or GPa. Equation 4.25 shows the relation between the contact area $A_{contact}$ of the indenter and the sample and the maximum force applied to the indenter F_{max}.

$$H = \frac{F_{max}}{A_{contact}} \tag{4.25}$$

To calculate the hardness one needs to know the contact area. In the past this has been done by measuring the diameter of the indentation imprint optically, today this approach is replaced by a depth sensing technique. Since the indenter geometry is known, one can calculate the resulting contact area using the known indentation depth. The indentation depth is tracked and controlled during the indentation process. Unfortunately it is impossible to create perfect indenter tips out of diamond. Thus each indenter needs to be calibrated beforehand to determine its characteristic shape and create an area (tip-shape) function to apply later to the various measured depths to calculate the hardness values correctly. The area of the diamond tip is calibrated using a known material (e.g. stainless steel or fused silica). Using the indenter, the calibration material is imprinted up to various depth. Since the values for the hardness of the calibration material are known, one can create a so-called diamond area function by applying corresponding correction factors accounting for the shape of the indenter. With this method it is possible to correct for wearing effects and not ideal indenter-tip geometries.

To determine the Young’s modulus using the indentation data, one can use the method developed and advanced by Oliver and Pharr [11, 12]. Figure 4.15 shows a typical indentation using a Berkovich indenter head on a PG sample. The slope of the unloading part of the data, dF/dh is representing the stiffness of the contact between the indenter and the sample. The contact stiffness can be used to calculate the reduced modulus $E_{reduced}$ or the so called indentation modulus using the following equations 4.26 and 4.27 [11, 12]:

$$S = \frac{dF}{dh} \tag{4.26}$$

$$E_{reduced} = \frac{1}{\beta} \cdot \frac{\sqrt{\pi}}{2} \cdot \frac{S}{\sqrt{A_p(h_c)}} \tag{4.27}$$

Where:

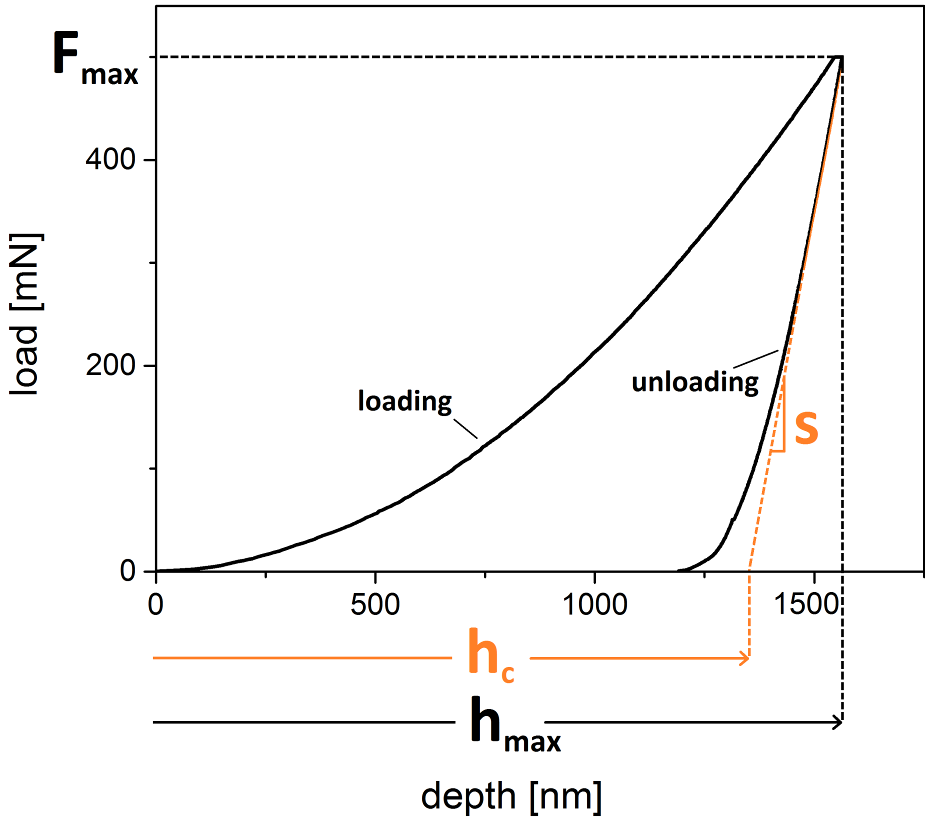

Figure 4.15: Typical indentation load vs depth signal on a steel sample performed with a Berkovich indenter head; important parameters which are extracted from the raw data are indicated and are required to calculate the hardness and Young's modulus (see equations 4.26 and 4.27)

- $S =$ the contact stiffness
- $F =$ the force applied to the indenter
- $h =$ the penetration depth of the indenter into the material
- $E_{reduced} =$ the reduced modulus (indentation modulus)
- $A_p(h_c) =$ the contact area between indenter tip and material at the depth h_c
- $\beta =$ a geometrical correction factor dependent on the indenter tip geometry

Since the raw data is a result from a dynamic system with two components, also the indenter component has to be accounted for within the calculations. Thus the indentation modulus is connected to the Young‘s modulus via the relation presented in equation 4.28 [11, 12]:

$$\frac{1}{E_{reduced}} = \frac{(1 - \nu_{indenter})}{E_{indenter}} + \frac{(1 - \nu)}{E} \tag{4.28}$$

Where:

- $E_{indenter}$ = the Young‘s modulus of the indenter tip material
- $\nu_{indenter}$ = the Poisson ratio of the indenter tip material
- E = the Young‘s modulus of the tested material
- ν = the Poisson ratio of the tested material

Additionally, the comparison of the ratio of hardness to reduced modulus provides useful informations on the structure of the material. A change of this ratio is an indication that the plastic deformation behavior is changing. For ion irradiated samples this could possibly be related to microstructural changes such as a ion induced phase transition [87, 88, 89].

Deformation mechanism of graphite:

The indentation hardness is generally the resistance of a solid to permanent deformation when a compressive force is applied. On an atomic scale, the value of hardness is dominated by the strength of inter-atomic bonds. For isotropic bulk samples, the hardness is determined by the flow stress which usually is around 5 times the shear strength of the material [90]. For the layered structure of graphite on the other hand, there exist only strong intra-planar bonds within the crystal while inter-planar bonds are very weak. Thus the shear resistance between two adjacent layers is very small. The small shear strength of the layered graphite leads to an anomaly that manifests in hardness values around 50 times the shear strength at low loads of up to 50 mN, depending on the indenter geometry [90]. The reason behind this anisotropy are the missing covalent bonds in between the graphene layers of the crystal. This leads to the special deformation mechanism of graphite. Under load the graphene layers start to form highly mobile twins which are reversible up to deformation angles of 3 ° - 4 °. Further deformation above this threshold leads to the formation of permanent twin boundaries which are described as dislocation tilt boundaries at unusual high angle of up to 20 °. These twin boundaries, together with cleaving, lead to a folding of the layers under any load that exceeds the shear resistance of two adjacent graphene layers [90]. After applying sufficient strain during an indentation these folded layers remain as plastic deformation that can be seen under the microscope subsequent to indentation of the surface (figure 4.16). The permanent deformations create a pile-up effect during an indentation, which leads to an additional error by the classical method due to an increased contact area. If applied loads are below the threshold for the permanent formation of twin boundaries, i.e. loads ranging in the elastic response regime of the material, the hardness values are largely elevated. This leads to a load dependent behavior of the hardness which allows to map the transition of the fully elastic response towards plastic deformation of the layers. On the other hand, if probed above the threshold for plastic deformation, the hardness of graphite becomes independent of the loads. Sharper indenter heads like a cube corner or the Berkovich require less force to create plastic deformation. Consequently it is favorable to map the layered graphite samples with a spherical indenter. The widely accepted

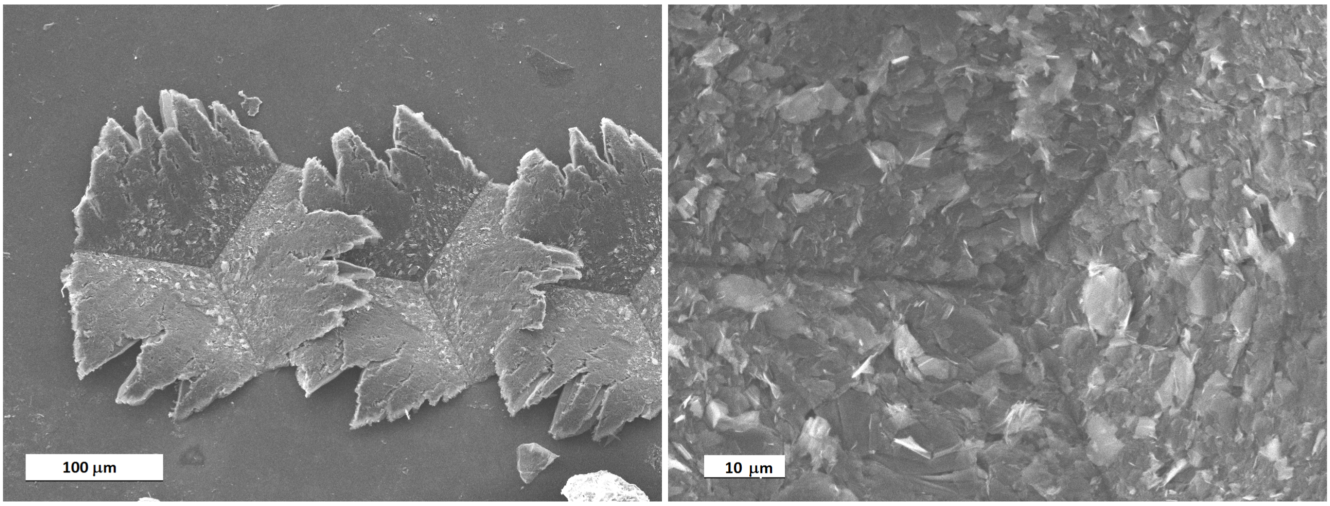

Figure 4.16: Left: Graphite layers pile-up in micro indents using a Berkovich diamond tip on non-irradiated HOPG visualized in an SEM; Right: A zoom into the center of the indentation imprint reveals folded and ruptured graphite layers.

and practiced method of Oliver and Pharr [11, 12] for the deconvolution of hardness from load vs displacement data does not completely apply when the materials response is fully elastic as shown in figure 4.17 [91]. Due to the elastic response of the material, the area function $A(h)$ of the contact area is generally overestimated since the software for most commercially used nano-indenter systems assumes a plastic deformation [92]. To extract the Young's modulus one can use equation 4.29 proposed by Sneddon [91, 93, 92] which is valid only for a spherical indenter geometry:

$$F(h) = \frac{4 \cdot E}{3 \cdot (1 - \nu^2)} \cdot \sqrt{R} \cdot h^{\frac{3}{2}} \tag{4.29}$$

Where $F(h)$ is the applied load, h is the penetration depth into the sample, E is the Young's modulus, R is the tip radius of the spherical indenter head and ν is the Poisson coefficient of the probed material. For all nano-indentation measurements within this thesis, a spherical indenter was used. The tip radius (3.125 μm) of the sphero-conical indenter is much larger than the penetration depth ($\leq$1000 nm) i.e. the indenter contact to the material equals that of a sphere. Results using Sneddons approach are presented and compared in Figure 4.18. The interpretation of hardness measurements on purely elastic materials is controversial. Since the material does not exhibit plastic deformation, obtaining a clear value for hardness in the classical sense (analyzing the load over penetration depth data) is not possible. Gross et al. [92] tried to characterize the indentation process using a finite element method to calculate stresses during indentation on a sample with a purely elastic response. They concluded that one can probe a material with a high elastic anisotropy for the elastic constants using indentation. Considering this idea while accounting for the fact that HOPG is highly anisotropic, one can extract more out

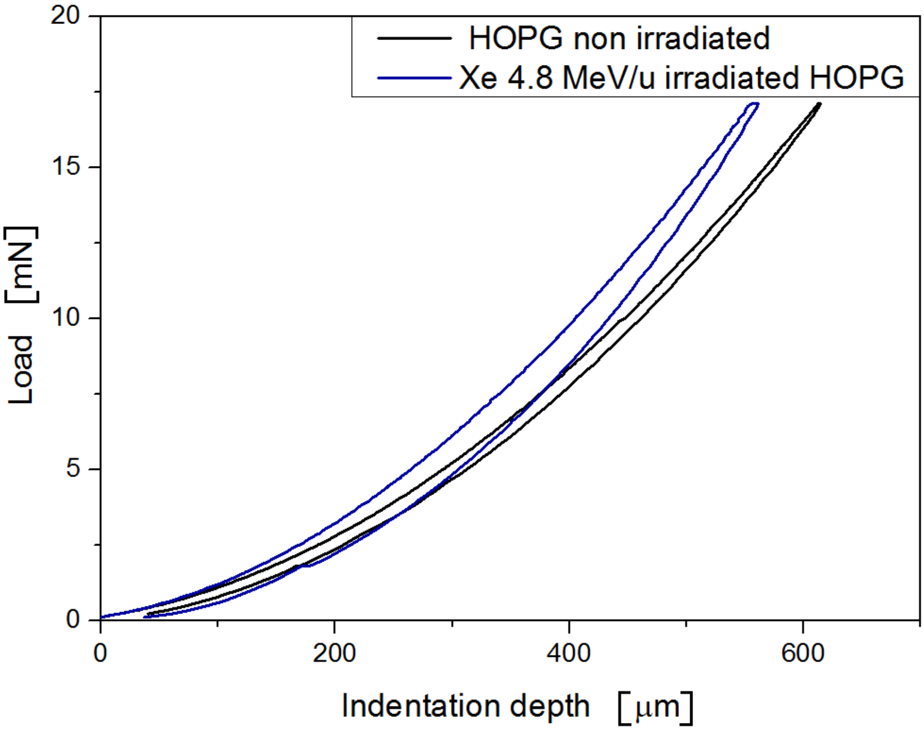

Figure 4.17: Indenter load as function of depth of HOPG, non irradiated and irradiated with 4.8MeV/u Xe ions of a fluence of 1×10^{13} ions/cm^2. For indentation a sphero-conical diamond indenter head with 60° angle and 3.125 μm tip radius was used.

of the indentation data. The values for hardness in this case describe the stiffness of the layered system when staying below the threshold for plastic deformation. In such a scenario the bonds between the carbon atoms within the plane can be considered as elastic springs, each with its own elastic constant according to the bond length. The stiffness of the whole layered system, i.e. the force acting against the indenter, is the sum of all the different bonds inside of the layers that are being probed by the indenter. Every atom inside a pristine graphene sheet has three nearest neighbors with a distance of 1.415 Å [35, 36, 39].

As mentioned above, the forces between layers are much smaller in comparison to the inter-layer bonds, enabling easy cleaving of the graphite crystals [36, 94]. There are several issues that need to be considered when indenting on the elastic surface. At first the effectively active forces during the indentation process should be considered. The angle θ of the resulting force that acts on the system is dependent on the geometry of the indenter tip used and the corresponding displacement into the sample, with the cube corner geometry reaching the largest angles [92]. Second, when probing a material with a purely elastic response, the measured data represents the response of the whole system, making it impossible to deconvolute the strength of single bonds. The sphero-conical indenter used in this work, with a fairly large radius compared to the displacement ratio, has a very small angle. The force is thus parallel to the indentation axis and approximately perpendicular to the graphene layers. Since in graphite the π-bonds in between layers are much weaker than the inter-atomic σ-bonds inside the graphene layers,

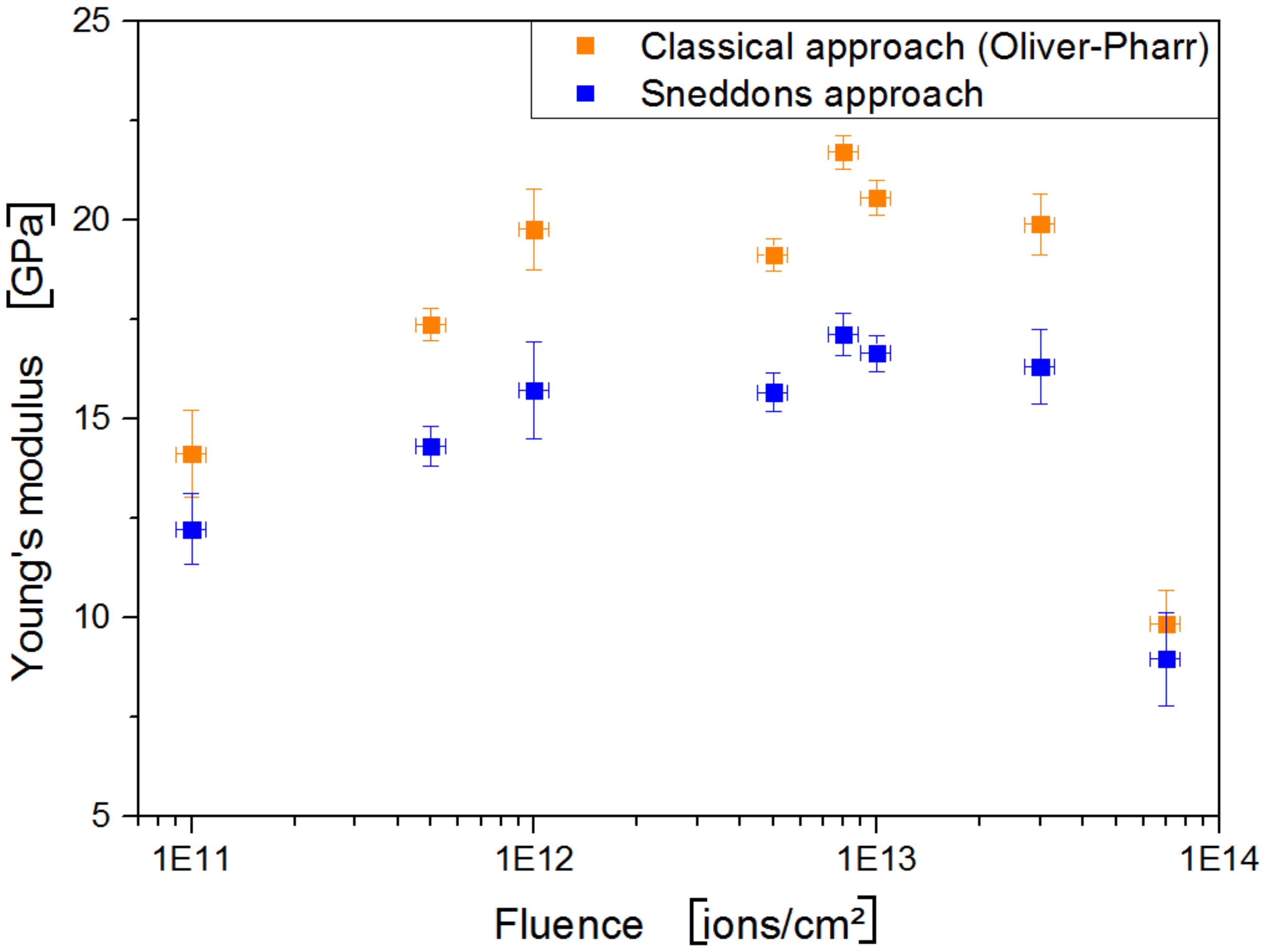

Figure 4.18: Young's modulus as a function of fluence of HOPG irradiated with 4.8 MeV/u ^{197}Au at 1-3×10^9 ions/cm^{2}s (frequency 45 Hz, pulse length 2 ms); The two data sets illustrate a comparison of the classical Oliver and Pharr method [11] and Sneddon's approach [93] to calculate the Young's Modulus for elastic contacts.

the probed layers will be pushed and bent along the indentation axis. This activates the strong σ-bonds significantly and contributes to the deformation resistance (hardness). Compared to the scale of the inter-atomic and inter-layer distances, the probed area is very large, making it impossible to locally probe the elastic constants of single bonds by means of nano-indentation. However, it allows for a qualitative analysis of the crystal.

Experimental setup: To determine ion beam-induced changes in hardness and Young's modulus, a NanoTest^{TM}Vantage system from Micro Materials was used. The system has a load range of 10 μN up to 500 mN. As an indenter tip, a sphero-conical diamond indenter with 60 ° and a tip radius of 3.125 μm was used for HOPG, whereas other materials were tested with a Berkovich diamond indenter. Compared to carbon, the diamond can be considered as infinitely rigid due to the large $E_{diamond}$ of 1141 GPa and $\nu_{diamond}$ of 0.07, compared to E_{carbon} of below 50 GPa [91]. Three indentation techniques were used:

- classical indentation where the penetration depth is monitored as a function of load
- indentation under large forces until failure of the layered graphite system leads to so called "**pop-ins**"
- impact indentations to probe the failure of materials under high strain rates and cyclic loads

Parameters: For the classical indentation test, the indentation depth was set to a maximum of 1000 nm and the load was limited to 17 mN. The loading is stopped after reaching either the load limit or the depth limit. To trigger "pop-ins", the indentation depth was set to a maximum of 20000 nm while the load was limited to 50 mN. The loading is stopped after creating a "pop-in" or reaching the load-limit. In both cases the loading rate is set to 1 mN/s while unloading is set to 3 mN/s. At the peak load there is a holding period of 20 sec. Thermal drift correction is checked post-indentation during the last 20 % of unloading for a duration of 60 sec and applied during the calculation. The data presented is typically the average of 100 indent sites chosen in a grid on the surface with x and y distances of 60 μm. The tip area is calibrated with a diamond area function on a known standard material (fused silica or quartz). For impact indentations, a cube corner geometry was used and an acceleration distance of 10 μm with an impact frequency of 0.5 Hz.

Analysis: The data were fit using Micromaterials NanotestVantage Software. All data points were fit with the Oliver and Pharr's model [11]. For an elastic material response, additional corrections were performed using Sneddon's model [93]. Uncertainties include the errors of the data-fits (models), the errors of the machine and statistical errors.

4.3.5 Electrical resistivity

Graphite exhibits a highly anisotropic electrical resistivity ρ. The Electrical conductivity within the basal planes is very high compared to the inter layer conductivity. Graphite exhibits a negative temperature coefficient up to about 500 °C which results in a decrease of resistivity when increasing the temperature [95]. Defects such as vacancy clusters, dislocation loops, and the formation of new grain boundaries reduce the free mean path of the electrons, leading to a decrease of the conductivity of the material. On-line resistivity monitoring is a sensitive method to investigate the generation of defects during ion irradiation [96]. Since the samples are heated by the ion beam, a series of off-line measurements to determine the temperature dependence of the resistivity were performed in order to determine the temperature dependence of ρ for graphite in the used setup. A 4-point setup was used both for the in situ experiments and for the temperature dependence measurements. Figure 4.19 presents the scheme of the setup, further details are provided in chapter 4.4. These measurements are done in order to have a temperature calibration function for the on-line measurements.

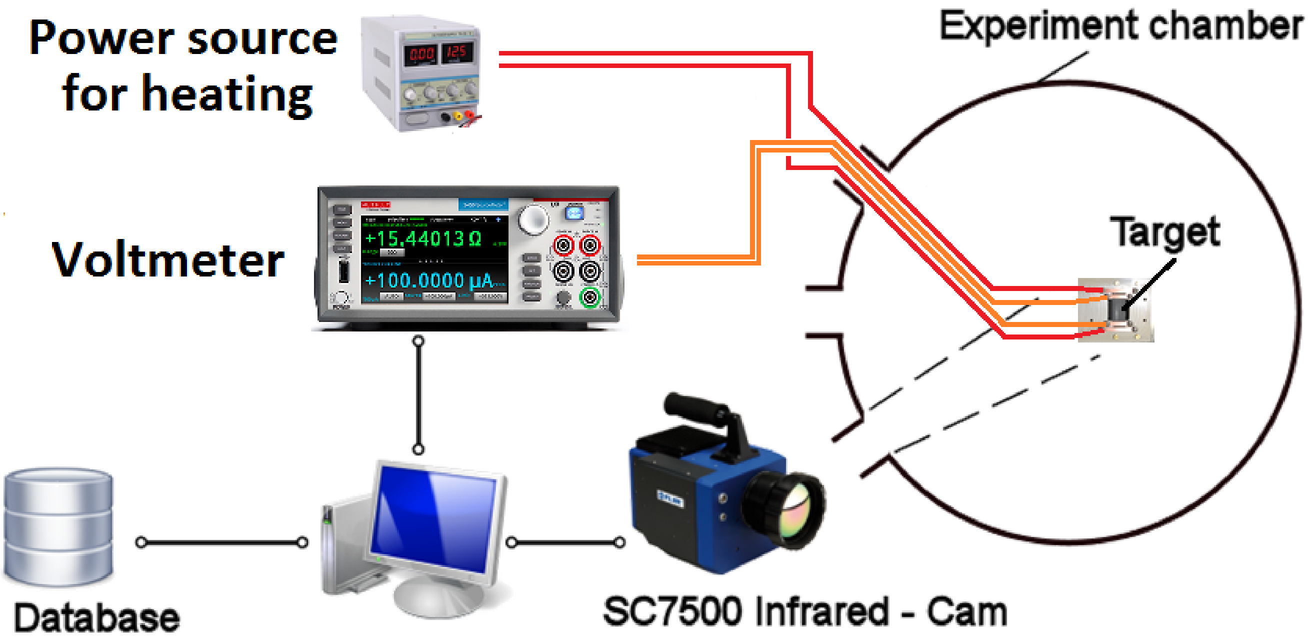

Figure 4.19: Setup of the off-line electrical resistivity measurement at the M3 beamline. The 4-electrode connection of the target can be viewed in figure 4.27

Experimental setup: A polycrystalline graphite sample of $30\times10\times0.05\ mm^3$ was used in the off-line measurement. The sample was heated by passing an electric current. The temperature is monitored by a FLIR thermal camera and the heating-induced voltage drop is measured by a source meter. As for the on-line measurements the same holder-setup was placed inside of an evacuated chamber with a vacuum of $(1\times10^{-8}$ mbar). The sample is heated for 2 minutes at different temperature steps until an equilibrium temperature was reached.

Parameters:

- direct current 100 mA to 9 A
- temperature 20 °C to 320 °C

Analysis: The voltage signal is measured by a Keithley 2540 source meter. Errors include the errors of the devices and an additionally assumed error of 5% due to the manual setting of the current in the power source and the manual data read out.

4.3.6 Profilometry study of beam induced stress/swelling

As mentioned in chapter 2, the defects induced by heavy ion irradiation introduce interlayer interstitial planes, bending and cross linking of basal planes. This leads to swelling and consequently to macroscopical internal stresses at the interface of irradiated and non-irradiated sample volume. In order to measure the beam induced stresses, cantilevers thick enough to completely stop the ion beam (12×2×0.95 mm^3) made from isotropic graphite were irradiated. The resulting bending R_r was measured using a DEKTAK profilometer. This experiment was performed off-line, 4 days after the samples were irradiated to minimize long term stress relaxation. Stoney's equation 4.30 [97] relates the measured bending radius to the stress.

$$\sigma_{rr}^{f} \approx \frac{E_s \cdot h_s^2}{6 \cdot (1 - \nu_s \cdot h_f)} \cdot \frac{1}{R_r} \tag{4.30}$$

Where:

- σ_{rr}^{f} = resulting stress
- E_s = Young's modulus of the sample
- h_s = total thickness of the sample
- h_f = range of the ions within the sample
- R_r = resulting bending radius
- ν_s = Poisson ratio of the material

Setup: The profilometer is shown in figure 4.20. For swelling measurements samples were partially masked during the irradiation. By scanning across the border between the covered and irradiated sample areas a step is measured. The height of the step is directly related to swelling. For stress measurements, polycrystalline graphite cantilevers (12×2×0.95 mm^3) were irradiated and the bending radius was measured. The stresses were calculated using Stoney's equation.

Parameters:

- tip radius = 12.5 μm
- load = 5 mg.
- scan length = 8 mm
- scan time = 120 seconds

Analysis: Data was analyzed using the Vision software provided by Veeco. Uncertainties include errors of the machine and an additionally assumed error due to a non-homogeneous stopping power dE/dx along the ion trajectory (thickness of the irradiated layer).

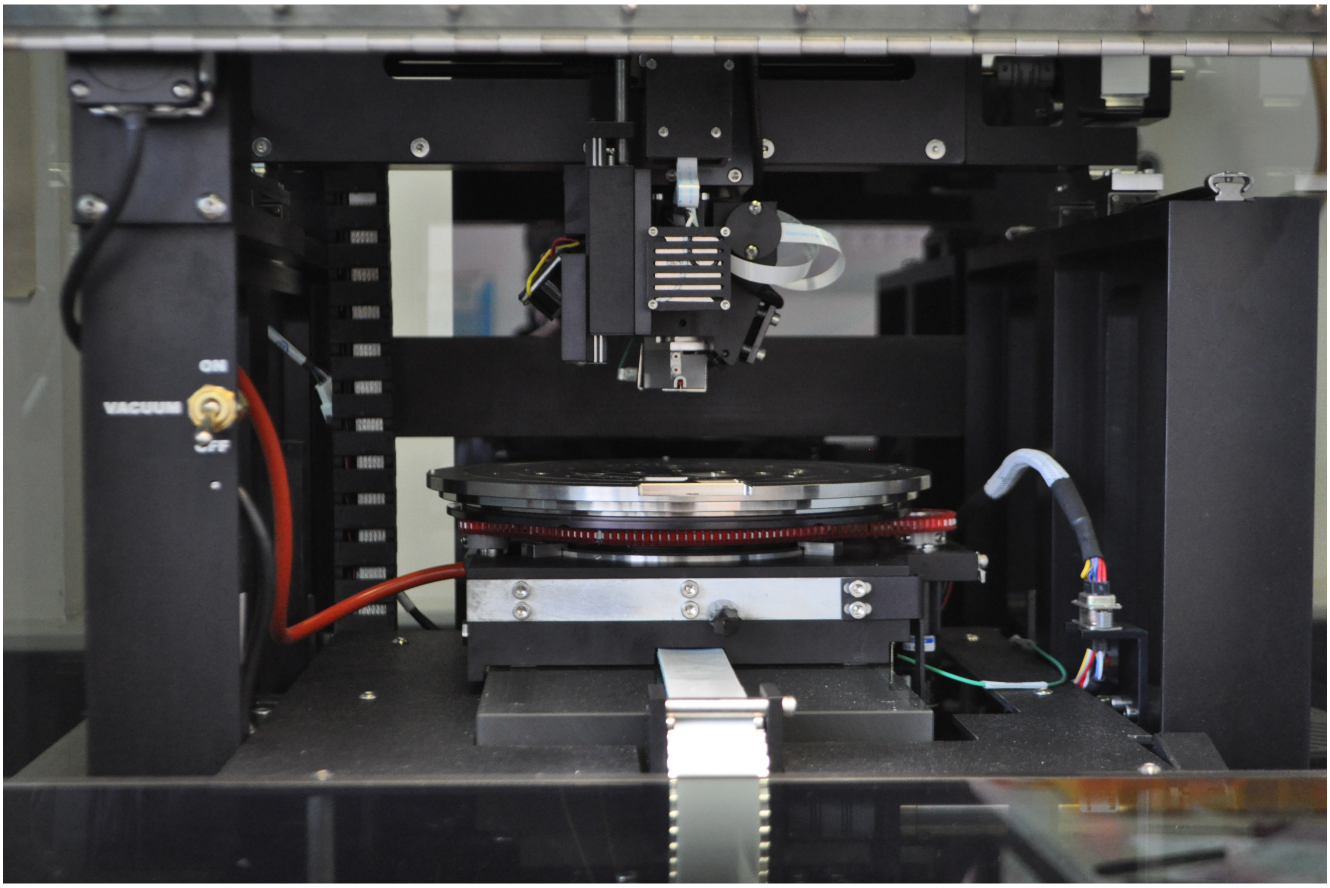

Figure 4.20: Dektak profilometer by Veeco

4.3.7 X-Ray Photoelectron Spectroscopy (XPS)

XPS (X-ray Photo-electron Spectroscopy) is a surface sensitive technique for characterization of elemental compositions, chemical and electronic states and binding energies. This technique was used in order to investigate irradiation induced changes of the bonding of the sample material. For carbon the method is of interest because it can distinguish between sp^2 and sp^3 hybridized carbon bonds. Graphite is in general a pure sp^2 material and only with the presence of defects and ion beam induced phase transitions, sp^3 bonds are observed. Ion irradiation can induce transformation of sp^2 graphite into a sp^2 disordered glassy carbon structure, a sp^3 containing amorphous carbon phase or even into diamond sp^3 structures [98].

In XPS, the core shell electrons are excited by photons of known energy. The measured kinetic energy of the subsequently ejected electrons contains information on the binding energies of the present molecules in the sample. The method is restricted to the superficial atomic layers since electrons from deeper layers will not be emitted far enough to reach the detector. To calculate the energy the following equation (4.31) is used [99].

$$E_{binding} = E_{photon} - (E_{kinetic} + \phi) \tag{4.31}$$

Where:

- $E_{binding}$ = binding energy of the electron
- E_{photon} = energy of the x-ray photons
- $E_{kinetic}$ = kinetic energy of the electron as measured by the instrument
- ϕ = work function dependent on both the measurement setup and the material

A typical C_{1s} spectrum for graphite can be seen in figure 4.21. The important binding energies are 284.5 eV for sp^2 carbon and 285.4 eV for sp^3 hybridized carbon. Peaks at 286.5 , 287.6 and 288.7 eV are assigned to C-O, C=O, and O-C=O bonds, respectively [100]. The sp^2 peak is fit with a Doniach-Sunjic-function whereas the peak of sp^3, C-O, C=O, and O-C=O are fit with a Voigt-function [100].

The presence of C-O, C=O and O-C=O bonds is a sign of defect enhanced dangling bonds concentration on the surface. After irradiation, the surface has an increased amount of dangling bonds and when coming in contact with an oxygen containing atmosphere, C-O, C=O, and O-C=O bonds are formed. This information can be used to further probe the surface of samples for defects.

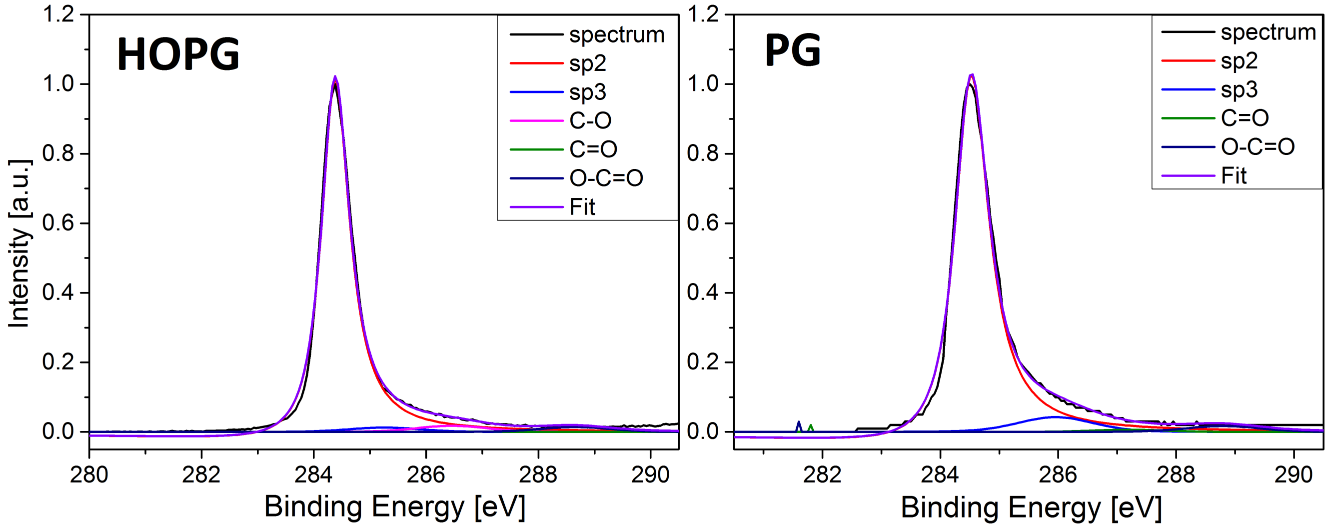

Figure 4.21: Typical C_{1s} XPS spectrum for non-irradiated HOPG (left) and isotropic graphite (PG) (right) including the corresponding fits for sp^2, sp^3, and different $C-O$ bonds.

Experimental setup: The used XPS is an ULVAC-PHI 5000 Versa Probe instrument. It uses a monochromatic Al K-alpha x-ray cathode and has an energy resolution of ≈0.6 eV. The calibration is done using a silver foil. The measurements are performed under an ultra high vacuum $\approx 10^{-9}$ mbar.

Parameters:

- excitation energy = 1486.6 eV
- x-ray Beam-spot = Ø100 μm
- x-ray power = 24.5 W
- acquisition time = 100 ms
- energy steps = 0.05 eV for detailed spectra and 0.8 eV for a survey spectrum

Analysis: Data are analyzed using Fityk [72] and the background is removed using a Shirley-function. Uncertainties include the errors of the data fits and the errors of the machine.

4.3.8 Differential Scanning Calorimetry (DSC)

Differential Scanning Calorimetry (DSC) is widely used to characterize crystallization and melting in polymers and other materials. It is a method that determines the difference in the heat necessary to increase the temperature of a reference sample and the desired specimen, monitored in parallel as a function of temperature. The temperature of the reference and the specimen are measured and the change in enthalpy is calculated by integrating the ΔT to T_{ref} data points [101, 102]. The basic principle of the DSC is shown in relation 4.32 with Φ_{FP} being the heat flow for the sample, Φ_{FR} being the heat flow for the reference and ΔT the temperature difference. Figure 4.22 shows an example of a specimen that undergoes a phase transition at temperature T_M [102]. The integrated area of the difference between the reference and the sample temperature is related to the transition enthalpy. The specific heat capacity c_P in $J/(kg \cdot K)$ can be calculated by the ratio of the heat flux given by ΔS and the heating rate divided by the mass (compare figure 4.22 [101, 102].

$$\Phi_{\mathrm{FP}} - \Phi_{\mathrm{FR}} \propto \Delta T \tag{4.32}$$

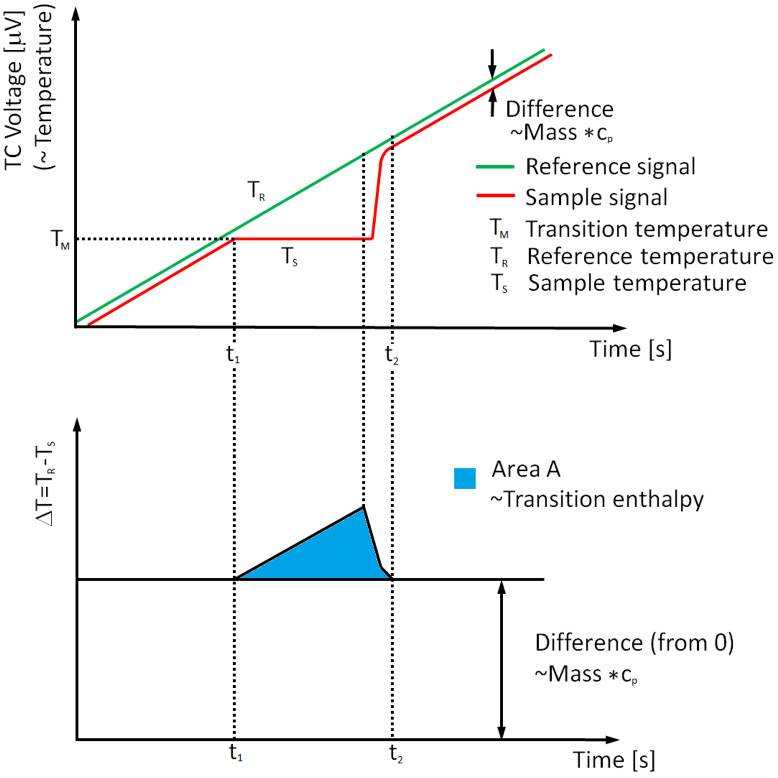

Figure 4.22: Working principles of a heat flux DSC system for a material undergoing a phase transition [102].

For carbon based materials, the DSC enables the observation of phase transitions during heat release. In case of radiation damage, it allows the observation of defect annealing processes. A well known example in graphite is the Wigner energy release [103, 104]. Wigner proposed in 1946 that lattice defects induced by radiation can recombine when overcoming their respective energy barrier, resulting in an energy release. In 2003 Ewels et al. [105] proposed that metastable defects (such as the intimate Frenkel pair) are associated with the Wigner energy release in graphite. Today the Wigner energy release is generally associated to the recombination of an intimate Frenkel pair - a vacancy and a close positioned interstitial (I-V). This recombination can be triggered by thermal excitation. The energy barrier for I-V recombination is 1.38 eV. In graphite the annealing of I-Vs starts around 200 °C [105]. The amount of energy set free by thermal excitation depends on the kind (size and structure) of the defects that recombine. Recombination processes can further heat the material, enabling more complex recombinations and, in extreme cases, lead to vaporization. This energy release was the cause of the first nuclear accident that happened in Windscale in 1957 as graphite moderators caught fire when engineers were trying to anneal the neutron induced radiation damage of the graphite parts [106]. Recombination or annealing processes that releases energy can be seen by a negative heat capacity in the DSC data, which means that the sample is heating itself.

Experimental setup: The DSC 404 F1 PEGASUS®from NETZSCH that was used during the measurements at the Forschungzentrum Jülich. The samples were placed into a crucible with good thermal conductivity inside of the platinum furnace that has an upper temperature limit of 1500 °C. During a measurement, Argon 5.0 is used to ensure an oxygen free environment so that the samples do not oxidize during the heating cycles. Temperatures are measured directly at the reference and sample crucibles. In most systems an empty crucible serves as a reference. Good thermal contact between the specimen and the sample holder disc is crucial to ensure reliable measurements.

Parameters:

- isothermal phase duration = 15 min at 40 °C
- heating program from 40 to 1400 °C using a heating rate of 20 K/min to increase the sensitivity
- data points every 5 K
- Protective gas = Ar 5.0 with a flow rate of 60 ml/min

Analysis: Data are fit using the NETZSCH Proteus® software. Measurements were difficult and the results have large errors due to problems with the sample geometry and thermal contacts during the measurements. Thus no quantitative analysis could be done but the data provide trends.

4.3.9 Scanning electron microscopy (SEM)

For imaging purposes a Phenom XL scanning electron microscope(SEM) from PhenomWorld was used (courtesy to LOT-Quantum Design in Darmstadt). The unit is equipped with an Energy dispersive x-ray (EDX) detector and a back scatter electron (BSE) detector. Electron microscopy uses electrons to create a contrast image of the measured sample. With the Phenon XL magnifications around 50000x were achieved on graphite due to the sub ideal contrast offered by the graphite. Accelerator voltages between 5 and 15 kV were used depending on the magnification. The images were recorded at the LOT Quantum Design facility in Darmstadt. Further details can be viewed in Ref [107].

4.4 In situ Measurements

4.4.1 X-ray diffraction

Additional to the off-line experiments we did some on-line XRD measurements at the M2 beam line which houses a SEIFERT 4-circle X-ray diffractometer with a Cu-Kα X-ray source [108]. The samples were tilted into a position normal to the ion beam. After a certain fluence, the ion beam was stopped and the samples was tilted back into the position for XRD analysis.

Setup: The samples are glued on silicon wavers which are glued to a copper sample holder. The sample holders are mounted on a movable stage attached in the 4 circle diffractometer. The chamber is under an ultra high vacuum of 1×10^{-8} mbar.

Parameters:

- acquisition time = 5 s to 10 s for each step
- re-scanning of each point 3 times
- 2Θ measurement range from 5° to 110°
- 2Θ measurement step size = 0.02°
- calibration by a Si-standard

Analysis: The data were fit according to the above mentioned methods using the Fityk software [72]. Uncertainties include the errors of the data fits and the errors of the machine. For conclusions of empirical equations additional errors of up to 10 % are assumed. For the ion-fluence an uncertainty of 10 % is assumed due to an indirect monitoring of the beam during irradiation (compare chapter 4.2.

4.4.2 Raman spectroscopy

Raman spectroscopy has been used both for off-line measurements and for on-line measurement. The on-line setup enables the investigation of a given sample area after each accumulated fluence step, which eliminates the influence of material inhomogeneities that typically appear when comparing two measurements done at different points. All off-line measurements presented here are the average of large mappings. Furthermore, the sample remains within vacuum and is thus not exposed to air, which keeps ion induced dangling bonds on the sample surface free of oxygen and hydrogen. The setup is described in figures 4.23 and 4.24 respectively. The target chamber houses a turnable sample stage with an attached z-manipulator and an objective. A micro-manipulator (Physics Instrument PI P-725.4CD) is used to focus the laser on the sample through the objective. It is controlled from outside via a control unit (Physics Instrument E-665.CR) and connected via a vacuum feed through. The sample is irradiated under an angle of 45° while the surface is normal to the incoming laser. The Laser (Laser Quantum Ventus 532 nm Laser with 90 mW power) hits the objective through the glass window. The confocal head (Horiba Superhead), is mounted on an XYZ stage in order to align the laser and the objective. A cold light source (Euromex EK1 cold light source), the laser and the Raman detector (Horiba Jobin Yvon iHR 320) are connected to the confocal head.

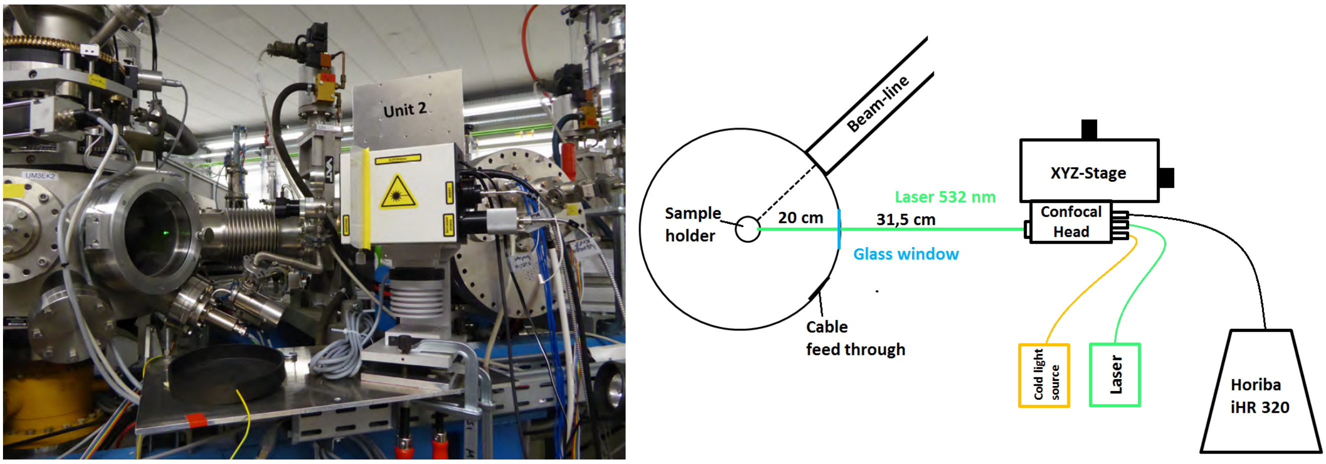

Figure 4.23: Left picture: Close up of the on-line Raman setup at the M3 beam-line of the UNILAC showing the mounted confocal head sending the green laser beam through the experimental chamber view port (made from glass) to the irradiated sample. The beam-line M3 is in the background; Right picture: Schematic of the whole setup [109]; Marked are the distance from objective to window (20 cm) and from window to the confocal head (31.5 cm).

Setup: The samples are mounted on an micro manipulator within an evacuated experimental chamber under an vacuum (1×10^{-8} mbar) with a glass view port at the M3 beam line. The Raman spectrometer is placed outside. The laser is focused on the sample through an Olympus SLMPlan N 50x objective (working distance: 18 mm) that is mounted inside. The detector and the laser optics are mounted outside. During irradiation no spectra are taken due to beam

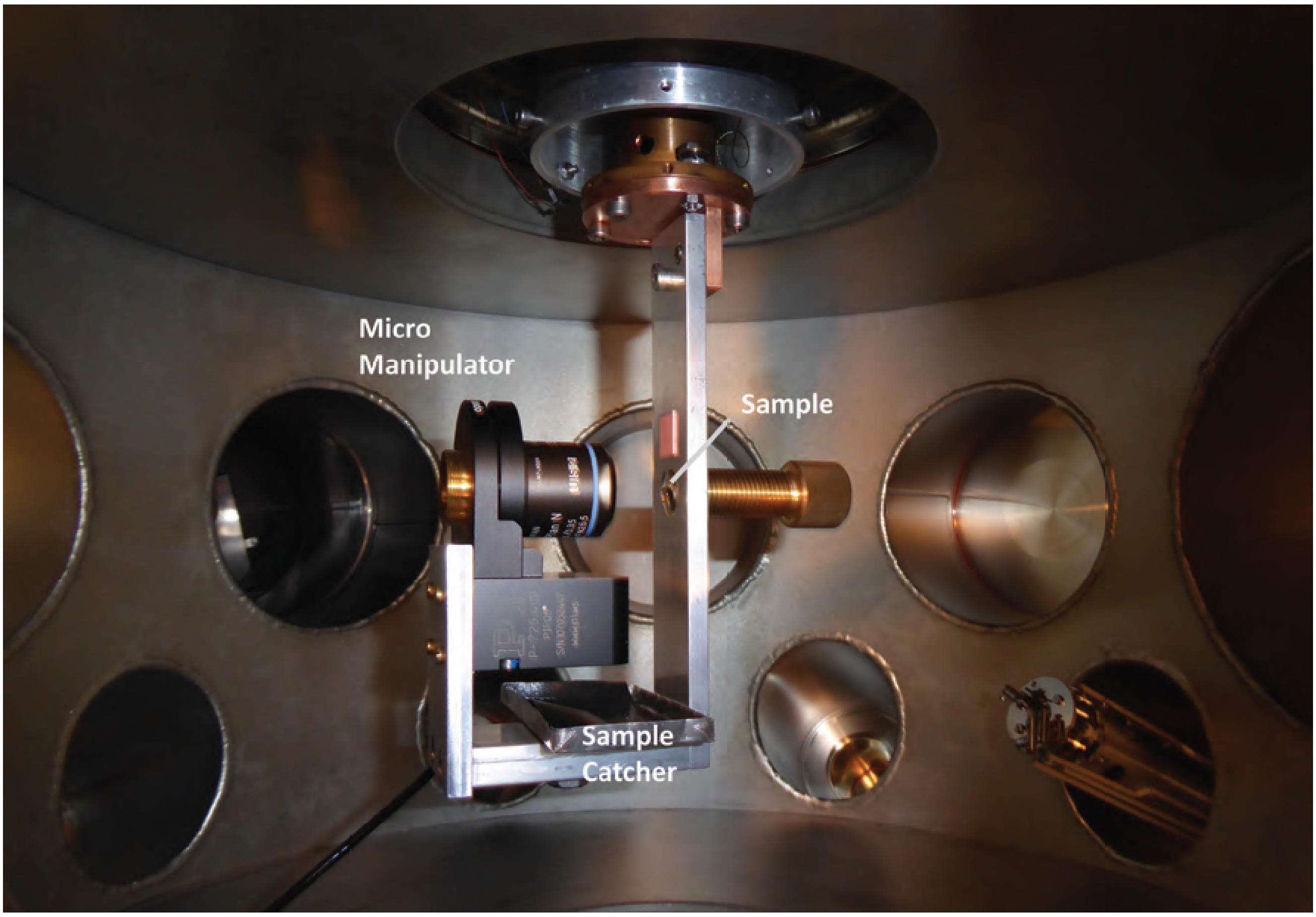

Figure 4.24: Sample holder inside the irradiation chamber at the beam-line. The sample is mounted an a screw for coarse focusing, the micro-manipulator (Physics Instrument PI P-725.4CD) is used for fine focusing. The objective (Olympus SLMPlan N 50x) has a working distance of 18 mm [109].

induced luminescence. The samples are irradiated under an angle of 45°.

Parameters:

- laser beam-spot = ≈10.5 μm in diameter
- exposure time = 45 sec
- repetitions per point = 3
- scan range = from 100 to 3000 cm^{-1}

Analysis: Data were acquired using Horiba's LabSpec 5 software. Data were fit using the Fityk software [72]. Error bars include the uncertainties of the data fits and the errors of the machine. For conclusions of empirical equations additional errors of up to 10 % are assumed. Some empirical methods yield errors of up to 35 % (due to a dependence on λ_{Laser}) and are thus mainly used to show trends and qualitative changes within the samples. For the ion-fluence an error of 10% is assumed due to an indirect monitoring of the beam during irradiation (see chapter 4.2).

4.4.3 IR thermography

In order to monitor the thermal conditions of the samples, a thermal camera from FLIR was used during most experiments. The camera viewed the beam-exposed side of the sample at 45° as presented in figure 4.25. For experiments operated above the Coulomb barrier (e.g. C-ions at 5.9 MeV/u or Xe-ions at 4.8 MeV/u) the camera was not used due to the increased neutron and gamma ray background at the beam line and the risk of radiation damage to the IR detector.

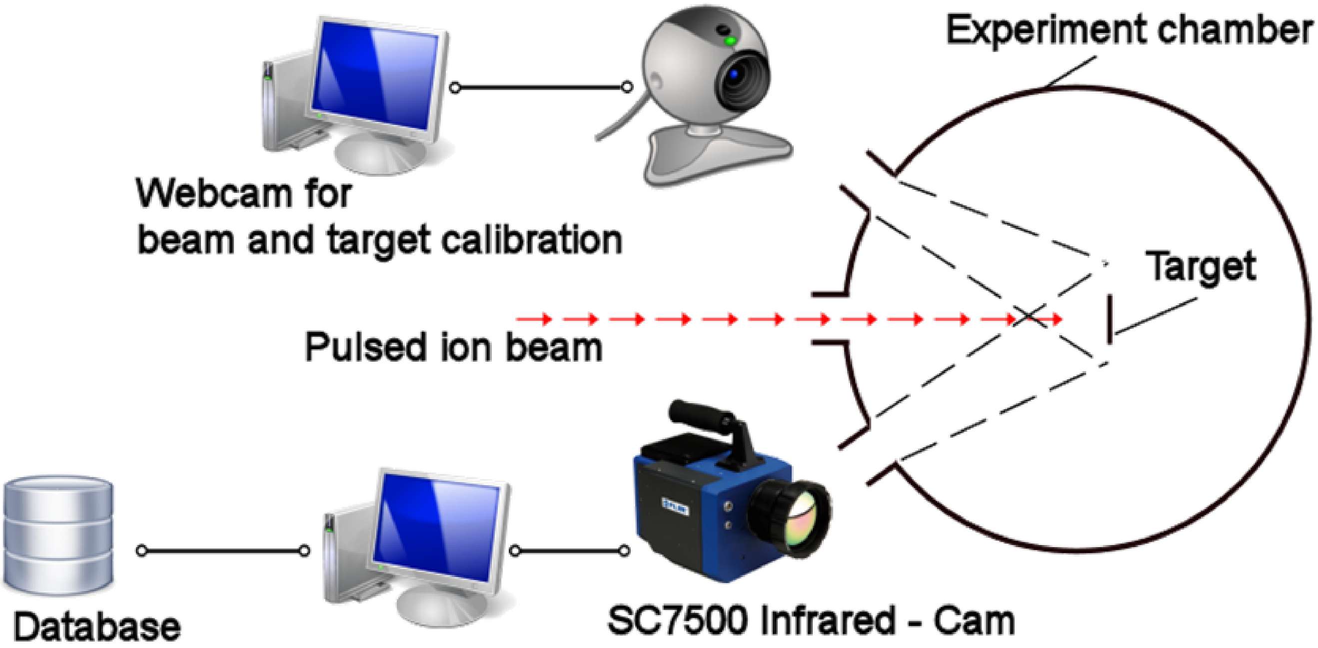

Figure 4.25: IR thermography setup for on-line monitoring of beam induced thermal effects at the M3 beam-line.

The IR-detector of the camera allows to probe temperatures up to 1500 °C using two additional filters and different exposure times. The thermal image recorded represents counts (referred to as digital levels) that have to be converted into absolute temperatures considering the emissivity of the sample combined with the IR detector exposure settings and (if used) filters. Typical temperatures reached during the sample irradiation range from 40 to 500 °C depending on the ion flux and duty cycle of the beam. Higher duty cycles create larger equilibrium temperatures (even with the same amount of ions/cm*s) since the time for the sample to cool down in between pulses is limited. The IR-camera can be operated at up to 1.4 kHz which enables the observation of each single beam pulse and its corresponding induced temperature as seen in figure 4.26. In order to determine the temperature evolution during irradiation, several flux tests were conducted. The camera operated in a not triggered free run mode, running with 300 to 1000 Hz.

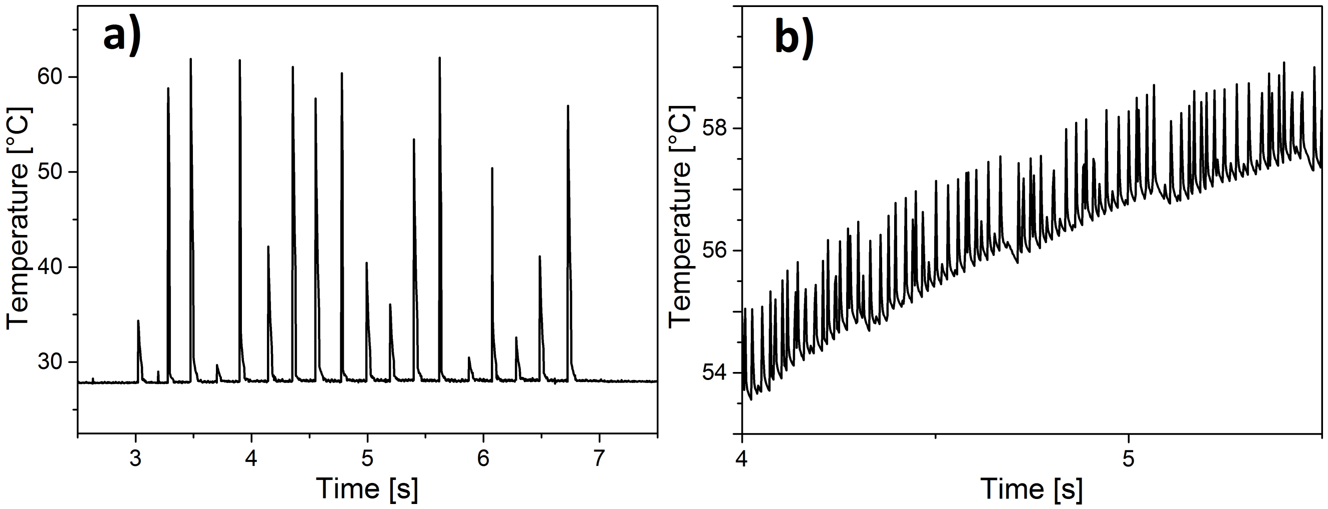

Figure 4.26: Temperature profile of PG during irradiation with low (left: 5 Hz) and high (right: 45 Hz) duty cycles of 4.8 MeV/u ^{197}Au as recorded by the FLIR IR-camera.

4.4.4 Electrical resistivity

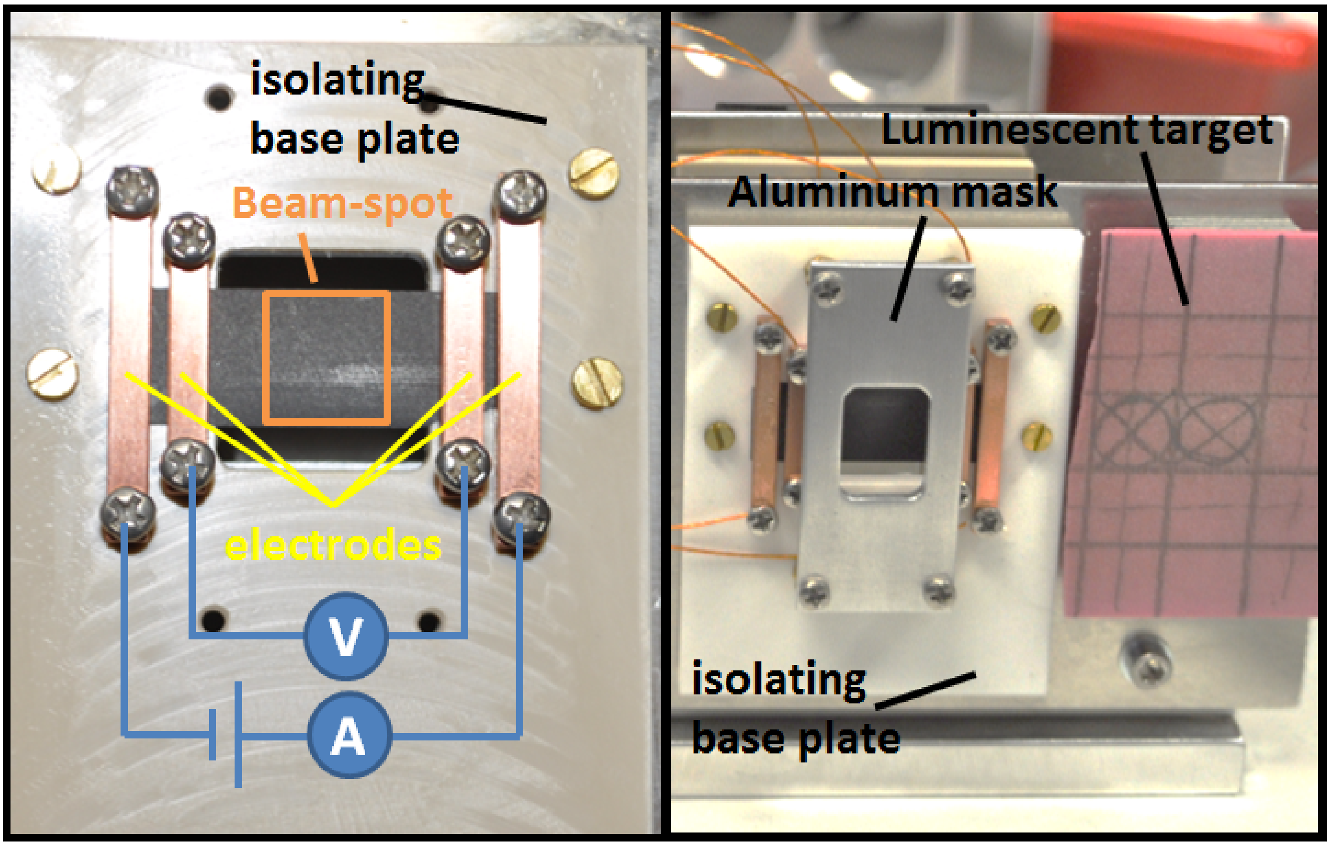

Figure 4.27: Front view of the on-line resistivity measurements setup for 4-probe on-line electrical resistivity measurements. Left: Sample with 4 Cu electrodes mounted on an isolating substrate (PEEK); beam spot and wiring are indicated. Right: Sample on final holder covered by an Al mask with 1 cm^2 aperture to ensure homogeneous irradiation; An alumina (Cr doped Al_2O_3) luminescent target is used to control the shape of the beam.

In parallel to the off-line resistivity measurements, on-line measurements were done during ion irradiation using the same setup, but at much lower currents (100 mA) to avoid current induced heating of the samples. For the resistivity monitoring of an irradiated sample, one has to differentiate between two possible cases. (i) the sample is fully irradiated and completely penetrated by the ion beam over the whole cross section of the specimen (figure 4.28). (ii) the ions are stopped within the sample and only a limited sample layer is irradiated. This corresponds to two resistors in parallel due to the different electrical resistivities of the irradiated and non-irradiated part of the sample (figure 4.29). In the on-line and off-line measurements the change in the voltage which is needed to maintain a constant current within the sample is constantly measured. Applying equation (4.33), the total resistance over time t - which translates into fluence accumulation Φ during the irradiation - of the whole system is directly measured as shown in figure 4.28 and in figure 4.29.

$$R_{electrical} = \frac{U}{I} \tag{4.33}$$

Where $R_{electrical}$ is the electrical resistance of a resistor with a known geometry and a known material composition (typically given in Ω), U is the voltage (given in V) and I is the current through the sample (given in A).

case(i): Fully ion-penetrated sample

For most of the on-line resistivity experiments we have chosen the thickness of the used front samples to be thin enough for full penetration by the ion beam as presented in figure 4.28. To ensure the complete/homogeneous irradiation of the sample, the beam spot was set to be ∼ 20% wider than the sample. Additionally a mask was used as shown in figure 4.27 to protect the electrodes and the sample holder from the beam spot. The contact to the sample is done using four Cu electrodes that fix the sample in place. Due to the sample holder geometry, it was possible to irradiate two samples in parallel. A first sample and a second sample behind that was only partially exposed.

The total resistance R_{total} is measured during the irradiation and can be regarded as being composed of 3 resistors. It can be described by equation4.34.

$$R_{total-serial} = \sum_{i=1}^{n} R_i \tag{4.34}$$

The resistance of the irradiated part (figure 4.28) adapted to case(i) is described in equation (4.35), where R_{Φ} is the measured total resistance at a given fluence Φ.

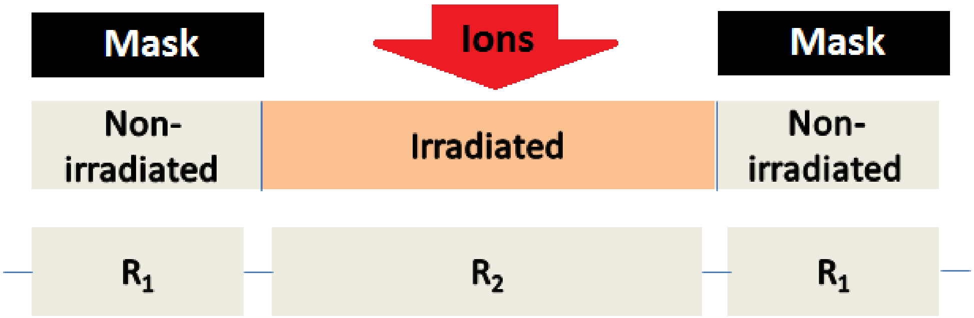

Figure 4.28: Scheme of the used electrical circuit for an irradiated front sample where the complete cross section was penetrated by the ions.

$$R_2 = R_\Phi - 2 \cdot R_1 \tag{4.35}$$

The electrical resistivity ρ of each part of the sample is given by equations 4.36.

$$\rho = \frac{A \cdot R}{l} \tag{4.36}$$

Where ρ is the electrical resistivity of the sample material in $\Omega \cdot \frac{mm^2}{m}$, A is the cross section of the sample in mm^2 which is simply the product of the ion penetration range in the sample h in mm (or sample thickness if the ion range h is larger than sample thickness) and the width of the irradiated specimen w in mm. l is the length of the corresponding resistor in m. The index represent the corresponding resistor according to figure 4.28 and 4.29. For the case, where one discards the swelling effect in the irradiated part and the heating effect of the sample by the current one can set additionally:

$$A_0 = A_1 = A_2 \tag{4.37}$$

$$\rho_0 = \rho_1 \tag{4.38}$$

where the indices are identical to the respective figure 4.28 and A_0 is the cross section at the beginning of the irradiation. The resistivity of the sample before irradiation is ρ_0.

The simple case, considering the equations (4.36) and (4.35) leads to the equation (4.39). This finally enables a calculation of the desired specific electrical resistivity of the irradiated sample while measuring R_ϕ and knowing the geometry of the different resistors within the system.

$$\rho_2 = \frac{A_2 \cdot (R_\phi - 2 \cdot R_1)}{l_2} \tag{4.39}$$

Where ρ_2 is the electrical resistivity of the irradiated part of the sample in $\Omega \cdot \frac{mm^2}{m}$ and R_ϕ is the measured resistance as a function of the ion fluence ϕ.

case(ii):Partially ion-penetrated sample

For the samples that were only partially penetrated by the ion beam we consider a more complex model as presented in figure 4.29.

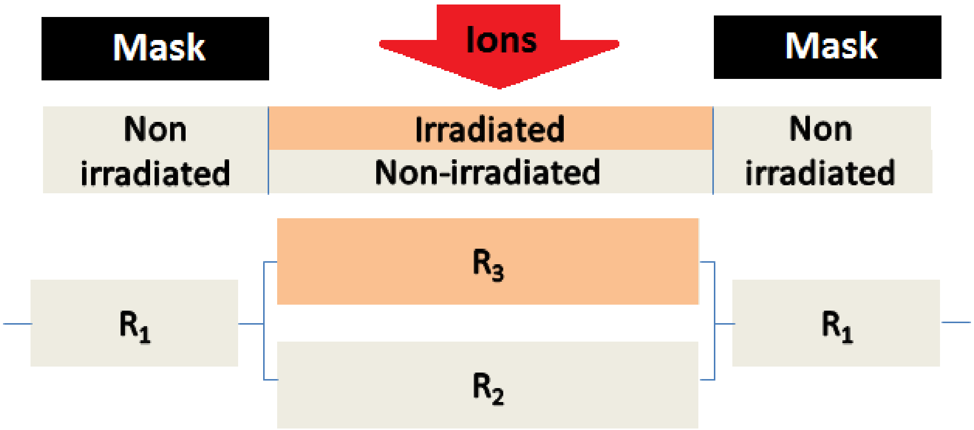

Figure 4.29: Equivalent circuit of an partially irradiated sample where the ion has been stopped within the sample.

The system is presented by a combination of serial and parallel connected resistors while we are only able to measure the resistance of the whole sample. To infer the desired electrical resistivity and its change with increasing ion fluence ϕ the following equations were used.

$$R_\phi = 2 \cdot R_1 + R_{||} \tag{4.40}$$

where $R_{||}$ is defined by equation 4.41 As for the simple case we have to solve the equation (4.34) for the desired resistance, in this case now called R_3. Since we are facing not only a serial alignment of resistors but also a parallel section, we have to include the equation (4.41).

$$\frac{1}{R_{||}} = \sum_{i=1}^{n} \frac{1}{R_i} \tag{4.41}$$

Where $R_{||}$ is considered the resistance of the whole configuration of parallel connected resistors R_i. Applying equation (4.41) for the resistors R_2 and R_3 will receive the total resistance $R_{||}$ for the parallel section within our system as seen in equation (4.42).

$$R_{||} = \frac{R_2 \cdot R_3}{R_2 + R_3} \tag{4.42}$$

And finally equation (4.36) can be substituted into equation (4.40) leading to equation (4.43) that allows to calculate the desired electrical resistivity ρ_3 of the irradiated part, for the corresponding fluence ϕ.

$$\rho_3 = \frac{(R_\phi \cdot R_2 - 2 \cdot R_1 \cdot R_2) \cdot A_3}{(2 \cdot R_1 + R_2 - R_\phi) \cdot l_3} \tag{4.43}$$

where $A_3 = w \cdot h$

Setup: The samples are mounted on an moving stage within an evacuated chamber at the M3 beam-line at UNILAC accelerator at GSI conditioned at an ultra high vacuum($1{\times}10^{-8}$ mbar). The temperature was monitored using the FLIR SC7500 infrared camera (compare figure 4.25). During the irradiation the voltage and the current signals are acquired using a source meter and an IEEE interface. The samples are irradiated under an angle of 90°.

Parameters:

- current $I = 100$ mA, to avoid ohmic heating
- data acquisition rate= 0.3 to 1 Hz
- sample temperature with beam = 50 to 130 °C to avoid significant temperature induced annealing
- sample temperature without beam = ≈ 22 °C
- ion flux limited to $1-3\ \times\ 10^9\ ions/cm^2 * s$ to limit beam induced temperature rise of the sample to 50 - 130° C

Analysis: The data were fit in Origin9G using the above mentioned algorithms. Errors include the errors of the data-fits and the errors of the devices. For conclusions of empirical equations additional errors of up to 10 % are assumed. For the ion-fluence an error of 10 % is assumed due to an indirect monitoring of the beam during irradiation (compare chapter 4.2).

5 Results and Discussion

The following Chapter summarizes selected results of the irradiation experiments and sample analysis by means of SEM, Raman spectroscopy, XRD, XPS, profilometry, electrical resistivity studies, LFA, DSC and nano/micro-indentation. To fully understand radiation damage, one has to understand the structural changes that come along with ion irradiation. These radiation-induced changes within the atomic structure of the material modify and alter the material properties. Some beam-induced effects can even be seen under the optical microscope.

5.1 Beam-induced surface effects in carbon materials studied by SEM

This subsection presents a selection of micrographs to introduce the used materials and their modification by ion irradiation. The model for a perfect graphite crystal is represented by HOPG, a layered structure as shown in figure 5.1a. Due to radiation-induced stresses or under physical force, these layers can be bent. An extreme case of bending due to an external physical force is presented in figure 5.1b.

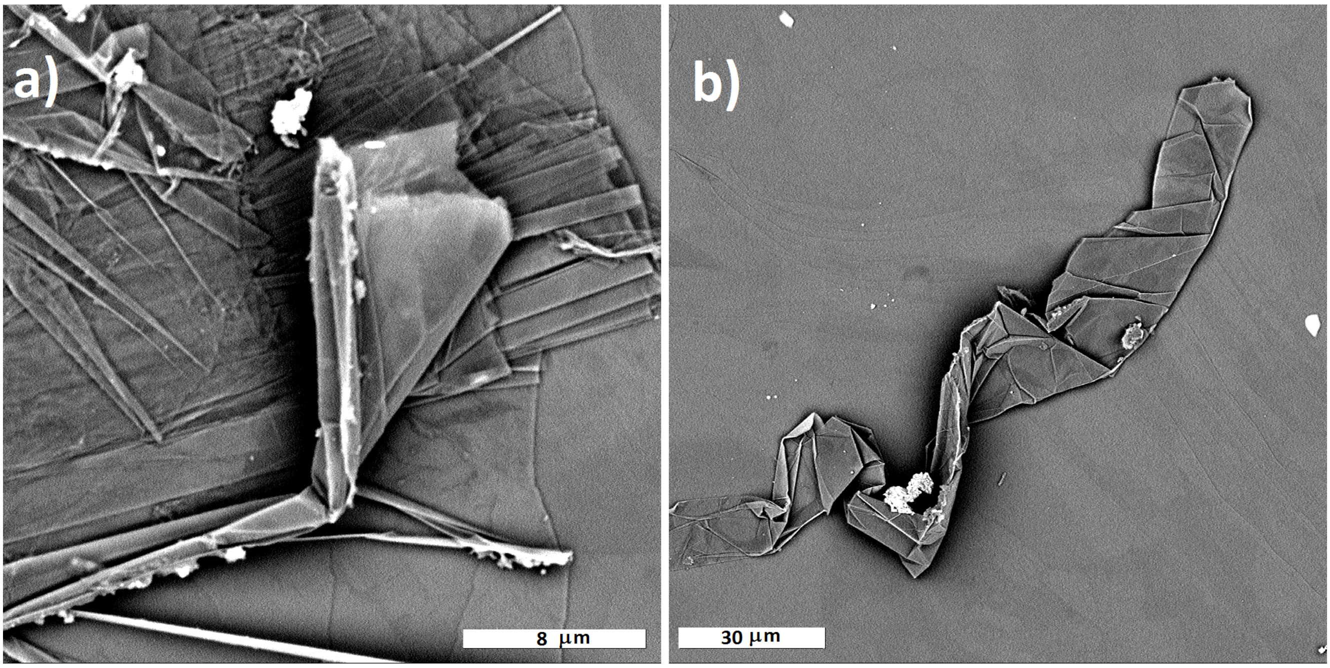

Figure 5.1: a) Surface of non-irradiated HOPG with an arrangement of folded layers; b) Surface of non-irradiated HOPG with a folded layer.

The model for a highly disordered sp^2 carbon structure is represented by the GC. Its glass like features and smooth surface are shown in figure 5.2. Beam-induced stresses will lead to micro cracks within the sample. If the beam-induced stresses become too high, the irradiated part starts to delaminate from the non-irradiated part.

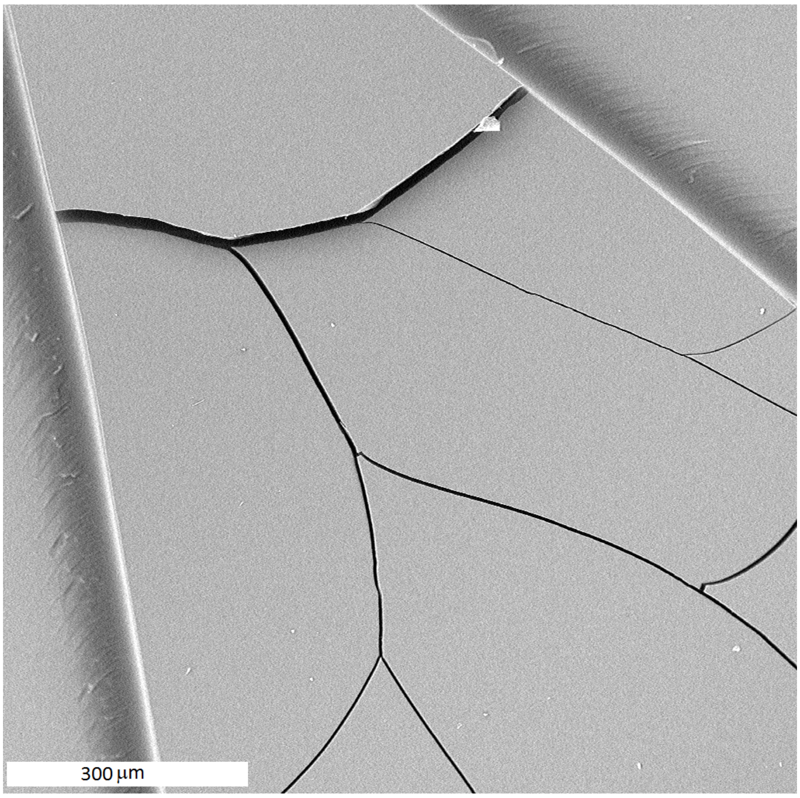

Figure 5.2: Surface of glassy carbon (GC) irradiated with 7×10^{13} ions/cm^2 4.8 MeV/u ^{238}U (frequency 1 Hz; pulse length 0.5 ms) showing irradiation-induced cracks.

Flexible graphite is represented in figure 5.3. To produce the FG, graphite is expanded using a gas and the expanded graphite flakes are laminated into 0.15 to 2 mm thick sheets. The presented cross sections reveal a strongly disordered structure within the FG around the end of the ion range where nuclear stopping is dominant (last 5 μm) which is visible even in the SEM micrographs.

Finally, polycrystalline graphite samples are presented in figures 5.5 and 5.4. Figure 5.5a shows a partially masked PG sample after irradiation with 4.8 MeV/u ^{197}Au ions at 45 Hz / 2 ms to a fluence of 2×10^{14}ions/cm^2. One can see the formation of nano-objects on the irradiated part and optically a brighter color that can be linked to smaller graphite crystals (figure 5.5b) due to ion beam milling and an increased formation of oxygen bonds. A whisker that resulted from ion impacts is shown in figure 5.5c. Whiskers or even onions (figure 5.4a) can be created when a sufficient volume of carbon is sputtered from the target and condensates on the surface. The PG is synthesized by graphitizing a biomass filler material and a graphite matrix at high temperatures. This often leaves behind pores within the bulk materials as shown in figure 5.5d. The porous character of the bulk material is also one of the reasons why the density of PG with $\approx$1.84 g/cm^3 is smaller than the theoretical density of graphite $\approx$2.27 g/cm^3. The cross section

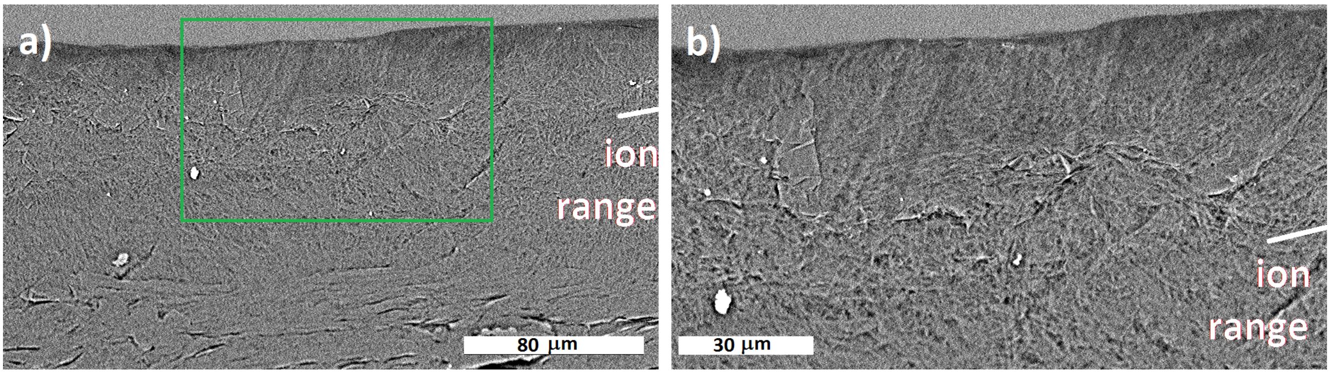

Figure 5.3: Cross section micrograph of flexible graphite (FG) irradiated with 7×10^{13} ions/cm^2 of 4.8 MeV/u ^{197}Au (frequency 45 Hz; pulse length 2 ms); The upper part of the sample shows the irradiated area, the end of the ion range is indicated by the white line; Left and Right show the same spot of the sample at different magnifications.

micro graphs of irradiated PG do not reveal significant changes compared to the non-irradiated samples.

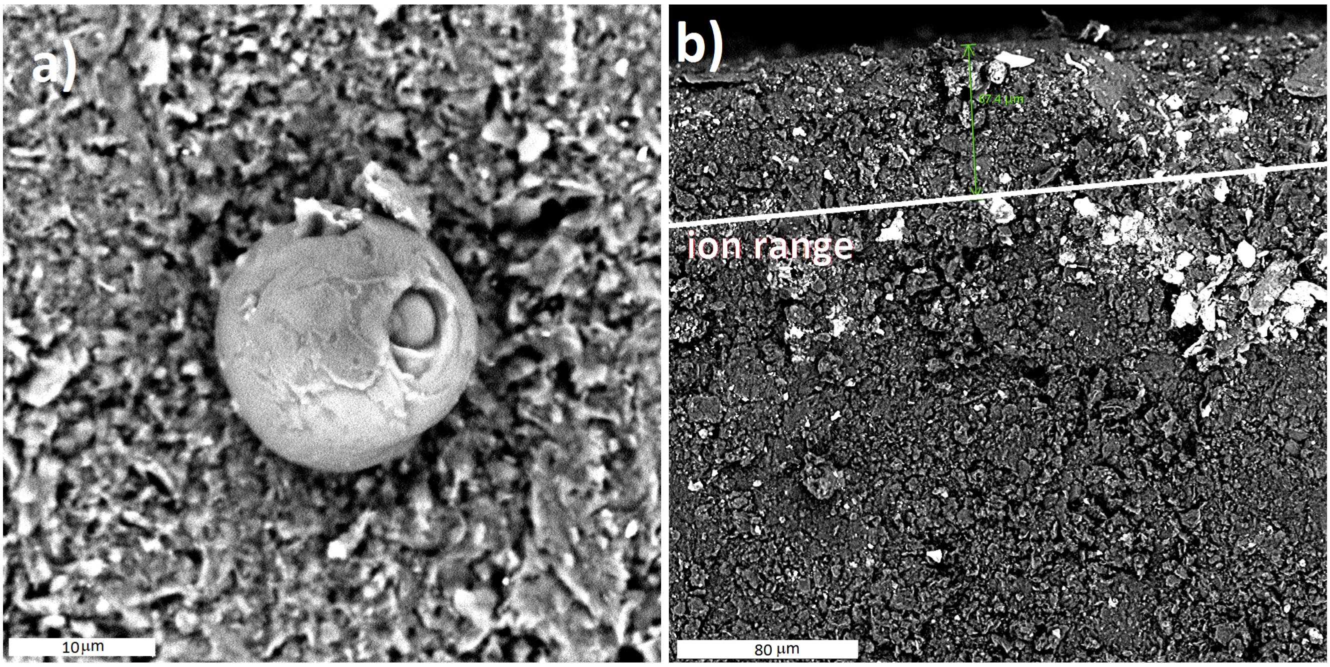

Figure 5.4: a) An onion on 4.8 MeV/u ^{197}Au at 45Hz / 2ms irradiated PG; b) Cross section of 4.8 MeV/u ^{238}U at 1 Hz / 0.5 ms irradiated PG (10^{13} $ions/cm^2$); the ion range is indicated by the white line, the upper part is irradiated.

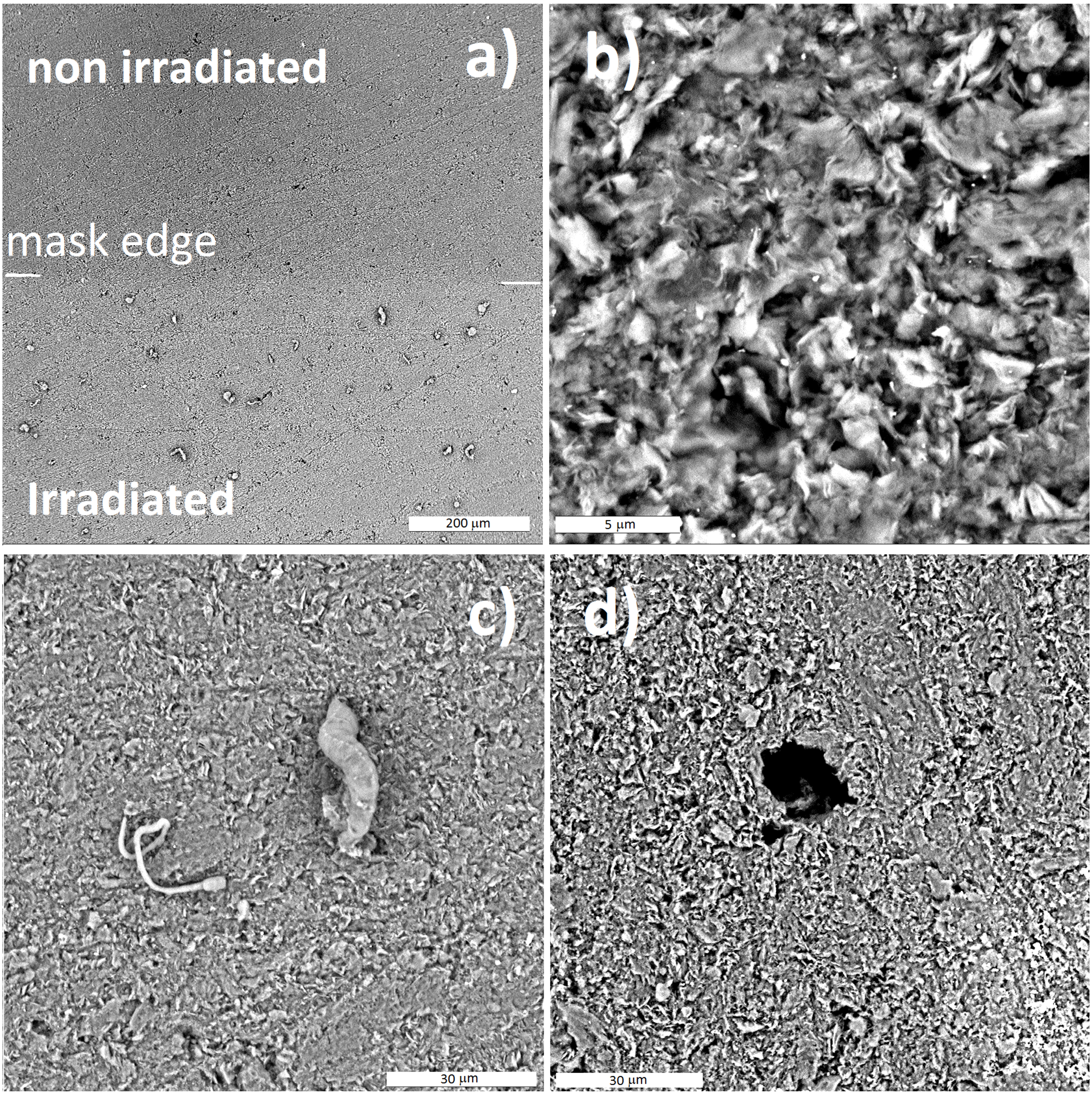

Figure 5.5: Surface of polycrystalline graphite (PG) irradiated with 2×10^{14} ions/cm^2 of 4.8 MeV/u ^{197}Au (frequency 45 Hz; pulse length 2 ms); a) Lower half is the irradiated surface, upper half was masked; formation of nano-objects on the irradiated part is visible b) Closeup of the irradiated PG surface; c) A whisker on the surface of the irradiated PG; d) A pore on the irradiated PG.

5.2 Beam-induced structural changes studied by Raman spectroscopy

To identify structural modifications, Raman spectroscopy and x-ray diffraction were used. The following chapter summarizes the Raman spectroscopy measurements, both post irradiation and in-situ, that were performed on irradiated samples of PG, FG, HOPG and GC. Samples of HOPG and GC act as a model material, with HOPG representing a perfect graphitic structure and GC representing a disordered sp^2 structure.

5.2.1 Post-irradiation investigations

As discussed in chapter 4.3.1, Raman spectroscopy allows to probe many defect-related changes within the graphitic structure. Figure 5.7 and 5.8 presents the results for the investigated HOPG samples and figure 5.10 and 5.11 presents the results for the investigated GC samples.

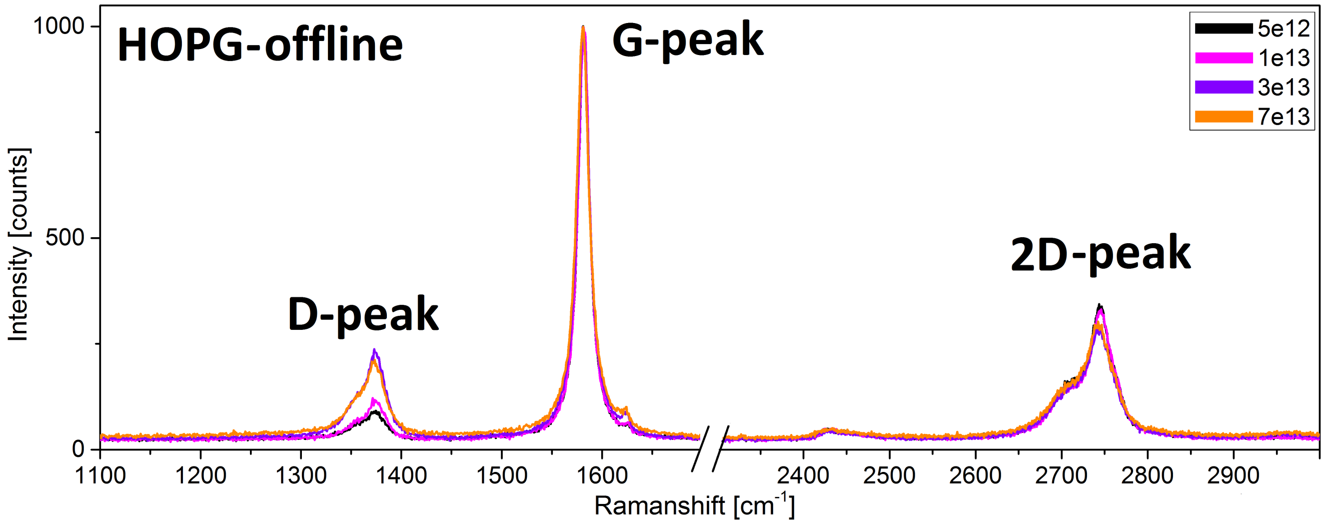

Figure 5.6: Representative Raman spectra evolution with accumulating fluence (post irradiation measurements) of HOPG irradiated with 4.8 MeV/u ^{197}Au at 2-3×10^9 ions/cm^2*s (frequency 45 Hz; pulse length 2 ms).

A selection of Raman spectra from irradiated HOPG is shown in figure 5.6. The appearance of the D-band as well as a change in the 2nd order D-band with increasing ion fluence can be observed. Most prominent effects related to irradiation-induced structural changes, include phase changes (e.g. amorphization), creation of defects and change of the stacking order. An important indicator in this regard is the full width at half maximum (FWHM) of the band. An increase of the Raman FWHM can be typically associated with disordering and amorphization of the crystal. The FWHM of the G-peak is increasing with ion fluence (figure 5.7a). The evolution of the FWHM provides an indication that there is a threshold for amorphization and disordering of graphite around a fluence of 1×10^{13} ions/cm^2. This broadening of the G-peak is not only fluence but also dE/dx dependent as heavier ions like ^{238}U and ^{197}Au have a larger effect than e.g. ^{131}Xe or ^{150}Sm. The samples irradiated by ^{209}Bi ions seem to be less affected even though ^{209}Bi ions have a larger dE/dx. This discrepancy can be explained by the dose rate effects and is further discussed in chapter 5.10. Raman spectroscopy provides a unique tool for investigating graphite. Since the intensity of the spectrum not only depends on the sampled material, but also on measurement parameters, only ratios of peak intensities are compared and not absolute

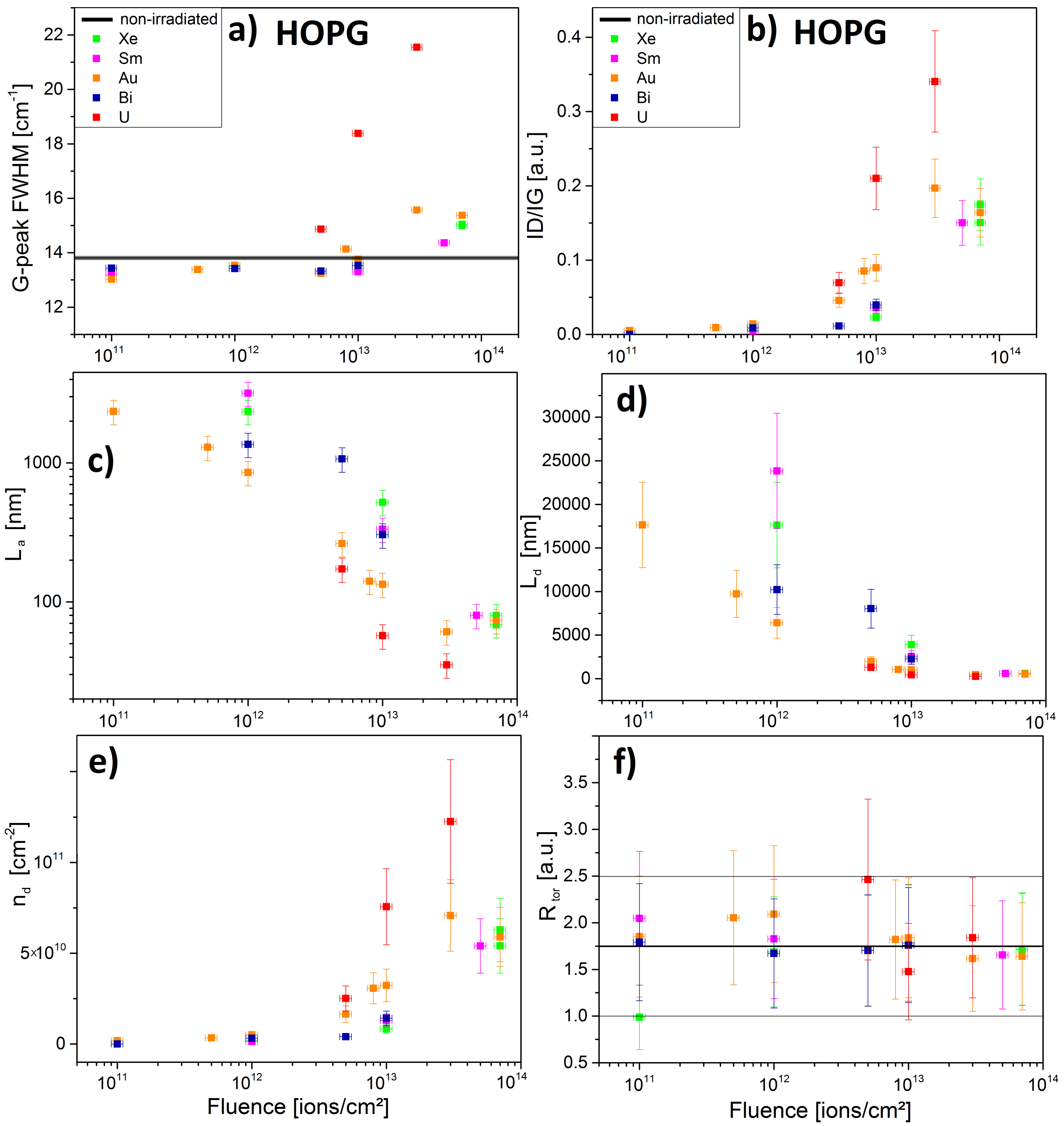

Figure 5.7: Fluence dependency of Raman graphitic parameters (post irradiation measurement) of HOPG irradiated with 4.8 MeV/u ions: ^{131}Xe 2-3×10^9 ions/cm^2*s (frequency 5 Hz; pulse length 1.2 ms), ^{150}Sm at 2-3×10^9 ions/cm^2*s (frequency 3.4 Hz; pulse length 1.2 ms), ^{197}Au at 2-3×10^9 ions/cm^2*s (frequency 45 Hz; pulse length 2 ms), ^{209}Bi at 2-5×10^9 ions/cm^2*s (frequency 3.4 Hz; pulse length 1 ms) and ^{238}U at 1-2×10^9 ions/cm^2*s (frequency 1 Hz; pulse length 0.5 ms); Results are given as a function of ion fluence; a)Full width half maximum (FWHM) of the G-peak; b) I_D/I_G; c) Average in-plane crystal size L_a; d) Average defect spacing L_d; e) Average density of defects n_d; f) Tortuosity R_{Tor}; Solid lines represent the values of pristine samples where the thin lines represent the error bar; some error bars are smaller than the symbols.

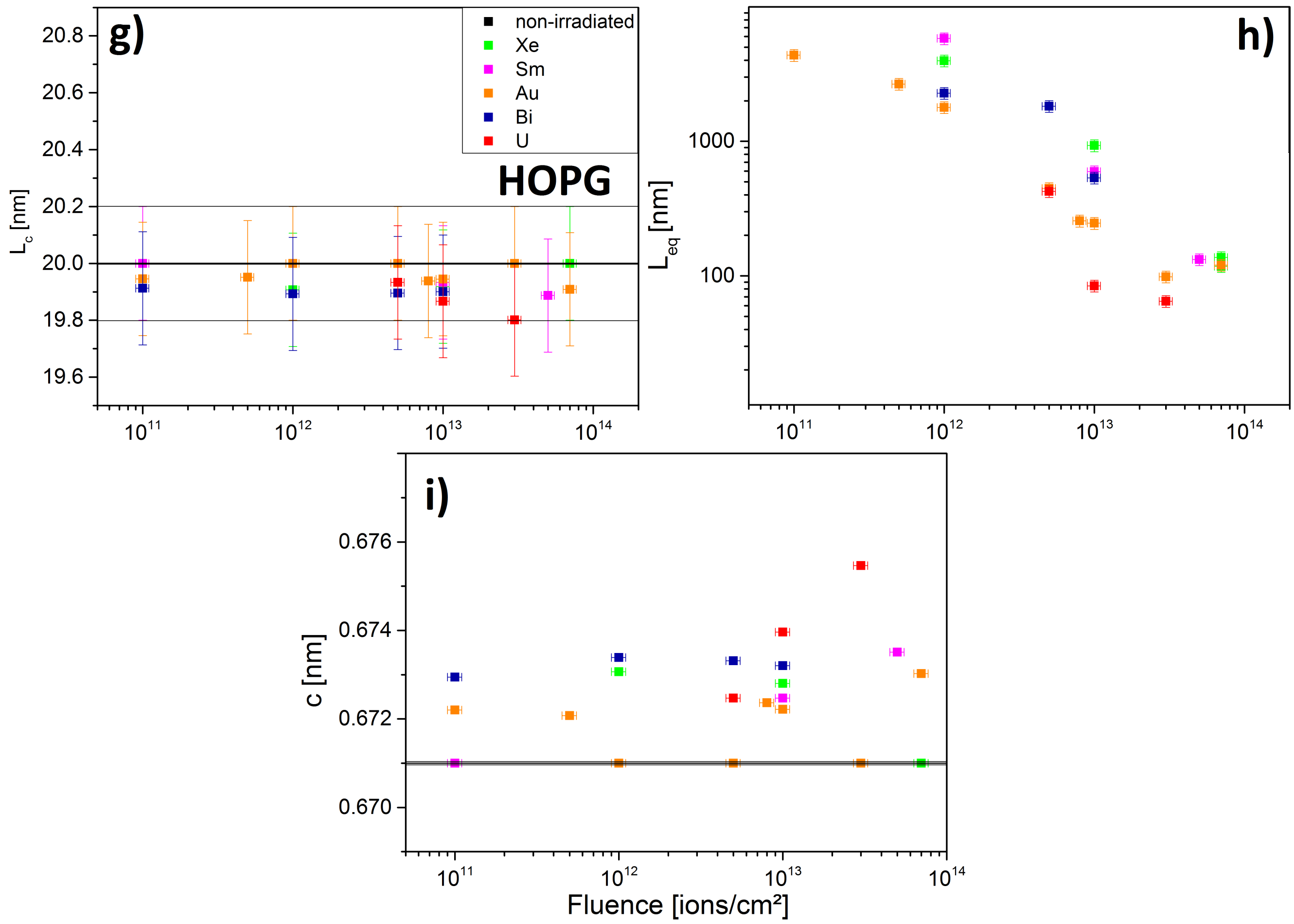

Figure 5.8: Fluence dependency of Raman graphitic parameters (post irradiation measurement) of HOPG irradiated with 4.8 MeV/u ions: ^{131}Xe 2-3×10^9 ions/cm^2*s (frequency 5 Hz; pulse length 1.2 ms), ^{150}Sm at 2-3×10^9 ions/cm^2*s (frequency 3.4 Hz; pulse length 1.2 ms), ^{197}Au at 2-3×10^9 ions/cm^2*s (frequency 45 Hz; pulse length 2 ms), ^{209}Bi at 2-5×10^9 ions/cm^2*s (frequency 3.4 Hz; pulse length 1 ms) and ^{238}U at 1-2×10^9 ions/cm^2*s (frequency 1 Hz; pulse length 0.5 ms); Results are given as a function of ion fluence; g)Average crystal size along the c-axis, L_c; h) Average graphene sheet length (including tortuosity) L_{eq}; i) Lattice parameter c; Solid lines represent the values of pristine samples where the thin lines represent the averaged uncertainties; some uncertainties are smaller than the symbols.

intensities. The main peak in graphitic systems is the G-peak (stretching of sp^2 bonds) located around 1580 cm^{-1} and it is used for normalization. The higher the amount of defect sites within the crystal, the higher the intensity of the D-peak. As the D-peak can only become active if there are edges and defects within the graphene sheets, the ratio of I_D/I_G presents a very important factor for most empirical characterization methods. This makes the D-peak one of the most important indicators for the characterization of disordering and defects in graphitic systems. Similar to the FWHM of the G-peak, the ratio I_D/I_G increases with the fluence as more and more defects are introduced and merge to larger clusters (figure 5.7b). There is a threshold to resolve the D-band given by the limitations of the Raman spectrometer. The signal to noise ratio of the D-peak below fluences of 1×10^{12} ions/cm^2 is very small and makes a characterization for the low fluence samples difficult. The D-peak contains information on both, size and number of defects. Larger defect-clusters as well as many single defects increase the intensity of the D-peak. Vacancy defects within graphite have a limited mobility. The high mobility of interstitials on the other hand leads to recombination. A dependence on dE/dx for the D-peak intensity is also visible and is in agreement with the G-peak FWHM. The average in-plane crystal size L_a (figure 5.7c), the average defect spacing L_d (figure 5.7d) and the average density of defects n_d (figure 5.7e) are all a function of the I_D/I_G and thus exhibit a similar trend. L_a of the non-irradiated HOPG is 5-10 μm for the used HOPG grade (as stated by the provider [110]). Following irradiation, the size of the crystals is milled down to 20-100 nm as the basal planes start to bend and break apart. For L_a a larger dE/dx leads to faster degradation of the crystal size.

In addition to the energy-loss-effect there is also a saturation in the fluence dependence above high fluences of 3×10^{13} ions/cm^2 that can be associated with the regime of track overlapping according to the Poisson law and the corresponding damage cross section of the ion species. L_d is inversely proportional to the average density of defects n_d ($n_d \approx 1/L_\mathrm{d}^2$). Finally, the tortuosity R_{Tor} (figure 5.7f), the average graphene sheet lengths L_{eq} (figure 5.8g), the out of plane lattice parameter c (figure 5.8i) and the average out of plane crystal thickness L_c (figure 5.8h) are related to the second order D-peak. R_{Tor} describes the amount of bending within a graphene layer with $R_{Tor} = 1$ corresponding to a perfect graphene layer (values below 1 have no physical meaning). The method to determine R_{Tor} is highly dependent on the fitting of the data and thus yields large error bars. Nevertheless, it shows a slight trend towards smaller R_{Tor} with increasing ion fluence(figure 5.7f). When the graphene sheets start to fragment into smaller pieces with increasing ion fluence due to defect-induced stresses, the extent of graphene bending decreases. The large error bars allow no further conclusions with regard to a possible dE/dx dependence. Connected to the tortuosity is the average graphene sheet length L_{eq}. L_{eq} is the product of the average in-plane crystal size L_a and the tortuosity R_{Tor} and thus considers bent and warped graphene layers (where L_a resembles an average projected graphene sheet length, L_{eq} resembles the real average graphene sheet length). As R_{Tor} is slowly decreasing with the ion fluence (fragmenting of graphene sheets in smaller layers and subsequent milling of crystals into smaller crystals), L_{eq} is decreasing in accord to L_a. The out of plane lattice parameter c is increasing with fluence as additional interstitial planes and bending pushes the layers of graphene further apart. L_c, the crystal thickness, slightly decreases with larger ion fluences, but the errors impede further conclusions.

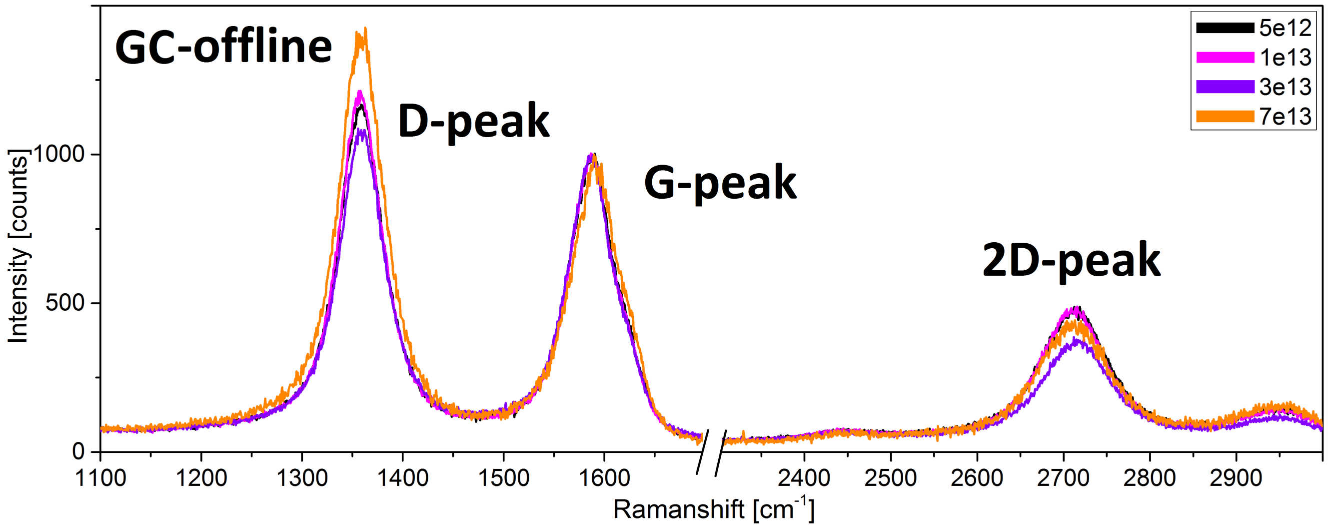

Figure 5.9: Representative Raman spectra evolution with accumulated fluence (post irradiation measurements) of glassy carbon (GC) irradiated with 4.8 MeV/u ^{197}Au at 2-3×10^{9} ions/cm^{2}*s (frequency 45 Hz; pulse length 2 ms).

In contrast to the pristine structure of HOPG, the glassy carbon (GC) is already a highly disordered carbon-based material with mainly sp^2 and some sp^3 and sp^1 bonds. Despite the large disorder in GC, ion irradiation still yields an additional amorphization and further degradation of the lamellar graphitic structures present within the sample as shown in a selection of different spectra presented in figure 5.9. The FWHM of the G-peak (figure 5.10a) slightly increases with the ion fluence. Even though there is a clear fluence dependence that is in agreement with the results obtained for HOPG, there is no clear evidence for a dE/dx dependence of the disordering in GC. This could be an indication that the observed disordering of the GC is dominated by elastic collisions and not by ionization processes. In contrast to HOPG, I_D/I_G (figure 5.10b) does not increase with the fluence for GC, even though figure 5.9 indicates otherwise. The reason for the ostensible increase of the D-band is caused by an increase of the underlying D2, D3 and D4-bands. Also larger dE/dx has no evident influence on the I_D/I_G. Since the material is already disordered to a large extend the ion beam has little effect on the creation of additional defects and scatter centers associated with the D-peak. This lack of sensitivity to fluence and dE/dx is subsequently present in L_a, L_d and n_d presented in figures 5.10c,d and e respectively. The presented results show that the effect of SHI irradiation on GC is very small or not clearly resolvable using Raman spectroscopy. L_a is for GC roughly 10 nm and thus around 4 times smaller than the L_a of HOPG at fluences above 3×10^{13} ions/cm^2. L_d of GC is

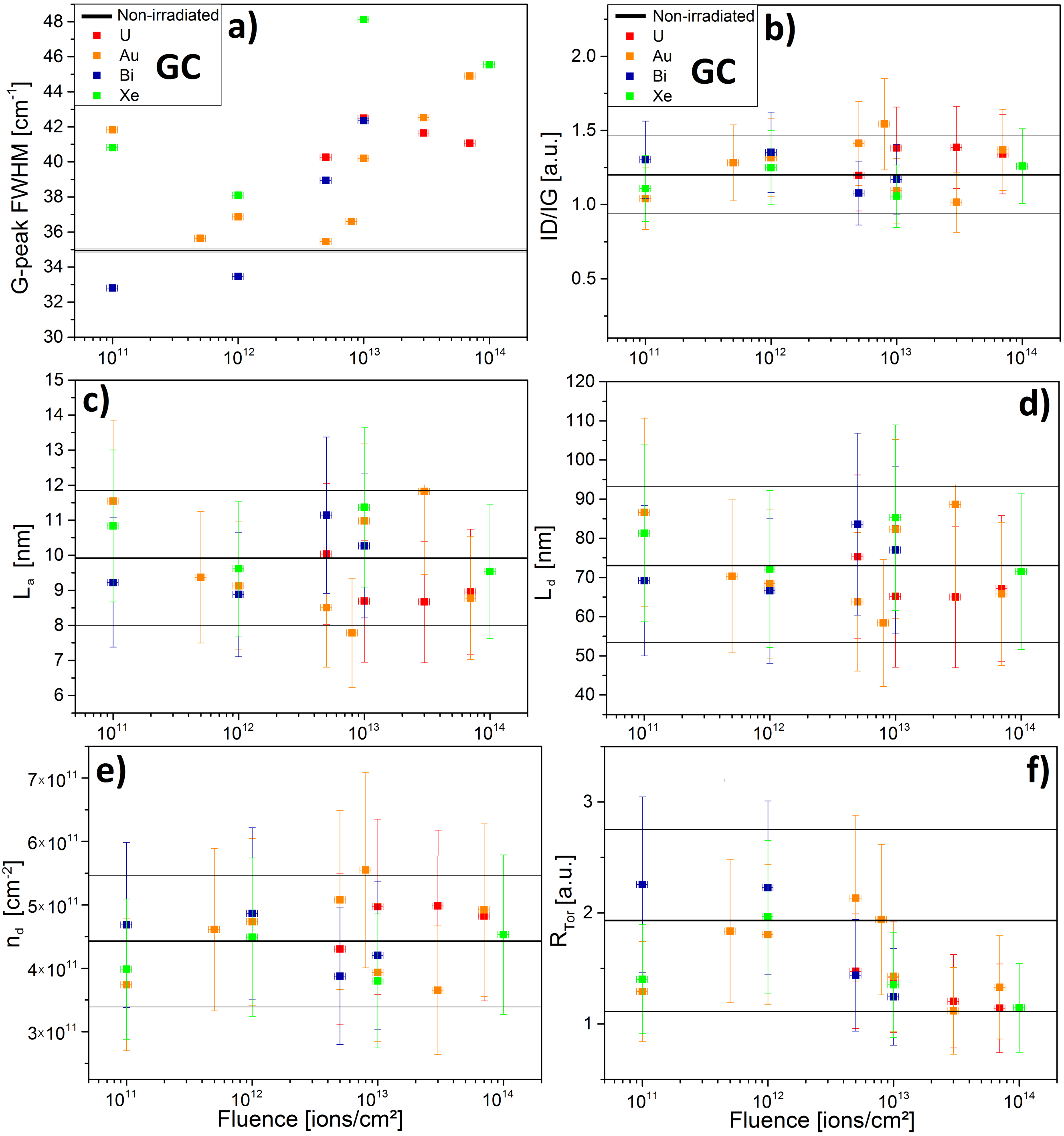

Figure 5.10: Fluence dependency of Raman graphitic parameters (post irradiation measurement) of GC irradiated with 4.8 MeV/u ions: ^{131}Xe at 2-3×10^9 ions/cm^2*s (frequency 5 Hz; pulse length 1.2 ms), ^{197}Au at 2-3×10^9 ions/cm^2*s (frequency 45 Hz; pulse length 2 ms), ^{209}Bi at 2-5×10^9 ions/cm^2*s (frequency 3.4 Hz; pulse length 1 ms) and ^{238}U at 1-2×10^9 ions/cm^2*s (frequency 1 Hz; pulse length 0.5 ms); Results are given as a function of ion fluence; a)Full width half maximum (FWHM) of the G-peak; b) I_D/I_G; c) Average in-plane crystal size L_a; d) Average defect spacing L_d; e) Average density of defects n_d; f) Tortuosity R_{Tor}; Solid lines represent the values of pristine samples where as the thin lines represents the averaged uncertainties; some uncertainties are smaller than the symbols.

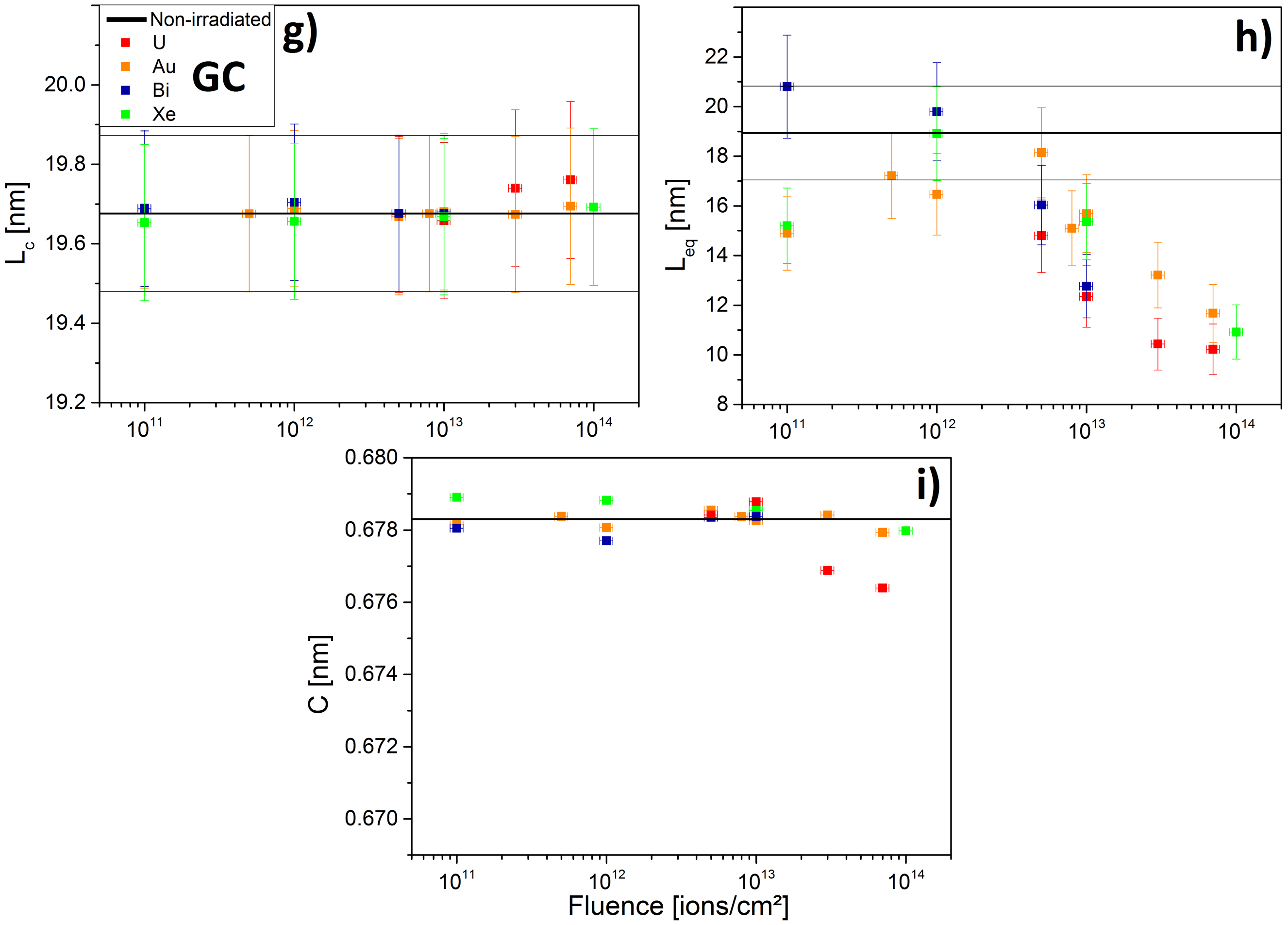

Figure 5.11: Fluence dependency of Raman graphitic parameters (post irradiation measurement) of GC irradiated with 4.8 MeV/u ions: ^{131}Xe at 2-3×10^9 ions/cm^2*s (frequency 5 Hz; pulse length 1.2 ms), ^{197}Au at 2-3×10^9 ions/cm^2*s (frequency 45 Hz; pulse length 2 ms), ^{209}Bi at 2-5×10^9 ions/cm^2*s (frequency 3.4 Hz; pulse length 1 ms) and ^{238}U at 1-2×10^9 ions/cm^2*s (frequency 1 Hz; Results are given as a function of ion fluence; g) Average crystal size along the c-axis, L_c; h) Average graphene sheet length L_{eq}; i) Lattice parameter c; some uncertainties are smaller than the symbols.

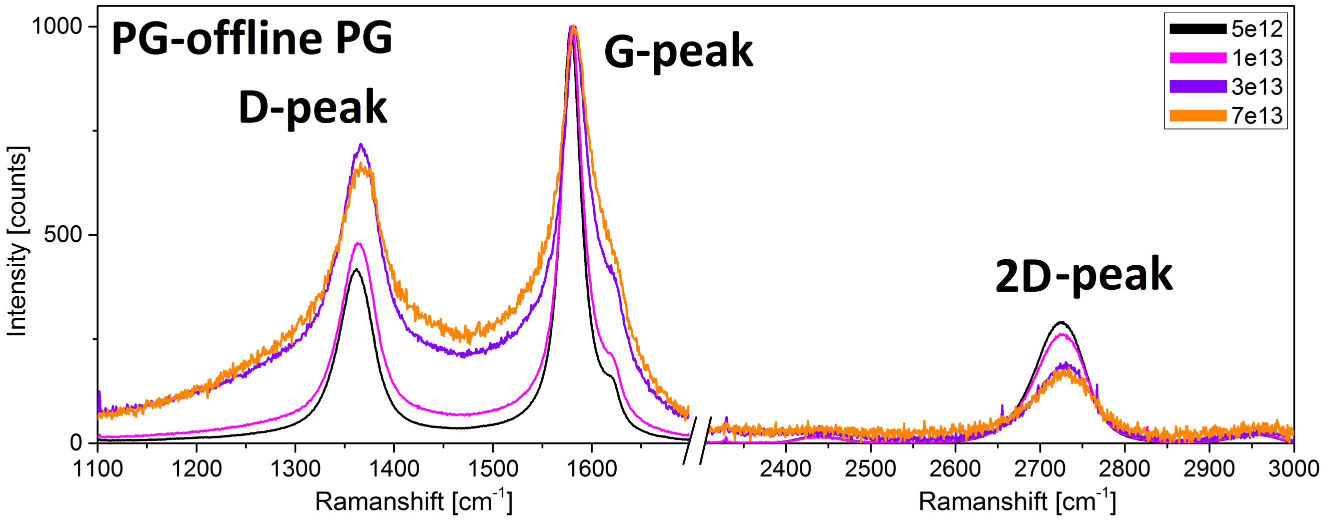

Figure 5.12: Representative Raman spectra evolution with accumulating fluence (post irradiation measurements) of PG irradiated with 4.8 MeV/u ^{197}Au at 2-3×10^{9} ions/cm^{2}*s (frequency 45 Hz; pulse length 2 ms).

much smaller than for HOPG and subsequently n_d much larger. The average number of defects per cm^2 n_d is around 4.5×10^{11} defects/cm^2 in GC, HOPG reaches a defect density of around 5×10^{10} to 1×10^{11} defects/cm^2 at high fluences. Since the ratio I_D/I_G does not change with the irradiation, one can attribute the broadening of the G-peak to further amorphization of the material and destruction of the residual graphitic structures within the material. The increase of the D3 and D4-peaks following irradiation is in agreement with the measurements. D3 and D4 can be related to soot like carbons [68, 111]. With an increasing bombardment of the structure and milling of the remaining graphitic structures, the tortuosity R_{Tor} (figure 5.10f) is decreasing. Subsequently, the average graphene sheet length L_{eq} (figure 5.11h) is decreasing as well, even though the average crystal size L_a remains unchanged with the fluence. As the basal planes get increasingly fragmented, the lattice parameter c is shrinking (figure 5.11i). L_c (figure 5.11g) remains unchanged. L_c in GC could be associated with the thickness of the sp^2 filaments within the GC as discussed by Harris et al. [46]. The crystalline fraction of GC is very small to begin with (compare chapter 8).

A selection of representative Raman spectra of the investigated high density isotropic polycrystalline graphite (PG) samples is given in figure 5.12. Figure 5.13 and 5.14 presents the corresponding analysis results. In agreement with HOPG and GC, the FWHM (figure 5.13a) of the G-peak for PG is also increasing with the fluence. Surprisingly in PG it seems that there is no obvious dE/dx dependence on the broadening of the G-peak. This is in agreement with the results obtained from the GC. The discrepancy of the ^{209}Bi irradiated samples that exhibit slightly elevated values can be attributed to a lower flux during irradiation (1×10^{9} i.e. 3 time lower) and thus a lower temperature. Irradiation at a higher temperature increases the rate of annealing. I_D/I_G (figure 5.13b) of PG increases with the fluence. A larger dE/dx also has an

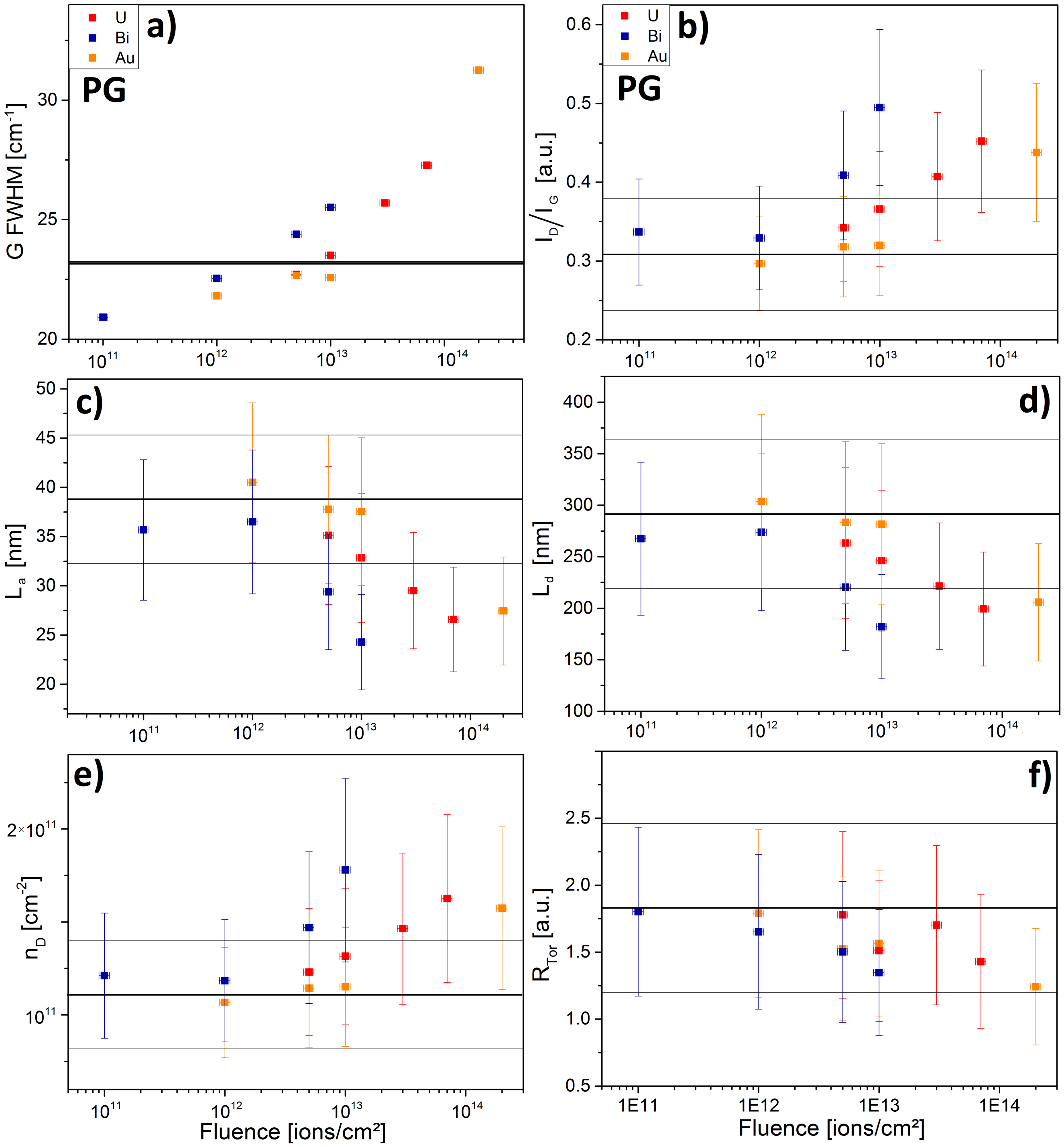

Figure 5.13: Fluence dependency of Raman graphitic parameters (post irradiation measurement) of PG irradiated with 4.8 MeV/u ions: ^{197}Au at 2-3×10^9 ions/cm^2*s (frequency 45 Hz; pulse length 2 ms), ^{209}Bi at 2-5×10^9 ions/cm^2*s (frequency 3.4 Hz; pulse length 1 ms) and ^{238}U at 1-2×10^9 ions/cm^2*s (frequency 1 Hz; pulse length 0.5 ms); Results are given as a function of ion fluence; a)Full width half maximum (FWHM) of the G-peak; b) I_D/I_G; c) Average in-plane crystal size L_a; d) Average defect spacing L_d; e) Average density of defects n_d; f) Tortuosity R_{Tor}; Solid lines represent the values of pristine samples where the thin lines represents the averaged uncertainties; some uncertainties are smaller than the symbols.

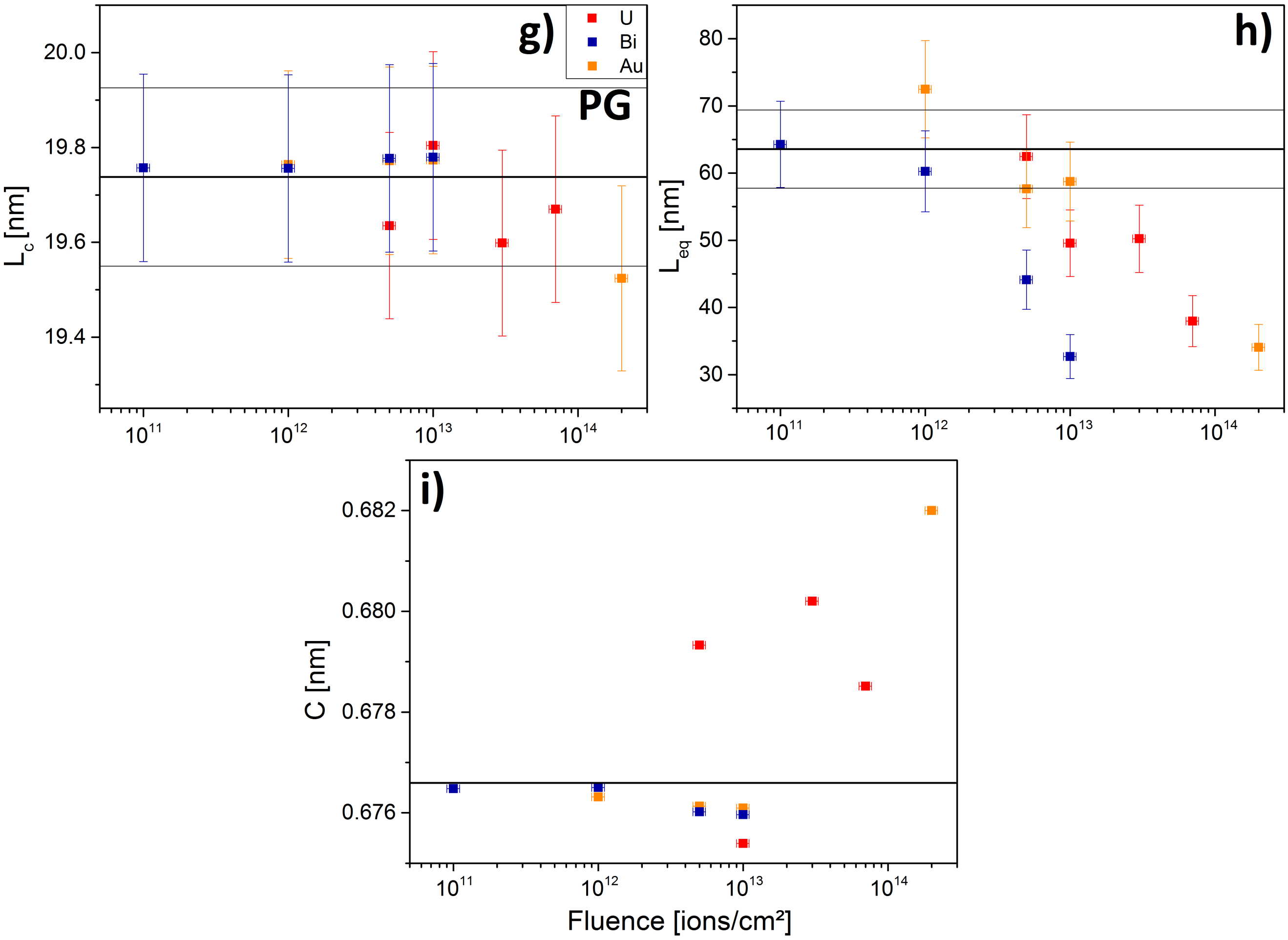

Figure 5.14: Fluence dependency of Raman graphitic parameters (post irradiation measurement) of PG irradiated with 4.8 MeV/u ions: ^{197}Au at 2-3×10^9 ions/cm^2*s (frequency 45 Hz; pulse length 2 ms), ^{209}Bi at 2-5×10^9 ions/cm^2*s (frequency 3.4 Hz; pulse length 1 ms) and ^{238}U at 1-2×10^9 ions/cm^2*s (frequency 1 Hz; pulse length 0.5 ms); Results are given as a function of ion fluence; g) Average crystal size along the c-axis, L_c; h) Average graphene sheet length L_{eq}; i) Lattice parameter c; Solid lines represent the values of pristine samples where the thin lines represents the averaged uncertainties; some uncertainties are smaller than the symbols.

influence on the I_D/I_G. The discrepancy between results for ^{209}Bi and ^{238}U irradiated PG can again be associated with different dose rates and subsequently different temperatures during irradiation.

The dependence of I_D/I_G on the energy loss in PG is not as prominent as for HOPG. Trends for L_a, L_d and n_d (figures 5.13c,d and e) are similar to HOPG. L_a of PG is between 40 and 25 nm and thus around 2-4 times larger than the L_a of GC. At fluences above 3×10^{13} ions/cm^2 the L_a of PG is in agreement with HOPG when comparing similar fluences. L_d and n_d follow this trend. The average number of defects per cm^2 n_d is around 1.5×10^{11} defects/cm^2 in PG and is 2-4 times smaller than the n_d of GC. The out of plane lattice parameter c is 0.671 nm for the perfect graphite crystal. In non-irradiated PG c is around 0.676 nm. At fluences above 1×10^{13} ions/cm^2 c increases up to 0.682 nm (figures 5.14i). Values for c increase with fluence as larger disordering mainly due to the formation of additional interstitial planes. A dE/dx dependence of c is not clear. Analysis of the 2nd order D-peak shows a transformation of the graphite phase towards turbostratic graphite with increasing fluence. L_a, R_{Tor} and L_{eq} are decreasing in PG as well, which agrees well with the results obtained from HOPG. Results allow the conclusion that PG transforms towards the structure of GC at fluences beyond 1×10^{13} ions/cm^2 with the preservation of sp^2 bonding as indicated by the spectra and evolution of the peaks.

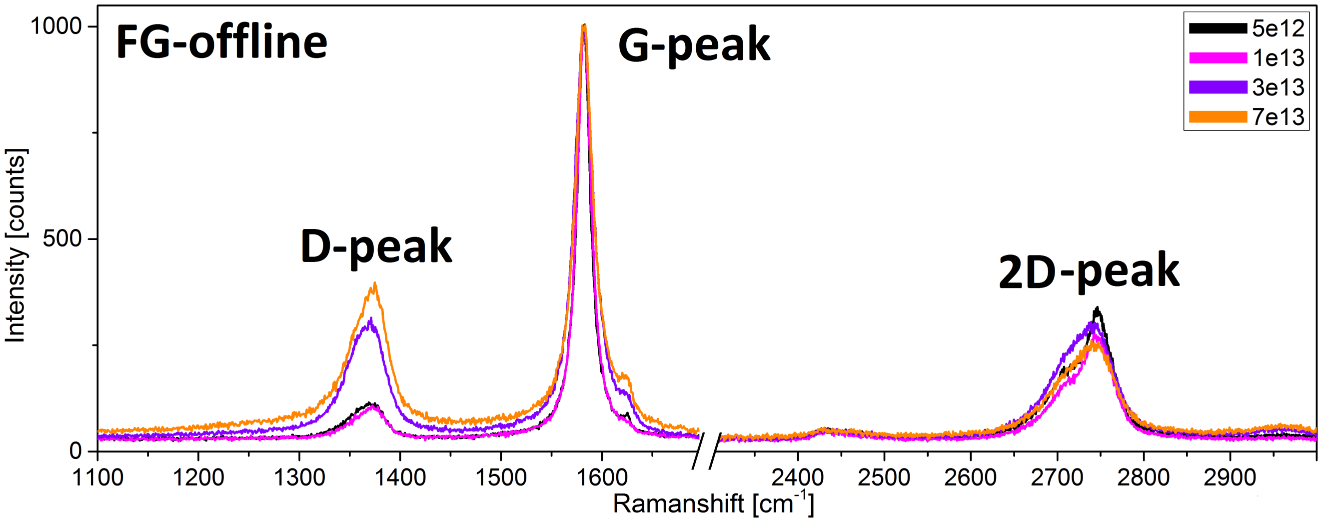

Figure 5.15: Representative Raman spectra evolution with accumulating fluence (post irradiation measurements) of FG irradiated with 4.8 MeV/u ^{197}Au at 2-3×10^9 ions/cm^2*s (frequency 45 Hz; pulse length 2 ms). A selection of spectra is presented to show general tendencies how the samples change with irradiation.

The investigated flexible graphite (FG) has a structure that is closely related to the structure of HOPG and thus similar results are to be expected. A selection of spectra is presented in figure 5.15. Figure 5.16 and 5.17 present the results for the investigated FG samples. The general Raman-spectroscopy results of FG are in very good agreement with HOPG. FWHM of the G-peak of FG is increasing with the fluence as also observed in HOPG, GC and PG (figure 5.16a).

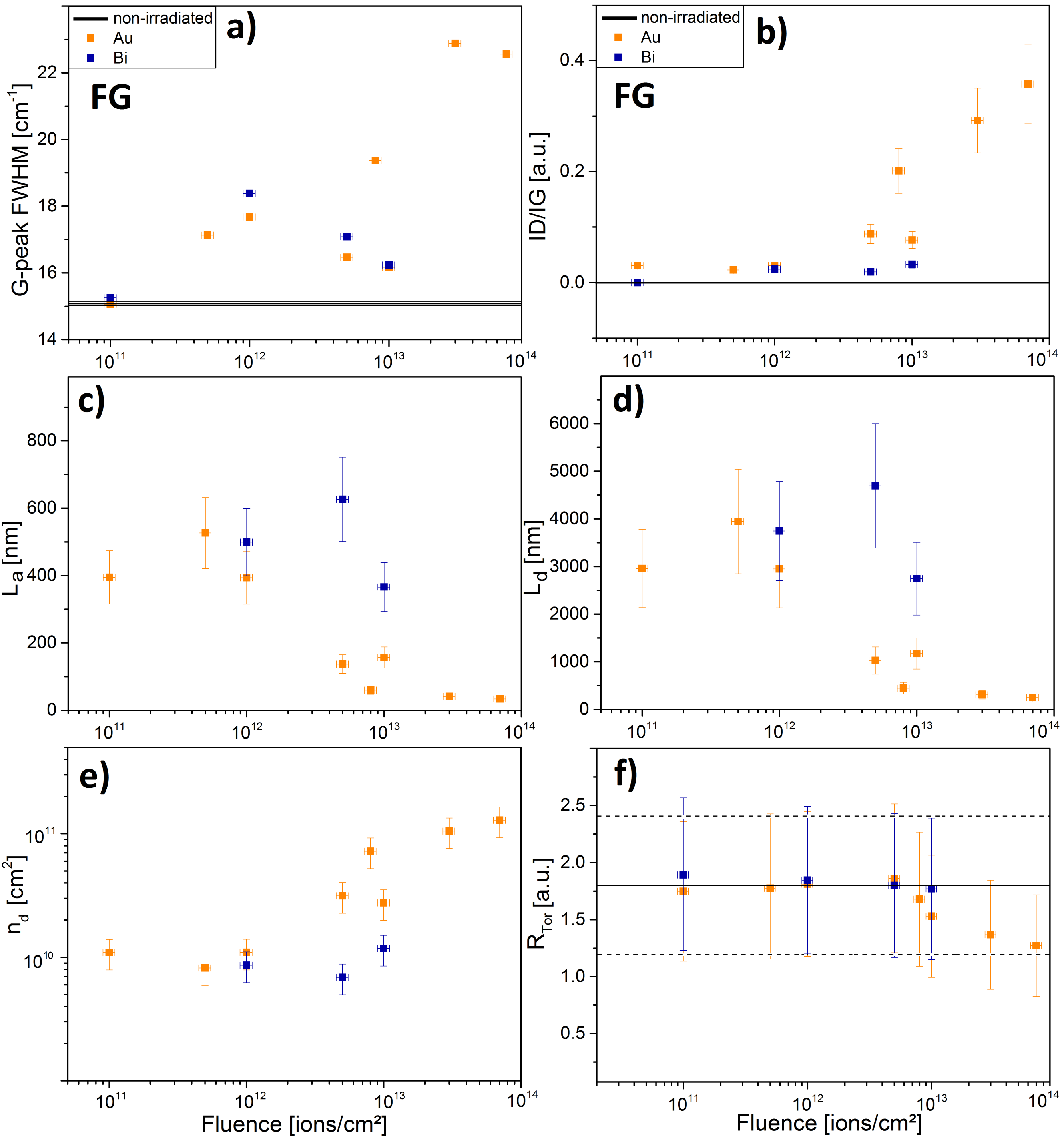

Figure 5.16: Fluence dependency of Raman graphitic parameters (post irradiation measurement) of FG irradiated with 4.8 MeV/u ions: ^{197}Au at 2-3×10^9 ions/cm^2*s (frequency 45 Hz; pulse length 2 ms), ^{209}Bi at 1-3×10^9 ions/cm^2*s (frequency 3.4 Hz; pulse length 1 ms); Results are given as a function of ion fluence; a)Full width half maximum (FWHM) of the G-peak; b) I_D/I_G; c) Average in-plane crystal size L_a; d) Average defect spacing L_d; e) Average density of defects n_d; f) Tortuosity R_{Tor}; Solid lines represent the values of pristine samples where as the thin lines represents the error bar; Uncertainties assume an error of 1 pixel on the detector and consider the uncertainty of the equipment; some uncertainties are smaller than the symbols.

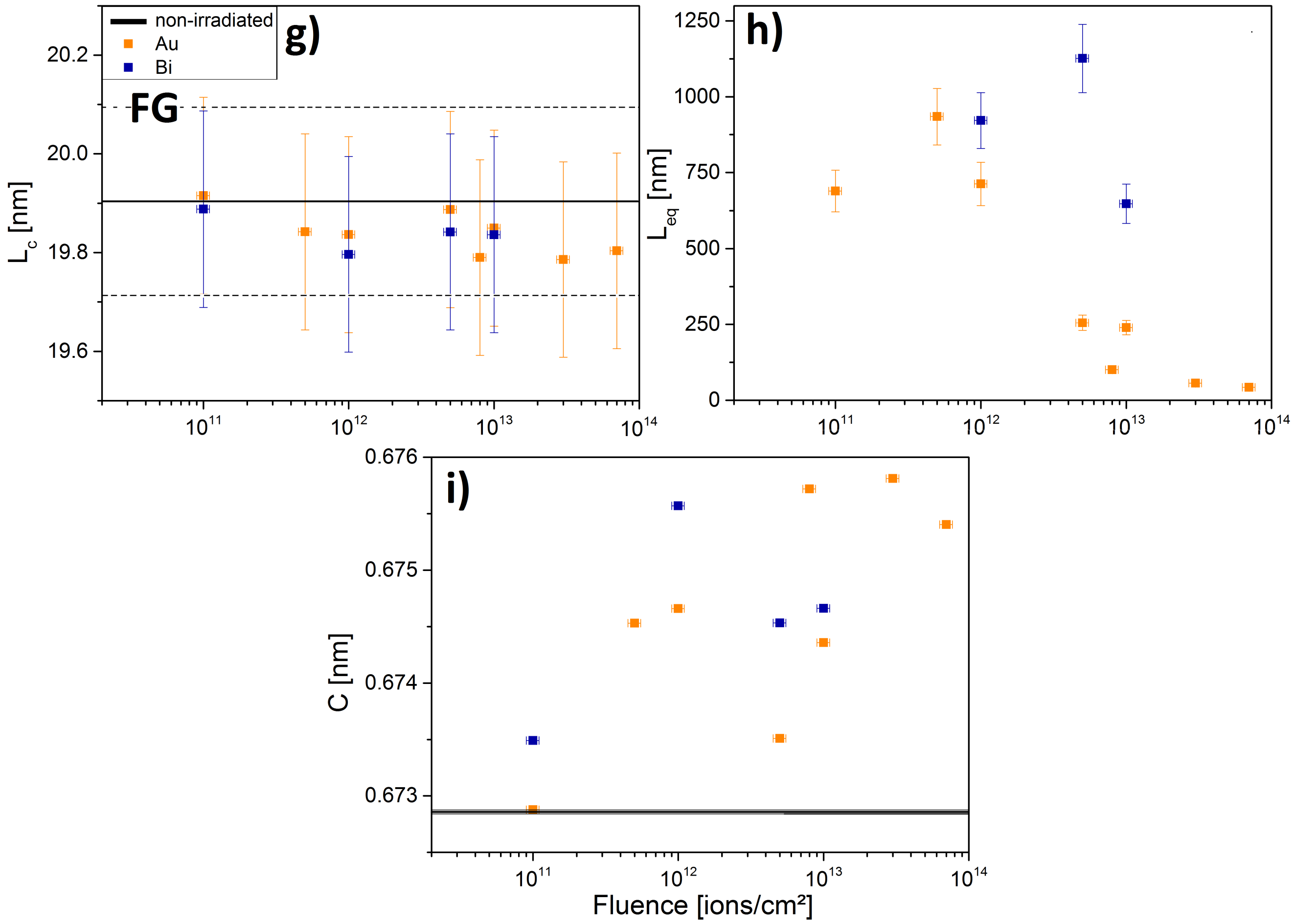

Figure 5.17: Fluence dependency of Raman graphitic parameters (post irradiation measurement) of FG irradiated with 4.8 MeV/u ions: ^{197}Au at 2-3×10^9 ions/cm^2*s (frequency 45 Hz; pulse length 2 ms), ^{209}Bi at 1-3×10^9 ions/cm^2*s (frequency 3.4 Hz; pulse length 1 ms); Results are given as a function of ion fluence; g) Average crystal size along the c-axis, L_c; h) Average graphene sheet length L_{eq}; i) Lattice parameter c; Solid lines represent the values of pristine samples where as the thin lines represents the error bar; Uncertainties assume an error of 1 pixel on the detector and consider the uncertainty of the equipment; some uncertainties are smaller than the symbols.

There is no clear dE/dx dependence. For the FG measurements smaller Raman mappings with only 4-8 points were used which is increasing the scattering of the data. I_D/I_G of FG increases with the fluence as well as with larger dE/dx (figure 5.16b). The dependence of the energy loss on I_D/I_G in FG is comparable to HOPG. In accord to the other measurements, the trends for L_a, L_d and n_d (figures 5.16c,d and e respectively) are similar to HOPG. L_a for FG decreases from about 600 to about 25 nm at the highest fluence. At fluences above 5×10^{12} ions/cm^2 the L_a of FG is in good agreement with HOPG. L_d and n_d also follow this trend. The average number of defects per cm^2 n_d increases from $\approx1\times10^{10}$ to 1×10^{11} defects/cm^2 in FG which is in very good agreement to HOPG. R_{Tor} is decreasing with the fluence (figure 5.16f). Subsequently, the average graphene sheet length L_{eq} is decreasing as well (figure 5.17h). As the basal planes get increasingly disordered, the lattice parameter c is increasing (figure 5.17i). L_c is also slightly decreasing with the ion fluence (figure 5.17g). We could observe that FG is a material related to HOPG with smaller in-plane crystal size, but with a very similar evolution of the irradiation damage as a function of fluence.

5.2.2 In situ experiments at UNILAC

Raman measurements of non-homogeneous materials, such as PG, require the use of mappings and average spectra. These mappings are time consuming and possibly contain additional errors due to inhomogeneous irradiation of the sample (different flux or shape of the beam-spot). In-situ Raman spectroscopy has the great advantage that it allows measurements of the sample within the same spot and monitor the corresponding damage evolution with increasing ion fluence. This eliminates the dependence of Raman spectra on the initial position and surface of the sample and thus allows an accurate observation of the relative structural change in a given spot. The disadvantage of the in-situ technique is a lower signal to noise ratio due to larger distances between the detector, the view port to the beam chamber and the difficulty to focus the laser on the sample in the used setup. Figure 5.18a) represents the Raman spectra of the HOPG irradiated by 4.8 MeV/u ^{150}Sm. As expected I_D/I_G increases with the fluence (figure 5.18b). For L_a, one can observe an increase at a very low fluence of 1×10^{11} ions/cm^2 and at further increasing fluences a clear decrease (figure 5.18c). This effect occurs in most of the samples at fluences $\leq1\times10^{12}$ ions/cm^2 and can be attributed to annealing of residual defects present in the non-irradiated sample. Pristine HOPG contains defects from the production and with a small ion fluence these defects recombine and stresses relax leading to a less disordered state. In agreement with the previous off-line measurements, L_a, L_d and n_d are changing with increasing fluence (figure 5.18c,d and e respectively). The extent of change due to ^{150}Sm ions is less pronounced than for ^{197}Au or ^{238}U irradiated samples due to the smaller dE/dx of the ^{150}Sm beam. Changes within the 2nd order D-peak are not very pronounced (figure 5.18a) which makes the analysis of the tortuosity R_{Tor}, the average graphene sheet length L_{eq} and the out of plane lattice parameter c very difficult. Due to the bad signal to noise ratio a quantitative analysis based on the 2nd order D-peak was not possible.

For the measurements of the PG, the focus of the laser on the sample was better, increasing the signal to noise ratio and enabling the analysis of R_{To} and L_{eq}. Figure 5.19 presents the spectra of the PG irradiated by 4.8 MeV/u ^{150}Sm. Due to the manufacturing of the PG, the pristine material is inhomogeneous and has multiple phasees, containing quenched-in defects and stresses. A first beam-induced annealing step is observed at fluences around $1{\times}10^{11}$ ions/cm^2 when these defects recombine and initial stresses relax. Fluences around $1{\times}10^{11}$ ions/cm^2 are typically reached within a time frame of 1-2 minutes. These initial annealing effects can be seen for all graphitic systems that were tested but due to a lack of low fluence samples are observed best in the online measurements. For PG this effect is very small and occurs around $1{\times}10^{11}$ ions/cm^2 resulting in a small dip of I_D/I_G (figure 5.20a) and a subsequent increase of L_a and L_d. Also the other measurements, L_a, L_d and n_d (figures 5.20b,c and d respectively) are in agreement with previous results and follow the trend of I_D/I_G, increasing with the fluence. The tortuosity ratio R_{Tor} (figure 5.20e) seems to be unchanged with increasing fluence, but decreases at very high fluences. This is ascribed to the milling of the basal planes that can also be seen in the decrease of the average in-plane crystal size L_a. The average graphene sheet length L_{eq} mainly depends on R_{Tor} and L_a. At very high fluences L_{eq} starts to approach L_a as the smaller basal planes are less warped and twisted. The online Raman spectra of PG follow closely the trends obtained with the post irradiation measurements. It is important to mention, that the online spectra were all acquired from the same spot. The post irradiation spectra for PG were measured using a mapping to average the results over the surface. Thus the results of the post irradiation measurements of PG give a better overview of the whole irradiated samples where as the online results represent the trend of a single spot as a function of fluence.

At higher fluences, the amorphization is visible by an intensity increase of the broad D3- and D4-peaks as presented in figure 5.19. The 2nd order D-peak barely changes in shape but only in intensity similar to the D-peak (figure 5.19). Even though apparently the D-peak increases, D3 and D4 start to dominate the D-band at higher fluences, lowering both G and D-peak. The disordering effect is shown by the intensity loss of the 2D-peak.

The acquired Raman data are in agreement with structural changes indicated by the XRD data. A transformation of the graphitic structures towards GC could be observed and is a clear indication of disordering due to swift heavy ion irradiation. How pronounced the disordering is, depends both on fluence and on dE/dx. Next steps could include in-depth Raman studies along the ion tracks in PG to further investigate the dE/dx influence along the ion track in respect to the induced structural changes. The Raman spectroscopy results conclude that ion irradiation leads to the formation of defects within the graphite structure observed in the evolution of the D-band. The formation of defects leads to a bending and warping of the graphene sheets observed in the 2D-band. Furthermore, an increase in the D3 and D4-bands was observed for all

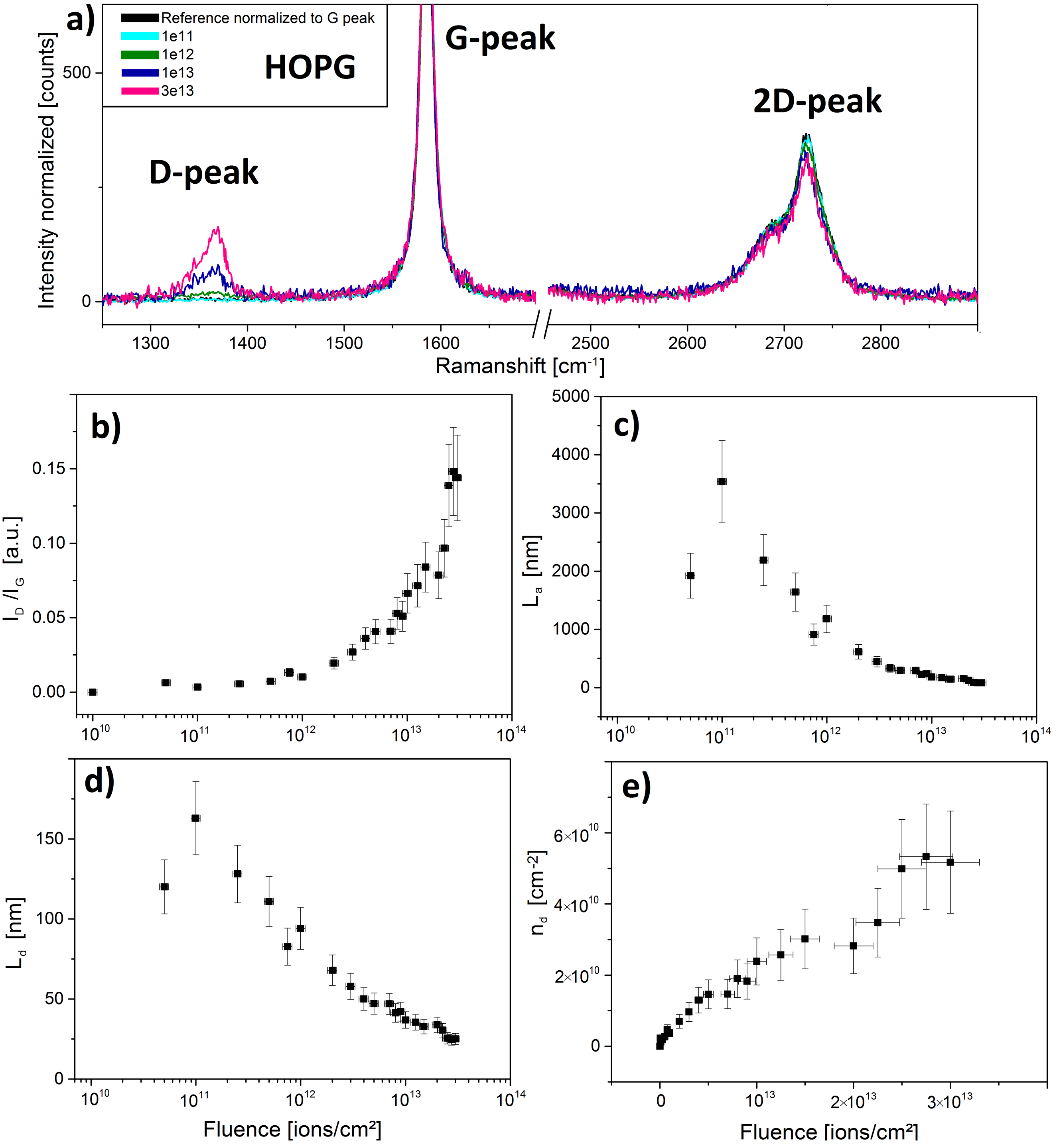

Figure 5.18: Presented are the analyzed online results of HOPG irradiated with 4.8 meV/u ^{150}Sm ions at a flux of 1-3$\times 10^9$ ions/cm^2 (1.2 ms; 3.4 Hz); Results are given as a function of ion fluence; a)I_D/I_G; b)Average in-plane crystal size L_a; c)Average defect spacing L_d; d) Average density of defects n_d; Evolution of the Raman spectra with fluence: e) D+G-Peak; f) 2D-Peak; Uncertainties assume an error of 1 pixel on the detector and consider the uncertainty of the equipment; some uncertainties are smaller than the symbols.

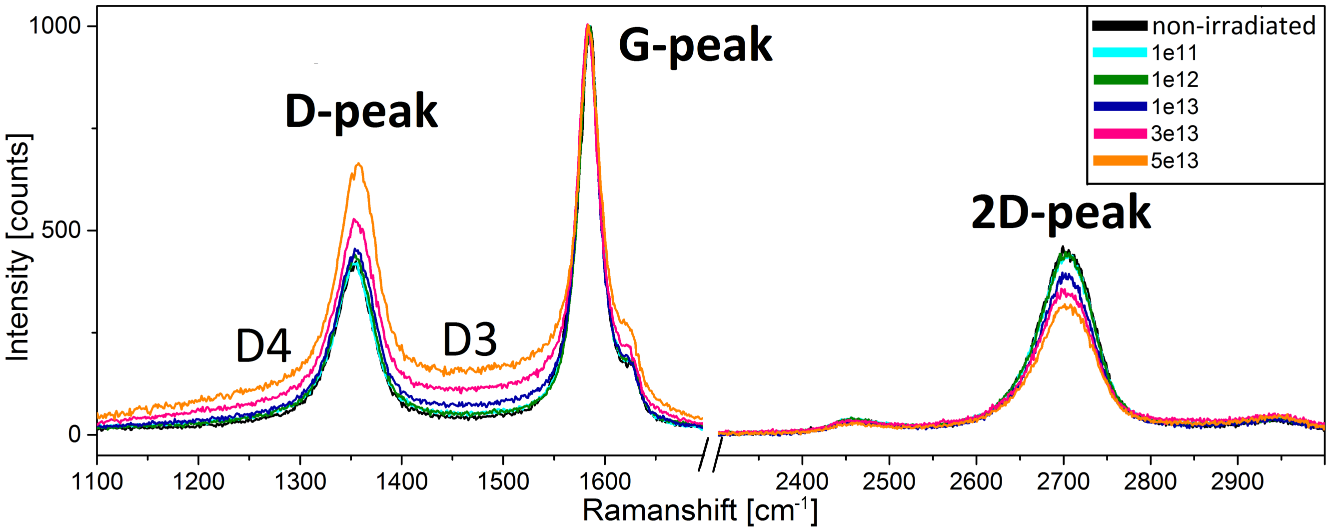

Figure 5.19: Evolution of the Raman spectra with fluence measured in-situ of PG irradiated with 4.8 meV/u ^{150}Sm ions at a flux of 1-3$\times10^9$ ions/cm^2(1.2 ms, 3.4 Hz).

carbon-based materials. These bands can be associated to soot like carbons and glassy carbons. Especially the in-situ measurements show the beam-induced annealing of residual defects in the samples at low fluences of $\approx1\times10^{11}$ ions/cm^2. A dE/dx influence on the defect formation could be observed when comparing different ion species, with heavier ions causing more damage to the structure. First signs of a dose-rate dependence on the defect creation inspired a series of flux tests on HOPG.

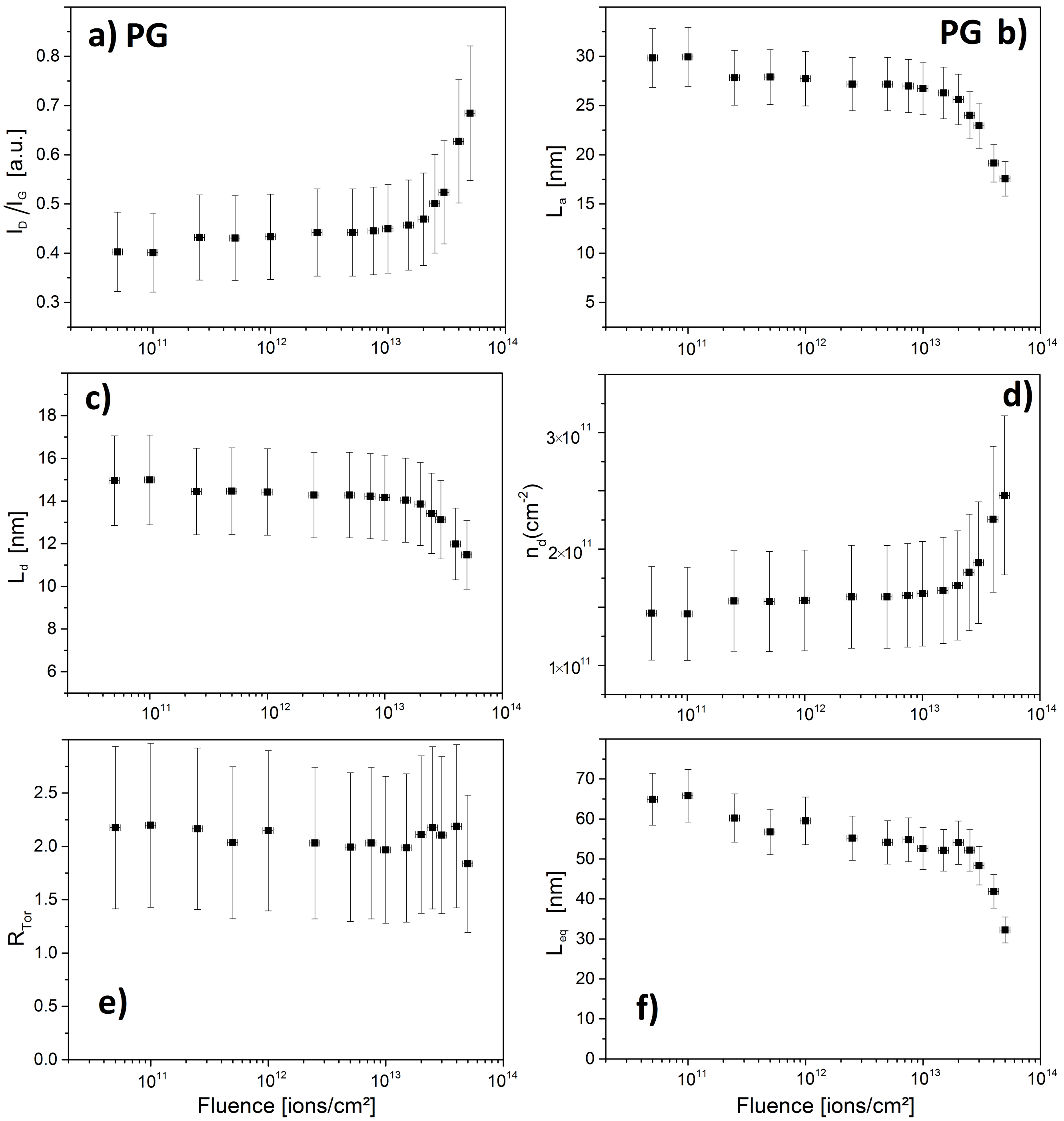

Figure 5.20: Presented are the analyzed online results of PG irradiated with 4.8 meV/u ^{150}Sm ions at a flux of 1-3$\times 10^9$ ions/cm^2(1.2 ms; 3.4 Hz); Results are given as a function of ion fluence; a) I_D/I_G; b) Average in-plane crystal size L_a; c)Average defect spacing L_d; d)Average density of defects n_d; e)Tortuosity R_{Tor}; f)Average graphene layer length L_{eq}; Uncertainties assume an error of 1 pixel on the detector and consider the uncertainty of the equipment; some uncertainties are smaller than the symbols.

5.3 Beam-induced structural changes studied by XRD

X-ray diffraction as a complementary method to Raman spectroscopy was performed to determine structural changes depending on beam parameters. Several sets of samples were measured off-line at the DESY Petra III synchrotron facility in Hamburg. In on case in-situ XRD measurements were performed at the M2 beamline equipped with x-ray diffractometer. No off-line measurements were done at GSI.

5.3.1 In situ XRD at M2-beamline at UNILAC

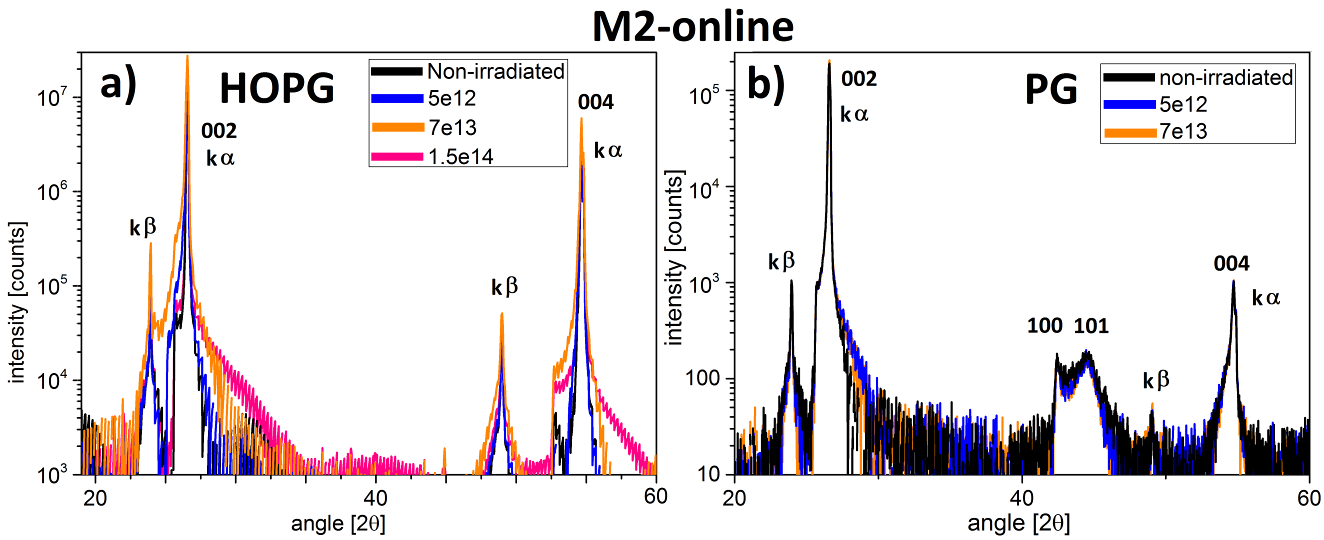

Figure 5.21: A selection of diffractograms of HOPG (a) and PG (b) at different fluences irradiated with 3.6 MeV/u ^{197}Au at 5×10^9 ions/cm^2*s (frequency 45Hz, pulse length 2ms).

It has to be mentioned beforehand that for the in-situ measurements at the M2 beamline, we observed only very small effects. This is due to the fact that the attenuation length of the X-rays in graphite (500 μm) surpasses by far the range of the ions (50 μm). Thus there is an overlaying signal of the non-irradiated material that accounts for $\approx$ 90% of the probed sample volume. The diffractograms of HOPG and PG samples are presented in figure 5.21. In the log-scale one can slso see the corresponding Cu-k$_\beta$ lines within the diffractograms. Figure 5.22 presents the position of the 002 reflection as a function of fluence for HOPG and PG respectively. The main effect that can be observed within the spectra is the broadening of the 002-peak. This can be attributed to an increase in the distribution of inter-planar distances following the formation of interstitial clusters, bending of graphene layers and crystallite size reduction and is in agreement with the data obtained from Raman-spectroscopy.

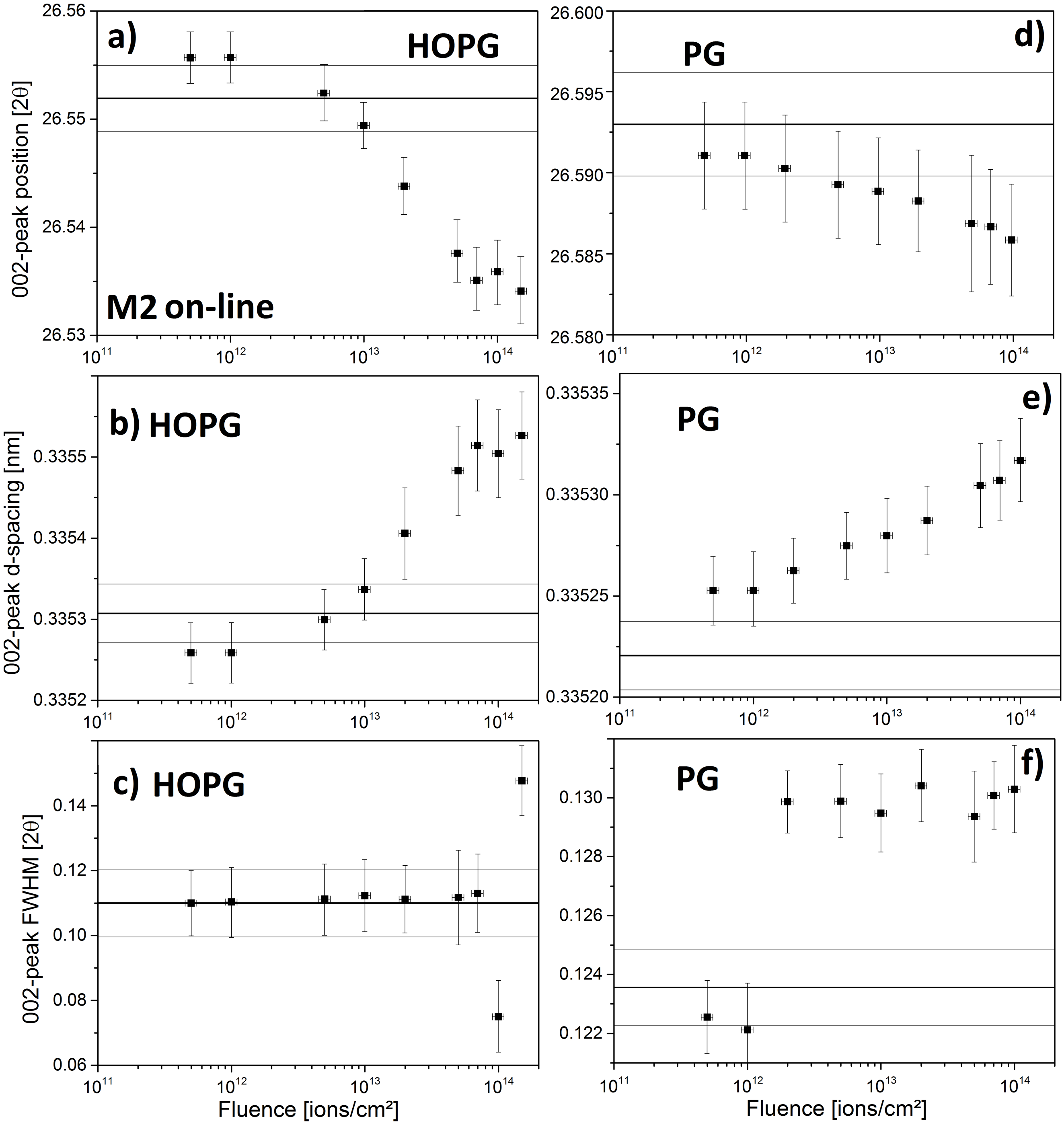

Figure 5.22: XRD analysis of HOPG (a-c) and PG (d-f) irradiated with 3.6 MeV/u ^{197}Au at 5×10^9 ions/cm^2*s (frequency 45Hz, pulse length 2ms); Results are given as a function of ion fluence; a) (002) position; b) d-spacing of [002]; c) FWHM of (002); d) (002) position; e) d-spacing of [002]; f) FWHM of (002); Solid lines represent values for non-irradiated samples; Uncertainties include only the errors of peak fits

5.3.2 Synchrotron radiation XRD

^{197}Au and ^{238}U irradiated polycrystalline graphite (PG) samples were measured at the DESY PETRA III synchrotron facility in Hamburg using a λ = 0.2913 Å beam. The first measurements

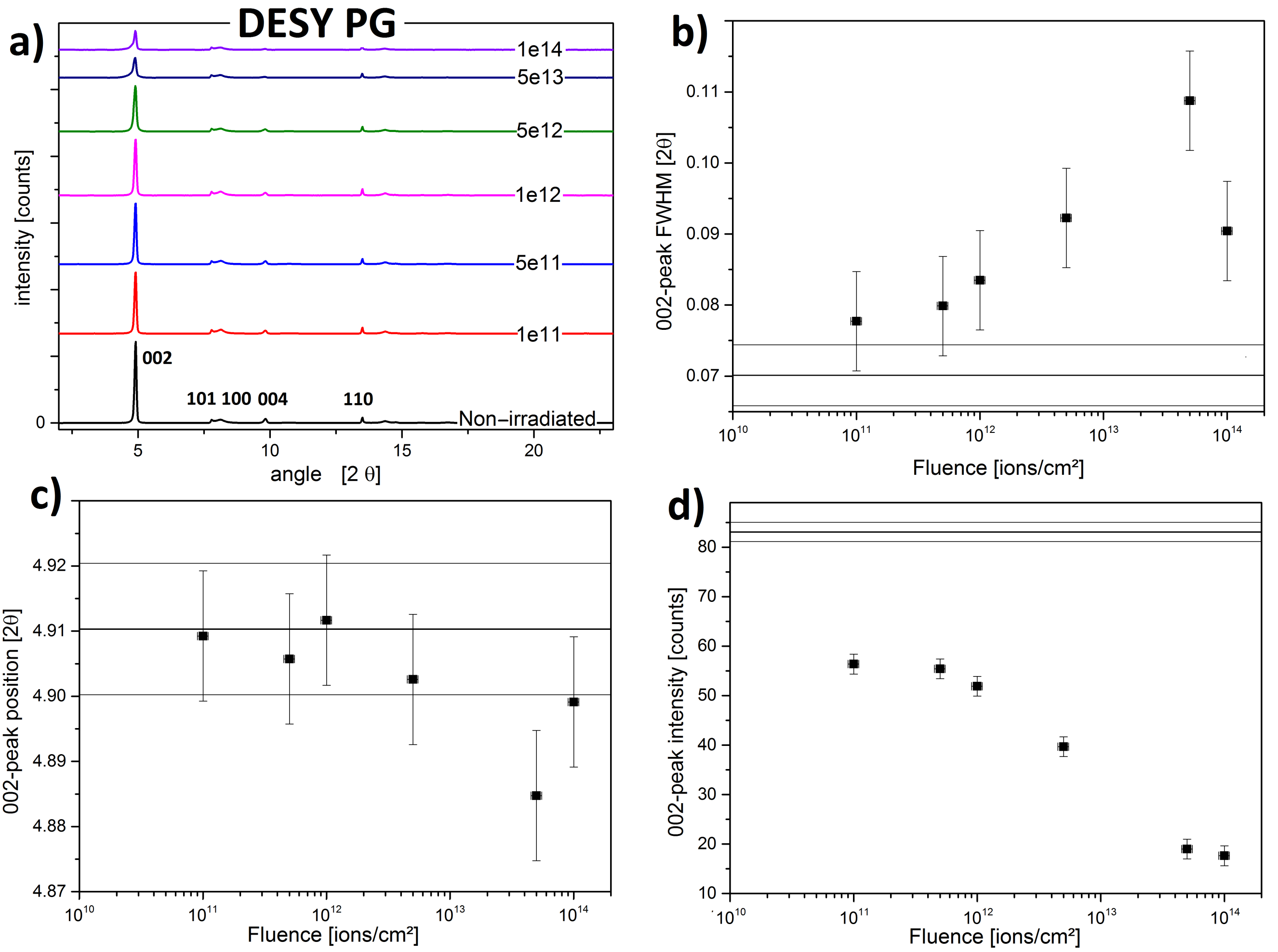

Figure 5.23: a) X-ray diffractograms of polycrystalline graphite (PG) irradiated with 4.8 MeV/u ^{197}Au at 1-2×10^9 ions/cm^2*s (frequency 45Hz; pulse length 3 ms); Results are presented as a function of ion fluence; b) FWHM of 002-peak; c) 002-peak position; d) 002-peak intensity; solid lines represent the values of the non-irradiated sample.

focused on thin irradiated samples with a sample thickness smaller than the ion range. Similar to the effects observed in Raman spectroscopy, the crystallinity decreases (loss of intensity of 002-peak) and disordering is indicated by peak broadening with increasing fluence. The results are presented in figure 5.23.

To complement the measurements performed in through-plane geometry, several samples were scanned in cross section along the ion trajectories (see experimental details in figure 4.11). This allowed a comparison of the effects of electronic and nuclear stopping on disordering (figure 5.24a). The results show that close to the nuclear stopping, the intensity of the 002-peak drops rapidly. This intensity decrease is a sign of disordering and thus indicates that indeed nuclear stopping is far more effective in the disordering of the sample than electronic stopping despite the fact that the electronic energy loss is larger. Since the beam-spot of the X-rays is 2×2 μm and thus larger than each scanning step of 1 μm the results are smeared out along the depth axis. An additional origin of uncertainties is a miss-alignment of the sample. Since the positioning of the sample is done manually, errors within 10 μm can occur. This explains to the low signal at the first 5 μm and smears out the end of the range where a clear step in intensity of the 002-peak is expected due to the end of the ion range. In ^{238}U irradiated samples a new phase can be observed (figure 5.24b). At small angles, meaning very large inter planar distances (d-spacing of 3.7-4.5 Å) and in between the 002-peak and the 100/101 peak (d-spacing of 2.1-3 Å) a set of new peaks appears at the surface. These new peaks fade further into the sample. d-spacings of $\geq$4 Å for carbon based systems are associated with fullerene like structures. The formation of fullerenes on the sample surface could happen due to extreme conditions in the ion tracks. Considering the common models, it is assumed that a local melting appears within the ion tracks which would lead to an increase in volume. This volume increase/melting within the tracks along with sputtering can lead to the formation whiskers or other surface objects and in this case fullerene like objects. It is notable that only samples irradiated with ion beams of large dE/dx contain these surface structures (compare figure 5.5). For Au irradiated samples with an energy loss around 20.5 keV/nm no new phases could be detected in the X-Ray data, whereas U ions have an energy loss around 25 keV/nm on the surface. This could be a hint, that there are either dE/dx thresholds for the formation of fullerene related phases on the surface, or that certain beam conditions (e.g. ions/pulse*cm^2) must be fulfilled. These extreme beam conditions could be triggered by many impacts within a small time frame on the same area i.e. that ions within different bunches in a beam pulse hit the same spot on the sample.

A third type of samples has been investigated in order to determine the effect of temperature during the irradiation. These thin PG samples were heated by electric current up to temperatures of 1500 °C during irradiation and have been completely penetrated by the projectiles. Results are shown in figure 5.25a and 5.25b). XRD measurements were taken at room temperature. The samples irradiated with 1×10^{13} ions/cm^2 and 8×10^{13} ions/cm^2 were done without additional current heating and were only heated by the ion beam achieving average temperatures of up to 400°C due to a large ion flux. Disordering by continuous irradiation can be observed in a broadening of the (002) and in an overall decrease of of the (002) intensity. At temperatures around 750 °C and a fluence of 1×10^{14} ions/cm^2, the (002) has lost intensity and is broadened which is evidence of severe disordering and amorphization. When increasing the temperature during irradiation up to 1250 °C, an annealing effect can be observed. The sample is in a less disordered state despite the fluence of 1×10^{14} ions/cm^2. When further increasing the temperature during irradiation to 1500 °C, the sample has annealed most of the ion induced defects, as the shape and intensity of the (002) is close to the state of a non-irradiated PG.

These results inspired measurements with the DSC to actively observe the annealing as a function of temperature and time.

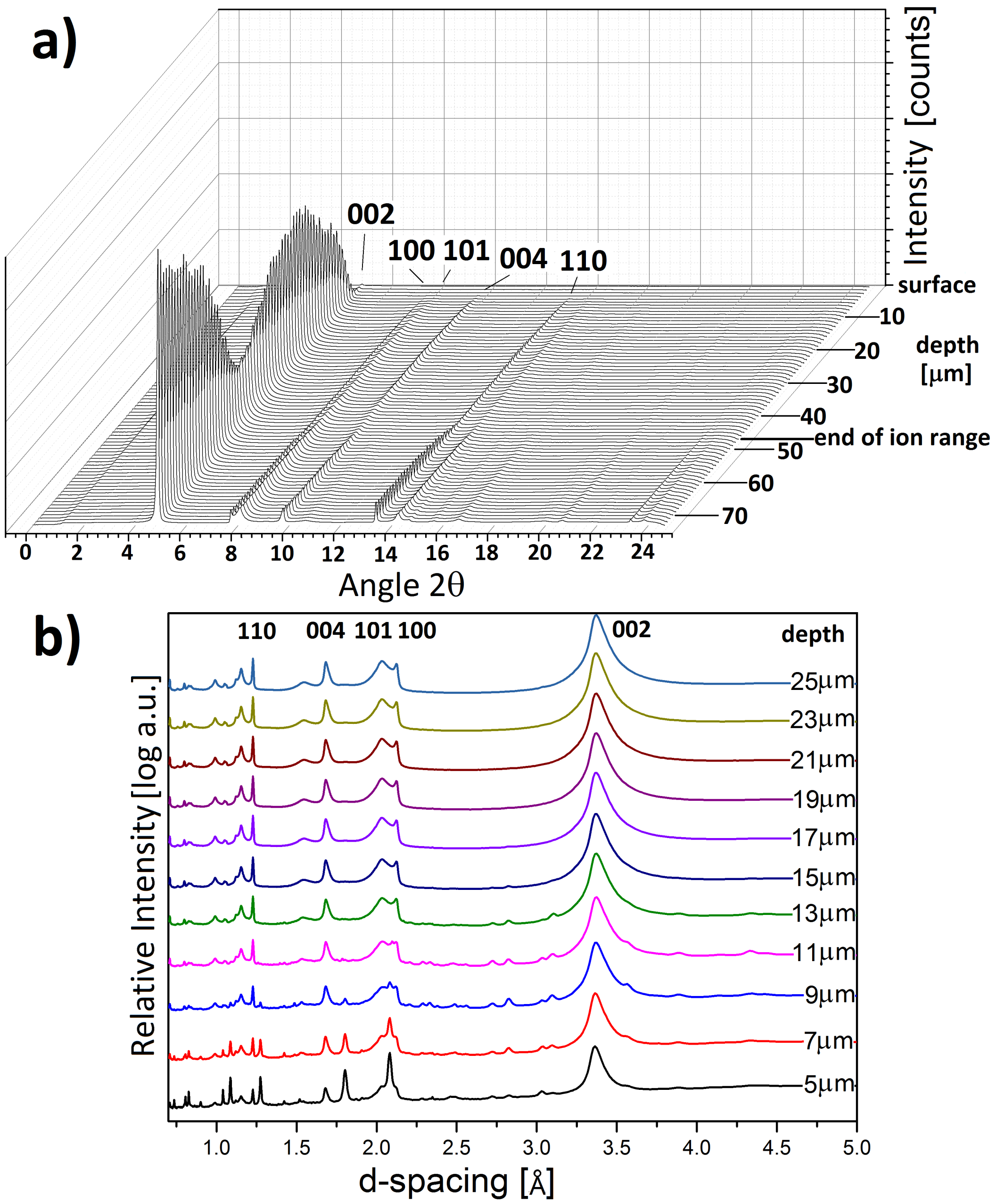

Figure 5.24: a) Diffractograms along the ion track of PG irradiated with 4.8 MeV/u ^{197}Au at 1-2×10^{9} ions/cm^{2}s (frequency 45Hz; pulse length 3 ms); b) Diffractograms along the ion track irradiated of PG irradiated with 5.9 MeV/u ^{238}U at 5-10×10^{9} ions/cm^{2}s (frequency 1Hz; pulse length 0.3 ms);

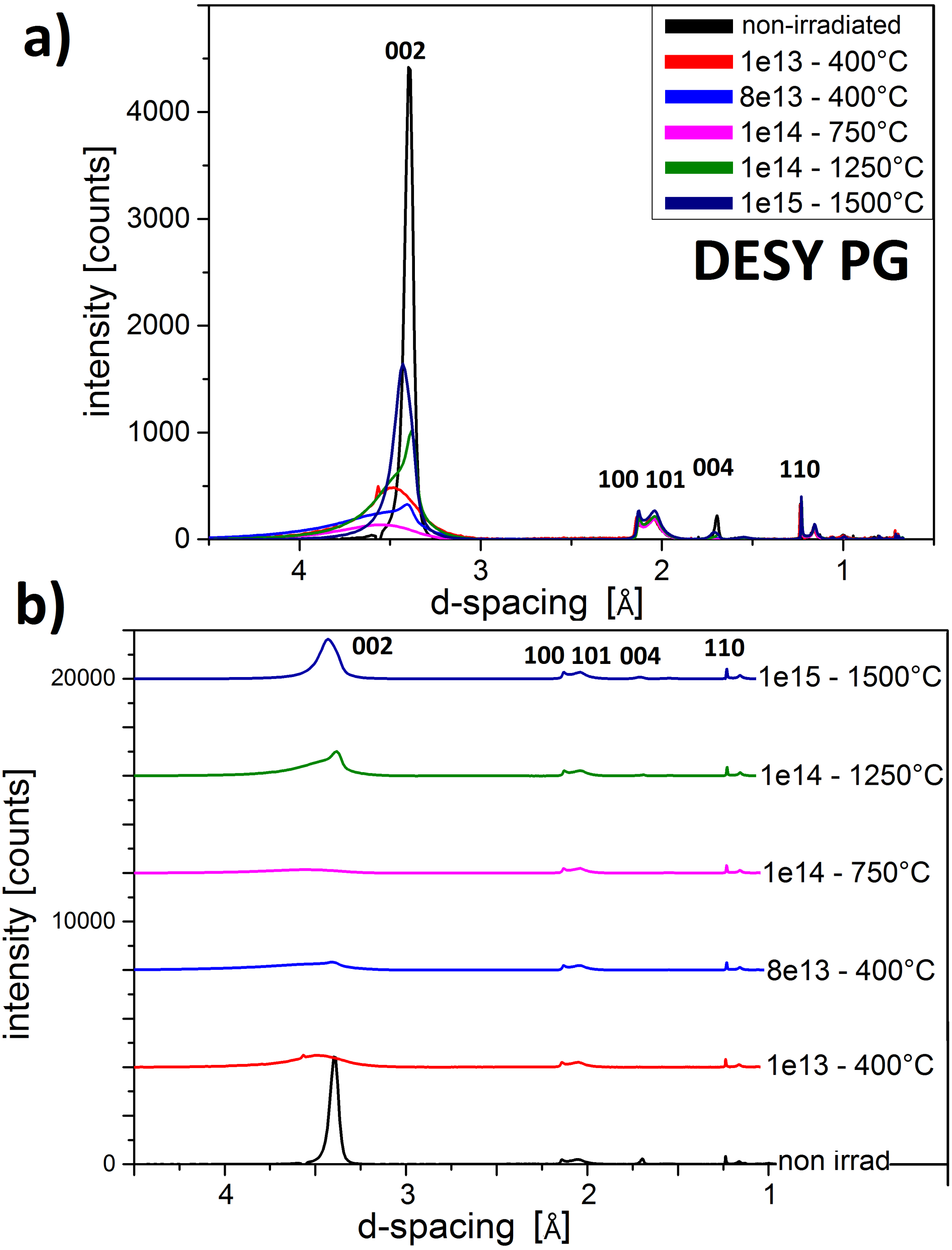

Figure 5.25: Off-line diffractograms done at DESY: a) Through-plane geometry of PG irradiated with Au 4.8 MeV/u ^{197}Au at 1-2×10^{1}0 ions/cm^{2}*s (frequency 45Hz; pulse length 3 ms) ions at different temperatures and fluences; b) Stacked presentation of the same data from a)

5.4 Beam-induced phase transitions and disordering studied by XPS

X-ray photo-electron spectroscopy (XPS) offers the possibility to probe the surface chemistry of a sample based on the binding energies of photo-electrons emitted under X-ray irradiation. The important binding energies are 284.5 eV for sp^2 carbon and 285.4 eV for sp^3 hybridized carbon. Peaks at 286.5 , 287.6 and 288.7 eV are assigned to C-O, C=O, and O-C=O bonds, respectively [100]. The sp^2 content is fit with a Doniach-Sunjic-function whereas sp^3, C-O, C=O, and O-C=O are fit with a Voigt-function [100]. A general spectrum can be viewed in figure 4.21. The most important features for graphite are the sp^2 and sp^3 hybridization bonds. XPS will be used to identify a phase transition that could be triggered within the ion track. The most interesting aspect for graphite is the transformation from sp^2 to sp^3 bonds and will be the core element of the analysis. Results for PG(a-c) and HOPG(d-f) samples are presented in figure 5.26. The spectra show an increase in sp^3 content with increasing fluence. The accumulation of defects within the graphene layers and their subsequent recombination not only leads to a bending of the planes and the formation of clusters but also to change from sp^2 to sp^3 bonds. Both materials also experience a large increase of oxygen content after the irradiation indicated by the increasing peak shoulders towards higher binding energies. The most prominent bonding types are C-O, C=O and O-C-O. Since XPS is limited to the surface of the sample, the increase in oxygen bonds is a sign of an oxidation. This oxidation is connected to the irradiation induced formation of dangling carbon bonds on the surface that allow to bind oxygen atoms. The amount of oxygen within the sample surface layer is thus a direct measure of dangling bonds created by the ion beam. The amount of oxygen is increasing with the fluence, but at high fluences ($\geq 2\times10^{13}$ $ions/cm^2$) the amount of dangling bonds is reduced. This could be explained by the defect density of the area surrounding a dangling bond, enabling a recombination of the carbon atoms. When comparing the values of non-irradiated PG and irradiated PG, a large drop in sp^3 bonds can be observed. This can be ascribed to the fact, that XPS probes only the very first layers of the material where many residual defects are present from producing and preparing the sample. These residual defects are annealed by the ion beam during the first minutes of irradiation. The obtained data is in agreement with XRD and Raman-spectroscopy, confirming the formation of sp^3-bonds, an overall disordering of the sample and the annealing of residual defects present in the material.

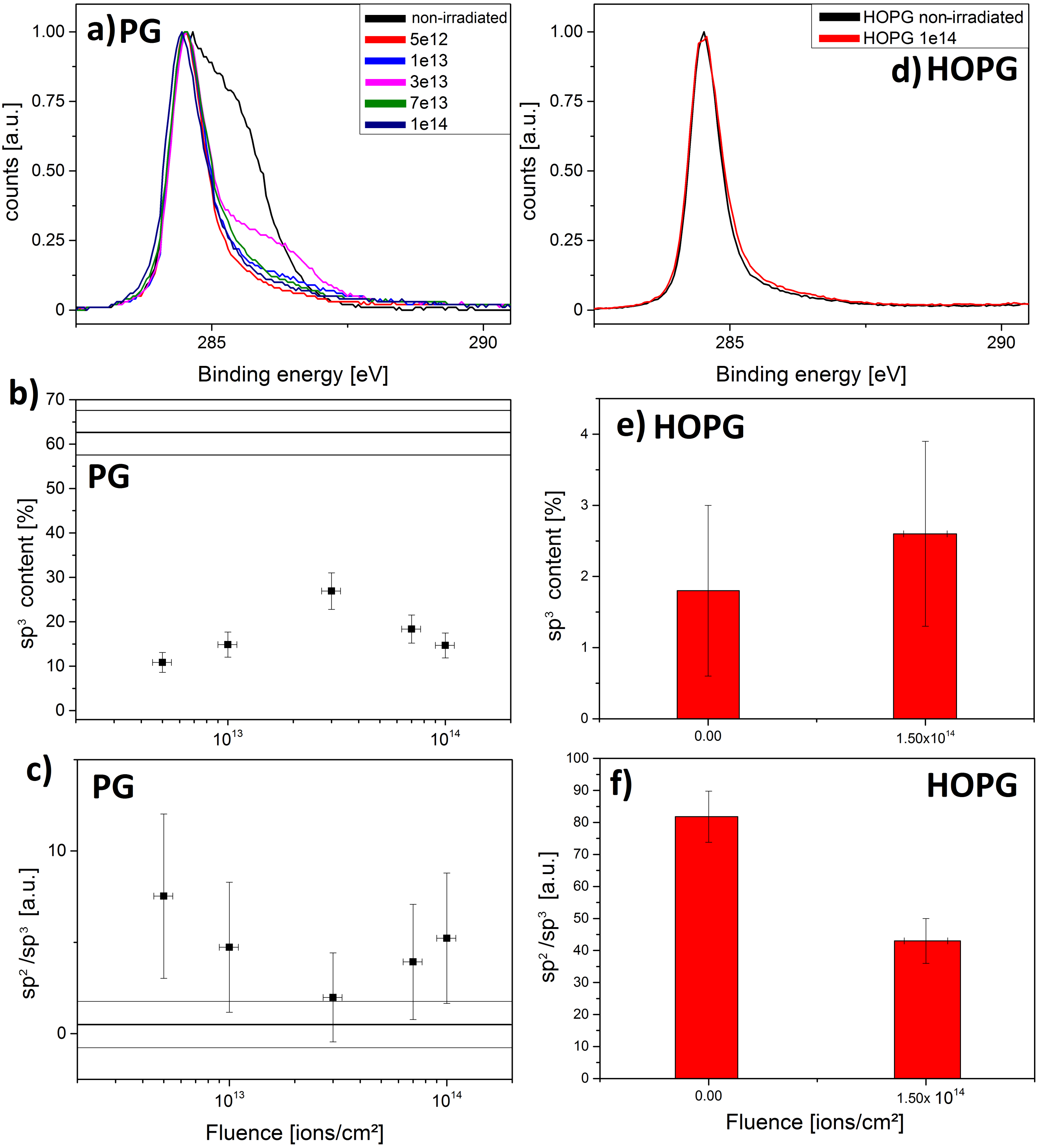

Figure 5.26: XPS spectra and analysis results; spectra are represented as a function of binding energy, analysis results are presented as a function of fluence; solid lines represent the value of the non-irradiated sample; a)XPS spectra of PG irradiated with 4.8 MeV/u ^{238}U at 2-3×10^9 ions/cm^{2}s (frequency 1 Hz; pulse length 0.3 ms); b) sp^3 content of PG; c) sp^2/sp^3 ratio of PG; d) XPS spectra of HOPG irradiated with 4.8 MeV/u ^{238}U at 2-3×10^9 ions/cm^{2}s (frequency 1 Hz; pulse length 0.3 ms); e) sp^3 content of HOPG; f) sp^2/sp^3 ratio of HOPG.

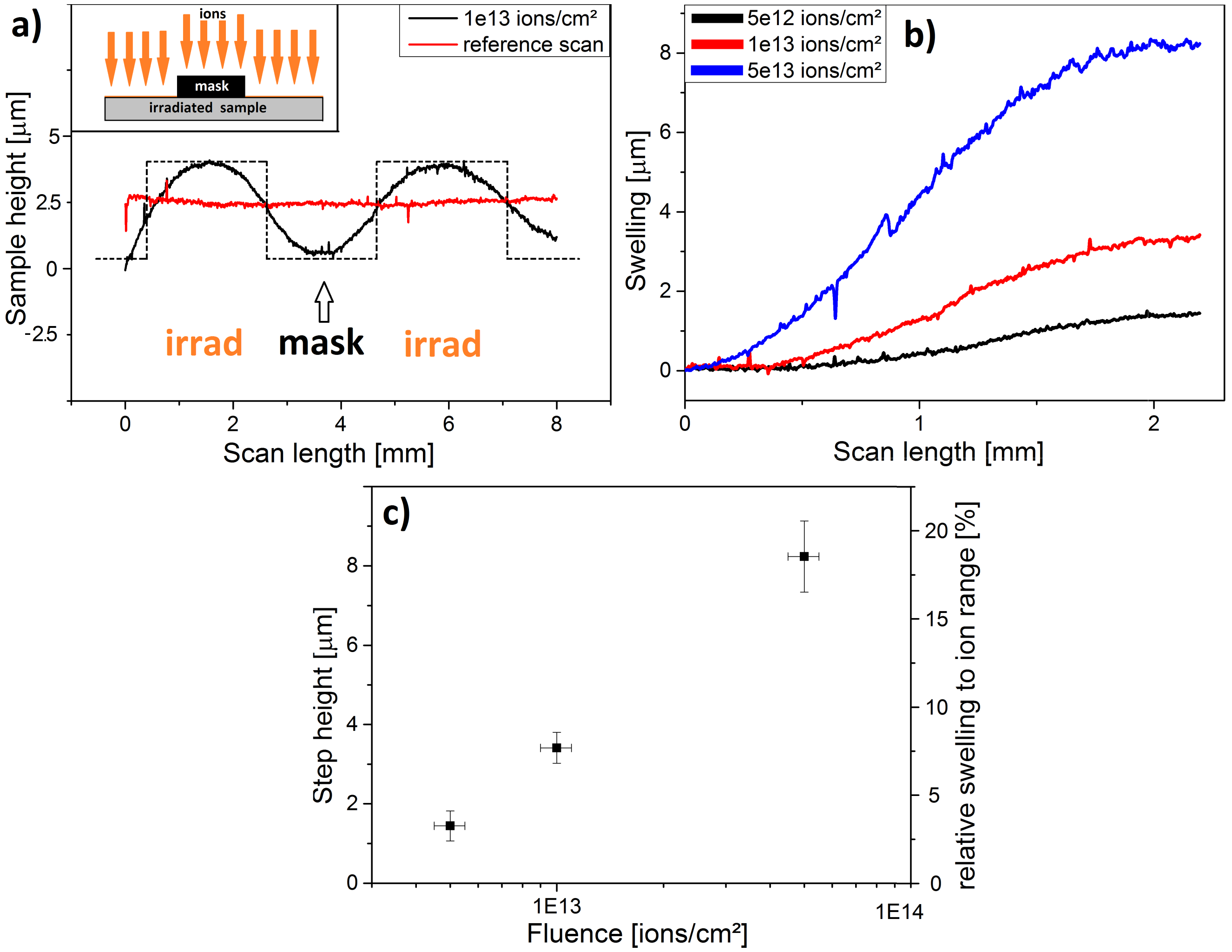

Figure 5.27: a) Data of profilometer scans across polycrystalline graphite samples irradiated with 4.8 MeV/u ^{197}Au at 3-4$\times 10^{9}$ ions/cm^{2}s (frequency 45Hz; pulse length 3 ms) to a fluence of 1×10^{13} ions/cm^{2}, the dashed line indicates the ideal case; inset: Scheme of the irradiation setup for masked samples; b) Step heights between masked and irradiated part of the sample; c) Absolute heights of the corresponding swelling steps as a function of fluence, the right y axis corresponds to swelling stepheight normalized by the ion range of 45.6 μm.

In all irradiated graphite samples, swelling effects and subsequent stress-induced bending was observed. These effects can be linked to structural changes induced by the heavy ions. As described in chapter 3.2, the formation of interstitial planes and disordering leads to swelling of the material. As described in chapter 4.3.6, two different types of graphite samples were investigated by profilometry. The obtained swelling results are summarized in Figure 5.27. Samples dedicated to swelling measurements were masked during irradiation. After the irradiation the region between masked and irradiated sample surface was scanned using a profilometer. Another set of samples were cantilevers (12×2×0.95 mm^{3}), horizontally fixed during irradiation and scanned after irradiation to measure the resulting bending radius. The swelling can be mainly attributed to vacancies and spiro-interstitials that push the graphene layers apart (see 5.2 and 5.3), form new layers and bend/warp existing layers. In the presented experiment, two effects smear out the swelling step expected at the edge of the mask. The most important factor is that the mask could only be positioned at a distance of roughly 3 mm in front of the sample. Another factor is the incident angle of the ion beam, that is set to 90 ° but in reality also has a small error due to divergent beam. A third factor is irradiation induced creep. The inset in figure 5.27a) indicates the ideal case with a sharp mask and a 100% parallel ion beam. The width of the used mask was 2 mm ± 0.3 mm. The stepheight measured is defined as the Δheight between the center of the mask and the center of the irradiated part. For each sample 5 horizontal scans were performed at y-distances of around 50 μm. The amount of swelling depends on the fluence. Swelling is also known to scale with dE/dx [112, 113] but could not be tested due to lack of beam time. A maximum swelling step height of $\approx$8 μm was measured for the sample irradiated with a fluence of $5\times10^{13} ions/cm^2$. This corresponds to a swelling relative to the range of the ion of around 18%. Comparing the density of non irradiated polycrystalline graphite (ρ_{PG}=1.84 g/cm^3) and glassy carbon (ρ_{GC}=1.54 g/cm^3) reveals a $\Delta\rho$ of around 19.5 % as given by $\Delta\rho=(\rho_{PG}\text{-}\rho_{GC})/\rho_{GC}$. This comparison suggests a mostly unidirectional relaxation where Δstep-height=Δvolume, an assumption that is in agreement with the highly anisotropic layered structure of HOPG. For polycrystalline graphite on the other hand Δstepheight$\neg\Delta$volume. This indicates that the irradiated volume of the sample is fixed within non-irradiated material volume and relaxation is only possible towards the free surface [113]. This is supported by the fact that the sample thickness (2 mm) is much larger than the ion range (45.6 μm) and that the masked sample volume is fully embedded in non-irradiated bulk material.

This observed volume increase leads to induced macroscopic stresses within the material that is largest at the interface of non-irradiated and irradiated sample volume. The presented experiment analyzes the induced stresses (σ^f_{rr}) in the sample using Stoney's description on the bending of rectangular beams as a function of stress 5.1.

$$\sigma^f_{rr} \approx \frac{E_s \cdot h_s^2}{6 \cdot (1 - \nu_s \cdot h_f)} \cdot \frac{1}{R_r} \tag{5.1}$$

The results for both, bending and stress calculations, are summarized in Figure 5.28. The analyzed cantilever samples were irradiated without a mask. The following parameters were used in the calculations:

- E_s = Young's Modulus of the graphite sample = 12.5 GPa [114]
- h_s = total sample thickness = $0,95\ mm$

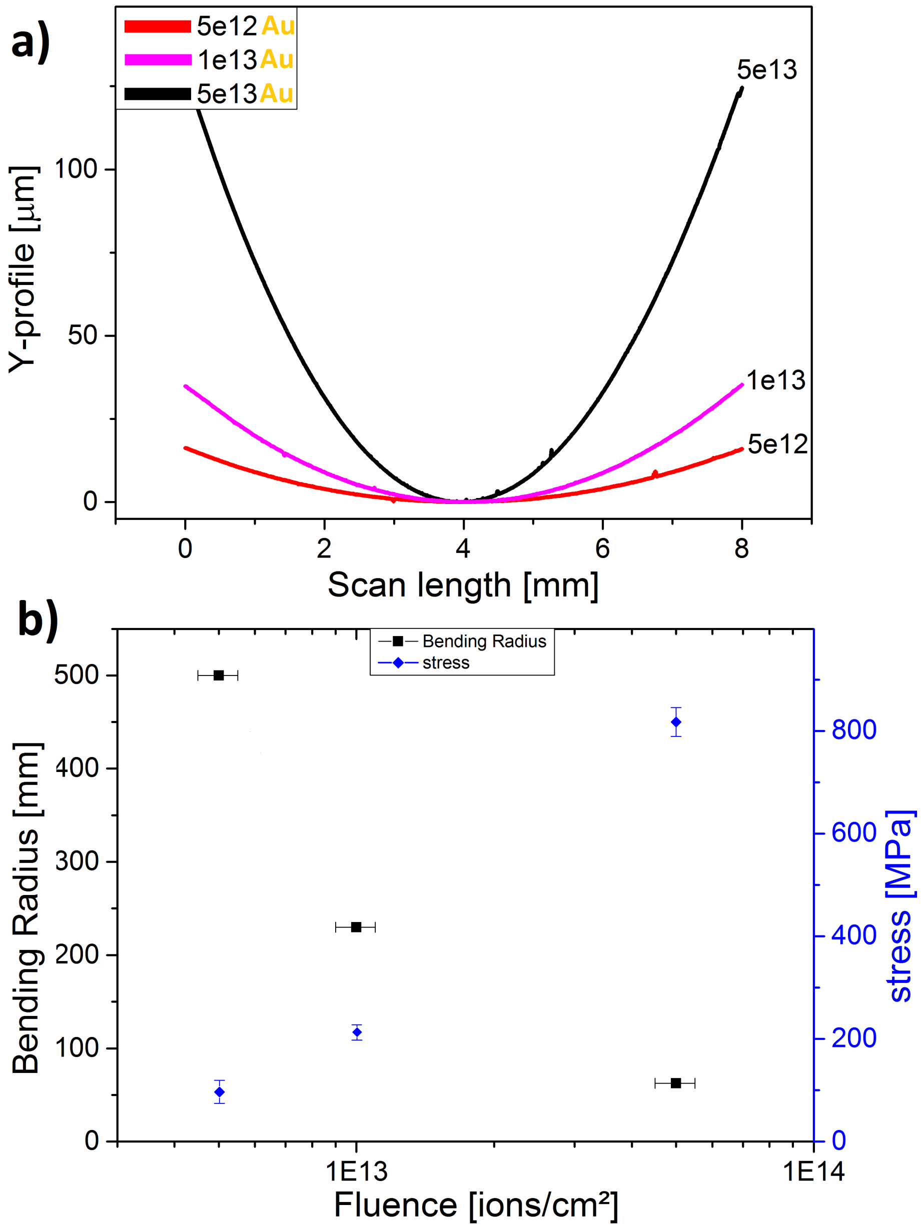

Figure 5.28: Data of a profilometer scans across thin poly crystalline graphite (PG) cantilevers irradiated with 4.8 MeV/u ^{197}Au at 3-4×10^9 ions/cm^2*s (frequency 45Hz; pulse length 3 ms); a) Raw data of profilometer scans across the irradiated samples to determine the bending radius; b) Bending radius and the calculated stress as a function of fluence

- h_f = range of the ions within graphite = $0.046\ mm$ [16]
- ν_s = Poisson ratio of graphite = 0.18 [115]

The measured bending (R_r) of the sample is also fluence dependent. The sample irradiated with a fluence of $5\times10^{13} ions/cm^2$, has a stress of ≈800 MPa. The analysis of swelling and bending does not consider the effects of radiation creep that is also happening during ion irradiation. First experiments to test creep effects were performed but are not complete for final conclusions by the time this thesis was composed. Overall it can be concluded, that the swelling gets more pronounced with increasing fluence due to a resulting higher defect density. Swelling also leads to induced macroscopical stresses within the materials. This swelling of material layers induces additional stress concentrators during the irradiation, resulting in cracks and nucleation points for other macro defects.

5.6 Online monitoring of electrical resistivity degradation during heavy ion irradiation

For many applications electrical resistivity is an important material property. How the irradiation with heavy ions affects the electrical resistivity is of interest for materials used in the components for the FAIR accelerator facility, as it affects the heat conduction by electrons. Since it is directly related to the mean free path of electrons, it is also a great indicator to probe the samples for irradiation induced defects. The following section focuses on the change of the resistivity as a function of fluence and energy loss of the ions. The on-line setup enables a direct observation of the resistivity changes within the sample during the irradiation. Two samples were irradiated simultaneously. The front sample was thin enough to be completely penetrated by the beam, while the beam was stopped in the back sample. Accurate measuring requires thin samples that are penetrated completely by the ions. The full data analysis was limited to the front samples due to a lack of suitable samples. The flux was limited to 3×10^9 ions/cm^2*s in order to keep the sample temperature below 150 °C and avoid beam induced annealing. A typical evolution of the resistivity of front (and back sample) as a function of fluence is presented in figure 5.29a. The resistivity increases with accumulated fluence and evolves towards saturation at large fluences. The fluctuations around 1.3×10^{13} ions/cm^2 are due to beam instabilities or short loss of beam and subsequent temperature changes within the sample. The inset of figure 5.29a shows the initial drop of resistivity due to beam heating of the sample when the irradiation starts. The resistivity increase in the back sample, where the beam is stopped, is significantly larger. This is ascribed to the fact that elastic collisions induce many defects in the last few μm of the ion trajectory as shown in the XRD cross section measurements (figure 5.24a). Figure 5.29b presents normalized results of the front samples from the on-line-measurement of PG irradiated with 4.8 MeV/u ^{131}Xe, ^{150}Sm, ^{197}Au and ^{238}U. The resistivity increase for all samples starts to saturate at a $\Delta\rho/\rho_0$ of about 40% as seen in figure 5.24a. Since all the samples are different, a normalization to a non-irradiated reference sample is not possible. Normalization to the pristine state has to be done for each individual sample. For ^{131}Xe, the lightest of the used ions, saturation sets in at a fluence of $\approx1\times10^{13}$ ions/cm^2. For this reason the fluence 1×10^{13} ions/cm^2 was chosen as a normalization basis to investigate relative changes. The measured absolut values in resistivity are not correct due to large errors when estimating the samples geometry. Due to the small sample thickness in the order of the ion range (30 to 55 μm) and the average grain size about 8 μm, the measured sample geometries contain large errors and are fluctuating along the sample. Additional cracks prior to the irradiation falsify the measured cross section further. For that reason the relative changes in resistivity have been analyzed.

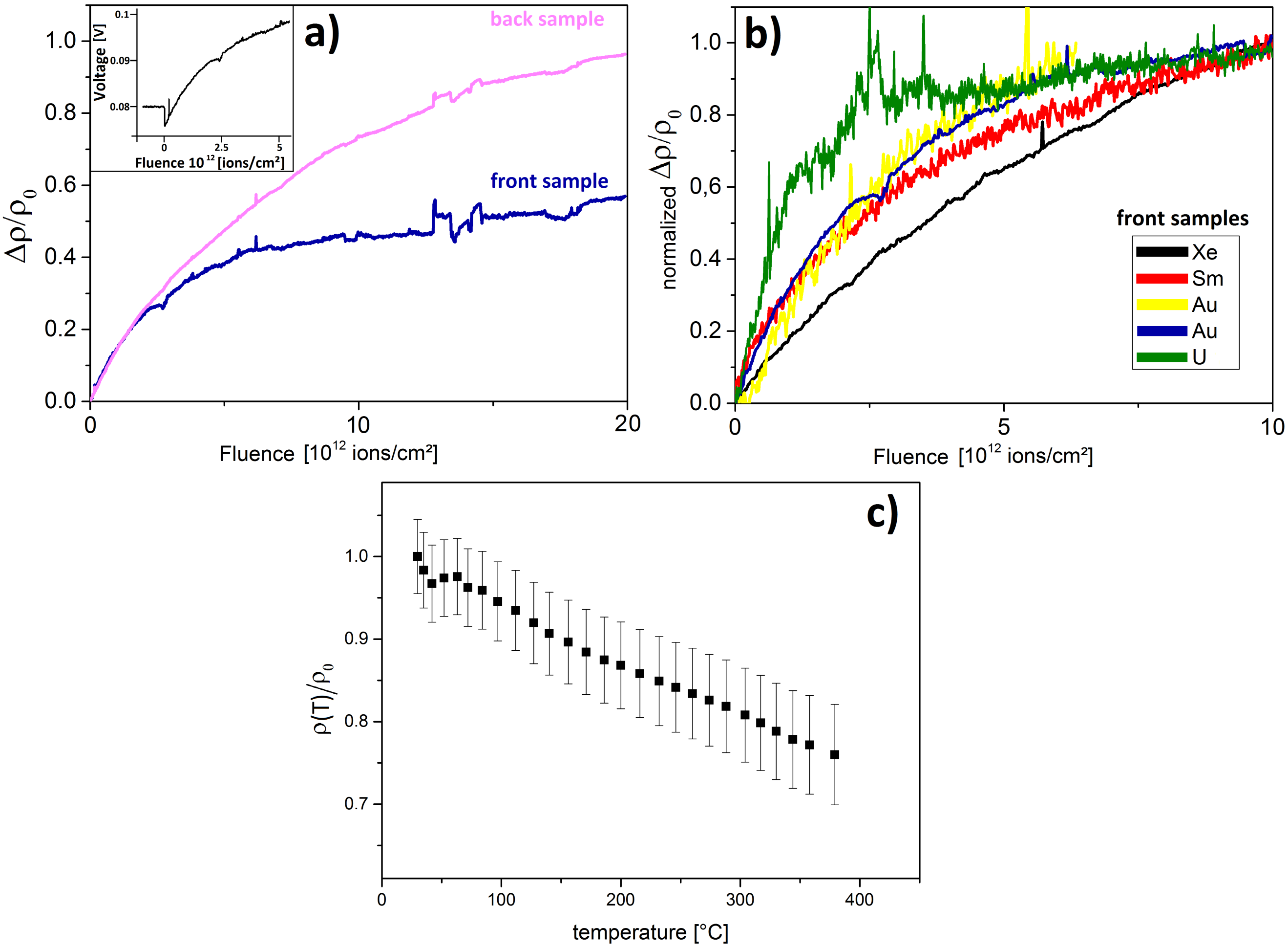

Figure 5.29: a) relative change of electrical resistivity $\Delta\rho/\rho_0$ of PG irradiated with 4.8 MeV/u ^{197}Au at 1-3×10^9 ions/cm^2*s (frequency 45 Hz; pulse length 3 ms) as a function of fluence; inset: raw signal during the monitoring showing the start of irradiation; b) $\Delta\rho/\rho_0$ normalized to $\rho_{1\times10^{13}\ ions/cm^2}$ as a function of fluence of PG irradiated with different ion species; c) $\rho(T)/\rho_0$ as a function of temperature [96]; these data were acquired using the setup shown in figure 4.19

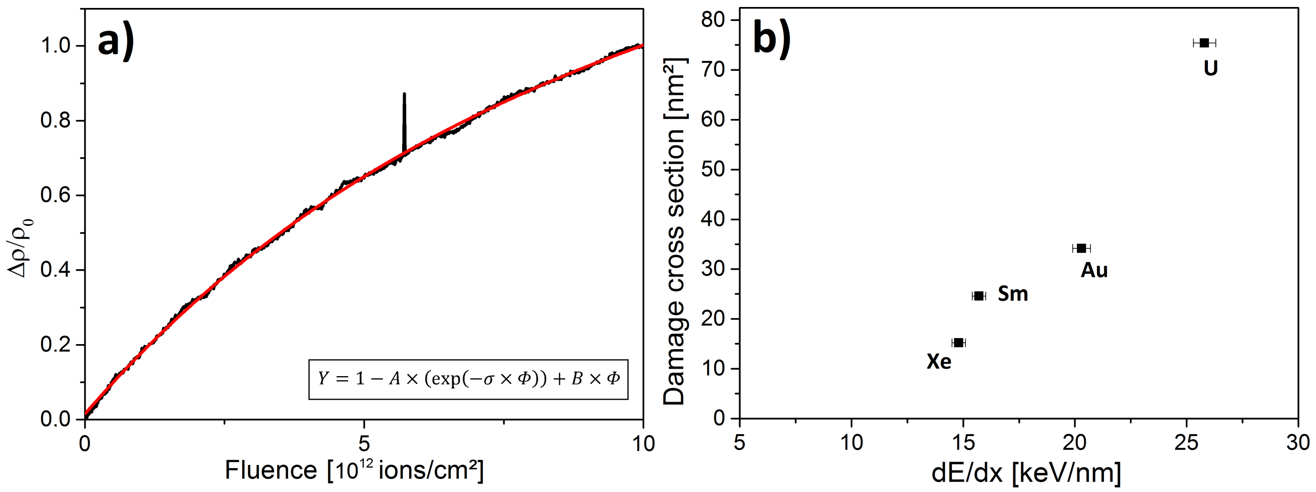

Figure 5.30: a) normalized $\Delta\rho/\rho_0$ of PG irradiated with 4.8 MeV/u ^{197}Au at 1-3×10^9 ions/cm^2*s (frequency 45 Hz; pulse length 3 ms) as a function of fluence Φ and a Poisson-fit to determine the damage cross sections; b) calculated damage cross sections as a function of dE/dx; uncertainties are smaller than the symbols. [96]

The electrical resistivity of a material is mainly influenced by the number and by the mean free path of the electrons. Ion-induced defects limit the free mean path of the electrons, thus resistivity measurements allow for a good estimation of the damage cross section of the impacting ions. In accordance to the Poisson law ($Y=1-A\times(\exp(-\sigma\times\Phi))$), a fit of the normalized results as a function of fluence allows to calculate the value for the damage cross section for each corresponding ion species. To consider the resistivity evolution with temperature a calibration measurement was done off-line (figure 5.29c). The evolution with temperature appears to be linear, that is why a linear correction ($+B\times\Phi$) was chosen for the Poisson fit. Figure 5.30a shows the data of ^{197}Au irradiated PG and a corresponding Poisson-fit including the linear correction factor that considers temperature induced changes of resistivity during the irradiation. The damage cross section of the ions seems to scale linear with the dE/dx as shown in figure 5.30b. It can be concluded, that both dE/dx and fluence Φ influence the electrical resistivity due to an increasing defect density in the material. While the electrical resistivity reaches a saturation for all used ions at fluences above 1-2×10^{13} ions/cm^2, a larger dE/dx leads to a faster resistivity increase.

5.7 Beam-induced changes to the thermal diffusivity studied by LFA

The following section presents and discusses the influence of the radiation induced structural changes on the thermal diffusivity. Since the main transport mechanism of heat within a material are phonons and the conduction of electrons, radiation induced defects lead to an increased scattering and thus thermal diffusivity. While defects reduce the free mean path for electrons, they also inhibit the transport of phonons due to scattering and deflection. The first measurements were done in the through-plane setup as described in chapter 4.3.3. Due to the small ion range ($\approx$50 μm) compared to the sample thickness (up to 2 mm), some of the samples were polished down to create fully ion penetrated samples. For partially irradiated samples we tried to apply a 2-layer model with two different diffusivities for the two different sample layers and a fixed contact resistance between the layers. Unfortunately the data was too noisy for an accurate application of the 2-layer model. Another problem is that the diffusivity within the irradiated layer changes along the ion trajectory due to different dE/dx. Due to additional difficulties to deconvolute the signals of short measurement signals in case of fully ion penetrated thin samples, the through-plane setup proved to be unsuitable and a switch towards the in-plane setup was done.

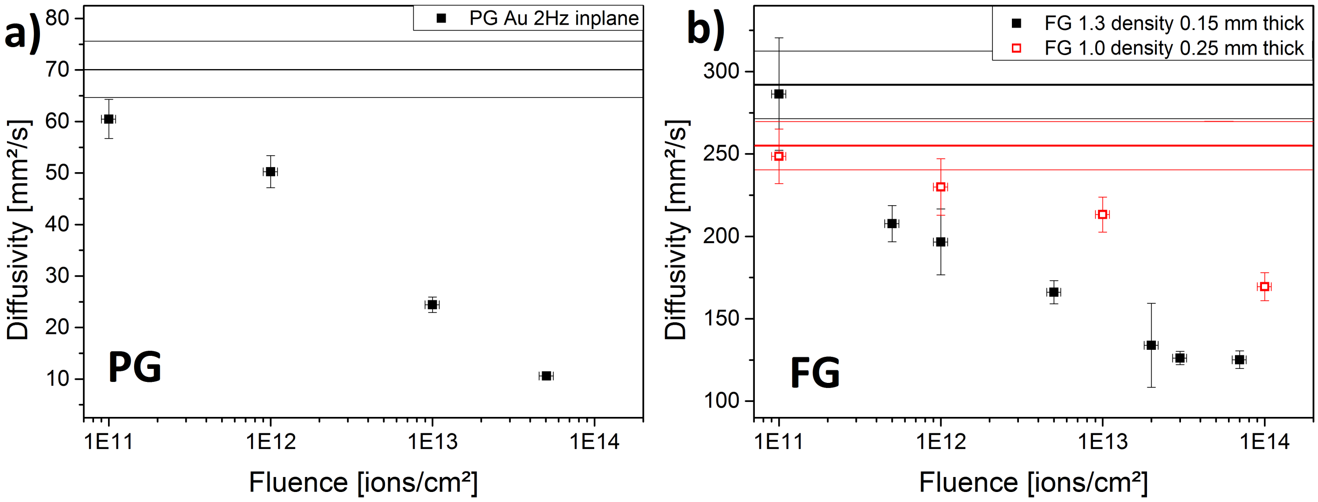

Figure 5.31: In-plane thermal diffusivity as a function of fluence; Irradiation was done with 4.8 MeV/u ^{197}Au at 1-3$\times$10^9 ions/cm^{2}s (frequency 2 Hz; pulse length 3 ms); Solid lines represent the values of the non-irradiated material and the corresponding uncertainties; a) polycrystalline graphite (PG) with a thickness of 30-50 μm; b) Various grades of flexible graphite (FG) with a thickness of 150-250 μm.

Figure 5.31a and 5.31b present the results of ^{197}Au irradiated PG and FG samples respectively. Both material exhibit a clear trend of degradation of the thermal diffusivity with increasing accumulated fluence. The diffusivity of PG drops significantly from roughly 70 mm^2/s (non-irradiated) to 10 mm^2/s for a fluence of ($\geq$5$\times$10^{13} ions/cm^2) while the in-plane diffusivity of the anisotropic FG drops from $\approx$ 270 mm^2/s (non-irradiated) to 120 mm^2/s for a fluence of

($\geq 5\times10^{13}$ ions/cm^2). The anisotropic nature of graphite leads to a large diffusivity difference for the in-plane ($\geq 270\ mm^2/s$) and through-plane ($\approx 5\ mm^2/s$) directions. This anisotropy and a larger crystallite size of the FG lead to the higher thermal diffusivity of the FG in comparison to the quasi-isotropic PG. Due to the ion-range limit, it is not possible to conclude that the relative drop in thermal diffusivity is larger in PG than in FG as the data suggests since only ≈35 % of the probed sample volume is irradiated within the FG samples with a thickness of 150 μm and only ≈20 % in the 250 μm thick samples. This effect can also be observed when comparing the results of the two different FG materials, where the thicker samples exhibits a smaller loss in thermal diffusivity. The main cause for a diffusivity drop are the defects induced by the ion beam reducing the mean free electron path and inducing phonon scatter centers within the material effectively hindering the heat transfer.

A set of in-plane measurements was performed at high temperature. The PG samples were fully irradiated with 4.8 MeV/u ^{131}Xe at 4-5$\times10^9$ ions/cm^2*s (frequency 5 Hz; pulse length 1.2 ms). The thermal diffusivity change between the heating and cooling cycle relative to the diffusivity at the maximum temperature ($\Delta Diff/Diff_{1000^\circ C}$) is presented in figure 5.32a and gives insight in the annealing behavior. It is evident that samples with larger accumulated fluences and thus larger defect densities are annealed more after the heating to $1000^\circ C$. Furthermore, the elastic collisions within the range of nuclear stopping affect the diffusivity to a larger extend, even after considering that the sample containing the nuclear stopping contains ≈50 % non irradiated material. This can be confirmed by the XRD data that suggests the nuclear collisions are more efficient in creating defects (compare figure 5.24a). The defect annealing observed in the XRD (compare figure 5.24c) can also be verified for the thermal diffusivity. The larger the fluence (i.e. defect density) and temperature, the larger the annealing effects. Figure 5.32b and 5.32c directly compare the heating and cooling cycle of two in-plane PG samples irradiated with 4.8 MeV/u ^{131}Xe at 4-5$\times10^9$ ions/cm^2*s (frequency 5 Hz; pulse length 1.2 ms) to a fluence of 1×10^{14} ions/cm^2. It can be observed that both samples have a first annealing step around $200-250^\circ C$ and a 2nd step starting around $400-500^\circ C$ that is represented by an increase of the diffusivity, opposed to the decreasing trend expected from the temperature dependence. The first step can be associated to the recombination of intimate vacancy-interstitial pairs. The second step is associated with the recombination of more complex defect structures possible due to defect diffusion inside of and in between graphene sheets [1]. It is also confirmed that the sample with the nuclear stopping has a larger annealing potential as already seen in figure 5.24a. Unfortunately the high temperature in-plane measurements contain an error that is represented in figure 5.32d that compares a non-irradiated PG sample measured before and after a certain amount of heating and cooling cycles. But it has to be noted that this error only effects the absolute values of diffusivity and not the trends. The temperature proved too high for the used sample-holder and the surface of the steel started to tarnish, changing the emissivity. As a result after an increasing number of heating cycles, values of diffusivity drop.

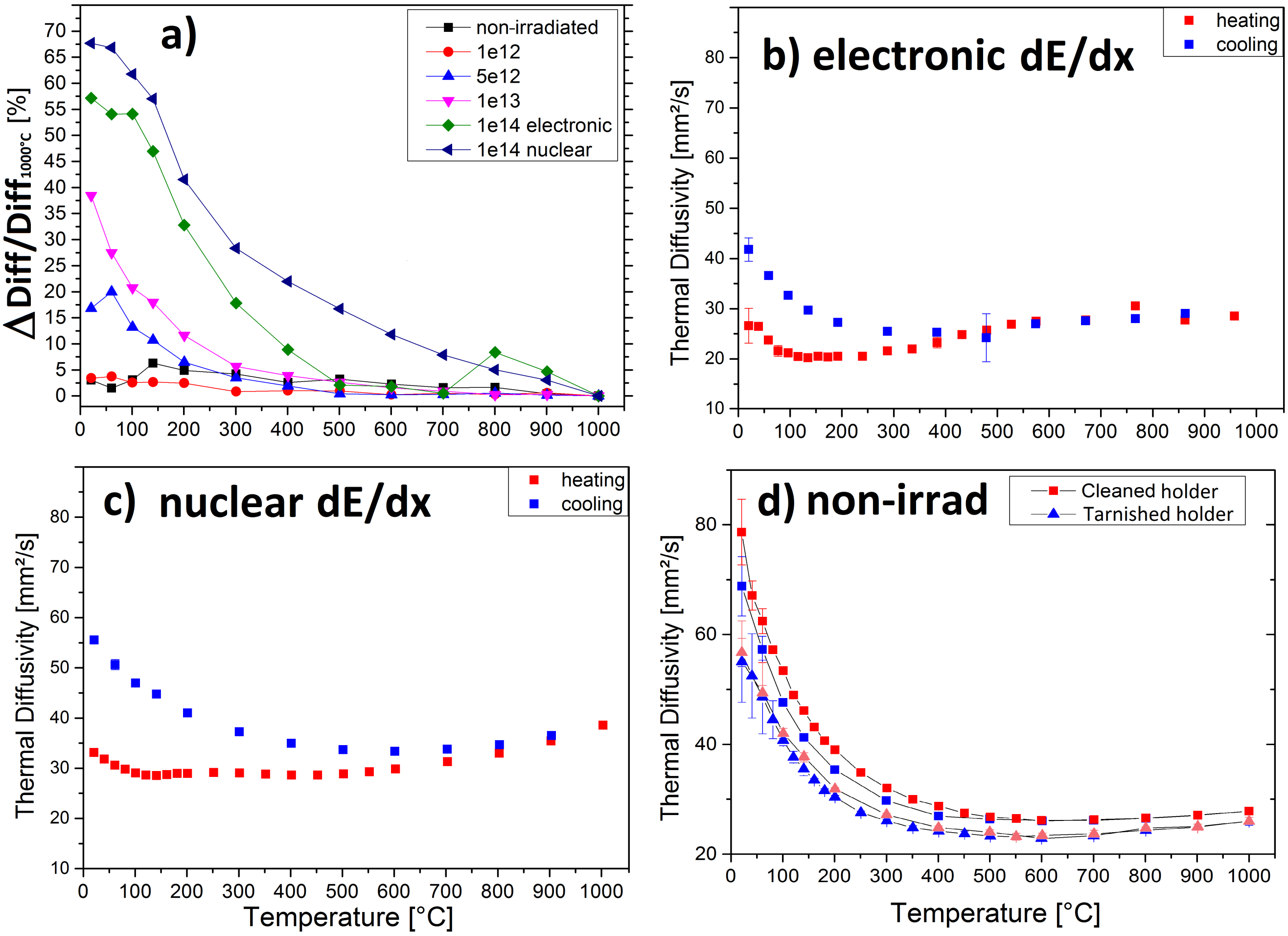

Figure 5.32: In-plane thermal diffusivity measurements of polycrystalline graphite irradiated by 4.8 MeV/u ^{131}Xe at 4-5$\times10^{9}$ ions/cm^{2}*s (frequency 5 Hz; pulse length 1.2 ms). Sample thicknesses range from 30-50μm; Results are given as a function of temperature; a) Change of thermal diffusivity between heating and cooling cycle relative to the value at max. temperature ($\Delta Diff/Diff_{1000°C}$) of PG samples with different accumulated fluences; b) Diffusivity of the heating and cooling cycle of a PG sample irradiated to a fluence of 1$\times10^{14}$ ions/cm^{2} that was fully penetrated (electronic dE/dx); c) Diffusivity of the heating and cooling cycle of a PG sample irradiated to a fluence of 1$\times10^{14}$ ions/cm^{2} that stopped the beam half way in the sample (nuclear dE/dx); d) Comparison of the diffusivities of two different measurement cycles of a non-irradiated PG sample showing deterioration of the holder after several heating cycles.

After cleaning the sample-holder, values for diffusivity are restored to the initial state. Effects due to the sample holder can be observed even within the same cooling cycle of one measurement, as the diffusivity is suddenly lower than during the corresponding heating cycle of the measurement.

Thermal diffusivity measurements show that at temperatures around 200 $°C$ a first annealing step can be seen indicated by a small increase in thermal diffusivity with increasing temperature (compare figure 5.32b and 5.32c) despite the negative diffusivity evolution with temperature. As expected, the thermal diffusivity decreases with increasing defect density (fluence). A dE/dx dependence could not be verified due to lack of samples but is to be expected in correlation to the results from Raman spectroscopy and XRD. These results inspired further investigations of the annealing and structural changes at high temperatures using differential scanning calorimetry (DSC).

5.8 Investigation of defect annealing in ion irradiated graphite using DSC

Differential scanning calorimetry was performed to investigate defect annealing in swift heavy ion irradiated graphite. DSC is a thermal method that monitors heat intake into a sample during a heating cycle. During defect recombination into states of lower energy, excess energy is emitted and heats the sample, which can be detected in a change of heat capacity c_p. The investigated samples were fully irradiated polycrystalline graphite (PG) discs of diameter 5 mm and thickness around 40-50 μm. Due to the large irradiation induced stress, the samples were bent and thus the thermal contact within the DSC sample holder was not ideal. One sample had to be crushed to a powder in order to get sufficient thermal contact (PG sample irradiated with 1×10^{13} ions/cm^2). As a consequence the measurements have a large variance, but the trend within all samples is similar. Figure 5.33 presents the evolution of the heat capacity c_p as a function of the temperature. In all investigated PG samples, an exothermic reaction can be observed around 200 $^\circ C$ resulting in a drop of the c_p which is associated with the recombination of intimate Frenkel pairs (interstitial-vacancy). Those also appear within the non-irradiated samples, but to a smaller extent and only during the first heating cycle (figure 5.33a). After the first and second heating cycles (up to 1400 °C), the non irradiated sample has annealed most defect originating from the manufacturing process. Within the irradiated samples (figure 5.33b) this initial recombination releases enough energy to heat up the sample in an exothermal reaction, leading to a negative c_p value. A second pronounced exothermal process is observed starting around 500 $^\circ C$ and ending around 750 $^\circ C$. It is known that more complex defect structures recombine at this temperature further lowering the overall energy of the structure [116, 117]. The last step of annealing starts around 1250 $^\circ C$ and is also visible within all samples and is exothermal for fluences $\geq\ 1\times10^{13}\ ions/cm^2$. XRD data suggested, that above temperatures of 1500 $^\circ C$ only newly formed planes and minor stacking faults remain within the sample. When comparing cycles 1 to 3 within the non-irradiated samples, one can observe that the final annealing step appears even after the first cycle and is only diminishing within the third cycle suggesting that the final recombination step needs a longer time frame to be completed. We can conclude that defects, ion induced or from the manufacturing process, can be annealed by heat. Defect recombinations release energy, and in cases of large defect densities are self heating. Three temperature ranges (200-300, 400-600 and 1200-1400 °C) have been observed where different structures within the graphite recombine. These data are in agreement with results from XRD and LFA measurements.

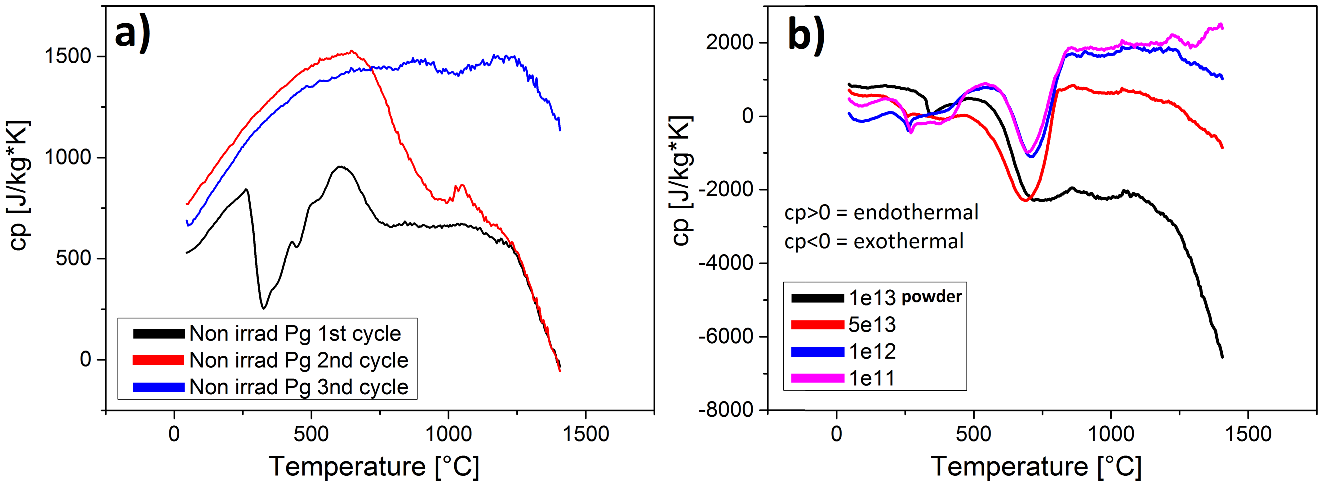

Figure 5.33: Heat capacity c_p of polycrystalline graphite (PG) irradiated with 4.8 MeV/u ^{197}Au at 1-3×10^9 ions/cm^2*s (frequency 45 Hz; pulse length 3 ms); Heating rate was set to 20 K/min; Results are presented as a function of temperature; a) 3 heating cycles of non-irradiated PG; b) First heating cycle of irradiated PG at various accumulated fluences; The sample with a fluence of 1×10^{13} ions/cm^2 was crushed to a powder to provide sufficient thermal contact to the sample holder

5.9 Beam-induced changes of hardness and elastic modulus studied by Micro/Nano-indentation

The following section summarizes the results obtained by micro- and nano-indentation to determine the evolution of hardness and Young's modulus during irradiation. The defects induced by heavy ions in the material lead to the observed increase in hardness and Young's modulus with respect to the non-irradiated sample. At very high fluences, the change of the lattice constant c, the tortuosity R_{Tor} and the FWHM of the G-peak confirm a disordering of the graphite crystal that initiates a phase transition from the regularly stacked ABAB structure to an irregular mixture of ABAB and ABC structure and finally towards a highly disordered structure. Raman spectroscopy data of the average in-plane crystal size L_a also suggest that at very high fluences ≥3e13 ions/cm^2 we can observe the milling effect of the heavy ions [118]. This milling effect describes the size reduction of the crystallites following ion irradiation. As mentioned in chapter 4.3, Sneddons equation (4.29) was used to calculate the Young's modulus due to the elastic response of the HOPG to the indentation and a subsequent overestimation of the contact area by the classical equations.

Micro-indentation shows, that hardness and modulus change only insignificantly with the ion irradiation in highly oriented pyrolytic graphite (HOPG) (figure 5.34). Micro-indentation on a HOPG sample exceeds the formation of elastic twins and thus activates a plastic deformation. The Berkovich diamond tip is pushing perpendicular to the graphene layers. Upon reaching the limit for recoverable twins, the bonds within the graphene start to break and the graphene layers

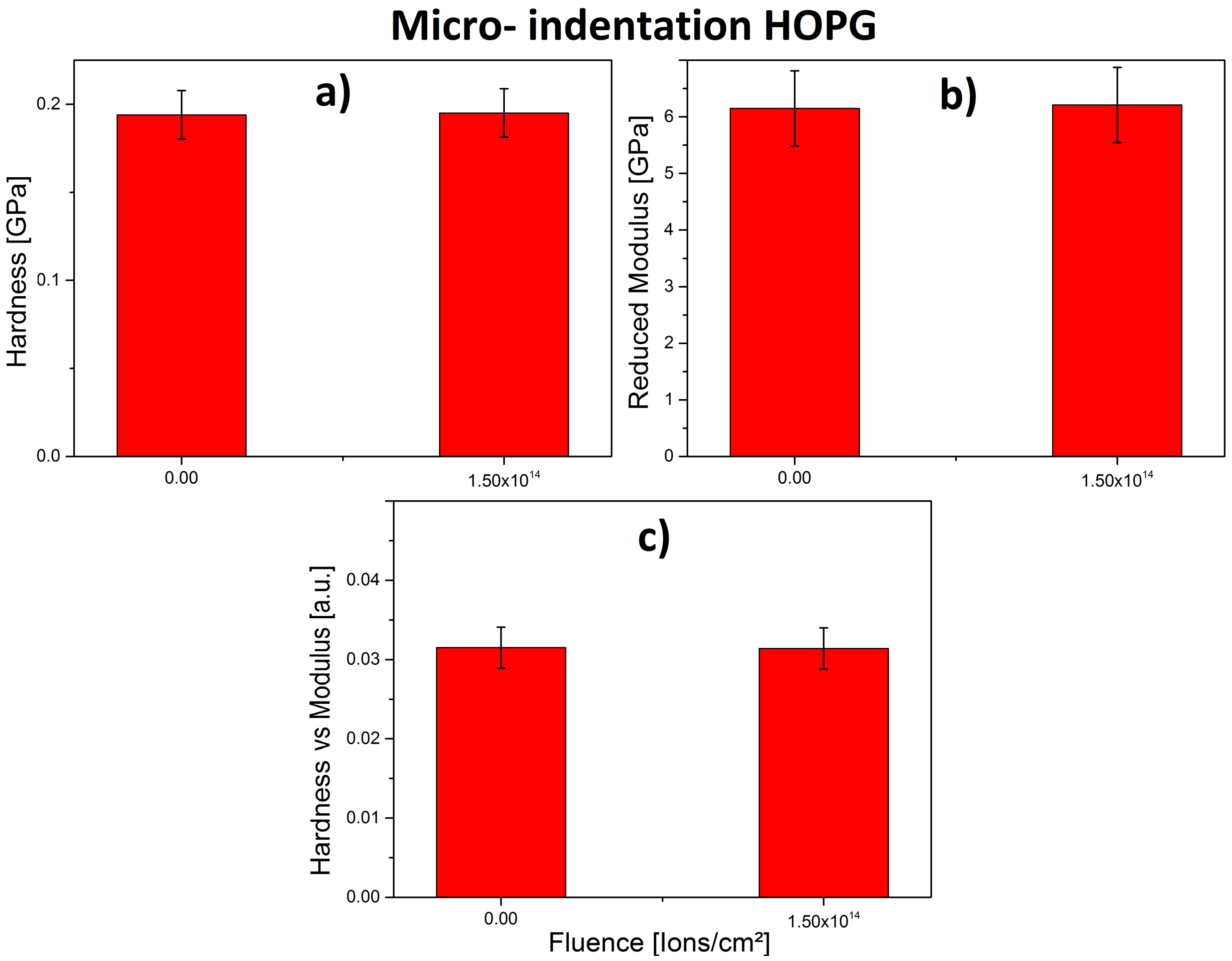

Figure 5.34: Micro-indentation results of HOPG irradiated by 4.8 MeV/u ^{197}Au at 1-3×10^{10} ions/cm^2*s (frequency 45 Hz; pulse length 3 ms); a)Hardness; b)Young's modulus; c)Hardness/Young's modulus.

fold along the indenter tip, resulting in a pile-up (compare figure 4.16). This stress-induced defect nucleation which results in a delamination process makes graphite a soft material due to missing inter-layer bonds between adjacent graphene layers. The introduction of defects within the HOPG layers increases the intra-layer stiffness but does not contribute to the delamination-resistance. Formation of sp^3 bonds and a change in the stacking order of the graphite increase the resistance to this deformation by delamination.

Polycrystalline graphite materials (SNG grade and R6650 grade) behave different due to the presence of many grain boundaries and additional pores (The difference between the grades of PG is the density: SNG grade 398: 1.7865 g/cm^3, SNG grade 953: 1.7119 g/cm^3 and R6650: 1.84 g/cm^3). Different orientations locally limit the deformation by delamination that is seen in HOPG resulting in a larger hardness and elastic modulus because the graphite anisotropy is irrelevant due to the different grain orientations. This results in a different behaviour of the material during micro-indentation, and a different evolution of hardness and Young's modulus with increasing ion fluence (figure 5.35 and figure 5.36). Both SNG grades and the PG exhibit similar trends, with Young's modulus and hardness increasing with the ion fluence. A milling of the crystals and the subsequent creation of more grain boundaries, combined with the defect-induced increase of the graphene sheet's stiffness results in an increased resistance to deformation. As already observed by Raman spectroscopy, a larger energy loss dE/dx results in a significantly larger hardening and increase of the Young's modulus. When comparing the hardening as a function of the energy loss, one can observe a step (figure 5.36d) in the trend of hardening. This can be connected to the formation of continuous tracks that has been reported by Liu et al. [119]. Liu et al. suggest that below 18 keV/nm no continuous tracks are formed in HOPG [5, 119]. Considering this, a linear fit only including ^{197}Au and ^{238}U irradiated samples ($dE/dx \geq 18$ keV/nm) suggests a threshold around 5 to 6 keV/nm, which lies within the range where track formation in HOPG starts [5, 119]. The pronounced difference in hardening of ^{131}Xe and ^{150}Sm in comparison to ^{197}Au and ^{238}U ion irradiated samples is most likely a further indicator that a significant change in the track formation between the different ion species exists. This may include a continuous damage morphology and a phase change in the tracks that becomes more prominent with higher dE/dx [96]. Another indicator for such a difference in the track formation is the hardness/modulus ratio. Changes in the ratio of hardness/modulus are an indication of a phase transformation of the material (see chapter 4.3.4). The increase of the ratio of hardness to reduced modulus for ^{197}Au and ^{238}U ion irradiated PG samples above fluences of 1×10^{13} ions/cm^2 indicates a change in the plastic deformation that is possibly related to micro-structural changes within the ion tracks. These structural changes could be transitions towards a amorphous or nano-crystalline structure within the ion tracks. Such a phase change may also explain the large hardening effect of ^{197}Au and ^{238}U irradiated PG samples compared to ^{131}Xe and ^{150}Sm irradiated PG samples [96].

Both fiber enhanced materials (carbon fiber composites (CFC) and molybdenum graphite (MoC)) follow the trend of the PG samples due to the fact that the matrix is composed of graphite.

In contrast to micro-indentation remains nano-indentation within the elastic deformation of graphite during measurements. There is an inherent difference in the elastic deformation and the deformation by delamination of graphene layers. Young's modulus of HOPG reaches values around 15 GPa in contrast to 6 GPa measured with the micro-indentation (figure 5.34 and 5.39). The ion induced defects increase the Young's modulus for HOPG, GC and PG. Among the tested materials, GC is affected the least by the ion irradiation, as to be expected of the already highly disordered structure (figure 5.40). HOPG is less influenced by introduced defects than PG (figure 5.39 and 5.41). This is once again due to the strong anisotropy of the HOPG in contrast to the quasi-isotropic structure of PG. Hardness for a fully elastic material response (as seen in HOPG) has no physical meaning, but it allows for a characterization of the layer stiffness. The introduction of defects and the subsequent recombination of the bonds within the layers that

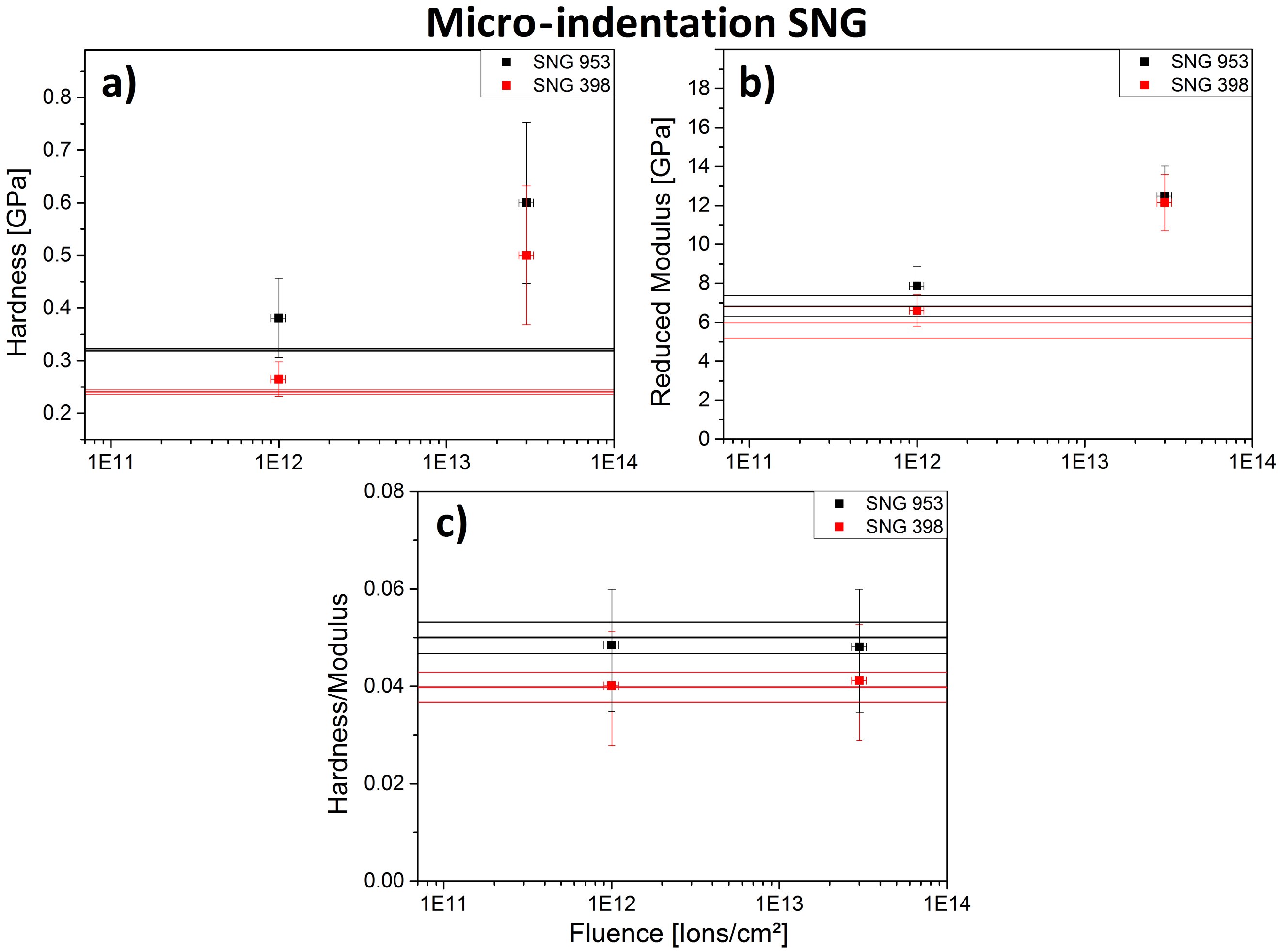

Figure 5.35: Micro-indentation results of polycrystalline graphite (SNG grade 953 and 398) irradiated by 4.8 MeV/u ^{150}Sm at 1-3×10^9 ions/cm^2*s (frequency 3.4 Hz; pulse length 1.2 ms); Solid lines represent the non-irradiated sample and corresponding error bars; Results are given as a function of fluence; a)Hardness; b) Young's modulus; c) Ratio of hardness/Young's modulus.

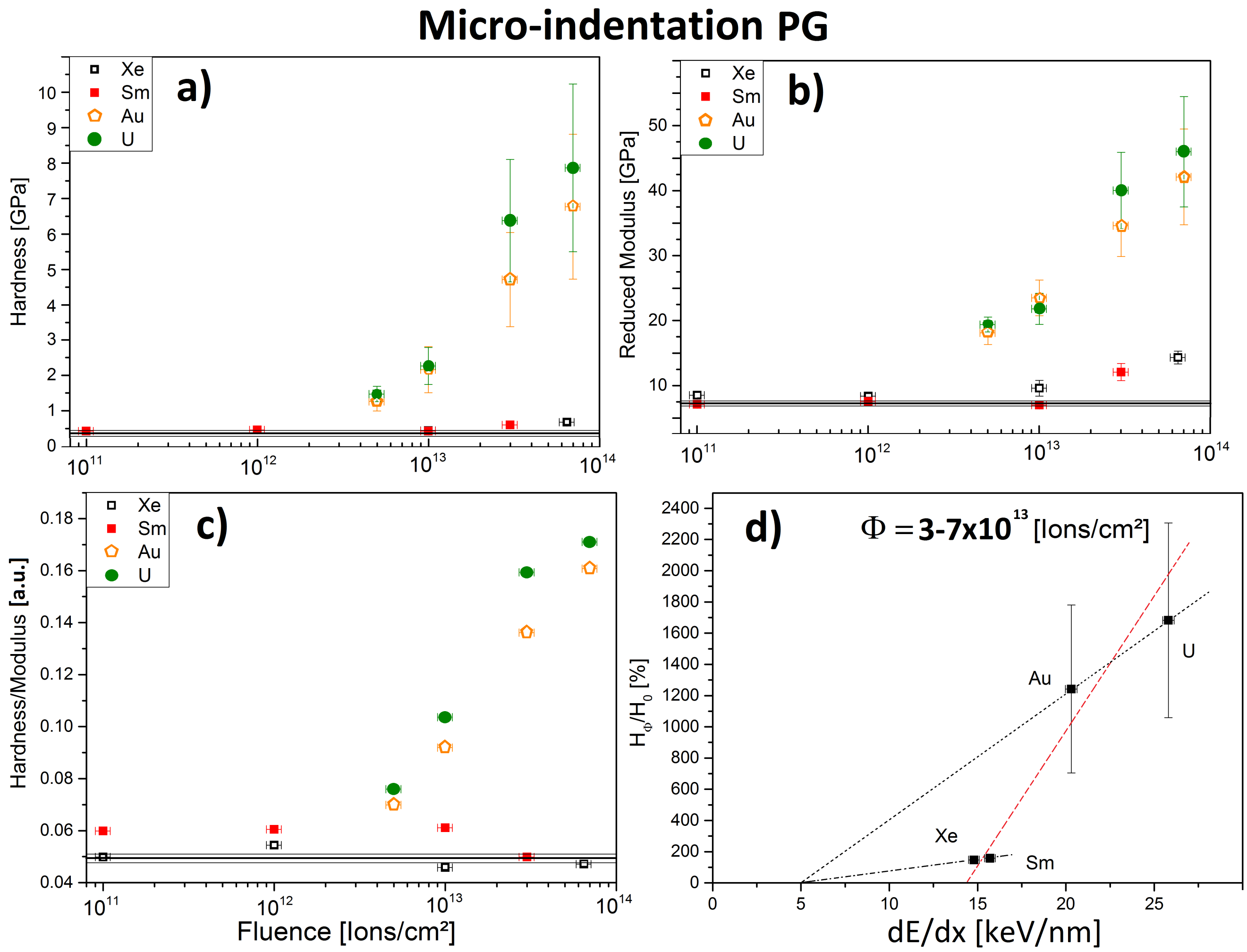

Figure 5.36: Micro-indentation results of polycrystalline graphite (R6650 grade) irradiated by 4.8 MeV/u ^{131}Xe at 2-3×10^9 ions/cm^2*s (frequency 5 Hz; pulse length 1.2 ms), 4.8 MeV/u ^{150}Sm at 2-3×10^9 ions/cm^2*s (frequency 3.4 Hz; pulse length 1.2 ms), 4.8 MeV/u ^{197}Au at 2-3×10^9 ions/cm^2*s (frequency 45.4 Hz; pulse length 2 ms) and 4.8 MeV/u ^{238}U at 1-2×10^9 ions/cm^2*s (frequency 1 Hz; pulse length 0.5 ms); Results are presented as a function of fluence; Uncertainties include fit and statistical errors; Solid lines represent values for non-irradiated material; a) Hardness; b)Young's modulus; c) Hardness/Young's modulus ratio; d) Hardening at the highest available fluence(3-7×10^{13} ions/cm^2) in % as a function dE/dx; The red dashed line represents a linear fit with all data points, the black dashed lines represent a fit with dE/dx above and below 18 keV/nm.[96]

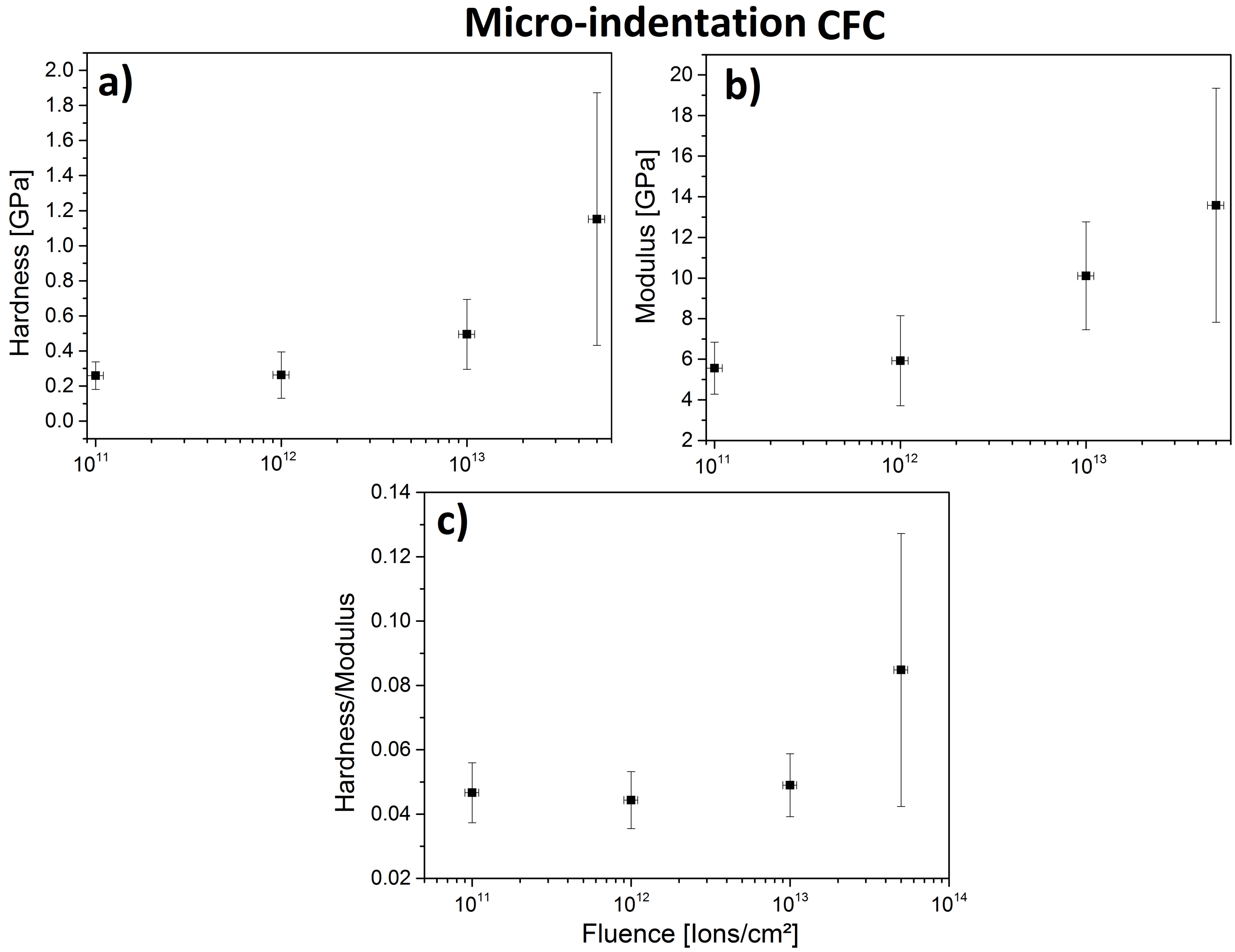

Figure 5.37: Micro-indentation results of carbon fiber composites (CFC) (transversal fiber orientation) irradiated by 4.8 MeV/u ^{197}Au at 1-3$\times 10^{9}$ ions/cm^{2}*s (frequency 45 Hz; pulse length 2 ms); Results are presented as a function of fluence; Uncertainties include fit and statistical errors; a) Hardness ; b) Young's modulus; c) Hardness/Young's modulus.

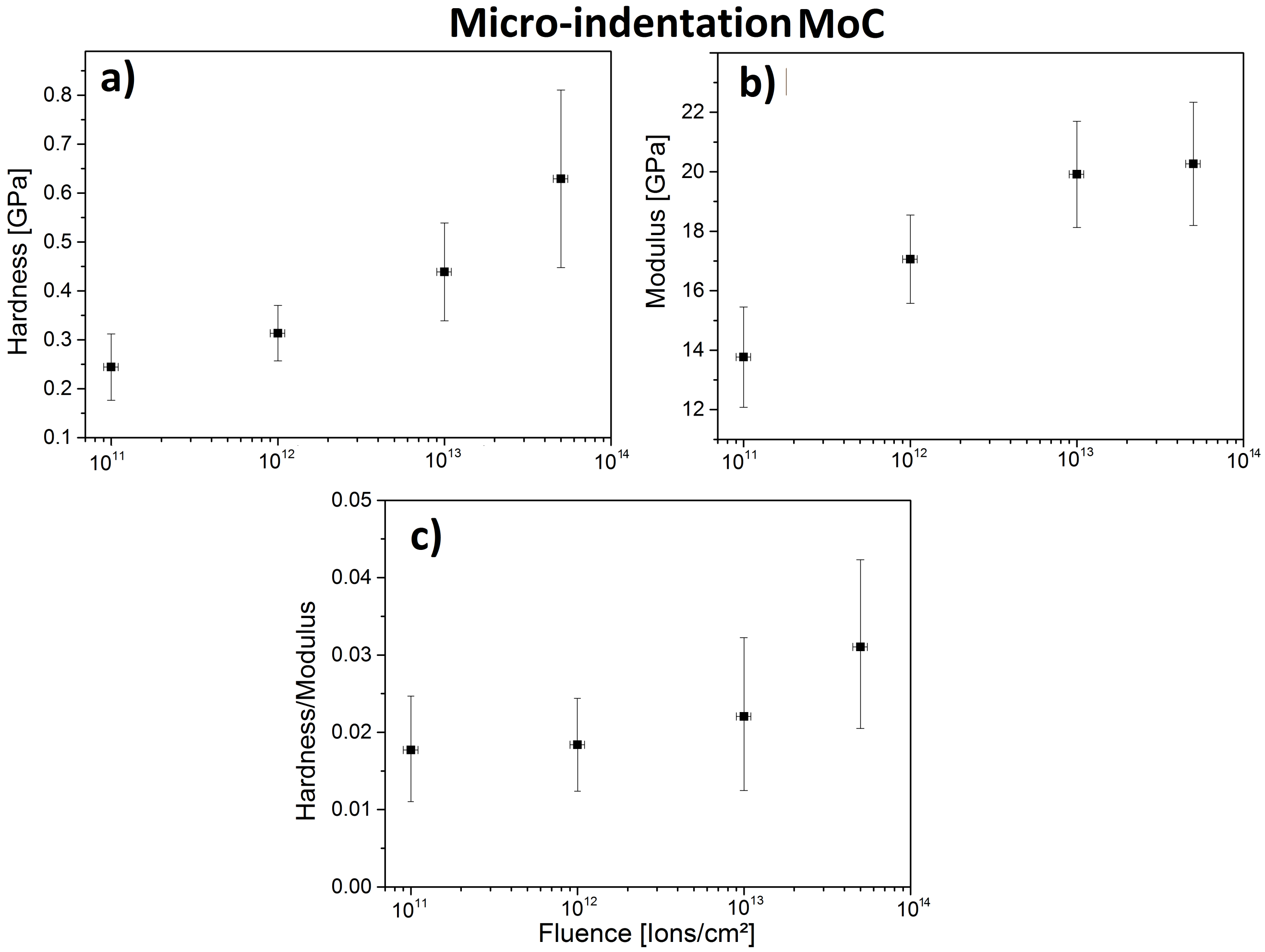

Figure 5.38: Micro-indentation results of molybdenum graphite composites (MoC) irradiated with 4.8 MeV/u ^{197}Au at 1-3$\times10^9$ ions/cm^2*s (frequency 45 Hz; pulse length 2 ms); Results are presented as a function of fluence; Uncertainties include fit and statistical errors; a) Hardness; 2) Young’s modulus; 3) Hardness/Young’s modulus.

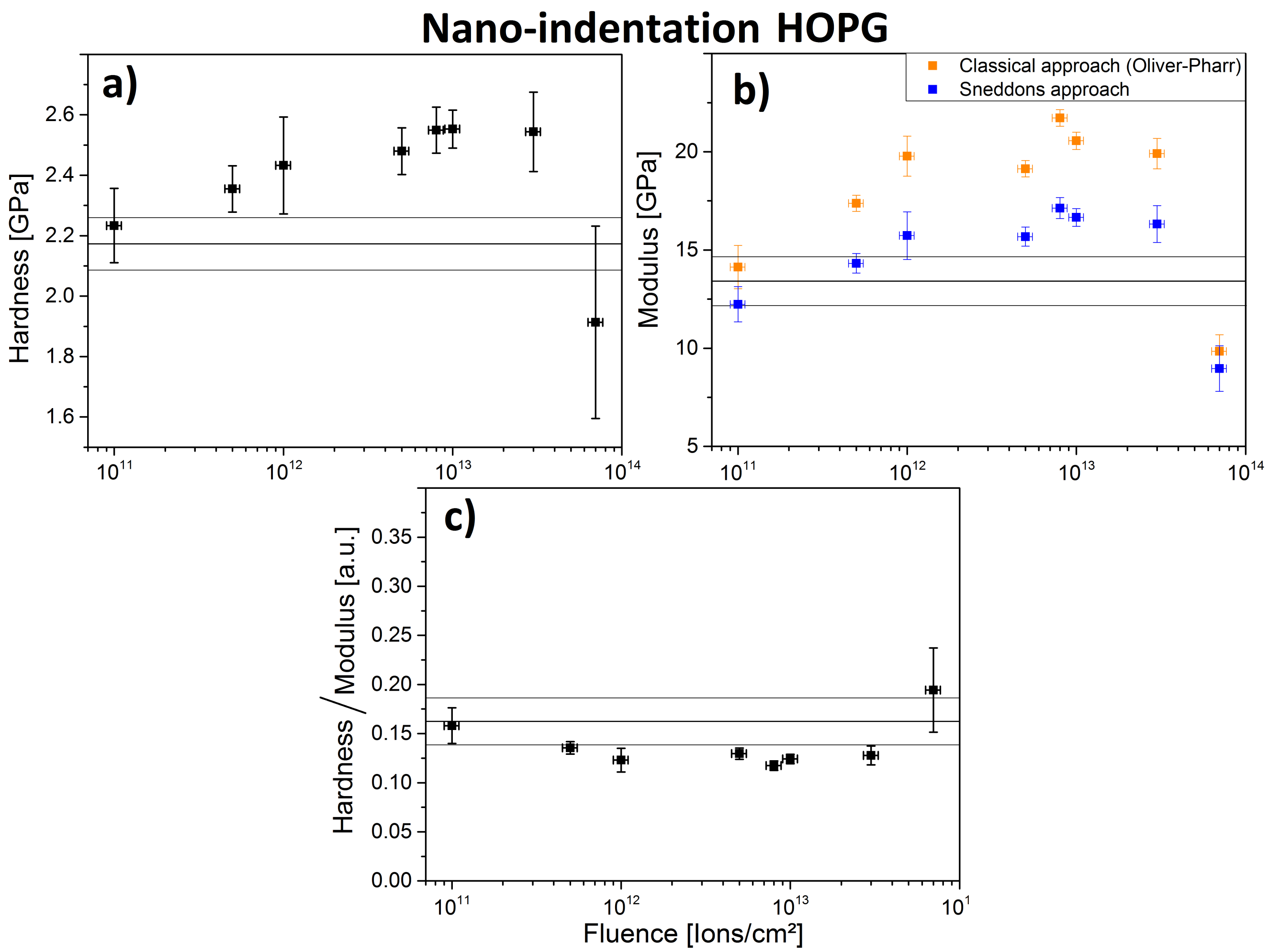

Figure 5.39: Nano-indentation results of highly oriented pyrolytic graphite (HOPG) irradiated with 4.8 MeV/u ^{197}Au at 1-3×10^9 ions/cm^2*s (frequency 45 Hz; pulse length 2 ms); Results are presented as a function of fluence; Solid lines represent the non-irradiated sample; Uncertainties include fit and statistical errors; a) Hardness; b) Young's modulus (Sneddon and Oliver/Pharr method); c) Hardness/Young's modulus.

tend to twist and warp the graphene sheets leads to a change in average bond length within the graphene. Different bond lengths are connected to different elastic constants and thus changing the elastic response. This makes hardness a useful measure of defect concentration within the material. In HOPG samples irradiated above ion fluences of 5×10^{13} ions/cm^2 one can observe an effect of nano-crystallization which results in a decrease of the layers stiffness below the values of non-irradiated HOPG (figure 5.39). This effect has not been observed in isotropic graphite or GC (figure 5.40 and 5.41).

When comparing the results of GC and PG, one can observe that PG surpasses the GC in Young's modulus at high doses. This suggests that the irradiation induced stress has an additional contribution in high fluence irradiations. Values for hardness can not be compared between GC and PG due to different deformation mechanisms of PG and GC. In order to eliminate dE/dx effects on the results, all samples have been irradiated with ^{197}Au ions using similar

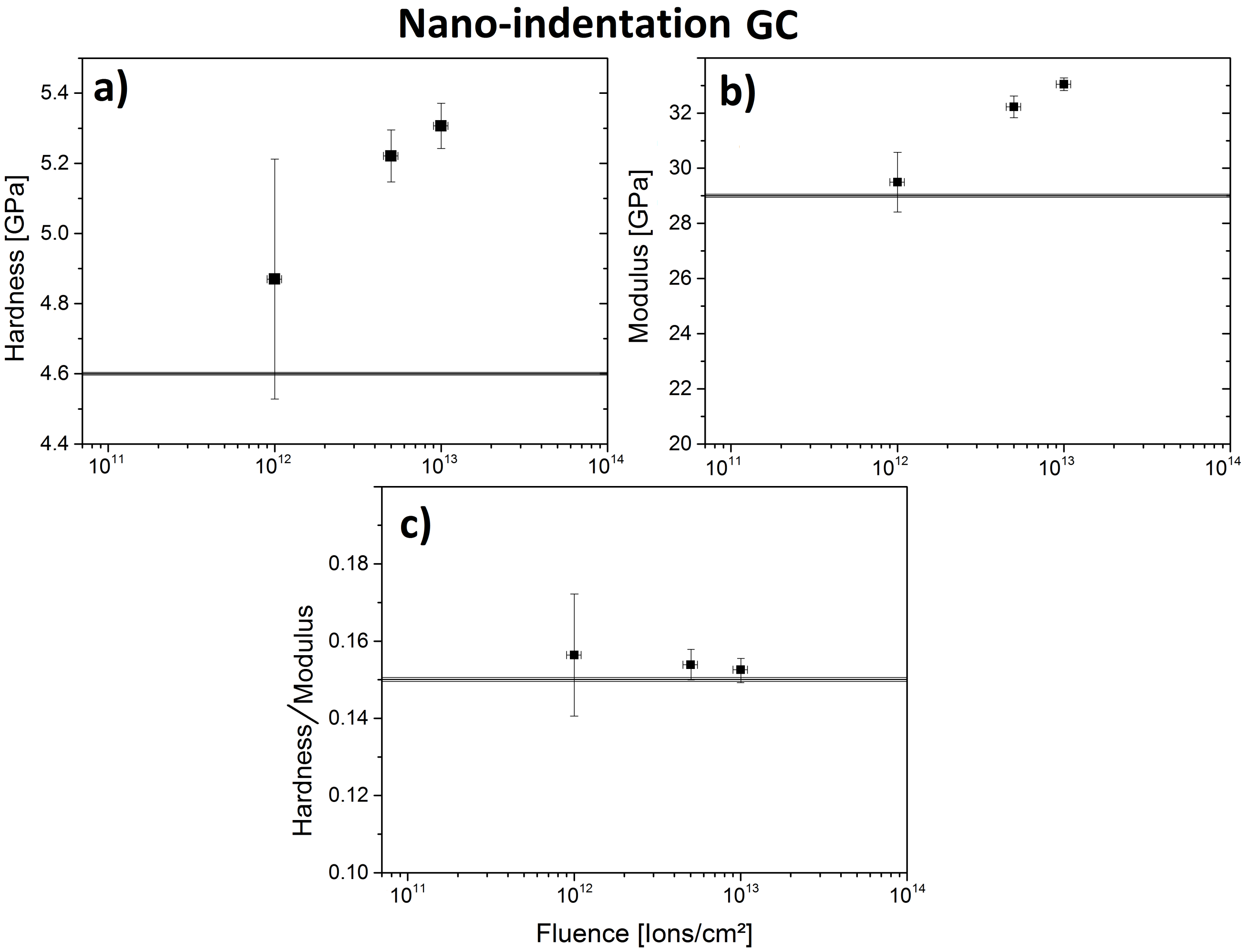

Figure 5.40: Nano-indentation results of glassy carbon (GC) irradiated with 4.8 MeV/u ^{197}Au at 1-3×10^9 ions/cm^2*s (frequency 45 Hz; pulse length 2 ms); Results are presented as a function of fluence; Solid lines represent the non-irradiated sample; Uncertainties include fit and statistical errors; a) Hardness; b) Young's modulus; c) Hardness/Young's modulus.

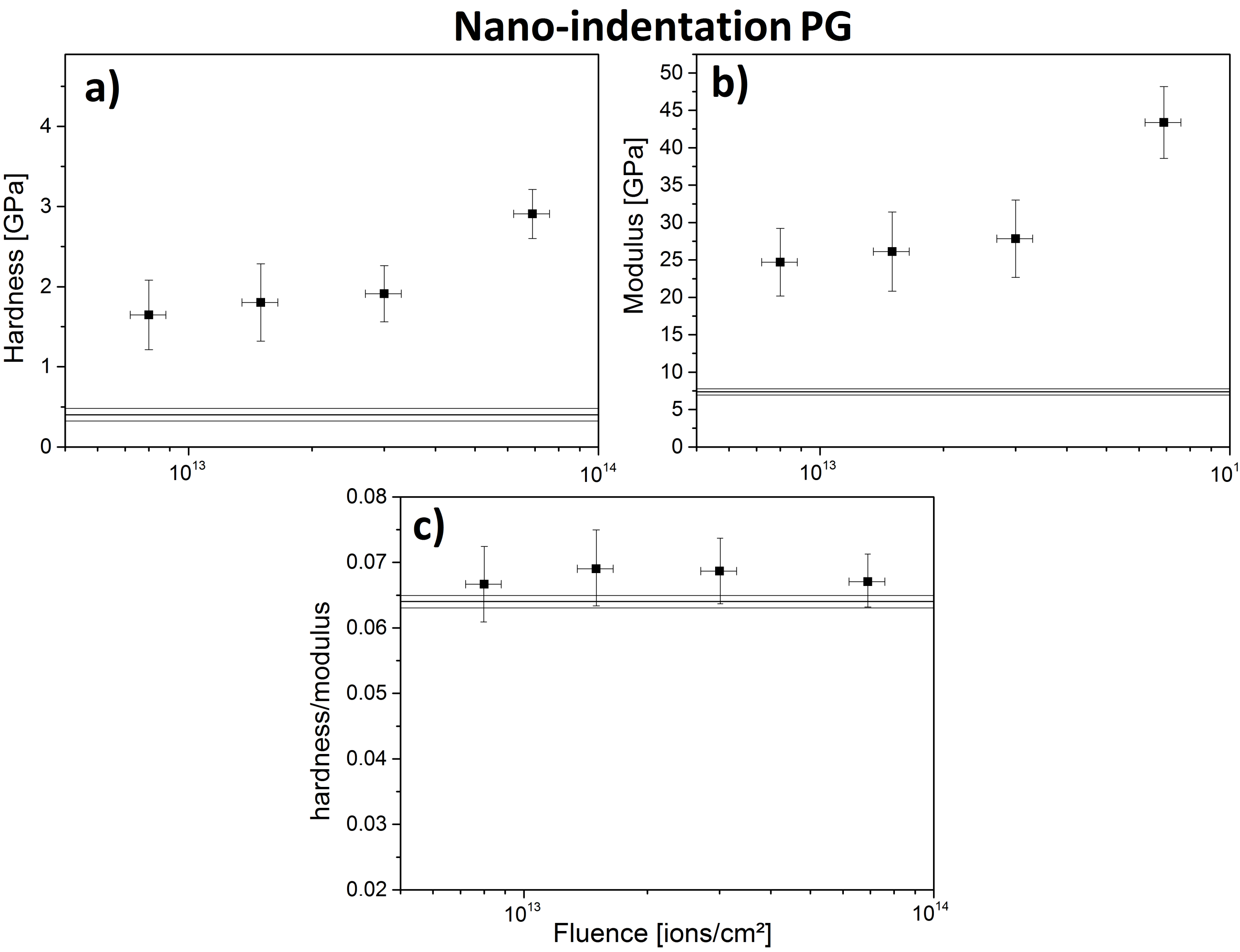

Figure 5.41: Nano-indentation results of polycrystalline graphite (PG) irradiated with 4.8 MeV/u ^{197}Au at 1-3×10^9 ions/cm^2*s (frequency 45 Hz; pulse length 2 ms); Results are presented as a function of fluence; Solid lines represent the non-irradiated sample; Uncertainties include fit and statistical errors; a) Hardness; b) Young's modulus; c) Hardness/Young's modulus.

flux and beam parameters. The obtained results agree with the general idea of a radiation hardening and suggest an embrittlement with increasing ion irradiation.
As mentioned above, one can interpret the results qualitatively with respect to defect concentration in the sample. More defects will increase the stiffness of the layer system, explaining the higher hardness value for larger fluences. Another contribution to the hardening is the reduced crystallite size following ion irradiation. Above the critical fluence for nano-crystallization there is a phase transition from a layered structure towards a highly disordered 3D structure. Following this transformation the hardness of the specimen drops significantly. Hardness over elastic modulus as a function of the ion fluence can be used to identify phase transitions - such as nano-crystallization - due to the change in the materials response with increasing fluence. At high fluences where track over-lapping becomes dominant (starting at $\sim 2{\times}10^{13}$ ions/cm^2 for ^{197}Au-ions and at $\sim 3{\times}10^{13}$ ions/cm^2 for ^{131}Xe-ions, respectively) a phase transition can be observed that manifests in a different indentation behavior and is a general indicator for nano-crystallization, as the Young's modulus drops with respect to the hardness. As a final method to characterize the defects in the HOPG, pop-ins and the corresponding forces needed to trigger the failure of the layers (and thus the change of deformation mechanism) were statistically analyzed. Figure 5.42 shows the histograms of selected fluences of ^{197}Au irradiated HOPG samples and their respective pop-in behaviors. The forces needed to trigger a pop-in shift towards higher values for samples of high fluences. This supports the assumption that the created defects in the layers increase the stiffness of the system.

Embrittlement due to structural defects following irradiation is a large problem for many materials. Impact tests enable a qualitative analysis of the brittleness. An indicator of fracture due to brittleness is any deviation from the ideal fatigue behavior of a material (e.g. the non-irradiated PG sample in figure 5.43). Deviations are represented as a linear increase or as steps on the fatigue curves in heavy duty cycle impact experiments. Each point in the presented impact data is the average of 10 different impact locations on the sample surface. All impacts used the same parameters (acceleration force, acceleration distance and impact frequency). One can observe that the structure of PG is hardening with increasing fluence as the impact resistance is increasing (figure 5.43a and 5.43b), but fractures occur only in the irradiated samples due to induced brittleness. As already seen in the nano-indentation, the structure of GC (figure 5.43c) is affected insignificantly by ion irradiation as the impact resistance does not change by a large margin with ion irradiation. Molybdenum enhanced graphite (MoC) follows the trend of the graphite matrix (figure 5.43d). We can conclude that graphite exhibits two different deformation mechanisms (elastic and plastic) depending on the strain on the sample. Hardness and Youngs's modulus increase with the ion fluence. This radiation hardening entails an embrittlement of the material that is highly depending on the dE/dx. Above dE/dx of 18 keV/nm a phase transition within the ion tracks becomes evident, increasing with fluence which could be the cause for the irradiation induced embrittlement. In the case of an elastic contact, an increasing

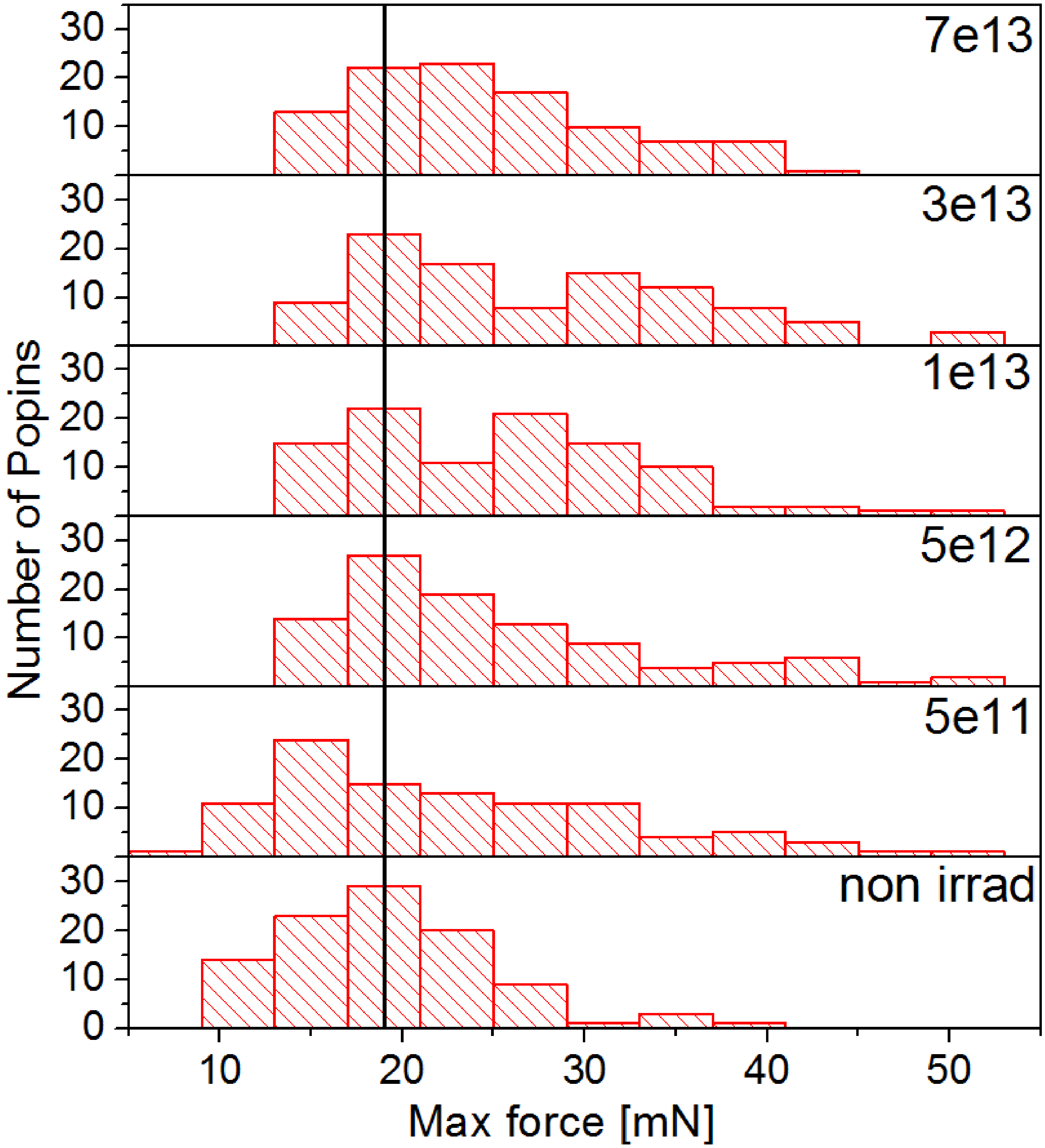

Figure 5.42: Histogram representing frequency of pop-ins as a function of load needed to trigger the pop-in in highly oriented pyrolytic graphite irradiated with 4.8 MeV/u ^{197}Au at 1-3×10^9 ions/cm^2*s (frequency 45 Hz; pulse length 2 ms) to different fluences i.e. defect concentrations; Following the guide for the eye one can observe a shift towards higher necessary forces to create pop-ins with increasing defect concentration.

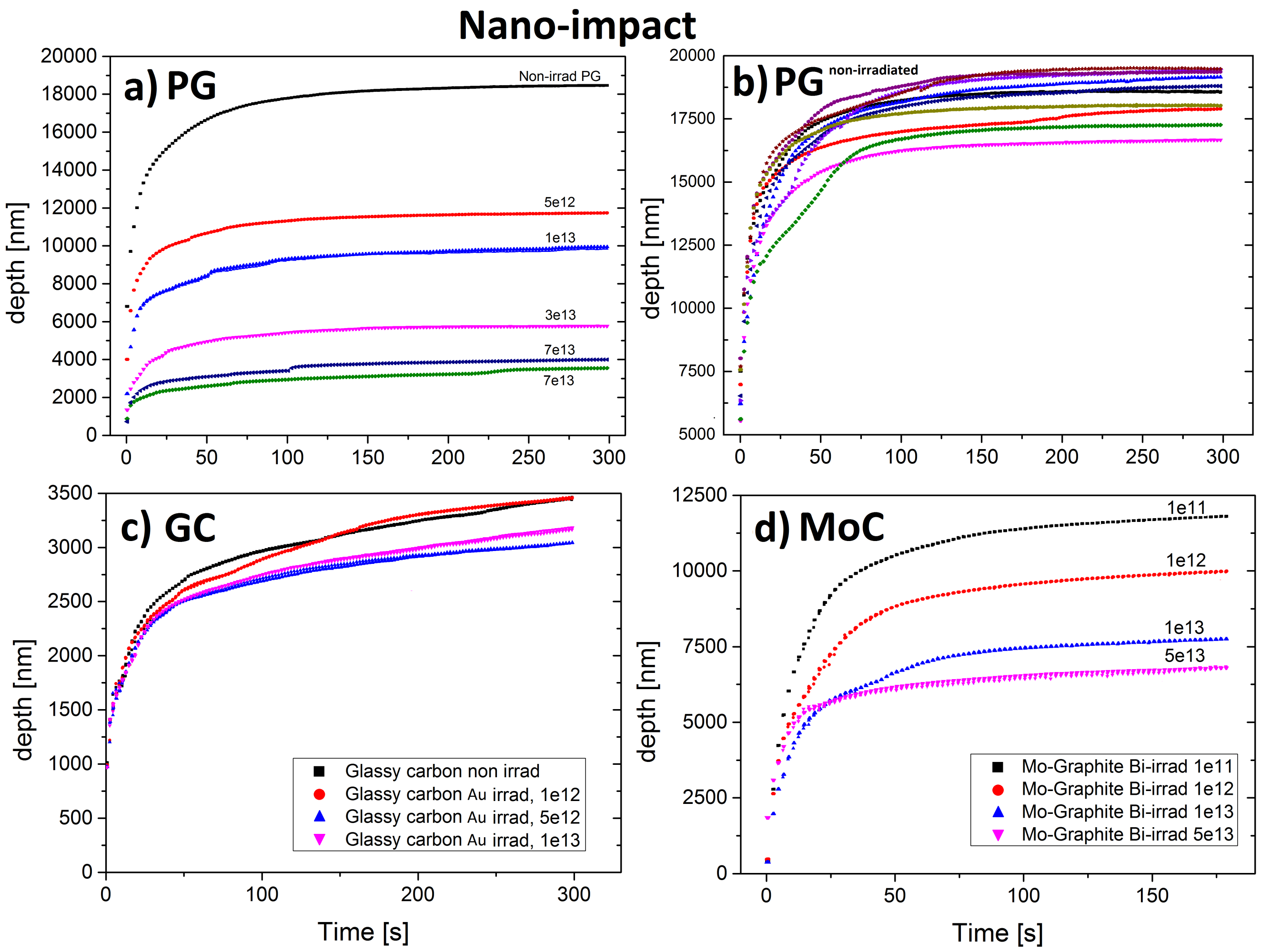

Figure 5.43: Nano-impact measurements on various materials irradiated with 4.8 MeV/u ^{197}Au at 1-3$\times$10^9 ions/cm^{2}s; each point represents the average of 10 impacts; for all presented results the impact parameters are equal (10 μm acceleration distance; frequency 0.5 Hz;); the used diamond indenter tip was as cube corner geometry. results are presented as a function of time; a) Impact depth on PG; b) Impact depth on non-irradiated PG; c) Impact depth on irradiated GC; 4)Impact depth on irradiated MoC.

defect density leads to stiffer layers and thus higher values for the hardness. The radiation damage induced embrittlement could also be shown in nano-impact measurements. Comparing the investigated materials, polycrystalline graphite (PG) was affected most by irradiation induced defects.

5.10 Influence of the beam flux on the defect creation in carbon materials

Figure 5.44 presents the influence of beam parameters on the defect creation. HOPG was used as the model material, irradiated with 4.8 MeV/u ^{197}Au ions at different fluxes. Measurements in the past indicated that the defect creation within the samples is not only depending on the energy loss dE/dx and the total fluence, but also on the flux. The defect creation within the graphene layers depends highly on two different mechanisms. The temperature during the irradiation affects the mobility of the defects increasing recombinations and annealing. Results of on-line temperature monitoring by the means of an IR camera of different materials are presented in figure 5.46. But there seems also to be a second important influence that is related to dynamic recombination. If one compares e.g. a flux of $1{\times}10^9$ and $1{\times}10^{10}$ ions/cm$^2 s$ where the beam structure (energy, pulse length and frequency) are the same, then a flux of $1{\times}10^{10}$ ions/cm$^2 s$ induces 10 times the defects per ion bunch compared to the lower flux of $1{\times}10^9$ ions/cm$^2 s$. This means 10 times more ion impacts and possible defects within the same time interval. It seems that the presence of a larger amount of defects leads to different recombination patterns within and between the layers leaving the material in a more disordered state. HOPG was chosen for the experiments to more easily identify the presence of defects (figure 5.44). When comparing the FWHM of the G-peak (figure 5.44a) which is in general a reference to the crystallinity of the graphite, one can observe that at fluences below $1{\times}10^{13}$ ions/cm^2, a flux of $1{\times}10^{10}$ ions/cm$^2 s$ has the highest damaging properties. This can also be seen in the I_D/I_G (figure 5.44b). At larger fluences beyond the threshold for track overlapping, meaning a 99% chance for a complete coverage of the surface with ion impacts (for Au ions $\geq 2{\times}10^{13}$ ions/cm^2), a lower flux contributes more towards a disordering in the sample. An exception is presented in the highest fluence available at $7{\times}10^{13}$ ions/cm^2 where once again a flux of $1{\times}10^{10}$ ions/cm$^2 s$ created the largest disorderd structure. The average in-plane crystal size L_a, the average defect spacing L_d and the average density of defects n_d (figure 5.44c,d and e) are all related to I_D/I_G and hence closely resemble this trend. It seems that both effects, creation of defects within the same bunch (number of parallel happening ion impacts), and an increased recombination depending on higher temperatures due to higher intensities, have an opposing effect. We can conclude that, with a larger flux, higher temperatures are induced into the sample, but in parallel more ion impacts happen within the same time frame enabling the formation of more complex defect structures. Which effect is larger is not known, but both are depending on the energy loss dE/dx and on the fluence. When comparing the different results, it also appears that both effects alternate in dominance, depending on the number of defects already present in the sample. More experiments are needed to gain a further understanding of this phenomena.

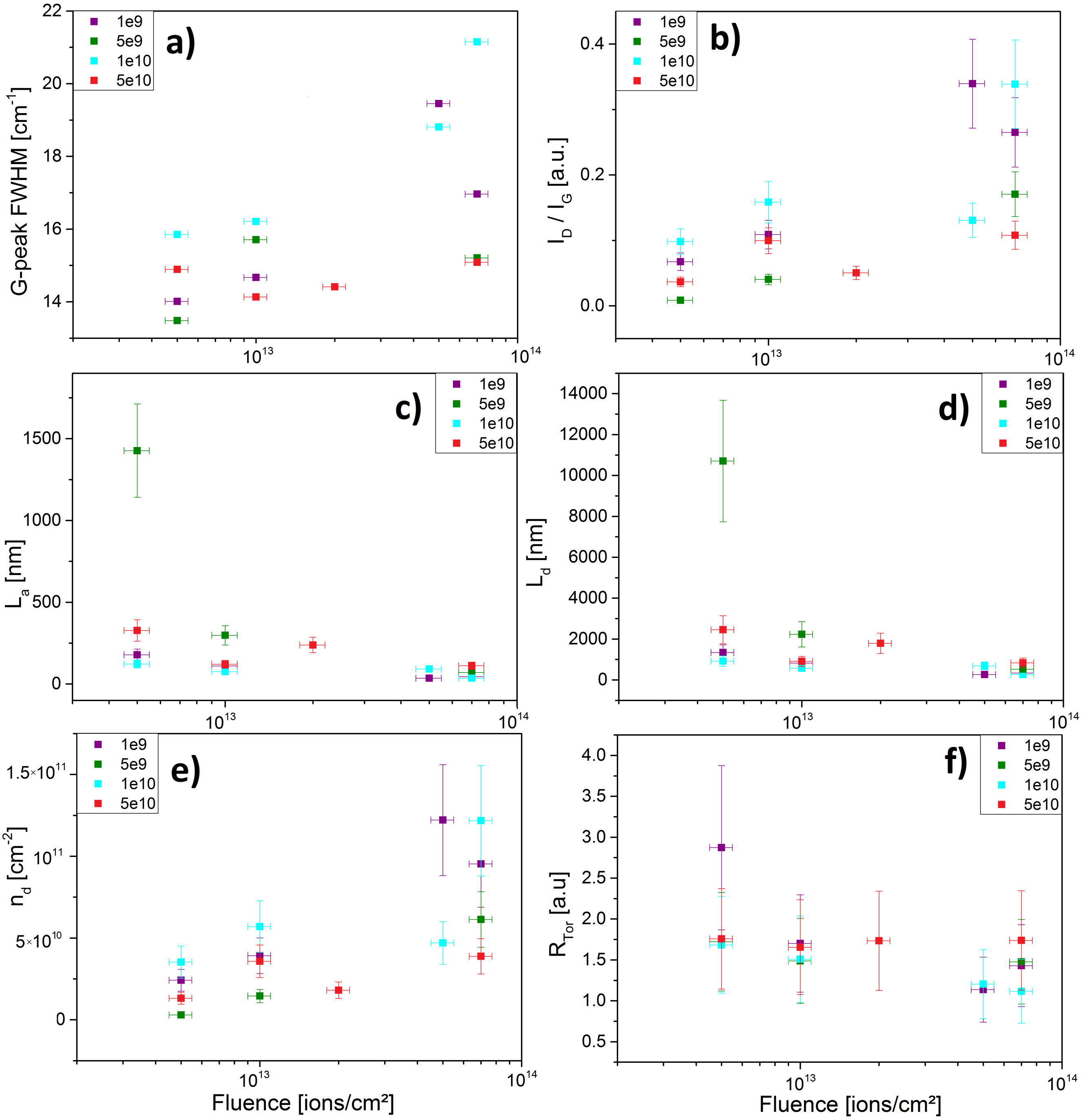

Figure 5.44: Raman spectroscopy results of HOPG irradiated with 4.8 MeV/u ^{197}Au (frequency 45 Hz; pulse length 2-3 ms) at different fluxes; Results are represented as a function of fluence; a) Full width half maximum (FWHM) of the G-peak; b) I_D/I_G; c) Average in-plane crystal size L_a; d) Average defect spacing L_d; e) Average density of defects n_d; f) Tortuosity R_{Tor}; Uncertainties assume an error of 1 pixel on the detector and consider the uncertainty of the equipment; some uncertainties are smaller than the symbols.

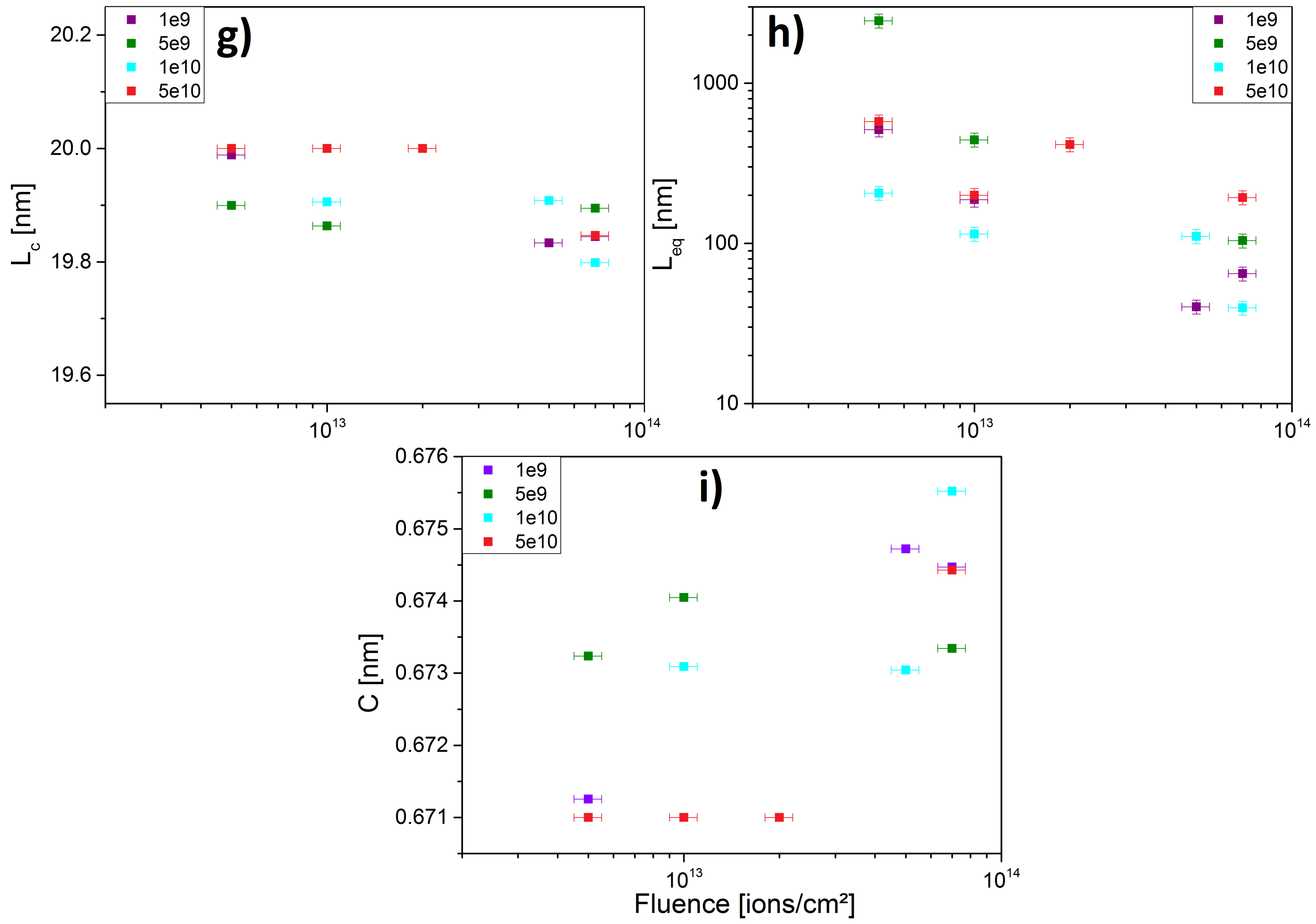

Figure 5.45: Raman spectroscopy results of HOPG irradiated with 4.8 MeV/u ^{197}Au (frequency 45 Hz; pulse length 2-3 ms) at different fluxes; Results are represented as a function of fluence; g) Average crystal size along the c-axis L_c; h) Average graphene sheet length L_{eq}; i) Lattice parameter c; Uncertainties assume an error of 1 pixel on the detector and consider the uncertainty of the equipment; some uncertainties are smaller than the symbols.

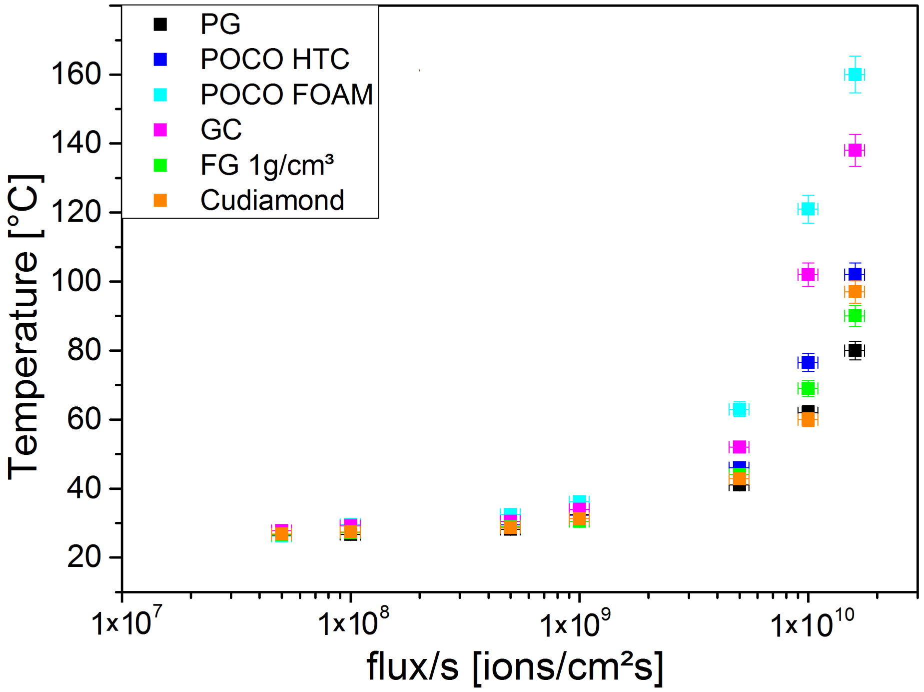

Figure 5.46: Results of a flux test on different carbon based materials; Average sample temperature as a function of flux in ions/cm^2*s of different carbon based materials irradiated by a ^{197}Au beam at 49 Hz with an energy of 4.8 MeV/u and an average pulse length of 2 ms; pristine samples were irradiated for intervals of 5 sec and the corresponding temperature recorded, maximum fluence accumulated during the complete temperature measurements is around 3-5×10^{11} ions/cm^2.

6 Conclusions and Outlook

As a classical candidate in nuclear applications, graphite is now also considered for components in fusion and accelerator applications operating in high-dose radiation fields and under heavy thermo-mechanical solicitations. Favorable characteristics include low-Z and low density composition, low cost, excellent radiation hardness and good thermo-mechanical properties. Despite the intense research on neutron-irradiated graphite, radiation damage due to high-energy heavy ions was not well understood.

Cross section x-ray diffraction scans of along the ion trajectory and thermal diffusivity measurements clearly show that damage creation due to electronic energy-loss is less pronounced and of a different nature than the stopping range of ions dominated by nuclear energy loss.

The presented results clearly show that the irradiation by swift heavy ions leads to considerable disordering within the graphitic structure as demonstrated by Raman spectroscopy, x-ray diffraction and x-ray photo-electron spectroscopy. These structural modifications consist of point defects such as interstitials and vacancies, as well as defect clusters and extended defects including grain boundaries and new disordered phases. In graphene, point defects can aggregate to defect clusters or form new structures that lead to bending of the graphene layers. Defect clusters can also produce stacking faults, dislocations, new planes within the crystal and the formation of sp^3 and dangling bonds.

Following the disordering of graphite as a function of the ion fluence, a reduction of the crystallite size was observed for most graphite materials. The structure of polycrystalline graphite transforms towards glassy carbon at fluences above $\approx 5\times10^{13}$ ions/cm^2 as indicated by Raman spectroscopy, whereas the structure of glassy carbon is only marginally affected at these high fluences. In contrast, HOPG is showing disordering at fluences as low as 5×10^{11} ions/cm^2. In all investigated materials the D3 and D4-Raman band increases with accumulated fluence indicating a transition towards soot-like carbons [68].

As a result of disordering, the irradiated material increases its volume, which is generally referred to as swelling. Swelling leads to macroscopic compressive stresses within the sample. Particularly the interface to non-irradiated material acts as a stress concentrator. The swelling measured for polycrystalline graphite gives further evidence that graphite transforms towards glassy carbon as the measured volume increase at high fluences ($\geq 5\times10^{13}$ ions/cm^2) correlates with the density difference between the two states.

For applications the thermal diffusivity is an important property as it will change over the component lifetime due to ion-induced radiation damage. Heat transfer within a given material depends on phonons and on conduction electrons. It is impeded by defects, resulting in a reduced thermal diffusivity with increasing defect density. At fluences above $\approx5\times10^{13}$ ions/cm^2 the thermal conductivity in polycrystalline graphite is reduced to ≈20% of the initial value.

Also the measured electrical resistivity increased as a function of applied fluence. At fluences above 5×10^{13} ions/cm^2 the initial resistivity value increased by 50 %. From the evolution of the electrical resistivity with fluence, the damage cross sections of the different ion species were deduced yielding values of $\approx15.2\pm0.2$ nm^2 (at 14.8 keV/nm for 4.8 MeV/u ^{131}Xe) and increasing to $\approx75.4\pm0.8$ nm^2 (at 25.7 keV/nm for 4.8 MeV/u ^{238}U).

Mechanical testing with nano/micro-indentation showed that two different deformation mechanisms exist for graphite depending on the strain. When exceeding the materials strength, the formation of twins may lead to a systematic delamination of the graphene layers as inter layer forces of graphene are very weak due to the lack of covalent bonds. Structural changes within the material also have a great influence on the mechanical properties. Indentation measurements confirmed that both hardness and Young's modulus increase with the ion fluence resulting in radiation-induced embrittlement. Among the investigated materials polycrystalline graphite was affected most. For high fluences ($\geq1\times10^{13}$ ions/cm^2) and large dE/dx (≥20 keV/nm), the increase in hardness and Young's modulus reached values of up to 500% and more, while a typical increase for highly oriented pyrolytic graphite and glassy carbon was below 100%. The radiation-induced embrittlement of graphite was verified by nano-impact measurements that show an earlier failure of the irradiated material in high strain rate fatigue tests. The ratio of hardness to Young's modulus was observed to change with increasing fluence, supporting the general thesis of a phase transformation occuring within the PG for high dose conditions (dE/dx × fluence).

This radiation-induced hardening as a function of dE/dx shows a steep increase for an energy loss above 18 keV/nm indicating a critical energy loss required to trigger the phase transition in graphite. Liu et al. suggested a threshold of 7.3 ±1.5 keV/nm for damage creation in highly oriented pyrolytic graphite and a threshold of around 18 keV/nm for the formation of continuous tracks [5, 119]. Linear fits of the available data points (hardening as a function of dE/dx) above and below 18 keV/nm suggest a critical dE/dx value of ≈5 keV/nm for the creation of defects in graphite. The obtained damage cross sections from the 4-point resistivity measurements presented as a function of dE/dx suggest a critical threshold of ≈11 keV/nm for damage creation.

For Raman spectroscopy, highly oriented pyrolytic graphite and glassy carbon served as model system for a perfect crystal and a disordered structure. Under swift heavy ion exposure glassy carbon remained almost unchanged. This radiation hardness was confirmed by nanoindentation showing only a minor hardening that did not exceed 20% even at fluences $\geq5\times10^{13}$ ions/cm^2. In contrast, radiation damage in highly oriented pyrolytic graphite as observed by Raman spectroscopy, started at fluences as low as 5×10^{11} ions/cm^2. The correlated radiation-induced hardening remained surprisingly low not exceeding 20% at fluences $\geq2\times10^{13}$ ions/cm^2. At fluences $\geq5\times10^{13}$ ions/cm^2, a softening of the material was observed, probably linked to the formation of 3D-structures within the anisotropic layered structure of HOPG. Most pronounced changes of the physical properties were identified for polycrystalline graphite. With increasing fluence the quasi-isotropic material converges to the properties of glassy carbon. As demonstrated by profilometry, even the materials density in the irradiated volume changes towards the density of glassy carbon.

Flexible graphite, a chemically expanded and then laminated HOPG, has a similar damage morphology as HOPG. The degradation of the thermal diffusivity of flexible graphite could not be determined precisely due to an unsuitable geometry of the samples, but results suggest a drastic decrease comparable to polycrystalline graphite.

The reinforcement of graphite by carbon fibers (CFC) is the attempt to increase the thermal conductivity of polycrystalline graphite by the introduction of HOPG like fibers. The mechanical properties of CFC change in a similar manner as the polycrystalline graphite matrix.

Doping graphite by molybdenum-carbide is the latest effort to create a material that has larger strength and thermal conductivity but retains the other beneficial properties of polycrystalline graphite. First results suggest that molybdenum-carbide enhanced graphite composites (MoC) are indeed less prone to embrittlement at high fluences $\geq 5\times10^{13}$ ions/cm^2.

Polycrystalline graphite is expected to provide a cost-efficient alternative for a quasi-isotropic material that exhibits excellent radiation hardness. Possible applications include collimator systems, beam catchers and the production target for the SUPER-FRS experiments at FAIR. Collimator systems are needed at the LHC to increase the quality of the beam and simultaneously protect beam line components by filtering the beam-halo of the primary beam. Beam catchers are required to dump unwanted primary beams or deflected beams.

The observed radiation damage in different carbon materials proves to be a risk for accelerator components. The tendency to become brittle with increasing fluence adds several challenges. Especially during irradiations at FAIR by fast extracted ion beams with a planned pulse length in the order of 60 nano-seconds, beam-induced shock and stress waves pose a threat to radiation-damaged, brittle materials. At the border of the beam spot, swelling of the material introduces stress concentrators. These stress centers present an additional risk to the integrity of components including targets, collimators and beam-stops. At the planned FAIR beam intensities, the heat generated by the ions may increase the temperature of graphite up to ≈950 °C. Due to degraded thermal diffusivity of beam exposed components, much higher temperatures may be reached. First simulations (using ANSYS) predict temperatures of 2000 °C and above which may induce severe problems for surrounding components.

Annealing of radiation damage is classically done by heating. Temperature-induced damage mitigation was observed in graphite starting around 200 °C. As demonstrated by on-line IR thermography, ion beam induced heating occurs at high beam flux ($\geq 5\times10^{9}$ ions/cm^{2}s) and can easily reach local temperatures above 300 °C. High temperatures enable recombination and diffusion of defects. Defect recombination processes are mostly exo-thermal and have to be controlled when defect densities surpass 1×10^{11} defects/cm^2. The restoration of the graphitic structure is obtained above temperatures of 1500 °C as demonstrated by x-ray diffraction and LFA. During the manufacturing process residual quenched-in defects are produced. These defects are annealed by the ion beam in all investigated materials at fluences up to 1×10^{12} ions/cm^2.

In parallel to temperature-induced defect annealing, a dose-rate effect was observed for the damage creation in HOPG. Raman spectroscopy showed that a higher beam flux at a given fluence induces a larger amount of defects. However, the irradiation at high flux increases the target temperature providing defect annealing. More research is needed in order to find ideal beam parameters to increase the lifetime of the accelerator components.

Component failure in the fast extraction operation mode is an important issue in cases where graphite will be used as a production target for secondary beams and for beam catchers. The planned beam conditions cannot be generated with the present accelerator facility. Thus simulations are needed in order to optimize the component design and make accurate lifetime predictions of key components. Important data for the simulations include the evolution of the Young's modulus, hardness and thermal conductivity with increasing ion fluence and temperature.

Graphite is a suitable candidate for large accelerator components like beam catchers and collimator systems. The problem of thermal shocks during irradiation and radiation-induced embrittlement could be solved by an intelligent design of a heating/cooling system in the components. If operated at high temperatures polycrystalline graphite is radiation hard, durable and cost efficient. With fiber or additive enhancements the properties can be further optimized for specific applications.

This work provides an increased understanding of ion-induced defect creation in graphite and other carbon-based materials and the corresponding effect on physical properties. Yet, there are still many challenges to overcome as the development of more extreme beams and conditions is mainly limited by the materials and their physical properties.

Future experiments should include measurements during irradiation to investigate the radiation-induced creep deformation under stress in the material that is still not well understood. An in-situ SEM connected to a nano-indenter could give more insight how defects change the deformation mechanisms of graphite. Another open question for the stress wave propagation is the evolution the dampening coefficient of the material with increasing fluence, which could be studied by nano-indentation single impact measurements. Last but not least there are several new interesting material compositions to be tested that may provide even better figures of merit. One example is copper diamond, designed as a heat sink material for high power electronics it is now considered for collimator systems at the LHC due to a very high thermal conductivity, a favorable impedance and excellent shock resistance.

7 Acknowledgments

In addition I greatly thank the following persons on no particular order:

- My supervisor and mentor Dr. Marilena Tomut for her endless patience and knowledge in the field which she readily shared. Her great support enabled me to finish the project within 3.5 years.
- My doctoral mother and mentor Prof. Dr. Christina Trautmann for helping and supporting me in all kind of situations and problems on the way.
- Dr. Kay Obbe-Voss for support during the planning and execution several in-situ measurements at the UNILAC and the SIS18 and many fruitful discussions.
- Katharina Kupka for support during all the beamtime shifts we shared and the many discussions about carbon.
- Anton Romanenko for support during all beamtimes (DESY-PETRA III, UNILAC-M2, UNILAC-M, SIS18-CaveA) and for many fruitful discussions around various topics in physics.
- Dr. Markus Bender and Dr. Daniel Severin for helping with beamtime at the M-branch and fruitful discussions.
- Dr. Beatrice Schuster "Queen of DESY" and Dr. Bruno Merk "King of DESY" for help during the DESY beamtime.
- Janina Krieg and Liana Movsesian for moral support during research and physical exercise and for fruitful discussions.
- M.Sc. Florian Mantel for consulting and discussions
- All other researchers and students in our department for being the best research group!

And last but not least, I would like to thank my parents, Annemarie and Walter Hubert, for always being there and supporting me during the hard times and my partner Olga Ishchuk for being there when I needed her most.

I would also like to thank and acknowledge the graduate school HGS-HiRe and HIC for FAIR. Only with the help of their financial funding I was able to perform my research on this topic. With their additional traveling fund it was possible for me to attend many workshops, conferences and meetings around the globe. I was able to participate at a variety of soft skill courses

and other seminars which were extremely helpful in regards of communicating with peers and colleagues in other fields of science.

Bibliography

[1] T. Trevethan, C.D. Latham, M.I. Heggie, M.J. Rayson, and P.R. Briddon. Interlayer vacancy diffusion and coalescence in graphite. *Phys Rev B*, 90:343–344, 2014.

[2] J. Liu, M.D. Hou, C. Trautmann, R. Neumann, C. Müller, Z.G. Wang, Q.X. Zhang, Y.M. Sun, Y.F. Jin, H.W. Liu, and H.J. Gao. {STM} and raman spectroscopic study of graphite irradiated by heavy ions. *Nuclear Instruments and Methods in Physics Research Section B: Beam Interactions with Materials and Atoms*, 212(0):303 – 307, 2003. Atomic Collisions in Solids - {ICACS20}.

[3] J. Liu, R. Neumann, C. Trautmann, and C. Mueller. Tracks of swift heavy ions in graphite studied by stm. *GSI Scientific Report*, 2000.

[4] J. Liu, C. Trautmann, C. Müller, and R. Neumann. Graphite irradiated by swift heavy ions under grazing incidence. *Nuclear Instruments and Methods in Physics Research Section B: Beam Interactions with Materials and Atoms*, 193(1–4):259 – 264, 2002.

[5] J. Liu, H.J. Yao, Y.M. Sun, J.L. Duan, M.D. Hou, D. Mo, Z.G. Wang, Y.F. Jin, H. Abe, Z.C. Li, and N. Sekimura. Temperature annealing of tracks induced by ion irradiation of graphite. *Nuclear Instruments and Methods in Physics Research Section B: Beam Interactions with Materials and Atoms*, 245(1):126 – 129, 2006. Swift Heavy Ions in Matter Proceedings of the Sixth International Symposium on Swift Heavy Ions in Matter (SHIM 2005) Sixth International Symposium on Swift Heavy Ions in Matter.

[6] A. Tripathi, S.A. Khan, M. Kumar, V. Baranwal, R. Krishna, and A.C. Pandey. {SHI} induced surface modification studies of {HOPG} using {STM}. *Nuclear Instruments and Methods in Physics Research Section B: Beam Interactions with Materials and Atoms*, 244(1):225 – 229, 2006. Synthesis and Modifications of Nano-Structured Materials by Energetic Ion Beams Proceedings of the Indo German Workshop on Synthesis and Modifications of Nano-Structured Materials by Energetic Ion Beams Indo German Workshop on Synthesis and Modifications of Nano-Structured Materials by Energetic Ion Beams.

[7] A.C. Ferrari. Raman spectroscopy of graphene and graphite: Disorder, electron–phonon coupling, doping and nonadiabatic effects. *Solid State Communications*, 143(1–2):47 – 57, 2007. Exploring graphene Recent research advances.

[8] A.C. Ferrari and J. Robertson. Interpretation of raman spectra of disordered and amorphous carbon. *Phys. Rev. B*, 61:14095–14107, May 2000.

[9] A. Jorio and C. Luiz Gustavo. Perspectives on raman spectroscopy of graphene-based systems: from the perfect two-dimensional surface to charcoal. *Phys. Chem. Chem. Phys.*, 14:15246–15256, 2012.

[10] L.G. Cancado. *Raman spectroscopy of nanographites*. PhD thesis, Universidade Federal de Minas Gerais, 2006.

[11] W.C. Oliver and G.M. Pharr. An improved technique for determining hardness and elastic modulus using load and displacement sensing indentation experiments. *Journal of Materials Research*, 7:1564–1583, 1992.

[12] W.C. Oliver and G.M. Pharr. Measurement of hardness and elastic modulus by instrumented indentation: Advances in understanding and refinements to methodology. *Journal of Materials Research*, 19:3–20, 2004.

[13] N. Itoh, K. Tanimura, and Y. Nakai. Radiation damage in nonmetallic solids under dense electronic excitation. *Nuclear Instruments and Methods in Physics Research Section B: Beam Interactions with Materials and Atoms*, 65(1–4):21 – 25, 1992.

[14] R.L. Fleischer, P.B. Price, and R.M. Walker. *Nuclear Tracks in Solids*. University of California Press., 1957.

[15] P. Sigmund. *Stopping of Heavy Ions: A Theoretical Approach*. Springer Verlag, 2004.

[16] J.F. Ziegler, M.D. Ziegler, and J.P. Biersack. {SRIM} – the stopping and range of ions in matter (2010). *Nuclear Instruments and Methods in Physics Research Section B: Beam Interactions with Materials and Atoms*, 268(11–12):1818 – 1823, 2010.

[17] R. Spohr. *Ion Tracks and Microtechnology*. Vieweg Verlag, 1990.

[18] F. Bloch. Zur bremsung rasch bewegter teilchen beim durchgang durch materie. *Ann. Phsik*, 16:285–320, 1933.

[19] J.D. Jackson. *Klassische Elektrodynamik*. Walter de Gruyter Verlag Berlin, 1983.

[20] B. Gervais and S. Bouffard. Simulation of the primary stage of the interaction of swift heavy ions with condensed matter. *Nuclear Instruments and Methods in Physics Research Section B: Beam Interactions with Materials and Atoms*, 88(4):355 – 364, 1994.

[21] J. Liu, R. Neumann, C. Trautmann, and C. Müller. Tracks of swift heavy ions in graphite studied by scanning tunneling microscopy. *Phys. Rev. B*, 64:184115, 2001.

[22] E. M. Bringa and R.E. Johnson. Coulomb explosion and thermal spike. *PACS numbers:61.80.Az.79.20.-m.34.50.Fa.79.20.Ap*, pages 1–4, 2008.

[23] E.M. Bringa and R.E. Johnson. Coulomb explosion and thermal spikes. *Phys. Rev. Lett.*, 88:165501, Apr 2002.

[24] R.L. Fleischer, P.B. Price, and R.M. Walker. Ion explosion spike mechanism for formation of charged-particle tracks in solids. *J. Appl. Phys*, 36(11):3645 – 3652, 1965.

[25] B. Schuster. *Oxide ceramics under extreme pressure and radiation conditions*. PhD thesis, Technische Universität Darmstadt, 2011.

[26] F. Dessauer. Über einige wirkungen von strahlen. i. *Zeitschrift für Physik*, 12(1):38–47, 1923.

[27] G.H. Vineyard. Thermal spikes and activated processes. *Radiation Effects*, 29(4):245–248, 1976.

[28] M. Toulemonde, C. Dufour, and E. Paumier. Transient thermal process after a high-energy heavy-ion irradiation of amorphous metals and semiconductors. *Phys. Rev. B*, 46:14362–14369, Dec 1992.

[29] M. Toulemonde, E. Paumier, and C. Dufour. Thermal spike model in the electronic stopping power regime. *Radiation Effects and Defects in Solids*, 126(1-4):201–206, 1993.

[30] M. Toulemonde, C. Dufour, A. Meftah, and E. Paumier. Transient thermal processes in heavy ion irradiation of crystalline inorganic insulators. *Nuclear Instruments and Methods in Physics Research Section B: Beam Interactions with Materials and Atoms*, 166–167(0):903 – 912, 2000.

[31] M. Lang, R. Devanathan, M. Toulemonde, and C. Trautmann. Advances in understanding of swift heavy-ion tracks in complex ceramics. *Current Opinion in Solid State and Materials Science*, 19(1):39 – 48, 2015. Ion Beam Modification of Materials.

[32] S.L. Daraszewicz and D.M. Duffy. Extending the inelastic thermal spike model for semiconductors and insulators. *Nuclear Instruments and Methods in Physics Research Section B: Beam Interactions with Materials and Atoms*, 269(14):1646 – 1649, 2011.

[33] Mineral-database; Retrieved March 13, 2015 from http://www.mindat.org/min-1282.html/ .

[34] Wikipedia page for graphene; Retrieved March 13, 2015 from http://upload.wikimedia.org/wikipedia/commons/9/9e/Graphen.jpg ; This picture is licensed under a Creative Commons Attribution 3.0; http://creativecommons.org/licenses/by-sa/3.0/.

[35] W. A. Harrison. *Electronic structure and the properties of solids: the physics of the chemical bond*. Dover Publications, 1989.

[36] C.E. Mortimer. *Chemie*. Georg Thieme Verlag, Stuttgart 2007.

[37] A. A. El-Barbary. *First principles characterisation of defects in irradiated graphitic materials*. PhD thesis, University of Sussex, 2005.

[38] J. C. Charlier, T. W. Ebbesen, and P. Lambin. Structural and electronic properties of pentagon–heptagon pair defects in carbon nanotubes. *Phys. Rev. B*, 53:11108–11113, 1996.

[39] Website of Advanced integrated Scanning Tools for Nano Technology; Retrieved February 28, 2015 from http://nanoprobes.aist-nt.com/apps/HOPG%20info.htm/ .

[40] Y. Amir. Graphene: Tri and tri again. *Nat Phys PY*, 7:925–926, 2011/2012.

[41] A.H. Castro Neto, F. Guinea, N.M.R. Peres, K.S. Novoselov, and A.K. Geim. The electronic properties of graphene. *Rev. Mod. Phys.*, 81:109–162, Jan 2009.

[42] Website of AIST-NT, retrieved November 10th 2015 from http://nanoprobes.aist-nt.com/apps/HOPG%20info.htm.

[43] HOPG-database; Retrieved March 14, 2015 from
http://www.2spi.com/catalog/new/hopgsub.php .

[44] A. W. Moore. *Chemistry and Physics of Carbon*, volume 11. Edited by J. Philip and L. Walker and P. A. Thrower published by Marcel Dekker, New York, 1973.

[45] X. Lu, H. Huang, N. Nemchuk, and R.S. Ruoff. Patterning of highly oriented pyrolytic graphite by oxygen plasma etching. *Applied Physics Letters*, 75(2):193–195, July 1999.

[46] P.J.F. Harris. Fullerene-related structure of commercial glassy carbons. *Philosophical Magazine*, 84(29):3159–3167, 2004.

[47] Website of HTW; Retrieved March 15, 2015 from http://www.htw-germany.com/technology.php5?lang=en&nav0=2&nav1=15.

[48] J.B. Gibson, A.N. Goland, M. Milgram, and G.H. Vineyard. Dynamics of radiation damage. *Phys. Rev.*, 120:1229–1253, Nov 1960.

[49] A.A. El-Barbary, R.H. Telling, M.I. Heggie, and C.P. Ewels. Wigner defects bridge the graphite gap. *Nat Matter*, 2:333–337, May 2003.

[50] J. Guo, J. Lee, C.I. Contescu, N.C. Gallego, S.T. Pantelides, S.J. Pennycook, B.A. Moyer, and M.F. Chisholm. Crown ethers in graphene. *Nat Commun*, 5(5389), November 2014.

[51] C.D. Latham, M.I. Heggie, M.Alatalo, S. Oberg, and P.R. Briddon. The contribution made by lattice vacancies to the Wigner effect in radiation-damaged graphite. *J Phys-Condens Mat*, 25(13):1–13, 2013.

[52] Website of Dr. Chris Ewels; retrieved September 27th 2015 from http://www.ewels.info/img/science/graphite/.

[53] L. Li, S. Reich, and J. Robertson. Defect energies of graphite: Density-functional calculations. *Phys. Rev. B*, 72:184109, Nov 2005.

[54] S. Amelinckx and P. Delavignette. Dislocation loops due to quenched-in point defects in graphite. *Phys. Rev. Lett.*, 5:50–51, Jul 1960.

[55] Website of Philip Small, www.Landprofile.com by Land Profile Inc; Retrieved January 30, 2015 from https://de.wikipedia.org/wiki/Debye-Scherrer-Verfahren; This picture is licensed under a Creative Commons Attribution 3.0 United States License; http://creativecommons.org/licenses/by/3.0/us/.

[56] J.-P. Deng, W.-H. Chen, S.-P. Chiu, C.-H. Lin, and B.-C. Wang. Edge-termination and core-modification effects of hexagonal nanosheet graphene. *Molecules*, 19:2361–2373, Feb 2014.

[57] A. Dunlop, G. Jaskierowicz, P. M. Ossi, and S. Della-Negra. Transformation of graphite into nanodiamond following extreme electronic excitations. *Phys. Rev. B*, 76:155403, Oct 2007.

[58] GSI Resource - Webpage; Retrieved June 11th 2015 from https://www.gsi.de/en/research/accelerator_facility.htm.

[59] GSI Resource - Webpage; Retrieved June 11th 2015 from https://www.gsi.de/en/work/fairgsi/linac_and_operations/linac/unilac.htm.

[60] GSI Resource - Webpage; Retrieved June 11th 2015 from http://www-bd.gsi.de/dokuwiki/lib/exe/fetch.php?media=projects:bif-monitor:unilac_bif_new_3.png.

[61] O. Baake et al. An apparatus for in situ spectroscopy of radiation damage of polymers by bombardment with high-energy heavy ions. *Rev. Sci. Instrum.*, 82, 2011.

[62] C. Kittel. *Introduction to Solid State Physics*. John Wiley & Sons; 8th edition, 2005.

[63] G. Gouadec and P. Colomban. Raman Spectroscopy of Nanomaterials: How Spectra Relate to Disorder, Particle Size and Mechanical Properties. *Progress in Crystal Growth and Characterization of Materials*, 53(1):1–56, 2007.

[64] J. Dubessy, M.-C. Caumon, and F. Rull. *Raman Spectroscopy Applied to Earth Sciences and Cultural Heritage, Volume 12*. European Mineralogical Union, Mineralogical Society of Great Britain&Ireland, 2012.

[65] I.H. Boyaci et al. Dispersive and ft-raman spectroscopic methods in food analysis. *RSC Adv.*, 5:56606–56624, 2015.

[66] C. Thomsen and S. Reich. Double resonant raman scattering in graphite. *PHYSICAL REVIEW LETTERS*, 85(24):5214–5217, Dezember 2000.

[67] N. Larouche and B.L. Stansfield. Classifying nanostructured carbons using graphitic indices derived from raman spectra. *Carbon*, 48(3):620 – 629, 2010.

[68] A. Sadezky, H. Muckenhuber, H. Grothe, R. Niessner, and U. Pöschl. Raman microspectroscopy of soot and related carbonaceous materials: Spectral analysis and structural information. *Carbon*, 43(8):1731 – 1742, 2005.

[69] L.G. Cançado, K. Takai, T. Enoki, M. Endo, Y.A. Kim, H. Mizusaki, A. Jorio, L.N. Coelho, R. Magalhães-Paniago, and M.A. Pimenta. General equation for the determination of the crystallite size la of nanographite by raman spectroscopy. *Applied Physics Letters*, 88(16):–, 2006.

[70] L. G. Cançado et al. Quantifying defects in graphene via raman spectroscopy at different excitation energies. *Nano Letters*, 11:3190, 2011.

[71] L.G. Cançado, K. Takai, T. Enoki, M. Endo, Y.A. Kim, H. Mizusaki, N.L. Speziali, A. Jorio, and M.A. Pimenta. Measuring the degree of stacking order in graphite by raman spectroscopy. *Carbon*, 46(2):272 – 275, 2008.

[72] Website of fityk; retrieved September 22th 2015 from http://fityk.nieto.pl/.

[73] H. Kuzmany. *Solid-State Spectroscopy - 2nd edition*. Springer-Verlag, 2009.

[74] N.H. Frank. The stability of electron orbits in the synchrotron. *Physical Review*, 70(2-3):177 – 183, 1946.

[75] J. Schwinger. On the classical radiation of accelerated electrons. *Phys. Rev.*, 75:1912–1925, Jun 1949.

[76] G. Will. *Powder Diffraction*. Springer-Verlag, 2006.

[77] L. Spieß, G. Teichert, R. Schwarzer, H. Behnken, and C. Genzel. *Moderne Röntgenbeugung*. Springer-Verlag, 2009.

[78] Website of Wikipedia; Retrieved January 30, 2015 from https://de.wikipedia.org/wiki/Debye-Scherrer-Verfahren; This picture is licensed under a Creative Commons Attribution 3.0; http://creativecommons.org/licenses/by-sa/3.0/.

[79] Website of the DESY; Retrieved July, 2015 from http://photon-science.desy.de/facilities/petra_iii/beamlines/p02_hard_x_ray_diffraction_beamline/unified_data_sheet/index_eng.html.

[80] A.P. Hammersley. Fit2d: An introduction and overview. *ESRF Internal Report*, page ESRF97HA02T, 1997.

[81] S. Hunklinger. *Festkörperphysik*. Oldenbourg; 2. Auflage, 2009.

[82] D.W. Lee and W.D. Kingery. Radiation energy transfer and thermal conductivity of ceramic oxides. *Journal of The American Ceramic Society*, 43(11):594 – 607, 1960.

[83] Website of the Netzsch; Retrieved July, 2015 from https://www.netzsch-thermal-analysis.com/en/products-solutions/thermal-diffusivity-conductivity/lfa-427.html.

[84] Manual of the Laser-Flash-Apparature LFA 427 from Netzsch; Netzsch. Wittelsbacherstr. 42 95100 Selb, Sept. 2010.

[85] W.J. Parker, R.J. Jenkins, C.P. Butler, and G.L. Abbott. Flash method of determining thermal diffusivity, heat capacity, and thermal conductivity. *Journal of Applied Physics*, 32(9):1679 – 1684, 1979(1961).

[86] R.D. Cowan. Pulse method of measuring thermal diffusivity at high temperatures. *Journal of Applied Physics*, 34(4):926 – 927, 1963.

[87] T.Y. Tsui, G.M. Pharr, W.C. Oliver, Y.W. Chung, E.C. Cutiongco, C.S. Bhatia, R.L. White, R.L. Rhoades, and S.M. Gorbatkin. Nanoindentation and nanoscratching of hard coating materials for magnetic disks. In *Symposium B2 – Thin Films: Stresses and Mechanical Properties V*, volume 356 of *MRS Online Proceedings Library*, 1994.

[88] D.L. Joslin and W.C: Oliver. A new method for analyzing data from continuous depth-sensing microindentation tests. *Journal of Materials Research*, 5:123–126, 1990.

[89] E.F. Finkin. Examination of abrasion resistance criteria for some ductile metals. *Journal of Lubrication Technology*, 96:210–214, 1974.

[90] J. Skinner and N. Gane. The deformation and twinning of grpahite crystals under point load. *Pilosophical Magazine*, 28:827–837, 1974.

[91] P. Diss, J. Lamon, L. Carpentier, J.L. Loubet, and Ph. Kapsa. Sharp indentation behavior of carbon/carbon composites and varieties of carbon. *Carbon*, 40(14):2567 – 2579, 2002.

[92] T.S. Gross, N. Timoshchuk, I.I. Tsukrov, R. Piat, and B. Reznik. On the ability of nanoindentation to measure anisotropic elastic constants of pyrolytic carbon. *ZAMM - Journal of Applied Mathematics and Mechanics*, 93(5):301–312, 2013.

[93] I.N. Sneddon. The relation between load and penetration in the axisymmetric boussinesq problem for a punch of arbitrary profile. *International Journal of Engineering Science*, 3:47–57, 1965.

[94] F. RozpÃloch, J. Patyk, and J. Stankowski. Graphenes bonding forces in graphite. *ACTA PHYSICA POLONICA A*, 112(3):557–562, 2007.

[95] W.W. Tyler and A.C. Wilson. Thermal conductivity, electrical resistivity, and thermoelectric power of graphite. *Phys. Rev.*, 89:870–875, 1953.

[96] C.Hubert, K.-O. Voss, C.Trautmann, K.Kupka, M. Bender, D. Severin, and M.Tomut. Swift heavy ion-induced radiation damage in isotropic graphite studied by micro-indentation and in-situ electrical resistivity. *Nuclear Instruments and Methods in Physics Research Section B: Beam Interactions with Materials and Atoms*, 2015.

[97] On the determination of film stress from substrate bending: Stoney‘s formula and its limits by N. Schwarzer and F. Richter; retrieved June 29th 2015 from http://www.qucosa.de/fileadmin/data/qucosa/documents/5126/data/Stoney.pdf.

[98] W. Möller. Modeling of the sp3/sp2 ratio in ion beam and plasma-deposited carbon films. *Applied Physics Letters*, 59(19):2391–2393, 1991.

[99] J.M. Hollas. *Moderne Methoden in der Spektroskopie*. Springer-Verlag GmbH, 1995.

[100] J.W. Suk, S. Murali, J. An, and R.S. Ruoff. Mechanical measurements of ultra-thin amorphous carbon membranes using scanning atomic force microscopy. *Carbon*, 50(6):2220 – 2225, 2012.

[101] B.F.M. Vincent and B. Luc. *Calorimetry and thermal analysis of polymers / ed. by Vincent B. F. Mathot. With contributions by L. Benoist*. Hanser, Frankfurt, 1994.

[102] Website of NETZSCH; Retrieved June 10th 2015 from http://www.netzsch-thermal-analysis.com/en/products-solutions/differential-scanning-calorimetry/dsc-404-f1-pegasus.html#!tabs/technique.

[103] E.P. Wigner. Theoretical physics in the metallurgical laboratoryof chicago. *Journal of Applied physics*, 17:857 – 863, November 1946.

[104] IAEA Technical documents from 2006; Retrieved June 10th 2015 from http://www-pub.iaea.org/MTCD/publications/PDF/te_1521_web.pdf.

[105] C.P. Ewels, R.H. Telling, A.A. El-Barbary, M.I. Heggie, and P.R. Briddon. Metastable frenkel pair defect in graphite: Source of wigner energy? *Phys. Rev. Lett.*, 91:025505, Jul 2003.

[106] L. Arnold. *Windscale 1957 — Anatomy of a Nuclear Accident*. Macmillan, 1992.

[107] Website of PhenonWorld; retrieved July 15th 2015 from http://www.phenom-world.com/microscopes/phenom-xl.

[108] GSI Resource - Webpage Talk of Head of Bio/Mat department Dr. Daniel Severin; Retrieved June 11th 2015 from http://www-carat.gsi.de/CARAT01/CARAT01Talks/Severin.pdf.

[109] S. Dedera. *Visualization of Ion-Induced Tracks in Carbonate Minerals*. PhD thesis, Uni Heidelberg, 2015.

[110] Website of the manufacturer Momentive; Retrieved February 28, 2015 from http://www.momentive.com/Products/Main.aspx?id=22817/ .

[111] K.H.Homann. Fullerenes and soot formation—new pathways to large particles in flames angew chem int ed. *Angew Chem Int Ed*, 37:2434–2451, 1998.

[112] C. Trautmann. *Spuren energiereicher Ionen in Polymeren und metallischen Gläsern*. PhD thesis, Universität Frankfurt, 1994.

[113] C. Trautmann, M. Boccanfuso, A. Benyagoub, S. Klaumünzer, K. Schwartz, and M. Toulemonde. Swelling of insulators induced by swift heavy ions. *Nuclear Instruments and Methods in Physics Research Section B: Beam Interactions with Materials and Atoms*, 191(1–4):144 – 148, 2002.

[114] Website of SGL-Carbon group; Retrieved March 15, 2015 from http://www.sglgroup.com/cms/_common/downloads/products/product-groups/gs/tds/iso/SIGRAFINE_TDS-R6650.02.pdf.

[115] A. Politano and G. Chiarello. Probing the young's modulus and poisson's ratio in graphene/metal interfaces and graphite: a comparative study. *Nano Research*, 8(6):1847–1856, 2015.

[116] J.H.W. Simmons. *Radiation Damage in Graphite: International Series of Monographs in Nuclear Energy*. Elsevier, 2013.

[117] K. Niwase and T. Tanabe. Defect structure and amorphization of graphite irradiated by d^+ and he^+. *Materials Transactions, JIM*, 34(11):1111–1121, 1993.

[118] M. Krause, M. Tomut, S. Amirthapandian, R. Neumann, C. Trautmann, and W. Ensinger. Micro structural changes of graphite irradiated with swift heavy ions. *GSI Scientific Report Materials-11*, 2008.

[119] J. Liu, M.D. Hou, C. Trautmann, R. Neumann, C. Müller, Z.G. Wang, Q.X. Zhang, Y.M. Sun, Y.F. Jin, H.W. Liu, and H.J. Gao. {STM} and raman spectroscopic study of graphite

irradiated by heavy ions. *Nuclear Instruments and Methods in Physics Research Section B: Beam Interactions with Materials and Atoms*, 212(0):303 – 307, 2003. Atomic Collisions in Solids - {ICACS20}.

[120] Website of Hofstra Group, retrieved April 26th 2016 from http://public.hofstragroup.com/4139.pdf.

[121] Website of SGL-Carbon group; Retrieved March 15, 2015 from http://www.sglgroup.com/cms/_common/downloads/products/product-groups/gs/tds/expanded/SIGRAFLEX_TDS-Folie_d.pdf.

[122] Website of HTW; Retrieved March 15, 2015 from http://www.wiyi.com.tw/Download/PDF/Data%20Sheet%20SIGRADUR.pdf.

[123] Website of HTW; Retrieved March 15, 2015 from http://www.htw-germany.com/technology.php5?lang=en&nav0=2&nav1=15.

List of Figures

2.1 Energy loss dE/dx of ^{238}U in carbon with a density of 1.84 g/cm^2 [16]; Representation (top) of the nuclear energy loss(red) and the electronic energy loss (black) as a function of projectile specific energy, with its 3 sub-regimes:1) Lindhard, Scharff, Schott(LSS); 2) Bethe-Bloch; 3) Relativistic; 11

2.2 Presented is the energy loss dE/dx of an ^{238}U ion in graphite with a density of 1.84 g/cm^2; Left: dE/dx as a function of the particle range [16]; Right: dE/dx of 4.8 MeV/u ^{238}U as a function of ion-penetration depth. The black dashed line represents electronic stopping power, the red dashed line indicates the range dominated by nuclear stopping 12

2.3 Ion displacements along the ion track of a fast moving ion inside of a solid target adapted from [17] 14

3.1 Schematic drawing of a graphene sheet adapted from [34] 19

3.2 a) Basal planes stacked as in graphite (ABAB); b) Basal planes stacked as in rombohedral graphite(ABC); adapted from [40] 19

3.3 a) Lattice structure of graphene with unit cell containing two atoms (A and B), the lattice vectors of the unit cell (a_1 and a_2) and the nearest neighbor vectors (δ_1, δ_2 and δ_3); b) $1st$ Brillouin zone of the graphene unit cell. The $K$and the K' point are the locations of the Dirac cones; adapted from [41] 20

3.4 Basic defects in graphite induced by swift heavy ions; Top: mono vacancy and interstitial in graphite [49]. Bottom: Relaxed vacancy clusters (a-d) within a graphene layer (n = 2, 4, 6 and 12 respectively); P indicates 5 atom carbon rings and n indicates the number of missing C-atoms [50]. 23

3.5 Vacancy cluster defects within carbon; Left picture shows a void, the cluster of many vacancies; Right picture shows a dislocation loop. 24

3.6 Top: Pentagon and heptagon within a graphene layer as top and side view [52]; Bottom: (a-d) Formation of a 5-7-7-5 configuration by a Stonewalls transformation; numbers indicate corresponding atom spacing [1, 51, 53]. 25

3.7 Stacking order defects in graphitic structures; Top left: The shift in stacking between two/three graphene layers with in graphite; Top axis represents the basal shift, Bottom axis indicates the energy state [49]. Top right: Formation of new layers and a resulting bending of the existing layers [54]; Bottom picture: Turbostratic stacking and graphite stacking [55]. 26

3.8 Interlayer diffusion of two mono vacancies. Three different vacancy configurations are presented(a-c,d-f,g-i) and the subsequent formation of a 5-8-5 on one layer and recombination to the perfect hexagonal structure on the other layer; The minimum energy paths to make the corresponding transition is shown on the right side [1]. 27

3.9 Illustration of different vacancy configurations and the subsequent deformation of a graphene layer; a) top view and b) side view; From left to right:mono-vacancy, di-vacancy, tri-vacancy, tetra-vacancy, hexa-vacancy [56] 28

4.1 Examples of typical sample geometries; a) and b) different carbon samples glued on a sample holder for irradiation at the M3-heater chamber; c) different carbon samples glued on a sample holder for irradiation at the X0 beamline; d) a slightly cracked PG sample to be mounted for 4-point resistivity measurements; e) LFA samples (PG) mounted for irradiation. 30

4.2 Schematic of the GSI facility including the linear accelerator UNILAC that serves as an injector for the heavy ion synchrotron SIS18 [58] 31

4.3 Schematic of UNILAC (Universal Linear Accelerator) adapted from [60] a) position of the ion sources (Penning and MEVVA; b) RFQ (radio frequency quadrupol) and pre-stripping acceleration, c) gas stripper; d) Alvarez accelerator; e) M-branch experimental hall; f) TK section (transfer channel towards the synchrotron) and additional foil stripper; g) X0-beamline 32

4.4 Schematic drawing of the M3 beamline at UNILAC adapted from Baake et al. [61] 33

4.5 Energy levels of Rayleigh scattering and the two forms of Raman scattering (Stokes and Anti-Stokes) [64]. 35

4.6 Intensities of Rayleigh scattering and the two forms of Raman scattering (Stokes and Anti-Stokes) [64, 65] 36

4.7 Raman spectra of non-irradiated HOPG and isotropic graphite (PG) and their corresponding deconvolution 37

4.8 Deconvoluted Raman spectra of HOPG. a) 2nd order D-peak of HOPG irradiated with 6.5e13 ions/cm^2; b) 2nd order D-peak of non-irradiated HOPG; In the irradiated sample the G'2D-peak in between the G'3DA-peak and the G'3DB-peak can be observed while the non irradiated HOPG only shows the typical G'3DA-peak and the G'3DB-peak; In all of our HOPG samples an additional shoulder at around 2765 cm^{-1} was present. 40
4.9 Schematic of the Debey-Scherrer method and the corresponding signal recorded on an image plate[78] 43
4.10 Typical spectrum for isotropic graphite, recorded at the DESY-PETRA III P02.2 - beam line 44
4.11 Schematic of the experimental setup at DESY - Petra III P02 in Hamburg; a) general setup; b) through-plane setup; c) cross section setup. 45
4.12 Thermal diffusivity of non-irradiated polycrystalline graphite with a density of 1.84 g/cm^3 as a function of temperature. 47
4.13 Photo (left) and scheme (right) of The Laser Flash Analysis 427 equipment from Netzsch [83]. 48
4.14 a)In-plane sample holder geometry for thin samples; b) through-plane method for bulk samples [83] 49
4.15 Typical indentation load vs depth signal on a steel sample performed with a Berkovich indenter head; important parameters which are extracted from the raw data are indicated and are required to calculate the hardness and Young's modulus (see equations 4.26 and 4.27) 52
4.16 Left: Graphite layers pile-up in micro indents using a Berkovich diamond tip on non-irradiated HOPG visualized in an SEM; Right: A zoom into the center of the indentation imprint reveals folded and ruptured graphite layers. 54
4.17 Indenter load as function of depth of HOPG, non irradiated and irradiated with 4.8MeV/u Xe ions of a fluence of 1×10^{13} ions/cm^2. For indentation a sphero-conical diamond indenter head with 60° angle and 3.125 μm tip radius was used. 55
4.18 Young's modulus as a function of fluence of HOPG irradiated with 4.8 MeV/u ^{197}Au at 1-3$\times 10^9$ ions/cm^{2}s (frequency 45 Hz, pulse length 2 ms); The two data sets illustrate a comparison of the classical Oliver and Pharr method [11] and Sneddon's approach [93] to calculate the Young's Modulus for elastic contacts. . . 56
4.19 Setup of the off-line electrical resistivity measurement at the M3 beamline. The 4-electrode connection of the target can be viewed in figure 4.27 58
4.20 Dektak profilometer by Veeco 61
4.21 Typical C_{1s} XPS spectrum for non-irradiated HOPG (left) and isotropic graphite (PG) (right) including the corresponding fits for sp^2, sp^3, and different $C-O$ bonds. 63

4.22 Working principles of a heat flux DSC system for a material undergoing a phase transition [102]. 64

4.23 Left picture: Close up of the on-line Raman setup at the M3 beam-line of the UNILAC showing the mounted confocal head sending the green laser beam through the experimental chamber view port (made from glass) to the irradiated sample. The beam-line M3 is in the background; Right picture: Schematic of the whole setup [109]; Marked are the distance from objective to window (20 cm) and from window to the confocal head (31.5 cm). 68

4.24 Sample holder inside the irradiation chamber at the beam-line. The sample is mounted an a screw for coarse focusing, the micro-manipulator (Physics Instrument PI P-725.4CD) is used for fine focusing. The objective (Olympus SLMPlan N 50x) has a working distance of 18 mm [109]. 69

4.25 IR thermography setup for on-line monitoring of beam induced thermal effects at the M3 beam-line. 70

4.26 Temperature profile of PG during irradiation with low (left: 5 Hz) and high (right: 45 Hz) duty cycles of 4.8 MeV/u ^{197}Au as recorded by the FLIR IR-camera. 71

4.27 Front view of the on-line resistivity measurements setup for 4-probe on-line electrical resistivity measurements. Left: Sample with 4 Cu electrodes mounted on an isolating substrate (PEEK); beam spot and wiring are indicated. Right: Sample on final holder covered by an Al mask with 1 cm^2 aperture to ensure homogeneous irradiation; An alumina (Cr doped Al_2O_3) luminescent target is used to control the shape of the beam. 71

4.28 Scheme of the used electrical circuit for an irradiated front sample where the complete cross section was penetrated by the ions. 73

4.29 Equivalent circuit of an partially irradiated sample where the ion has been stopped within the sample. 74

5.1 a) Surface of non-irradiated HOPG with an arrangement of folded layers; b) Surface of non-irradiated HOPG with a folded layer. 76

5.2 Surface of glassy carbon (GC) irradiated with 7×10^{13} ions/cm^2 4.8 MeV/u ^{238}U (frequency 1 Hz; pulse length 0.5 ms) showing irradiation-induced cracks. 77

5.3 Cross section micrograph of flexible graphite (FG) irradiated with 7×10^{13} ions/cm^2 of 4.8 MeV/u ^{197}Au (frequency 45 Hz; pulse length 2 ms); The upper part of the sample shows the irradiated area, the end of the ion range is indicated by the white line; Left and Right show the same spot of the sample at different magnifications. 78

5.4 a) An onion on 4.8 MeV/u ^{197}Au at 45Hz / 2ms irradiated PG; b) Cross section of 4.8 MeV/u ^{238}U at 1 Hz / 0.5 ms irradiated PG (10^{13} $ions/cm^2$); the ion range is indicated by the white line, the upper part is irradiated. 78

5.5 Surface of polycrystalline graphite (PG) irradiated with 2×10^{14} ions/cm^2 of 4.8 MeV/u ^{197}Au (frequency 45 Hz; pulse length 2 ms); a) Lower half is the irradiated surface, upper half was masked; formation of nano-objects on the irradiated part is visible b) Closeup of the irradiated PG surface; c) A whisker on the surface of the irradiated PG; d) A pore on the irradiated PG. 79

5.6 Representative Raman spectra evolution with accumulating fluence (post irradiation measurements) of HOPG irradiated with 4.8 MeV/u ^{197}Au at 2-3×10^{9} ions/cm^2*s (frequency 45 Hz; pulse length 2 ms). 80

5.7 Fluence dependency of Raman graphitic parameters (post irradiation measurement) of HOPG irradiated with 4.8 MeV/u ions: ^{131}Xe 2-3×10^{9} ions/cm^2*s (frequency 5 Hz; pulse length 1.2 ms), ^{150}Sm at 2-3×10^{9} ions/cm^2*s (frequency 3.4 Hz; pulse length 1.2 ms), ^{197}Au at 2-3×10^{9} ions/cm^2*s (frequency 45 Hz; pulse length 2 ms), ^{209}Bi at 2-5×10^{9} ions/cm^2*s (frequency 3.4 Hz; pulse length 1 ms) and ^{238}U at 1-2×10^{9} ions/cm^2*s (frequency 1 Hz; pulse length 0.5 ms); Results are given as a function of ion fluence; a)Full width half maximum (FWHM) of the G-peak; b) I_D/I_G; c) Average in-plane crystal size L_a; d) Average defect spacing L_d; e) Average density of defects n_d; f) Tortuosity R_{Tor}; Solid lines represent the values of pristine samples where the thin lines represent the error bar; some error bars are smaller than the symbols. 81

5.8 Fluence dependency of Raman graphitic parameters (post irradiation measurement) of HOPG irradiated with 4.8 MeV/u ions: ^{131}Xe 2-3×10^{9} ions/cm^2*s (frequency 5 Hz; pulse length 1.2 ms), ^{150}Sm at 2-3×10^{9} ions/cm^2*s (frequency 3.4 Hz; pulse length 1.2 ms), ^{197}Au at 2-3×10^{9} ions/cm^2*s (frequency 45 Hz; pulse length 2 ms), ^{209}Bi at 2-5×10^{9} ions/cm^2*s (frequency 3.4 Hz; pulse length 1 ms) and ^{238}U at 1-2×10^{9} ions/cm^2*s (frequency 1 Hz; pulse length 0.5 ms); Results are given as a function of ion fluence; g)Average crystal size along the c-axis, L_c; h) Average graphene sheet length (including tortuosity) L_{eq}; i) Lattice parameter c; Solid lines represent the values of pristine samples where the thin lines represent the averaged uncertainties; some uncertainties are smaller than the symbols. 82

5.9 Representative Raman spectra evolution with accumulated fluence (post irradiation measurements) of glassy carbon (GC) irradiated with 4.8 MeV/u ^{197}Au at 2-3×10^{9} ions/cm^2*s (frequency 45 Hz; pulse length 2 ms). 84

5.10 Fluence dependency of Raman graphitic parameters (post irradiation measurement) of GC irradiated with 4.8 MeV/u ions: ^{131}Xe at 2-3×10^9 ions/cm^2*s (frequency 5 Hz; pulse length 1.2 ms), ^{197}Au at 2-3×10^9 ions/cm^2*s (frequency 45 Hz; pulse length 2 ms), ^{209}Bi at 2-5×10^9 ions/cm^2*s (frequency 3.4 Hz; pulse length 1 ms) and ^{238}U at 1-2×10^9 ions/cm^2*s (frequency 1 Hz; pulse length 0.5 ms); Results are given as a function of ion fluence; a)Full width half maximum (FWHM) of the G-peak; b) I_D/I_G; c) Average in-plane crystal size L_a; d) Average defect spacing L_d; e) Average density of defects n_d; f) Tortuosity R_{Tor}; Solid lines represent the values of pristine samples where as the thin lines represents the averaged uncertainties; some uncertainties are smaller than the symbols. 85

5.11 Fluence dependency of Raman graphitic parameters (post irradiation measurement) of GC irradiated with 4.8 MeV/u ions: ^{131}Xe at 2-3×10^9 ions/cm^2*s (frequency 5 Hz; pulse length 1.2 ms), ^{197}Au at 2-3×10^9 ions/cm^2*s (frequency 45 Hz; pulse length 2 ms), ^{209}Bi at 2-5×10^9 ions/cm^2*s (frequency 3.4 Hz; pulse length 1 ms) and ^{238}U at 1-2×10^9 ions/cm^2*s (frequency 1 Hz; Results are given as a function of ion fluence; g) Average crystal size along the c-axis, L_c; h) Average graphene sheet length L_{eq}; i) Lattice parameter c; some uncertainties are smaller than the symbols. 86

5.12 Representative Raman spectra evolution with accumulating fluence (post irradiation measurements) of PG irradiated with 4.8 MeV/u ^{197}Au at 2-3×10^9 ions/cm^2*s (frequency 45 Hz; pulse length 2 ms). 87

5.13 Fluence dependency of Raman graphitic parameters (post irradiation measurement) of PG irradiated with 4.8 MeV/u ions: ^{197}Au at 2-3×10^9 ions/cm^2*s (frequency 45 Hz; pulse length 2 ms), ^{209}Bi at 2-5×10^9 ions/cm^2*s (frequency 3.4 Hz; pulse length 1 ms) and ^{238}U at 1-2×10^9 ions/cm^2*s (frequency 1 Hz; pulse length 0.5 ms); Results are given as a function of ion fluence; a)Full width half maximum (FWHM) of the G-peak; b) I_D/I_G; c) Average in-plane crystal size L_a; d) Average defect spacing L_d; e) Average density of defects n_d; f) Tortuosity R_{Tor}; Solid lines represent the values of pristine samples where the thin lines represents the averaged uncertainties; some uncertainties are smaller than the symbols. 88

5.14 Fluence dependency of Raman graphitic parameters (post irradiation measurement) of PG irradiated with 4.8 MeV/u ions: ^{197}Au at 2-3×10^{9} ions/cm^{2}*s (frequency 45 Hz; pulse length 2 ms), ^{209}Bi at 2-5×10^{9} ions/cm^{2}*s (frequency 3.4 Hz; pulse length 1 ms) and ^{238}U at 1-2×10^{9} ions/cm^{2}*s (frequency 1 Hz; pulse length 0.5 ms); Results are given as a function of ion fluence; g) Average crystal size along the c-axis, L_c; h) Average graphene sheet length L_{eq}; i) Lattice parameter c; Solid lines represent the values of pristine samples where the thin lines represents the averaged uncertainties; some uncertainties are smaller than the symbols. 89

5.15 Representative Raman spectra evolution with accumulating fluence (post irradiation measurements) of FG irradiated with 4.8 MeV/u ^{197}Au at 2-3×10^{9} ions/cm^{2}*s (frequency 45 Hz; pulse length 2 ms). A selection of spectra is presented to show general tendencies how the samples change with irradiation. 90

5.16 Fluence dependency of Raman graphitic parameters (post irradiation measurement) of FG irradiated with 4.8 MeV/u ions: ^{197}Au at 2-3×10^{9} ions/cm^{2}*s (frequency 45 Hz; pulse length 2 ms), ^{209}Bi at 1-3×10^{9} ions/cm^{2}*s (frequency 3.4 Hz; pulse length 1 ms); Results are given as a function of ion fluence; a)Full width half maximum (FWHM) of the G-peak; b) I_D/I_G; c) Average in-plane crystal size L_a; d) Average defect spacing L_d; e) Average density of defects n_d; f) Tortuosity R_{Tor}; Solid lines represent the values of pristine samples where as the thin lines represents the error bar; Uncertainties assume an error of 1 pixel on the detector and consider the uncertainty of the equipment; some uncertainties are smaller than the symbols. 91

5.17 Fluence dependency of Raman graphitic parameters (post irradiation measurement) of FG irradiated with 4.8 MeV/u ions: ^{197}Au at 2-3×10^{9} ions/cm^{2}*s (frequency 45 Hz; pulse length 2 ms), ^{209}Bi at 1-3×10^{9} ions/cm^{2}*s (frequency 3.4 Hz; pulse length 1 ms); Results are given as a function of ion fluence; g) Average crystal size along the c-axis, L_c; h) Average graphene sheet length L_{eq}; i) Lattice parameter c; Solid lines represent the values of pristine samples where as the thin lines represents the error bar; Uncertainties assume an error of 1 pixel on the detector and consider the uncertainty of the equipment; some uncertainties are smaller than the symbols. 92

5.18 Presented are the analyzed online results of HOPG irradiated with 4.8 meV/u ^{150}Sm ions at a flux of 1-3×10^9 ions/cm^2 (1.2 ms; 3.4 Hz); Results are given as a function of ion fluence; a)I_D/I_G; b)Average in-plane crystal size L_a; c)Average defect spacing L_d; d) Average density of defects n_d; Evolution of the Raman spectra with fluence: e) D+G-Peak; f) 2D-Peak; Uncertainties assume an error of 1 pixel on the detector and consider the uncertainty of the equipment; some uncertainties are smaller than the symbols. 95

5.19 Evolution of the Raman spectra with fluence measured in-situ of PG irradiated with 4.8 meV/u ^{150}Sm ions at a flux of 1-3×10^9 ions/cm^2(1.2 ms, 3.4 Hz). 96

5.20 Presented are the analyzed online results of PG irradiated with 4.8 meV/u ^{150}Sm ions at a flux of 1-3×10^9 ions/cm^2(1.2 ms; 3.4 Hz); Results are given as a function of ion fluence; a) I_D/I_G; b) Average in-plane crystal size L_a; c)Average defect spacing L_d; d)Average density of defects n_d; e)Tortuosity R_{Tor}; f)Average graphene layer length L_{eq}; Uncertainties assume an error of 1 pixel on the detector and consider the uncertainty of the equipment; some uncertainties are smaller than the symbols. 97

5.21 A selection of diffractograms of HOPG (a) and PG (b) at different fluences irradiated with 3.6 MeV/u ^{197}Au at 5×10^9 ions/cm^2*s (frequency 45Hz, pulse length 2ms). 98

5.22 XRD analysis of HOPG (a-c) and PG (d-f) irradiated with 3.6 MeV/u ^{197}Au at 5×10^9 ions/cm^2*s (frequency 45Hz, pulse length 2ms); Results are given as a function of ion fluence; a) (002) position; b) d-spacing of [002]; c) FWHM of (002); d) (002) position; e) d-spacing of [002]; f) FWHM of (002); Solid lines represent values for non-irradiated samples; Uncertainties include only the errors of peak fits 99

5.23 a) X-ray diffractograms of polycrystalline graphite (PG) irradiated with 4.8 MeV/u ^{197}Au at 1-2×10^9 ions/cm^2*s (frequency 45Hz; pulse length 3 ms); Results are presented as a function of ion fluence; b) FWHM of 002-peak; c) 002-peak position; d) 002-peak intensity; solid lines represent the values of the non-irradiated sample. 100

5.24 a) Diffractograms along the ion track of PG irradiated with 4.8 MeV/u ^{197}Au at 1-2×10^9 ions/cm^{2}s (frequency 45Hz; pulse length 3 ms); b) Diffractograms along the ion track irradiated of PG irradiated with 5.9 MeV/u ^{238}U at 5-10×10^9 ions/cm^{2}s (frequency 1Hz; pulse length 0.3 ms); 102

5.25 Off-line diffractograms done at DESY: a) Through-plane geometry of PG irradiated with Au 4.8 MeV/u ^{197}Au at 1-2×$10^1$0 ions/cm^2*s (frequency 45Hz; pulse length 3 ms) ions at different temperatures and fluences; b) Stacked presentation of the same data from a) 103

5.26 XPS spectra and analysis results; spectra are represented as a function of binding energy, analysis results are presented as a function of fluence; solid lines represent the value of the non-irradiated sample; a)XPS spectra of PG irradiated with 4.8 MeV/u ^{238}U at 2-3×10^9 ions/cm^{2}s (frequency 1 Hz; pulse length 0.3 ms); b) sp^3 content of PG; c) sp^2/sp^3 ratio of PG; d) XPS spectra of HOPG irradiated with 4.8 MeV/u ^{238}U at 2-3×10^9 ions/cm^{2}s (frequency 1 Hz; pulse length 0.3 ms); e) sp^3 content of HOPG; f) sp^2/sp^3 ratio of HOPG. 105

5.27 a) Data of profilometer scans across polycrystalline graphite samples irradiated with 4.8 MeV/u ^{197}Au at 3-4×10^9 ions/cm^{2}s (frequency 45Hz; pulse length 3 ms) to a fluence of 1×10^{13} ions/cm^2, the dashed line indicates the ideal case; inset: Scheme of the irradiation setup for masked samples; b) Step heights between masked and irradiated part of the sample; c) Absolute heights of the corresponding swelling steps as a function of fluence, the right y axis corresponds to swelling stepheight normalized by the ion range of 45.6 μm. 106

5.28 Data of a profilometer scans across thin poly crystalline graphite (PG) cantilevers irradiated with 4.8 MeV/u ^{197}Au at 3-4×10^9 ions/cm^2*s (frequency 45Hz; pulse length 3 ms); a) Raw data of profilometer scans across the irradiated samples to determine the bending radius; b) Bending radius and the calculated stress as a function of fluence 108

5.29 a) relative change of electrical resistivity $\Delta\rho/\rho_0$ of PG irradiated with 4.8 MeV/u ^{197}Au at 1-3×10^9 ions/cm^2*s (frequency 45 Hz; pulse length 3 ms) as a function of fluence; inset: raw signal during the monitoring showing the start of irradiation; b) $\Delta\rho/\rho_0$ normalized to $\rho_{1\times10^{13}\ ions/cm^2}$ as a function of fluence of PG irradiated with different ion species; c) $\rho(T)/\rho_0$ as a function of temperature [96]; these data were acquired using the setup shown in figure 4.19 111

5.30 a) normalized $\Delta\rho/\rho_0$ of PG irradiated with 4.8 MeV/u ^{197}Au at 1-3×10^9 ions/cm^2*s (frequency 45 Hz; pulse length 3 ms) as a function of fluence Φ and a Poisson-fit to determine the damage cross sections; b) calculated damage cross sections as a function of dE/dx; uncertainties are smaller than the symbols. [96] . 112

5.31 In-plane thermal diffusivity as a function of fluence; Irradiation was done with 4.8 MeV/u ^{197}Au at 1-3×10^9 ions/cm^{2}s (frequency 2 Hz; pulse length 3 ms); Solid lines represent the values of the non-irradiated material and the corresponding uncertainties; a) polycrystalline graphite (PG) with a thickness of 30-50 μm; b) Various grades of flexible graphite (FG) with a thickness of 150-250 μm. 113

5.32 In-plane thermal diffusivity measurements of polycrystalline graphite irradiated by 4.8 MeV/u ^{131}Xe at 4-5×10^9 ions/cm^2*s (frequency 5 Hz; pulse length 1.2 ms). Sample thicknesses range from 30-50μm; Results are given as a function of temperature; a) Change of thermal diffusivity between heating and cooling cycle relative to the value at max. temperature ($\Delta Diff/Diff_{1000°C}$) of PG samples with different accumulated fluences; b) Diffusivity of the heating and cooling cycle of a PG sample irradiated to a fluence of 1×10^{14} ions/cm^2 that was fully penetrated (electronic dE/dx); c) Diffusivity of the heating and cooling cycle of a PG sample irradiated to a fluence of 1×10^{14} ions/cm^2 that stopped the beam half way in the sample (nuclear dE/dx); d) Comparison of the diffusivities of two different measurement cycles of a non-irradiated PG sample showing deterioration of the holder after several heating cycles. 115

5.33 Heat capacity c_p of polycrystalline graphite (PG) irradiated with 4.8 MeV/u ^{197}Au at 1-3×10^9 ions/cm^2*s (frequency 45 Hz; pulse length 3 ms); Heating rate was set to 20 K/min; Results are presented as a function of temperature; a) 3 heating cycles of non-irradiated PG; b) First heating cycle of irradiated PG at various accumulated fluences; The sample with a fluence of 1×10^{13} ions/cm^2 was crushed to a powder to provide sufficient thermal contact to the sample holder 118

5.34 Micro-indentation results of HOPG irradiated by 4.8 MeV/u ^{197}Au at 1-3×10^{10} ions/cm^2*s (frequency 45 Hz; pulse length 3 ms); a)Hardness; b)Young's modulus; c)Hardness/Young's modulus. 119

5.35 Micro-indentation results of polycrystalline graphite (SNG grade 953 and 398) irradiated by 4.8 MeV/u ^{150}Sm at 1-3×10^9 ions/cm^2*s (frequency 3.4 Hz; pulse length 1.2 ms); Solid lines represent the non-irradiated sample and corresponding error bars; Results are given as a function of fluence; a)Hardness; b) Young's modulus; c) Ratio of hardness/Young's modulus. 121

5.36 Micro-indentation results of polycrystalline graphite (R6650 grade) irradiated by 4.8 MeV/u ^{131}Xe at 2-3×10^9 ions/cm^2*s (frequency 5 Hz; pulse length 1.2 ms), 4.8 MeV/u ^{150}Sm at 2-3×10^9 ions/cm^2*s (frequency 3.4 Hz; pulse length 1.2 ms), 4.8 MeV/u ^{197}Au at 2-3×10^9 ions/cm^2*s (frequency 45.4 Hz; pulse length 2 ms) and 4.8 MeV/u ^{238}U at 1-2×10^9 ions/cm^2*s (frequency 1 Hz; pulse length 0.5 ms); Results are presented as a function of fluence; Uncertainties include fit and statistical errors; Solid lines represent values for non-irradiated material; a) Hardness; b)Young's modulus; c) Hardness/Young's modulus ratio; d) Hardening at the highest available fluence(3-7×10^{13} ions/cm^2) in % as a function dE/dx; The red dashed line represents a linear fit with all data points, the black dashed lines represent a fit with dE/dx above and below 18 keV/nm.[96] 122

5.37 Micro-indentation results of carbon fiber composites (CFC) (transversal fiber orientation) irradiated by 4.8 MeV/u ^{197}Au at 1-3×10^9 ions/cm^2*s (frequency 45 Hz; pulse length 2 ms); Results are presented as a function of fluence; Uncertainties include fit and statistical errors; a) Hardness ; b) Young's modulus; c) Hardness/Young's modulus. 123

5.38 Micro-indentation results of molybdenum graphite composites (MoC) irradiated with 4.8 MeV/u ^{197}Au at 1-3×10^9 ions/cm^2*s (frequency 45 Hz; pulse length 2 ms); Results are presented as a function of fluence; Uncertainties include fit and statistical errors; a) Hardness; 2) Young's modulus; 3) Hardness/Young's modulus. 124

5.39 Nano-indentation results of highly oriented pyrolytic graphite (HOPG) irradiated with 4.8 MeV/u ^{197}Au at 1-3×10^9 ions/cm^2*s (frequency 45 Hz; pulse length 2 ms); Results are presented as a function of fluence; Solid lines represent the non-irradiated sample; Uncertainties include fit and statistical errors; a) Hardness; b) Young's modulus (Sneddon and Oliver/Pharr method); c) Hardness/Young's modulus. 125

5.40 Nano-indentation results of glassy carbon (GC) irradiated with 4.8 MeV/u ^{197}Au at 1-3×10^9 ions/cm^2*s (frequency 45 Hz; pulse length 2 ms); Results are presented as a function of fluence; Solid lines represent the non-irradiated sample; Uncertainties include fit and statistical errors; a) Hardness; b) Young's modulus; c) Hardness/Young's modulus. 126

5.41 Nano-indentation results of polycrystalline graphite (PG) irradiated with 4.8 MeV/u ^{197}Au at 1-3×10^9 ions/cm^2*s (frequency 45 Hz; pulse length 2 ms); Results are presented as a function of fluence; Solid lines represent the non-irradiated sample; Uncertainties include fit and statistical errors; a) Hardness; b) Young's modulus; c) Hardness/Young's modulus. 127

5.42 Histogram representing frequency of pop-ins as a function of load needed to trigger the pop-in in highly oriented pyrolytic graphite irradiated with 4.8 MeV/u ^{197}Au at 1-3×10^9 ions/cm^2*s (frequency 45 Hz; pulse length 2 ms) to different fluences i.e. defect concentrations; Following the guide for the eye one can observe a shift towards higher necessary forces to create pop-ins with increasing defect concentration. 129

5.43 Nano-impact measurements on various materials irradiated with 4.8 MeV/u ^{197}Au at 1-3×10^9 ions/cm^{2}s; each point represents the average of 10 impacts; for all presented results the impact parameters are equal (10 μm acceleration distance; frequency 0.5 Hz;); the used diamond indenter tip was as cube corner geometry. results are presented as a function of time; a) Impact depth on PG; b) Impact depth on non-irradiated PG; c) Impact depth on irradiated GC; 4)Impact depth on irradiated MoC. 130

5.44 Raman spectroscopy results of HOPG irradiated with 4.8 MeV/u ^{197}Au (frequency 45 Hz; pulse length 2-3 ms) at different fluxes; Results are represented as a function of fluence; a) Full width half maximum (FWHM) of the G-peak; b) I_D/I_G; c) Average in-plane crystal size L_a; d) Average defect spacing L_d; e) Average density of defects n_d; f) Tortuosity R_{Tor}; Uncertainties assume an error of 1 pixel on the detector and consider the uncertainty of the equipment; some uncertainties are smaller than the symbols. 133

5.45 Raman spectroscopy results of HOPG irradiated with 4.8 MeV/u ^{197}Au (frequency 45 Hz; pulse length 2-3 ms) at different fluxes; Results are represented as a function of fluence; g) Average crystal size along the c-axis L_c; h) Average graphene sheet length L_{eq}; i) Lattice parameter c; Uncertainties assume an error of 1 pixel on the detector and consider the uncertainty of the equipment; some uncertainties are smaller than the symbols. 134

5.46 Results of a flux test on different carbon based materials; Average sample temperature as a function of flux in ions/cm^2*s of different carbon based materials irradiated by a ^{197}Au beam at 49 Hz with an energy of 4.8 MeV/u and an average pulse length of 2 ms; pristine samples were irradiated for intervals of 5 sec and the corresponding temperature recorded, maximum fluence accumulated during the complete temperature measurements is around 3-5×10^{11} ions/cm^2. 135

8.1 Data-sheet for poly crystalline graphite (PG) SIGRAFINE®6650 from the SGL-Carbon group[114] 165

8.2 Data-sheet for Highly oriented pyrolytic graphite (HOPG) from Momentive[120] . 166

8.3 Data-sheet for flexible graphite (FG) SIGRAFLEX®from the SGL-Carbon group[121]167

8.4 Data-sheet for glassy carbon (GC) SIGRADUR®from HTW [122] 168

8.5 TEM pictures of glassy carbon (GC) SIGRADUR®G and SIGRADUR®K from HTW showing the fullerene like curved and bent graphite planes [123] 169

List of Tables

4.1 Overview of the investigated carbon materials with densities and sample dimensions. Note that for some methods (TMA, DSC, LFA, online-resistivity etc.) the dimensions need to be adjusted accordingly; Densities for the MoC compound vary between 2.4 and 2.6 g/cm^3according to the Mo content 31
4.2 Beam parameters of the used ion beams. Energies ranged from 3.6 to 11.4 MeV/u, for more details view the appendix 32

8.1 Overview of the used ions in the irradiation with the corresponding irradiation parameters 170
8.2 Overview of the used ions in the irradiation with the corresponding irradiation parameters 171

8 Appendix

Material data sheets

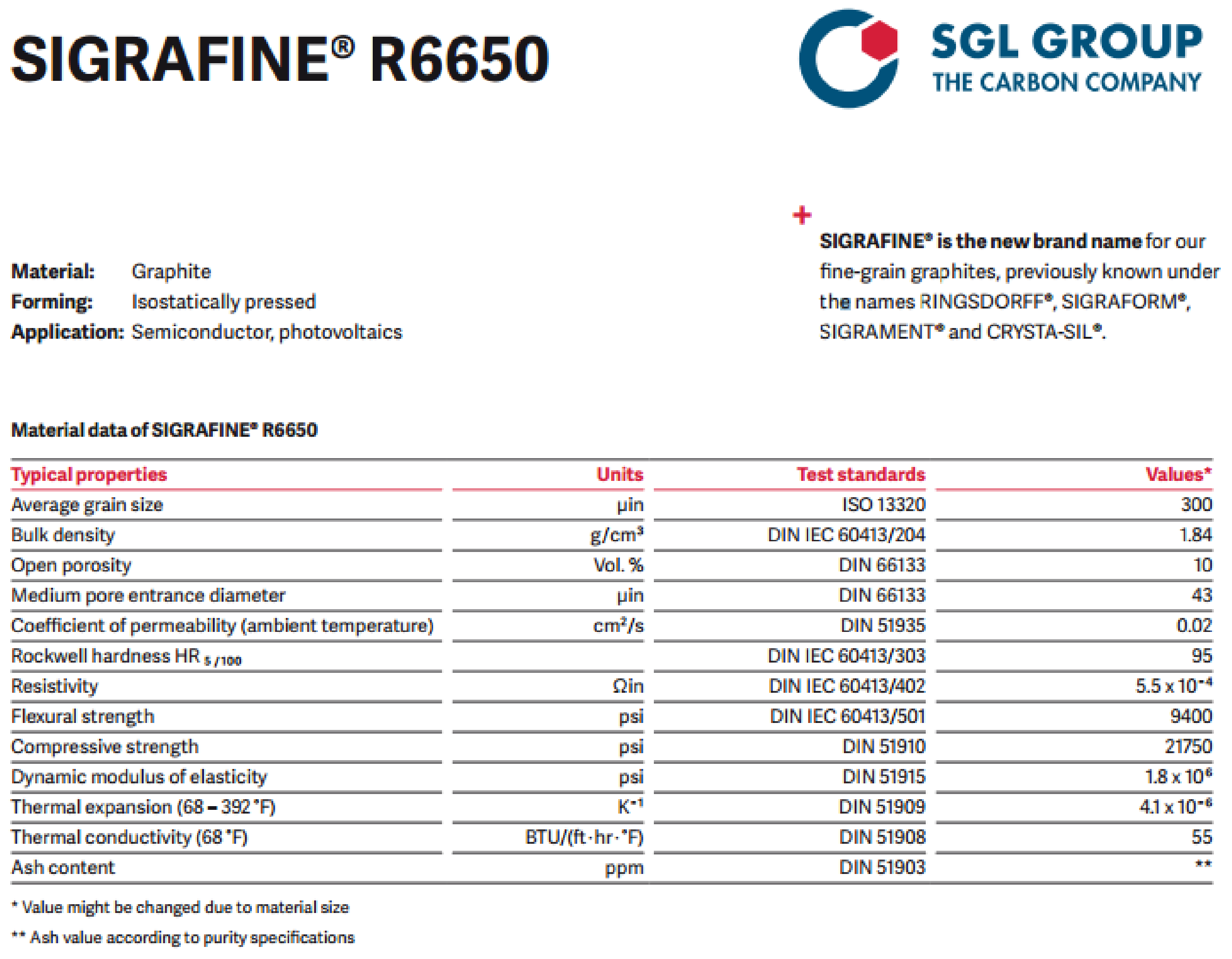

SIGRAFINE® R6650

SGL GROUP
THE CARBON COMPANY

SIGRAFINE® is the new brand name for our fine-grain graphites, previously known under the names RINGSDORFF®, SIGRAFORM®, SIGRAMENT® and CRYSTA-SIL®.

Material: Graphite
Forming: Isostatically pressed
Application: Semiconductor, photovoltaics

Material data of SIGRAFINE® R6650

Typical properties	Units	Test standards	Values*
Average grain size	µin	ISO 13320	300
Bulk density	g/cm³	DIN IEC 60413/204	1.84
Open porosity	Vol. %	DIN 66133	10
Medium pore entrance diameter	µin	DIN 66133	43
Coefficient of permeability (ambient temperature)	cm²/s	DIN 51935	0.02
Rockwell hardness $HR_{5/100}$		DIN IEC 60413/303	95
Resistivity	Ωin	DIN IEC 60413/402	5.5×10^{-4}
Flexural strength	psi	DIN IEC 60413/501	9400
Compressive strength	psi	DIN 51910	21750
Dynamic modulus of elasticity	psi	DIN 51915	1.8×10^{6}
Thermal expansion (68 – 392 °F)	K^{-1}	DIN 51909	4.1×10^{-6}
Thermal conductivity (68 °F)	BTU/(ft·hr·°F)	DIN 51908	55
Ash content	ppm	DIN 51903	**

* Value might be changed due to material size

** Ash value according to purity specifications

Figure 8.1: Data-sheet for poly crystalline graphite (PG) SIGRAFINE®6650 from the SGL-Carbon group[114]

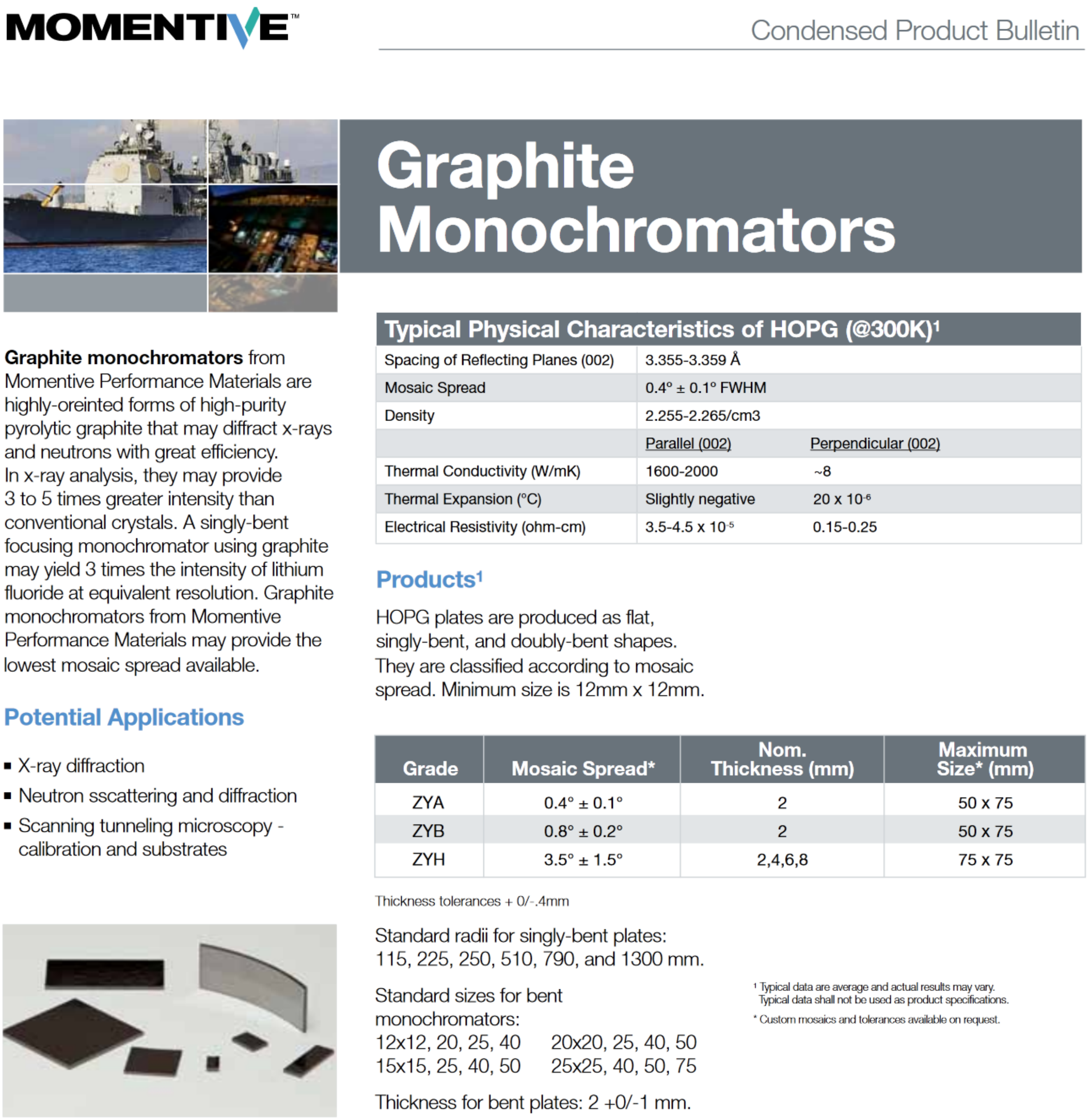

MOMENTIVE™

Condensed Product Bulletin

Graphite Monochromators

Graphite monochromators from Momentive Performance Materials are highly-oreinted forms of high-purity pyrolytic graphite that may diffract x-rays and neutrons with great efficiency. In x-ray analysis, they may provide 3 to 5 times greater intensity than conventional crystals. A singly-bent focusing monochromator using graphite may yield 3 times the intensity of lithium fluoride at equivalent resolution. Graphite monochromators from Momentive Performance Materials may provide the lowest mosaic spread available.

Potential Applications

- X-ray diffraction
- Neutron sscattering and diffraction
- Scanning tunneling microscopy - calibration and substrates

Typical Physical Characteristics of HOPG (@300K)[1]

Spacing of Reflecting Planes (002)	3.355-3.359 Å	
Mosaic Spread	0.4° ± 0.1° FWHM	
Density	2.255-2.265/cm3	
	Parallel (002)	Perpendicular (002)
Thermal Conductivity (W/mK)	1600-2000	~8
Thermal Expansion (°C)	Slightly negative	20 x 10^{-6}
Electrical Resistivity (ohm-cm)	3.5-4.5 x 10^{-5}	0.15-0.25

Products[1]

HOPG plates are produced as flat, singly-bent, and doubly-bent shapes. They are classified according to mosaic spread. Minimum size is 12mm x 12mm.

Grade	Mosaic Spread*	Nom. Thickness (mm)	Maximum Size* (mm)
ZYA	0.4° ± 0.1°	2	50 x 75
ZYB	0.8° ± 0.2°	2	50 x 75
ZYH	3.5° ± 1.5°	2,4,6,8	75 x 75

Thickness tolerances + 0/-.4mm

Standard radii for singly-bent plates:
115, 225, 250, 510, 790, and 1300 mm.

Standard sizes for bent monochromators:

12x12, 20, 25, 40	20x20, 25, 40, 50
15x15, 25, 40, 50	25x25, 40, 50, 75

Thickness for bent plates: 2 +0/-1 mm.

[1] Typical data are average and actual results may vary. Typical data shall not be used as product specifications.

* Custom mosaics and tolerances available on request.

Figure 8.2: Data-sheet for Highly oriented pyrolytic graphite (HOPG) from Momentive[120]

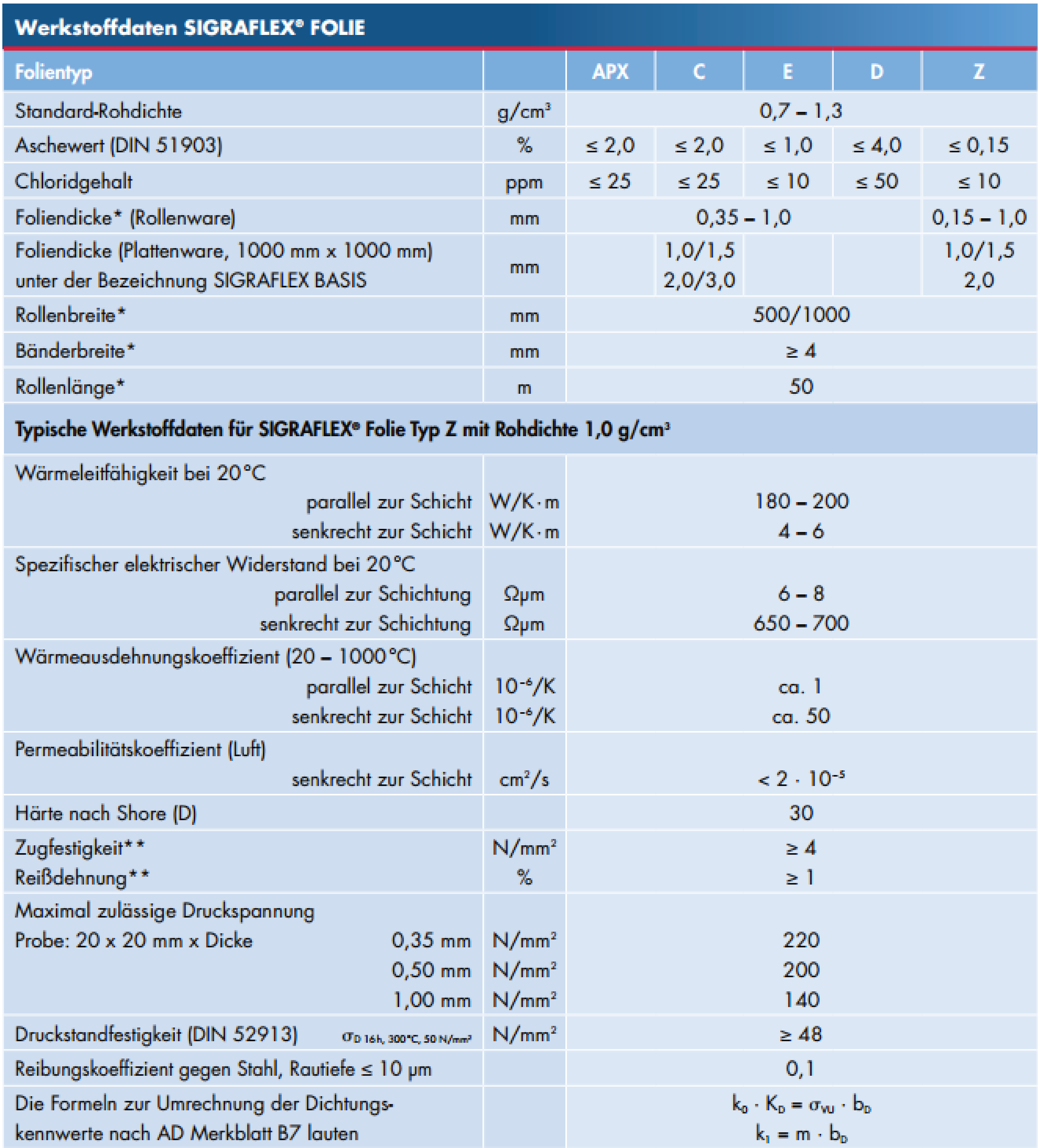

Werkstoffdaten SIGRAFLEX® FOLIE

Folientyp		APX	C	E	D	Z
Standard-Rohdichte	g/cm³	0,7 – 1,3				
Aschewert (DIN 51903)	%	≤ 2,0	≤ 2,0	≤ 1,0	≤ 4,0	≤ 0,15
Chloridgehalt	ppm	≤ 25	≤ 25	≤ 10	≤ 50	≤ 10
Foliendicke* (Rollenware)	mm	0,35 – 1,0				0,15 – 1,0
Foliendicke (Plattenware, 1000 mm x 1000 mm) unter der Bezeichnung SIGRAFLEX BASIS	mm		1,0/1,5 2,0/3,0			1,0/1,5 2,0
Rollenbreite*	mm	500/1000				
Bänderbreite*	mm	≥ 4				
Rollenlänge*	m	50				
Typische Werkstoffdaten für SIGRAFLEX® Folie Typ Z mit Rohdichte 1,0 g/cm³						
Wärmeleitfähigkeit bei 20 °C						
parallel zur Schicht	W/K · m	180 – 200				
senkrecht zur Schicht	W/K · m	4 – 6				
Spezifischer elektrischer Widerstand bei 20 °C						
parallel zur Schichtung	Ωµm	6 – 8				
senkrecht zur Schichtung	Ωµm	650 – 700				
Wärmeausdehnungskoeffizient (20 – 1000 °C)						
parallel zur Schicht	10^{-6}/K	ca. 1				
senkrecht zur Schicht	10^{-6}/K	ca. 50				
Permeabilitätskoeffizient (Luft)						
senkrecht zur Schicht	cm²/s	$< 2 \cdot 10^{-5}$				
Härte nach Shore (D)		30				
Zugfestigkeit**	N/mm²	≥ 4				
Reißdehnung**	%	≥ 1				
Maximal zulässige Druckspannung						
Probe: 20 x 20 mm x Dicke 0,35 mm	N/mm²	220				
0,50 mm	N/mm²	200				
1,00 mm	N/mm²	140				
Druckstandfestigkeit (DIN 52913) $\sigma_{D\ 16h,\ 300°C,\ 50\ N/mm^2}$	N/mm²	≥ 48				
Reibungskoeffizient gegen Stahl, Rautiefe ≤ 10 µm		0,1				
Die Formeln zur Umrechnung der Dichtungskennwerte nach AD Merkblatt B7 lauten		$k_0 \cdot K_D = \sigma_{VU} \cdot b_D$ $k_1 = m \cdot b_D$				

Figure 8.3: Data-sheet for flexible graphite (FG) SIGRAFLEX®from the SGL-Carbon group[121]

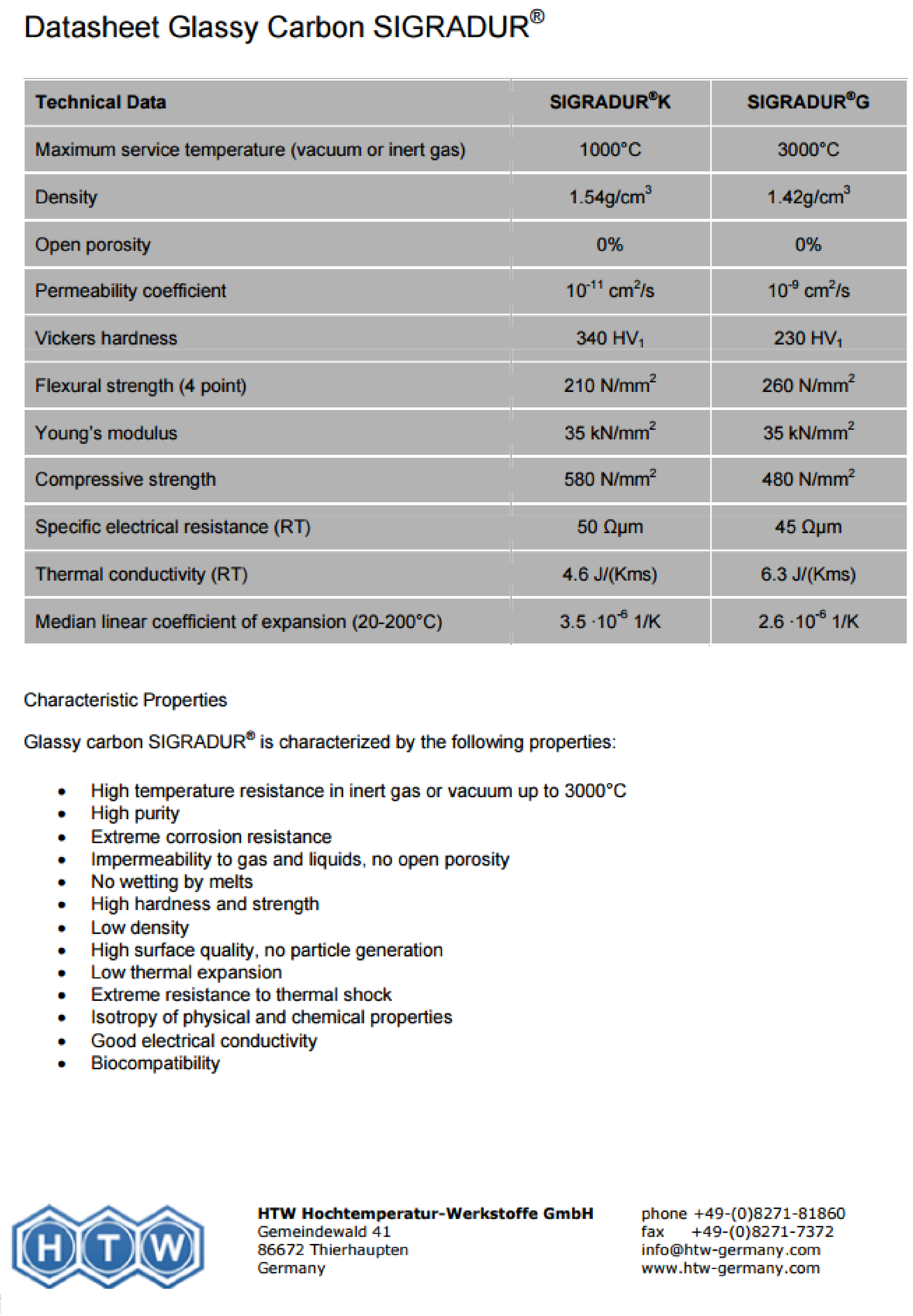

Datasheet Glassy Carbon SIGRADUR®

Technical Data	**SIGRADUR®K**	**SIGRADUR®G**
Maximum service temperature (vacuum or inert gas)	1000°C	3000°C
Density	1.54g/cm^3	1.42g/cm^3
Open porosity	0%	0%
Permeability coefficient	10^{-11} cm^2/s	10^{-9} cm^2/s
Vickers hardness	340 HV$_1$	230 HV$_1$
Flexural strength (4 point)	210 N/mm^2	260 N/mm^2
Young's modulus	35 kN/mm^2	35 kN/mm^2
Compressive strength	580 N/mm^2	480 N/mm^2
Specific electrical resistance (RT)	50 Ωμm	45 Ωμm
Thermal conductivity (RT)	4.6 J/(Kms)	6.3 J/(Kms)
Median linear coefficient of expansion (20-200°C)	$3.5 \cdot 10^{-6}$ 1/K	$2.6 \cdot 10^{-6}$ 1/K

Characteristic Properties

Glassy carbon SIGRADUR® is characterized by the following properties:

- High temperature resistance in inert gas or vacuum up to 3000°C
- High purity
- Extreme corrosion resistance
- Impermeability to gas and liquids, no open porosity
- No wetting by melts
- High hardness and strength
- Low density
- High surface quality, no particle generation
- Low thermal expansion
- Extreme resistance to thermal shock
- Isotropy of physical and chemical properties
- Good electrical conductivity
- Biocompatibility

HTW Hochtemperatur-Werkstoffe GmbH
Gemeindewald 41
86672 Thierhaupten
Germany

phone +49-(0)8271-81860
fax +49-(0)8271-7372
info@htw-germany.com
www.htw-germany.com

Figure 8.4: Data-sheet for glassy carbon (GC) SIGRADUR®from HTW [122]

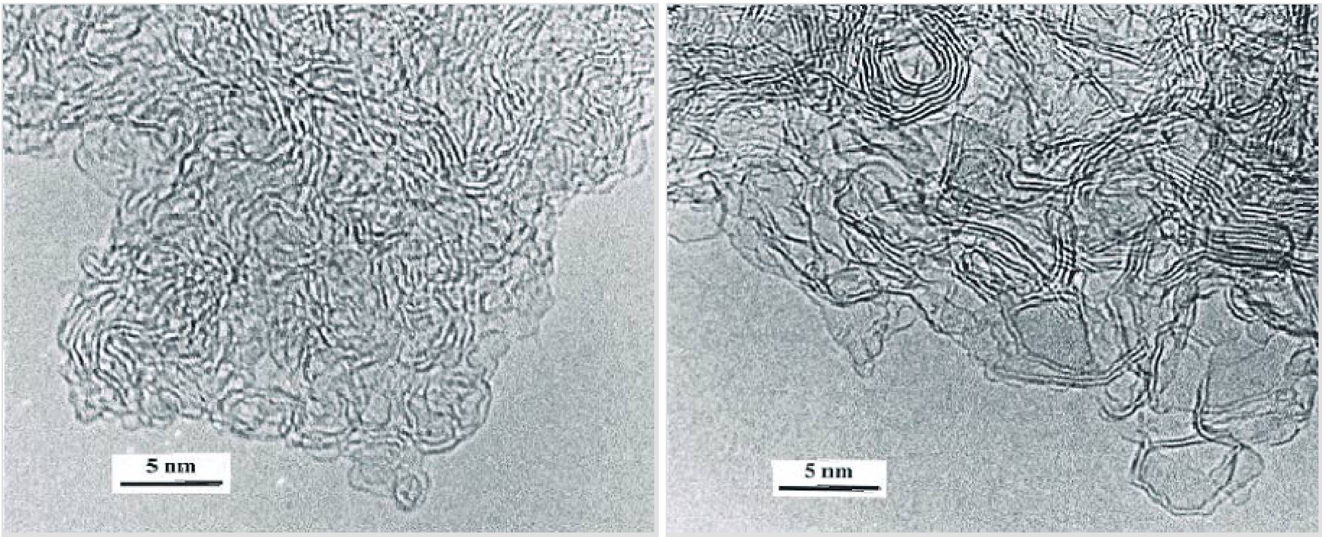

Figure a: TEM images of glassy carbon SIGRADUR© K

Figure b: TEM images of glassy carbon SIGRADUR© G

Figure 8.5: TEM pictures of glassy carbon (GC) SIGRADUR®G and SIGRADUR®K from HTW showing the fullerene like curved and bent graphite planes [123]

Beam conditions

Method	Material	Ion	Energy in MeV/u	Flux in $ions/cm^2s$	Pulse length in ms	Frequency, Hz in Hz
Raman	HOPG	Xe	4.8	$2-3\times10^9$	1.2	5
Raman	HOPG	Sm	4.8	$2-3\times10^9$	1.2	3.4
Raman	HOPG	Au	4.8	$2-3\times10^9$	2	45
Raman	HOPG	Bi	4.8	$1-2\times10^9$	1	3.4
Raman	HOPG	U	4.8	$1-2\times10^9$	0.5	1
Raman	GC	Xe	4.8	$2-3\times10^9$	1.2	5
Raman	GC	Au	4.8	$2-3\times10^9$	2	45
Raman	GC	Bi	4.8	$1-2\times10^9$	1	3.4
Raman	GC	U	4.8	$1-2\times10^9$	0.5	1
Raman	PG	Au	4.8	$1-3\times10^9$	2	45
Raman	PG	Bi	4.8	$1-2\times10^9$	1	3.4
Raman	PG	U	4.8	$1-3\times10^9$	0.5	1
Raman	FG	Au	4.8	$1-3\times10^9$	2	45
Raman	FG	Bi	4.8	$1-3\times10^9$	1	3.4
Raman(InSitu)	HOPG	Sm	4.8	$1-3\times10^9$	1.2	3.4
Raman(InSitu)	PG	Sm	4.8	$1-3\times10^9$	1.2	3.4
Raman Flux	HOPG	Au	4.8	$1-15\times10^9$	2	45
XRD(InSitu)	HOPG	Au	3.6	$3-5\times10^9$	2	45
XRD(InSitu)	PG	Au	3.6	$3-5\times10^9$	2	45
XRD DESY	PG	Au	4.8	$1-2\times10^9$	3	45
XRD DESY	PG	U	5.9	$5-10\times10^9$	0.3	1
XPS	HOPG	U	4.8	$2-3\times10^9$	0.3	1
XPS	PG	U	4.8	$2-3\times10^9$	0.3	1
Dektak	PG	Au	4.8	$3-4\times10^9$	3	45
Resistivity	PG	Xe	4.8	$1-2\times10^9$	1.2	5
Resistivity	PG	Sm	4.8	$1-3\times10^9$	1.2	3.4
Resistivity	PG	Au	4.8	$1-3\times10^9$	3	2 ; 45
Resistivity	PG	U	4.8	$1-3\times10^9$	0.5	1

Table 8.1: Overview of the used ions in the irradiation with the corresponding irradiation parameters

Method	Material	Ion	Energy in MeV/u	Flux in $ions/cm^2s$	Pulse length in ms	Frequency, Hz in Hz
LFA	FG	Au	4.8	$1-3\times10^9$	3	2
LFA	PG	Au	4.8	$1-3\times10^9$	3	2
LFA	PG	Xe	4.8	$4-5\times10^9$	1.2	5
DSC	PG	Au	4.8	$1-3\times10^9$	3	45
Micro-ind	HOPG	Au	4.8	$1-3\times10^9$	2	45
Micro-ind	SNG	Sm	4.8	$1-3\times10^9$	1.2	3.4
Micro-ind	PG	Xe	4.8	$2-3\times10^9$	1.2	5
Micro-ind	PG	Sm	4.8	$2-3\times10^9$	1.2	3.4
Micro-ind	PG	Au	4.8	$2-3\times10^9$	2	45
Micro-ind	PG	U	4.8	$1-2\times10^9$	0.5	1
Micro-ind	CFC	Au	4.8	$1-3\times10^9$	2	45
Micro-ind	MoC	Au	4.8	$1-3\times10^9$	2	45
Nano-inde	HOPG	Au	4.8	$1-3\times10^9$	2	45
Nano-inde	GC	Au	4.8	$1-3\times10^9$	2	45
Nano-inde	PG	Au	4.8	$1-3\times10^9$	2	45
Nano-impact	PG	Au	4.8	$1-3\times10^9$	2	45
Nano-impact	GC	Au	4.8	$1-3\times10^9$	2	45
Nano-impact	MoC	Au	4.8	$1-3\times10^9$	2	45
Nano-popins	HOPG	Au	4.8	$1-3\times10^9$	2	45
IR-camera	PG	Au	4.8	$0.05-20\times10^9$	2	49
IR-camera	GC	Au	4.8	$0.05-20\times10^9$	2	49
IR-camera	POCO-foam	Au	4.8	$0.05-20\times10^9$	2	49
IR-camera	POCO-HTC	Au	4.8	$0.05-20\times10^9$	2	49
IR-camera	Cu-dia	Au	4.8	$0.05-20\times10^9$	2	49
IR-camera	FG	Au	4.8	$0.05-20\times10^9$	2	49
IR-camera	PG	Au	4.8	$0.8-15\times10^9$	2	44
IR-camera	HOPG	Au	4.8	$0.8-15\times10^9$	2	44
IR-camera	POC-HTC	Au	4.8	$0.8-15\times10^9$	2	44
IR-camera	Cu-dia	Au	4.8	$0.8-15\times10^9$	2	44

Table 8.2: Overview of the used ions in the irradiation with the corresponding irradiation parameters

9 Curriculum Vitae

Schulische Ausbildung	
1991-1995	Grundschule, Volksschule Haibach
1995-2005	Gymnasium, Kronberg-Gymnasium Aschaffenburg, Bayern
07/2005	Allgemeine Hochschulreife
Studium	
2005-2009	Maschinenbau und Kunststofftechnik, Hochschule Darmstadt Fachrichtung: Kunststofftechnik
03/2009	Abschluss: Bachelor of Engineering; B.Eng.
2009-2011	Maschinenbau und Kunststofftechnik, Hochschule Darmstadt Fachrichtung: Kunststofftechnik
09/2011	Abschluss: Master of Engineering; M.Eng.
2012-2016	Material- und Geowissenschaften, Technische Universitaet Darmstadt Promotion: Materialwissenschaften
04/2016	Abschluss: Doktor der Ingenieurwissenschaften; Dr.-Ing.
Publikationen	
	C. Hubert et al. Swift heavy ion-induced radiation damage in isotropic graphite studied by micro-indentation and in-situ electrical resistivity, Nuclear Inst. and Methods in Physics Research, B, May 2015, Volume 365, pp 509 - 514, DOI http://dx.doi.org/10.1016/j.nimb.2015.08.056
	K. Kupka **C. Hubert** et al. Intense heavy ion beam-induced temperature effects in carbon-based stripper foils, Journal of Radioanalytical and Nuclear Chemistry, September 2015, Volume 305, Issue 3, pp 875-882, DOI http://dx.doi.org/10.1007/s10967-015-4057-x
	S. Dedera, **C. Hubert** et al.: On-line Raman spectroscopy of calcite and malachite during irradiation with swift heavy ions: Nuclear Inst. and Methods in Physics Research B, May 2015, Volume 365, pp 564 - 568, DOI http://dx.doi.org/10.1016/j.nimb.2015.09.079